UNIVERZITA PALACKÉHO V OLOMOUCI

PŘÍRODOVĚDECKÁ FAKULTA

KATEDRA EXPERIMENTÁLNÍ FYZIKY

DISERTAČNÍ PRÁCE

Funkční nanokompozity pro duální zobrazování fluorescencí a magnetickou rezonancí

Autor práce: Mgr. Radek Ostruszka

Studijní program: Nanotechnologie

Vedoucí práce: doc. RNDr. Karolína Šišková, Ph.D.

Olomouc 2024

BIBLIOGRAFICKÁ IDENTIFIKACE

Jméno a příjmení autora: Radek Ostruszka

Název práce:

Funkční nanokompozity pro duální zobrazování fluorescencí a magnetickou rezonancí

Typ práce: Disertační

Pracoviště: Katedra experimentální fyziky

Vedoucí práce: doc. RNDr. Karolína Šišková, Ph.D.

Rok obhajoby práce: 2024

Abstrakt:

Předložená dizertační práce se především zaměřuje na poskytnutí širšího vhledu do problematiky kovových nanostruktur (NSs) a nanokompozitů (NCPs). Na počátku je práce věnována velikostním přechodům kovového materiálu z makroskopických rozměrů do velikostního režimu nanočástic (NPs) a dále nanoklastrů (NCs), přičemž přechod mezi posledně zmíněnými NSs je pro případ Au detailněji rozebrán. Posléze je text zaměřen na kovové NSs, se kterými jsem se v rámci studia setkal. Jedná se o zlaté nanoklastry (AuNCs) a superparamagnetické nanočástice oxidů železa (SPIONs). V případě AuNCs jsou popisovány vlastnosti optické, zejména tedy absorpční a luminiscenční, a v případě SPIONs pak vlastnosti magnetické. V obou případech jsou rovněž uvedeny jednotlivé strategie syntéz a také praktické využití těchto NSs. Následně práce pojednává o bimetalických NCPs tvořených jak z AuNCs, tak SPIONs, jejich syntéze a praktickém využití. Posléze je popsána matrice užívaná pro syntézu zmíněných NSs, kterou je protein, albumin hovězího séra (BSA). Závěrečná část dizertační práce se věnuje shrnutí vědecké činnosti jejího autora spolu s poznatky z přiložených publikací, které svou náplní postupně směřují od systému referenčního (tj. monometalický nanokompozit sestávající z proteinové matrice a AuNCs, nebo proteinové matrice a SPIONs) až k systému bimetalickému, který kombinuje jak vlastnosti AuNCs, tak i SPIONs. Optimalizované optické a superparamagnetické vlastnosti byly využity při *in vivo* fluorescenčním zobrazování (FI) a zobrazování magnetickou rezonancí (MRI), přičemž prezentovaný optimalizovaný bimetalický systém má potenciál sloužit jakožto efektivní inertní kontrastní látka pro duální FI/MRI.

Klíčová slova:

Zlaté nanoklastry, superparamagnetické nanočástice oxidů železa, hovězí sérový albumin, nanokompozity, monometalické nanokompozity, bimetalické nanokompozity, duální zobrazování, fluorescenční zobrazování, zobrazování magnetickou rezonancí.

Počet stran: 64

Počet příloh: 4

Jazyk: Český

BIBLIOGRAPHICAL IDENTIFICATION

Author's first name and surname: Radek Ostruszka

Title of thesis:

Functional nanocomposites for dual fluorescence and magnetic resonance imaging

Type of thesis: Doctoral

Department: Department of experimental physics

Supervisor: doc. RNDr. Karolína Šišková, Ph.D.

The year of defence: 2024

Abstract:

The presented dissertation thesis mainly focuses on providing a broader insight into the issue of metal nanostructures (NSs) and nanocomposites (NCPs). Initially, the thesis is devoted to the size transitions of the metallic material from the macroscopic dimensions to the size regime of nanoparticles (NPs) and then to nanoclusters (NCs). In the case of Au, the transition between the last mentioned NSs is analysed in more detail. Afterwards, the thesis is focused on the metallic NSs, which I encountered during my studies; namely, gold nanoclusters (AuNCs) and superparamagnetic iron oxide nanoparticles (SPIONs). In the case of AuNCs, optical properties are described, specifically absorption and luminescence. Regarding SPIONs, a description of the magnetic properties is given. In both cases, individual synthetic strategies and the practical use of these NSs are also presented. Subsequently, the thesis discusses bimetallic NCPs formed of both the AuNCs and SPIONs, their synthesis and practical usage. Then, the protein matrix (namely, bovine serum albumin, BSA) employed for the synthesis of the mentioned NSs is introduced. The final part of the dissertation thesis is dedicated to a summary of the scientific activity of its author together with findings described in the attached publications. The content of these publications gradually goes from a reference system (i.e., monometallic nanocomposite consisting of a protein matrix and AuNCs, or a protein matrix and SPIONs) towards a bimetallic system, which combines the properties of both the AuNCs and SPIONs. The optimized optical and superparamagnetic properties have been exploited in *in vivo* fluorescence imaging (FI) and magnetic resonance imaging (MRI). The presented optimized bimetallic system has the potential to serve as an effective inert contrast agent for dual FI/MRI.

Prohlašuji, že jsem tuto disertační práci vypracoval samostatně, pod vedením doc. RNDr. Karolíny Šiškové, Ph.D. a za použití literatury uvedené v kapitole 4. Reference.

V Olomouci dne……………………   ………………………………..…

SEZNAM ZKRATEK uvedených v textu

Zkratka	Český název/*Anglický název*
AuNCs	zlaté nanoklastry/*gold nanoclusters*
AuNPs	zlaté nanočástice/*gold nanoparticles*
AuNSs	zlaté nanostruktury/*gold nanostructures*
BSA	hovězí sérový albumin/*bovine serum albumin*
DMSA	2,3-dimerkaptobutandiová kyselina/*2,3-dimercaptobutanedioic acid*
DOS	hustota energetických stavů/*density of states*
ECL	elektrochemiluminiscence/*electrochemiluminescence*
EDS	energiově disperzní spektroskopie/*energy dispersive spectroscopy*
EPR	elektronová paramagnetická rezonance/*electron paramagnetic resonance*
FI	fluorescenční zobrazování/*fluorescence imaging*
GSH	glutathion/*glutathione*
HOMO	nejvyšší obsazený molekulový orbital/*highest occupied molecular orbital*
HRTEM	transmisní elektronová mikroskopie s vysokým rozlišením/*high-resolution transmission electron microscopy*
HZT	hustota zářivého toku během doby jednoho laserového impulzu/*fluence*
LMCT	přenos náboje z ligandu na kov/*ligand-to-metal charge transfer*
LMMCT	přenos náboje z ligandu na systém kov-kov/*ligand-to-metal-metal charge transfer*
LUMO	nejnižší neobsazený molekulový orbital/*lowest unoccupied molecular orbital*
MRI	zobrazování magnetickou rezonancí/*magnetic resonance imaging*
MUA	11-merkaptoundekanová kyselina/*11-mercaproundecanoic acid*
NCs	nanoklastry/*nanoclusters*
NCP	nanokompozit/*nanocomposite*
NCPs	nanokompozity/*nanocomposites*
NHS	N-hydroxysukcinimid
NPs	nanočástice/*nanoparticles*
NSs	nanostruktury/*nanostructures*
PL	fotoluminiscence/*photoluminescence*
QY	kvantový výtěžek/*quantum yield*
SPIONs	superparamagnetické nanočástice oxidů železa/*superparamagnetic iron oxide nanoparticles*
SPR	povrchová plazmonová rezonance/*surface plasmon resonance*
SR	thiolát/*thiolate*
UV	ultrafialová/*ultraviolet*
UVA oblast	ultrafialová oblast A/*ultraviolet region A*
vis	viditelná/*visible*

OBSAH

1. Rozšířený přehled problematiky

1.1. Od objemového kovu k NCs

Jedním z faktorů ovlivňujících fyzikálně-chemické vlastnosti kovového materiálu je jeho velikost, přičemž s její změnou lze odlišit několik rozeznatelných přechodových oblastí (viz Obrázek 1) [1].
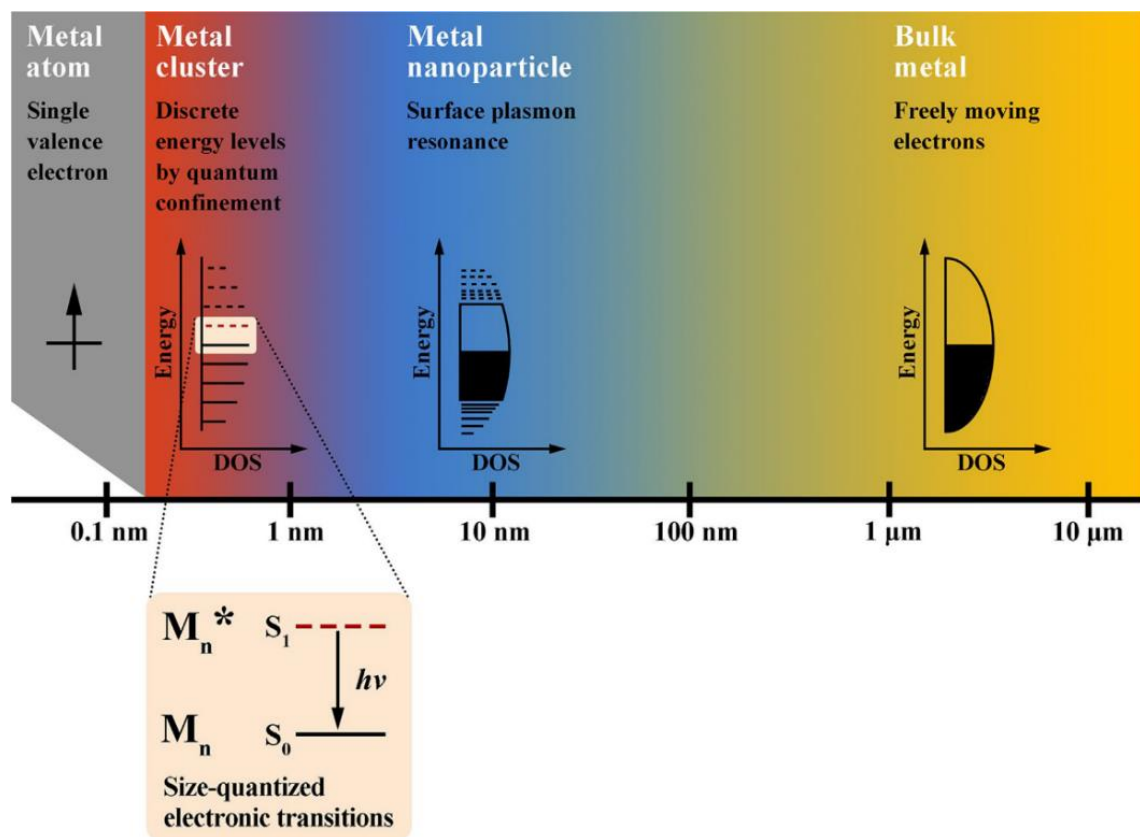
Obrázek 1: *Rozdílná hustota energetických stavů (DOS) v závislosti na velikosti kovového materiálu. Zprava jdeme z oblasti objemového kovu, kdy je DOS tvořena spojitými pásy, přes oblast nanočástic, kdy se spojitost pásů začíná s úbytkem atomů rozpadat, až se dostáváme do oblasti nanoklastrů, jejichž DOS je tvořena víceméně diskrétními energetickými hladinami, mezi kterými může při interakci se zářením docházet k elektronovým přechodům. Převzato z [2].*

Kovy makroskopických rozměrů jsou tvořeny tak obrovským množstvím atomů, že jejich hustota energetických stavů (DOS) je natolik vysoká, že se projevuje existencí spojitých energetických pásů (viz Obrázek 1), které jsou výsledkem lineárních kombinací nezměrného počtu energeticky velice podobných atomových orbitalů. Pásovou strukturu kovů lze charakterizovat pomocí valenčního a vodivostního pásu, zatímco zakázaný pás

v případě kovů neexistuje, jelikož se oba zmíněné pásy částečně překrývají [1,3]. Vlivem této skutečnosti se elektrony mohou za normálních podmínek vyskytovat volně také v pásu vodivostním, díky čemuž jsou kovy výbornými elektrickými vodiči [4]. Emise záření při excitaci objemového Au, Cu a jejich slitiny byla poprvé demonstrována v roce 1969 autorem Mooradian (1969) [5] jako neefektivní proces s QY v řádu 10^{-10}. Podstatou tohoto optického jevu je zářivá rekombinace vodivostních elektronů s energií nižší, než je energie Fermiho hladiny, a děr nacházejících se v d pásu, které lze indukovat excitací jak argonovým laserem, tak i vysokotlakou rtuťovou obloukovou lampou [5].

Zmenšíme-li velikost kovové částice na hodnotu srovnatelnou či menší, než je střední volná dráha vodivostních elektronů, dostaneme se do oblasti kovových NPs, kdy pohyb elektronů začíná být omezován rozměrem kovu, a k interakcím se zářením tak dochází primárně v rámci povrchu částice [3]. Tato skutečnost je příčinou optického jevu nazývaného jako povrchová plazmonová rezonance (SPR), jejíž podstatou jsou kolektivní oscilace vodivostních elektronů během interakce se zářením [1,3]. Díky tomuto NPs vykazují silnou absorpci světla, nicméně intenzita fluorescence je relativně slabá, kdy QY se pohybuje řádově od 10^{-7} do 10^{-2}, přičemž velikost, tvar a metoda přípravy NPs mají vliv na hodnotu QY [6]. DOS je charakterizována existencí kvazi-spojité pásové struktury (viz Obrázek 1) [7,8].

Zmenšujeme-li velikost kovové částice nadále, až na hodnotu srovnatelnou s Fermiho vlnovou délkou elektronu (tj. de Broglieho vlnová délka elektronu na Fermiho hladině, přičemž pro případ Au je ≈ 0,5 nm [9]), dochází postupně k dalšímu řídnutí energetických hladin, a tím k rozpadu kvazi-spojité pásové struktury NPs, kdy DOS začíná být tvořena víceméně diskrétními energetickými hladinami (viz Obrázek 1), mezi kterými může docházet k elektronovým přechodům vlivem interakce se zářením [3,10,11]. Dostáváme se do oblasti NCs, jejichž chování je podobné molekulám a jejich chemické, optické a elektrické vlastnosti se výrazně odlišují jak od NPs, tak rovněž i od objemového kovu [3,7,10]. Průměr kovového jádra takovýchto NSs bývá zpravidla menší než 2 nm [12–18]. Průměr větší než 2 nm stanovený pomocí transmisní elektronové mikroskopie s vysokým rozlišením (HRTEM) může souviset se změnou vlastností studovaného systému v důsledku *in situ* tvorby zlatých nanočástic (AuNPs), jež byla autory Ostruszka a kol. (2022) [19] pozorována pod fokusovaným svazkem elektronů při uplatnění většího zvětšení v případě HRTEMu a/nebo během mapování s využitím energiově disperzní spektroskopie (EDS). Pozorovaná *in situ* tvorba NPs může být

vysvětlena schopností elektronů redukovat přítomné kationtové stavy Au, konkrétně Au(I) a Au(II), na Au(0), jež mohou být k BSA slaběji vázány, díky čemuž může docházet k jejich migraci a koalescenci (slučování se) s jinými Au(0), a tudíž k tvorbě větších NSs [19]. NCs již nevykazují SPR [1,3], naproti tomu však vykazují silnou luminiscenci s QY v řádu jednotek, a dokonce i desítek procent [12,13,16,18].

V případě zlatých nanostruktur (AuNSs) byl přechod mezi NPs a NCs, tedy mezi chováním kovovým (plazmonickým) a nekovovým (tj. chování podobné molekulám), mnoha autory studován [14,17,20–25], nicméně stále existuje nejasnost týkající se přechodové oblasti (viz Obrázek 2).
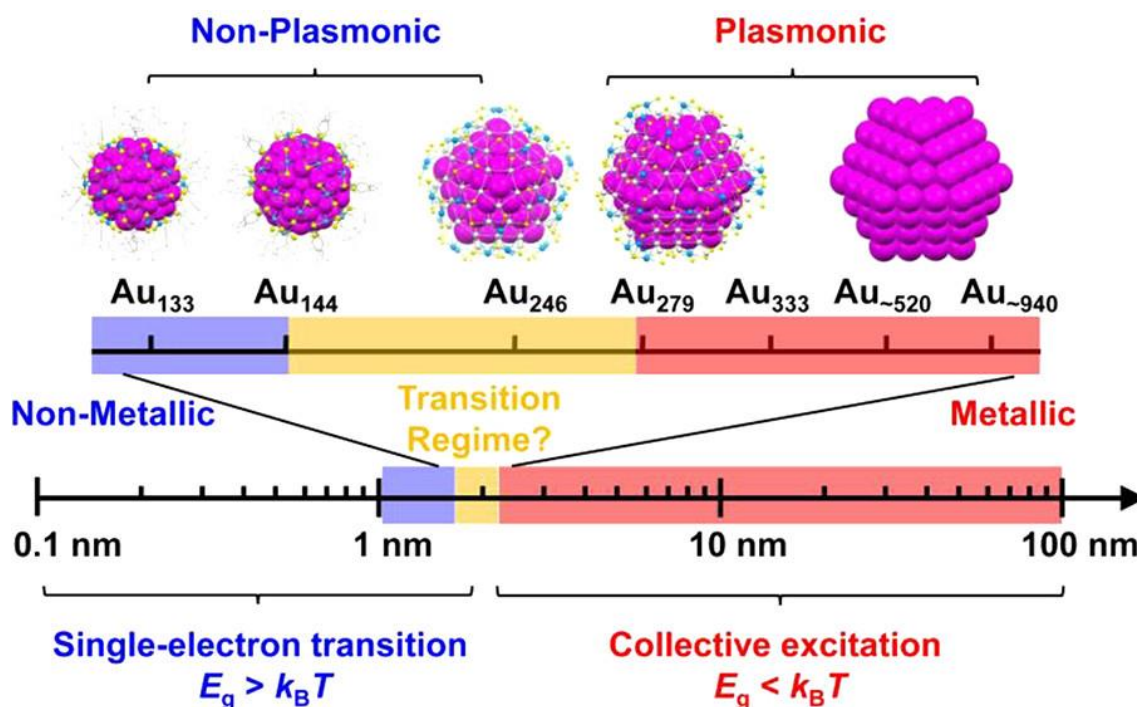
Obrázek 2: *Diagram zobrazující přechod mezi kovovým (plazmonickým, $\geqq Au_{279}$) chováním NPs, kdy energetický rozdíl mezi nejvyšším obsazeným molekulovým orbitalem a nejnižším neobsazeným molekulovým orbitalem značený jako $E_g < k_B T$ (kde $k_B = 8{,}617333262 \cdot 10^{-5}$ $eV \cdot K^{-1}$ značí Boltzmannovu konstantu a T označuje termodynamickou teplotu; v případě, kdy $T = 293{,}15$ K je $E_g \approx 25$ meV), a nekovovým (neplazmonickým, $\leqq Au_{144}$) chováním NCs, kdy $E_g > k_B T$. Převzato z [8].*

Ke studiu tohoto přechodu lze využít NCs tvořené přesným počtem atomů Au se známou krystalickou strukturou [8]. Zatímco definice kovového chování je relativně jednoduchá, tj. stav, kdy je energetický rozdíl mezi nejvyšším obsazeným molekulovým orbitalem (HOMO) a nejnižším neobsazeným molekulovým orbitalem (LUMO) značený jako E_g

3

zanedbatelně malý (řádově $k_B T$, kde $k_B = 8{,}617333262 \cdot 10^{-5}$ eV·K^{-1} značí Boltzmannovu konstantu a T označuje termodynamickou teplotu; pro $T = 293{,}15$ K je $k_B T \approx 25$ meV), experimentální určení takovýchto malých hodnot E_g je komplexní z důvodu možných tepelných excitací valenčních elektronů [8]. Jin a spol. [8] shrnují kritéria rozhodující o kovovém či nekovovém chování dané nanostruktury z hlediska použité metody (viz Tabulka 1).

Tabulka 1: *Kritéria pro rozlišení mezi kovovým chováním nanočástic a nekovovým chováním nanoklastrů a jejich věrohodnost. Převzato z [8], upraveno s využitím [26] a přeloženo.*

Kritérium	Kovové nanostruktury	Nekovové nanostruktury	Věrohodnost
Definice	$E_g \leq k_B T$	$E_g \geq k_B T$	(teoretické)
Optická absorpční měření E_g	-	až do ≈ 500 meV	střední
ECH měření E_g	-	až do ≈ 100 meV (možná i 50 meV)	vysoká
UV-vis-NIR absorpce	jeden pík SPR (sférické částice)	více píků (nezávislé na tvaru částic)	střední
Absorpce při nízkých teplotách	spektrum méně ovlivněné teplotou	píky jsou ostřejší, intenzivnější a hypsochromně posunuté	vysoká
TA – průběh spektra	jeden pík GSB (sférické částice)	více píků GSB (nezávislé na tvaru)	střední
TA – ESLT	1-5 ps (e-ph interakce) 10-100 ps (ph-ph interakce)	několik ps až µs (závislé na velikosti a struktuře)	nízká/střední
TA – závislost ESLT na HZT	ano (výraznější s rostoucí velikostí)	ne	střední
TA – frekvence oscilací	platí zákon 1/R (závislé na velikosti)	neplatí zákon 1/R (závislé na struktuře)	střední

Pozn. 1: *e-ph interakce = interakce mezi elektronem a fononem, ECH = elektrochemická, ESLT = doba života excitovaného stavu, GSB = vybělování základního stavu, HZT = hustota zářivého toku během doby jednoho laserového impulzu (anglicky fluence), NIR oblast = blízká infračervená oblast, ph-ph interakce = interakce mezi fonony, SPR = povrchová plazmonová rezonance, TA – tranzientní absorpce, UV oblast = ultrafialová oblast, vis oblast = viditelná oblast.* **Pozn. 2:** *Hypsochromní posun je posun směrem ke kratším vlnovým délkám. Zákon 1/R popisuje závislost frekvence koherentních oscilací ve spektru tranzientní absorpce na reciproké hodnotě poloměru nanočástice.*

V práci Varnavski a kol. (2010) [20] zjistili, že absorpční spektra měřená v hexanu vykazují pík SPR při vlnové délce 520 nm pouze v případě AuNSs o velikosti 3 a 4 nm a že změna v dynamice časově rozlišených spektroskopií (konkrétně tranzientní absorpce a fluorescence) a také účinném průřezu dvoufotonové absorpce nastává ve všech třech případech mezi velikostmi 2,2 a 3 nm. Z tohoto tedy vyplývá, že kritickou velikostí pro pozorování efektu kvantového omezení je 2,2 nm ($\approx$ 300 atomů Au [20]). Na druhou stranu Philip a kol. (2012) [21] srovnali průběh nelineární propustnosti připravených AuNSs a Au nanokrystalů o velikosti 4 nm, z čehož vyvodili, že $Au_{25}(SR)_{18}$ a $Au_{38}(SR)_{24}$ nevykazují žádné kovové chování, kdežto $Au_{144}(SR)_{60}$ vykazuje mírný náznak kovového chování. Dále Negishi a kol. (2015) [14] zkoumali průběh teplotní závislosti absorpčních spekter (šířka, pozice a intenzita píků) připravených AuNSs a zjistili, že v případě $Au_{144}(SR)_{60}$ (o průměru 1,6 $\pm$ 0,1 nm) a NSs menších dochází se snižující se teplotou (až na 25 K) k hypsochromnímu posunu (tj. posun směrem ke kratším vlnovým délkám), zužování a zvyšování intenzity píků, což poukazuje na nekovové chování NCs, kdežto v případě $Au_{187}(SR)_{68}$ (o průměru 1,8 $\pm$ 0,3 nm) a NSs větších se v rozsahu vlnových délek 520 – 540 nm nachází pík SPR, přičemž se změnou teploty nedochází ke změně parametrů spektra, což naopak poukazuje na chování kovové. Navíc, s využitím teorie funkcionálu hustoty srovnali teoretická absorpční spektra některých AuNSs se spektry experimentálními a získali jejich dobrou shodu. Z průběhu absorpčních spekter Zhou a kol. (2016) [22] vyvodili, že v případě Au_{144} a menších NSs se ve spektru vyskytuje několik absorpčních píků, zatímco v případě Au_{333} a větších NSs se nachází pouze výrazný pík SPR, který se se snižující velikostí kovového jádra rozšiřuje. Následně s pomocí femtosekundové tranzientní absorpční spektroskopie zkoumali závislost doby života excitovaného stavu na hustotě zářivého toku během doby jednoho laserového impulzu (HZT; jedná se o množství energie obsažené v jednom impulzu přepočtené na jednotku plochy; anglicky fluence), pomocí čehož prokázali kompletní nezávislost doby života excitovaného stavu na HZT v případě Au_{144} (a to pro dvě různé vlnové délky), což poukazuje na chování nekovové. Naopak v případě Au_{333} se začíná projevovat slabá závislost jak v případě vlnové délky píku SPR, tak i jiné zkoumané vlnové délky. Nicméně, v průběhu spektra tranzientní absorpce Au_{333} (viz Obrázek 3) je patrný výskyt dvou píků vybělování základního stavu a dále také interakce e-ph (interakce mezi elektronem a fononem) je pomalejší, což nakonec indikuje, že Au_{333} vykazuje jak kovové, tak i nekovové chování. Autoři poté zkoumali katalytické účinky těchto NSs na oxidaci

CO a elektrokatalytické účinky na oxidaci ethanolu, kdy byl pozorován vliv přechodové oblasti na účinnost katalýzy.
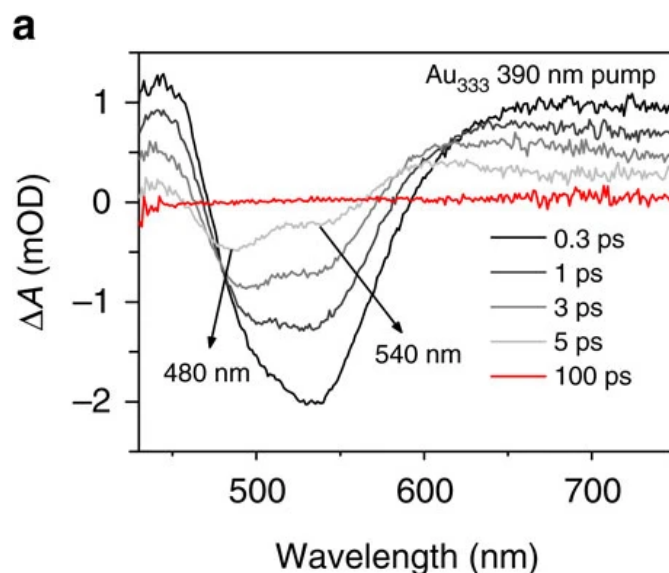
Obrázek 3: *Spektrum tranzientní absorpce Au$_{333}$ při různých časových zpožděních. Vlnová délka pump pulzu je 390 nm. Převzato z [22].*

Podobných výsledků z absorpční spektroskopie a tranzientní absorpční spektroskopie dosáhli i Kwak a kol. (2017) [23], kdy se v případě Au$_{333}$(SR)$_{79}$ objevuje v absorpčním spektru pík SPR a začíná se projevovat slabá závislost doby života excitovaného stavu na HZT. Zhou a kol. (2017) [24] připravili pouze Au$_{246}$(SR)$_{80}$, přičemž v absorpčním spektru se vyskytuje několik píků a doba života excitovaného stavu je nezávislá HZT. Obojí poukazuje na nekovové chování této nanostruktury. Sakthivel a kol. (2018) [17] studovali AuNSs jednak pomocí ustálené (anglicky steady-state) a časově rozlišené absorpční spektroskopie, jednak prostřednictvím teoretických výpočtů s využitím časově závislé teorie funkcionálu hustoty. Vzhledem k přítomnosti píku SPR v absorpčním spektru Au$_{279}$(SR)$_{84}$, průběhu spektra tranzientní absorpce a závislosti doby excitovaného stavu na HZT rozhodli o kovovém chování této nanostruktury. Na kovovém chování Au$_{279}$(SR)$_{84}$ se shodují také Higaki a kol. (2018) [25], kteří pozorovali ostrý přechod mezi Au$_{246}$(SR)$_{80}$ a Au$_{279}$(SR)$_{84}$, který je patrný jednak z absorpčního spektra (pík SPR při vlnové délce 506 nm; jeho poloha se se změnou teploty nemění), jednak z průběhu spektra tranzientní absorpce a také ze závislosti doby života excitovaného stavu na HZT.

Přehled připravených AuNSs včetně počtu atomů Au, průměru kovového jádra, užitého thiolového ligandu a barevného odlišení kovového a nekovového chování jsou uvedeny v tabulce níže (viz Tabulka 2).

Tabulka 2: *Shrnutí připravených AuNSs značených jako $Au_x(SR)_y$, kde index x představuje počet atomů Au a index y označuje počet thiolátových (SR) ligandů, uvedených s příslušným průměrem kovového jádra d_j.*

Reference	Thiolový ligand	$Au_x(SR)_y$	d_j [nm]
[20]	1-hexanthiol	$Au_{25}(SR)_{18}$	$1,1 \pm 0,2$
		$Au_{144}(SR)_{60}$	$1,7 \pm 0,2$
		$Au_{309}(SR)_{92}$	$2,2 \pm 0,2$
		$Au_{976}(SR)_{187}$	$3,0 \pm 0,3$
		$Au_{2406}(SR)_{326}$	$4,0 \pm 0,1$
[21]	2-fenylethanthiol	$Au_{25}(SR)_{18}$	-
		$Au_{38}(SR)_{24}$	-
		$Au_{144}(SR)_{60}$	-
[14]	1-dodekanthiol	$Au_{38}(SR)_{24}$	$1,1 \pm 0,1$
		$Au_{104}(SR)_{45}$	$1,4 \pm 0,3$
		$Au_{130}(SR)_{50}$	$1,5 \pm 0,3$
		$Au_{144}(SR)_{60}$	$1,6 \pm 0,1$
		$Au_{187}(SR)_{68}$	$1,8 \pm 0,3$
		$Au_{\approx226}(SR)_{\approx76}$	$2,0 \pm 0,5$
		$Au_{\approx253}(SR)_{\approx90}$	$2,1 \pm 0,4$
		$Au_{329}(SR)_{84}$	$2,2 \pm 0,4$
		$Au_{\approx356}(SR)_{\approx112}$	$2,2 \pm 0,3$
		$Au_{\approx520}(SR)_{\approx130}$	$2,4 \pm 0,2$
[22]	2-fenylethanthiol	Au_{25}	$1,0$
		Au_{38}	$1,2$
		Au_{144}	$1,7$
		Au_{333}	$2,3$
		$Au_{\approx520}$	$2,9$
		$Au_{\approx940}$	$3,5$
[23]	1-hexanthiol	$Au_{25}(SR)_{18}$	-
		$Au_{38}(SR)_{24}$	-
		$Au_{67}(SR)_{35}$	-
		$Au_{102}(SR)_{44}$	-
		$Au_{144}(SR)_{60}$	-
		$Au_{333}(SR)_{79}$	-
[24]	4-methylbenzenthiol	$Au_{246}(SR)_{80}$	$2,2$
[17]	4-*tert*-butylbenzenthiol	$Au_{36}(SR)_{24}$	$1,3$
		$Au_{44}(SR)_{28}$	$1,4$
		$Au_{133}(SR)_{52}$	$1,7$
		$Au_{279}(SR)_{84}$	$2,2$
[25]	4-*tert*-butylbenzenthiol	$Au_{246}(SR)_{80}$	$2,2$
		$Au_{279}(SR)_{84}$	$2,25$

Pozn.: *modrý text = nekovové chování, zelený text = přechodová oblast, červený text = kovové chování.*

## 1.2. AuNCs a jejich optické vlastnosti ovlivněné několika faktory

AuNCs značené jako $Au_n(SR)_m$, kde *n* označuje počet atomů Au a *m* počet thiolátových (SR) ligandů, představují modelový systém, jehož **struktura** se obecně skládá z kovového jádra a vnějšího obalu tvořeného jak povrchovými atomy Au, tak samotnými SR ligandy. Přítomnost tohoto obalu komplikuje studium optických vlastností AuNCs vzhledem k tomu, že nejen kovové jádro, ale i obal přispívá svými energetickými hladinami k hraničním molekulovým orbitalům [26], tj. HOMO a LUMO. Výzkumný tým Jin a spol. [27] poprvé uvedli do souvislosti krystalovou strukturu a optické vlastnosti aniontu modelové sloučeniny $Au_{25}(SR)_{18}^-$ (kde $R = CH_2CH_2Ph$ představuje fenylethylový zbytek) provedením výpočtů s užitím časově závislé teorie funkcionálu hustoty týkajících se elektronové struktury (viz Obrázek 4A) a optického absorpčního spektra (viz Obrázek 4B) [27].
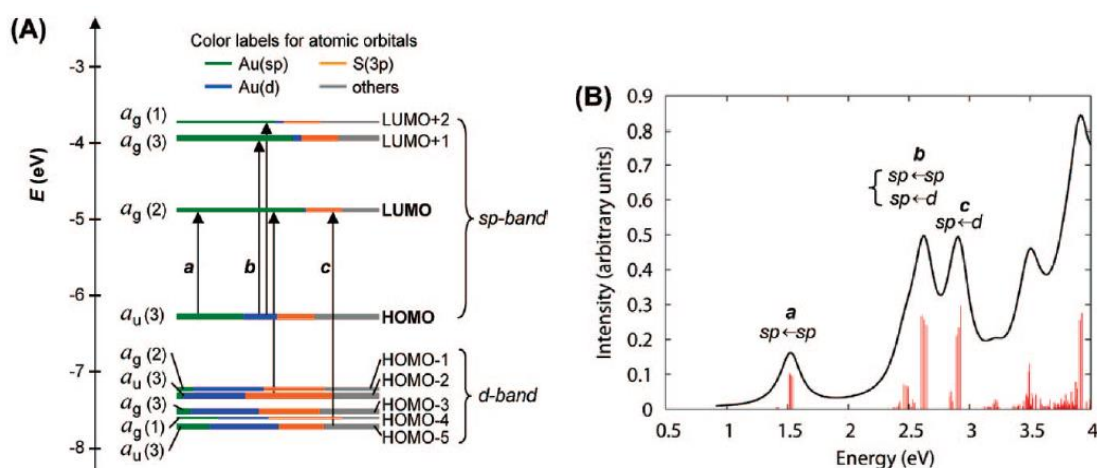
Obrázek 4: *(A) Kohn-Shamův diagram energetických hladin molekulových orbitalů aniontu modelové sloučeniny $Au_{25}(SR)_{18}^-$, kde R představuje fenylethylový zbytek. Barevné označení každého molekulového orbitalu naznačuje relativní příspěvek atomových orbitalů Au (6sp) (zeleně), Au (5d) (modře), S (3p) (oranžově) a ostatních komponent (šedě). Nalevo je uvedena symetrie (a_g, a_u) a stupeň degenerace (číslo v závorce) daného molekulového orbitalu. HOMO = nejvyšší obsazený molekulový orbital, LUMO = nejnižší neobsazený molekulový orbital. (B) Teoretické absorpční spektrum $Au_{25}(SR)_{18}^-$. Převzato z [27].*

Na základě Kohn-Shamova diagramu energetických hladin molekulových orbitalů Jin a spol. [27] přisoudili jednotlivé píky v teoretickém absorpčním spektru (viz Obrázek 4B) aniontu modelové sloučeniny elektronovým přechodům mezi jejími energetickými hladinami (viz Obrázek 4A). Pík při 1,52 eV (≈ 816 nm) přiřadili přechodu

mezi hladinami HOMO a LUMO, jenž je v obou obrázcích označen písmenem a. Jde tedy v podstatě o vnitropásový (sp ← sp) přechod. Pík při 2,63 eV (≈ 471 nm) přiřadili jak vnitropásovému, tak mezipásovému (sp ← d) přechodu (oba označeny písmenem b) a pík při 2,91 eV (≈ 426 nm) přiřadili mezipásovému přechodu, který je označen písmenem c. Jelikož jsou hladiny HOMO a LUMO (a také HOMO-1 a LUMO+1) složeny převážně z atomových orbitalů Au v kovovém jádru, na pík při 1,52 eV lze pohlížet jako na přechod, jenž je zcela definován elektronovou a geometrickou strukturou kovového jádra [27]. K odlišnému výsledku dospěli Nobusada a Iwasa (2007) [28], kteří přisoudili absorpční pík při 1,77 eV (≈ 702 nm) přechodu mezi hladinami HOMO a LUMO, kdy LUMO je primárně tvořen orbitaly nacházejícími se okolo atomu Au sdíleného dvěma ikosaedrálními Au_{13} jádry. Rozdílnost výsledků obou skupin autorů poukazuje na vliv struktury nanoklastru na jeho absorpční vlastnosti. Tvar teoretického (viz Obrázek 4B) a experimentálního (viz Obrázek 5) absorpčního spektra si odpovídá, nicméně je pozorovatelný bathochromní posun (tj. posun směrem k delším vlnovým délkám) píků v teoretickém spektru, který lze přisoudit interakcím zjednodušených ligandů [6].
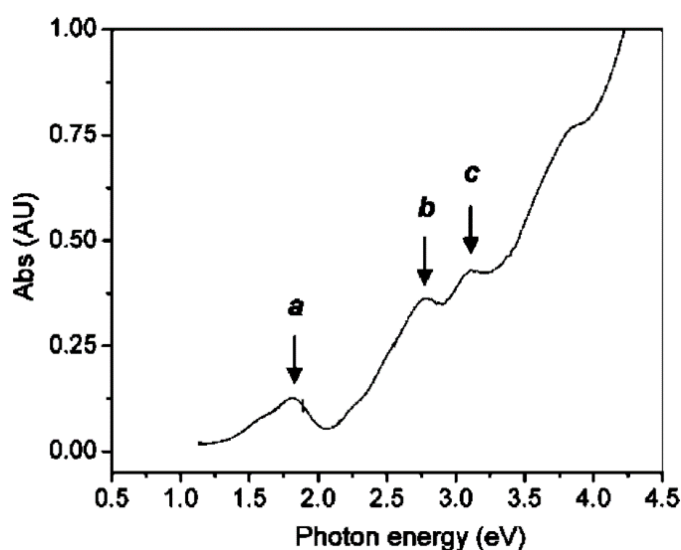
Obrázek 5: *Experimentální absorpční spektrum aniontu modelové sloučeniny $Au_{25}(SR)_{18}^{-}$, přičemž R představuje fenylethylový zbytek. Pík a se nachází při 1,8 eV (≈ 689 nm), pík b při 2,75 eV (≈ 451 nm) a pík c při 3.1 eV (≈ 400 nm) [27]. Převzato z [27].*

Rentgenová krystalografická analýza odhalila, že Au_{25} nanoklastr se skládá z centrovaného ikosaedrálního Au_{13} jádra, které je obklopeno vnějším obalem složeným

ze zbývajících 12 atomů Au a 18 thiolátových ligandů, přičemž komponenty vnějšího obalu spolu vytvářejí motiv, v rámci kterého jsou 3 atomy S a 2 atomy Au uspořádány do tvaru písmene V (-S-Au-S-Au-S-) a jsou k jádru vázány skrze S-Au a Au-Au vazby (viz Obrázek 6) [27].
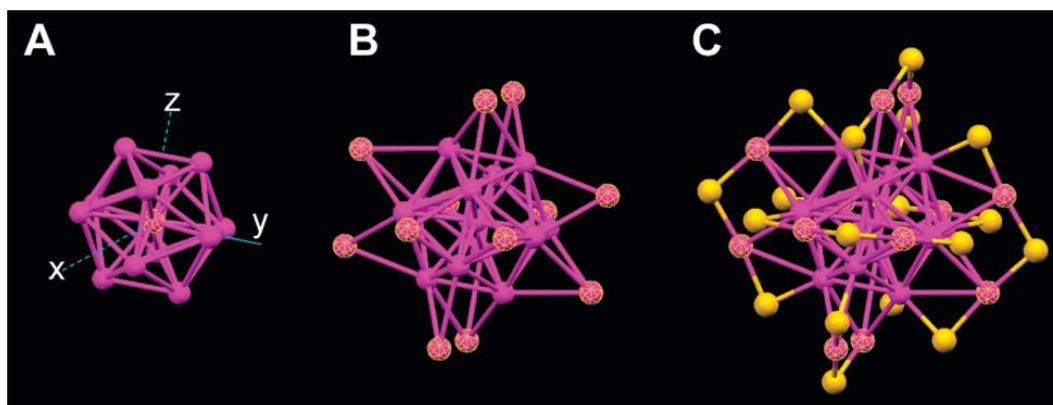
Obrázek 6: *Krystalová struktura aniontu modelové sloučeniny $Au_{25}(SR)_{18}^-$ (R představuje fenylethylový zbytek). (A) centrované ikosaedrální Au_{13} jádro, (B) Au_{13} jádro s vnějšími 12 atomy Au (purpurová), (C) Au_{13} jádro s vnějšími 12 atomy Au a 18 atomy S (žlutá) thiolátových ligandů (fenylethylové zbytky jsou pro lepší přehlednost vynechány). Převzato z [27].*

Kromě struktury nanoklastru má na optické vlastnosti vliv i jeho **velikost**. Zhou a kol. (2019) [26] připravili sérii 16 různých AuNCs lišící se svou velikostí (v rozsahu počtu atomů Au od Au_{23} po Au_{246}) a případně i strukturou, přičemž využili tripeptid glutathion (GSH) jakožto stabilizující a redukční činidlo. Na základě srovnání průběhů ustálených absorpčních spekter, spekter tranzientní absorpce, velikosti E_g a dynamiky excitovaného stavu rozdělili AuNCs do tří velikostních režimů (viz Tabulka 3).

Tabulka 3: *Velikostní režimy AuNCs dle [26]. Veličina E_g představuje energetický rozdíl mezi nejvyšším obsazeným molekulovým orbitalem a nejnižším neobsazeným molekulovým orbitalem.*

AuNCs	Počet atomů Au	E_g [eV]	ESLT	Optické vlastnosti
Ultramalé	< 50	2,1–1,3	≈ 100 ns	primárně dány strukturou
Středně velké	50–100	1,3–0,4	100–1 ns	některé dány spíše strukturou, jiné velikostí
Velké	> 100	0,4–0,0	700–1,5 ps	výhradně dány velikostí

Pozn.: *ESLT = doba života excitovaného stavu.*

Také **oxidační stav** může ovlivnit průběh absorpčního spektra. Aniont modelové sloučeniny $Au_{25}(SC_2H_4Ph)_{18}^-$ vykazuje 3 hlavní absorpční píky nacházející se při 400, 450 a 670 nm (viz Obrázek 7) a také široké rameno okolo 800 nm a menší rameno okolo 550 nm [29]. Oxidací této sloučeniny Liu a kol. (2011) [7] získali neutrální formu $Au_{25}(SC_2H_4Ph)_{18}^0$ a pozorovali, že se pík při 400 nm stal více výrazným (viz Obrázek 7), zatímco pík při 450 nm naopak méně výrazným, a současně rameno okolo 800 nm zaniklo a objevilo se malé rameno okolo 630 nm. Takováto změna v absorpčním spektru je konzistentní s pozorováním Zhu a kol. (2008) [29], kteří ponechali roztok čistého $Au_{25}(SC_2H_4Ph)_{18}^-TOA^+$ (TOA^+ označuje tetraoktylamonný kationt) samovolně oxidovat na vzduchu za přeměny v neutrální $Au_{25}(SC_2H_4Ph)_{18}^0$. Další oxidací Liu a kol. (2011) [7] získali kladně nabitou formu $Au_{25}(SC_2H_4Ph)_{18}^+$, přičemž pozorovali, že píky při 400 a 450 nm jsou méně výrazné (viz Obrázek 7) a že v případě píku při 670 nm dochází k mírnému hypsochromnímu posunu k 660 nm.
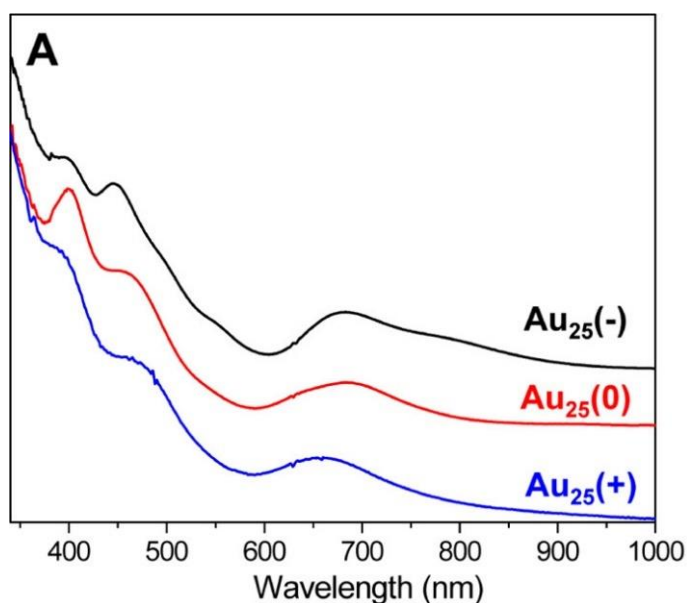
Obrázek 7: *Absorpční spektra [Au₂₅(SR)₁₈]ᵍ, kde R představuje fenylethylový zbytek a q = {-1, 0, 1}. Převzato z [30].*

Teplota je dalším faktorem, který může mít na absorpční spektrum vliv. Devadas a kol. (2011) [31] připravili $Au_{25}(SC_6H_{13})_{18}$ a $Au_{38}(SC_2H_4Ph)_{24}$ mající různý počet atomů Au (jak v jádře, tak i počet atomů celkový), každý s využitím jiného thiolového ligandu (postupně 1-hexanthiol a 2-fenylethanthiol). S klesající teplotou se píky v absorpčním spektru stávaly ostřejšími, přičemž se začala se objevovat vibrační struktura, a rovněž se

11

absorpční maxima posouvala směrem ke kratším vlnovým délkám (viz Obrázek 8) [31]. Objevení vibrační struktury vysvětlují na základě snížení interakcí mezi elektrony a fonony.
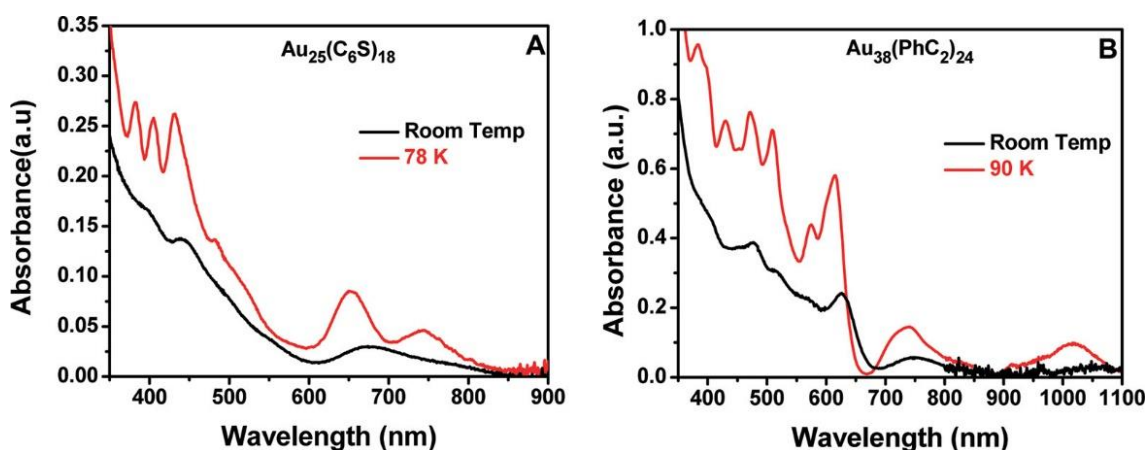

Obrázek 8: *Absorpční spektra (A) $Au_{25}(C_6S)_{18}$ a (B) $Au_{38}(PhC_2)_{24}$ při dvou různých teplotách (pokojová teplota a 78 K nebo 90 K). Převzato z [31].*

Užitečnou možností, jak ovlivnit optické vlastnosti nanoklastrů, může být využití optického jevu zvaného jako **dvoufotonová absorpce**, kterou v případě AuNCs poprvé demonstrovali Ramakrishna a kol. (2008) [32]. Připravili $Au_{25}(SC_6H_{13})_{18}$ vykazující emisi s maximem při 830 nm po dvoufotonové excitaci vlnovou délkou 1290 nm a při 510 nm po dvoufotonové excitaci vlnovou délkou 800 nm. Jednou z možností využití tohoto jevu je *in vitro* [33,34] či *in vivo* [34] zobrazování, jehož výhodou oproti zobrazování s využitím jednofotonové excitace je pronikání záření do hlubších vrstev tkáně, méně intenzivní autofluorescence tkáně a méně intenzivní rozptyl záření [4,35]. Dalšími možnostmi využití jsou například *in vitro* sledování interakce proteinů [36] či *in vivo* fotodynamická terapie [37].

Velmi studovanou optickou vlastností AuNCs je jejich schopnost vykazovat **luminiscenci**. Jsou přijímány dva primární **mechanismy** fotoluminiscence (PL) AuNCs: (i) efekt kvantového omezení a (ii) přenos náboje, jenž zahrnuje přenos náboje z ligandu na kov (LMCT) a z ligandu na systém kov-kov (LMMCT) [38]. Link a kol. (2002) [39] připravili AuNCs s využitím GSH jako thiolového ligandu, které po předchozí excitaci vlnovou délkou 514 nm vykazují emisi jak ve viditelné (při 1,55 eV ≈ 800 nm), tak i v infračervené (při 1,13 eV ≈ 1097 nm) oblasti. Strukturu energetických hladin a původ

PL píků poté prezentují na základě dvou modelů: pevnolátkového (viz Obrázek 9a) a molekulárního (viz Obrázek 9b).
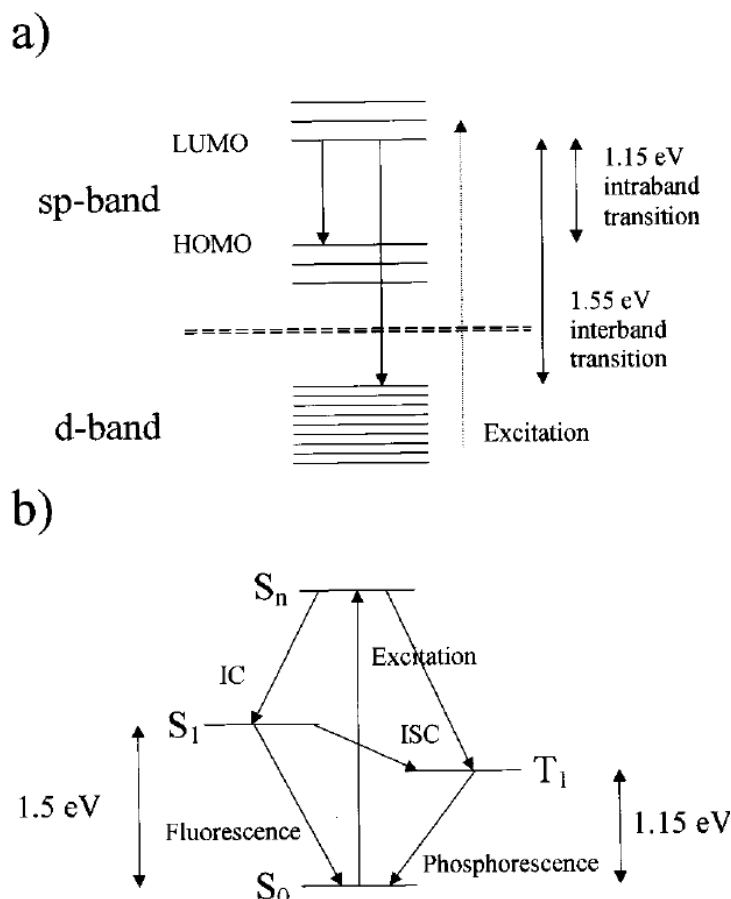
Obrázek 9: *Modely popisující původ fotoluminiscenčních píků: a) pevnolátkový model b) molekulární model. Převzato z [39].*

Na základě pevnolátkového modelu přiřadili PL ve viditelné oblasti mezipásovému přechodu (6sp → 5d), kdežto PL v oblasti infračervené přechodu vnitropásovému (sp → sp) mezi hladinami HOMO a LUMO. Na základě molekulárního modelu pak přisoudili pík ve viditelné oblasti fluorescenci a pík v infračervené oblasti fosforescenci. K opačnému závěru však došli autoři Devadas a kol. (2010) [40], kteří připravili AuNCs odlišující se svými thiolovými ligandy, kdy využili jednak 1-hexanthiol, jednak GSH. Oba systémy vykazovaly PL jak ve viditelné, tak infračervené oblasti. Fotoluminiscenci ve viditelné oblasti přiřadili přechodu mezi hladinami HOMO a LUMO kovového jádra, kdežto PL v oblasti infračervené přiřadili přechodu mezi hladinami kovového jádra a hladinami vnějšího obalu. Wen a kol. (2012) [41] připravili AuNCs s využitím BSA

jakožto stabilizujícího a redukčního činidla. Teplotně závislá emisní spektra zkoušeli nafitovat a zjistili, že PL v červené oblasti se skládá ze dvou píků s maximy při 710 a 640 nm. Teplotní závislost emise při vlnové délce 710 nm poukazuje na to, že se jedná o polovodičové chování, a přiřazují tedy jeho původ přechodu mezi hladinami HOMO a LUMO. Pík při 640 nm přisuzují dominantnímu příspěvku vnějšího obalu. Je tedy zřejmé, že na PL budou mít vliv vlastnosti jak kovového jádra, tak vnějšího obalu. Závěr autorů Link a kol. (2002) [39] podporují výsledky autorů Li a kol. (2019) [42] a Zhou a Song (2021) [43], kteří uvádějí, že původcem PL v infračervené oblasti je kovové jádro. Zhou a Song (2021) [43] také dále uvádějí, že zdrojem PL ve viditelné oblasti je přenos náboje mezi kovovým jádrem a vnějším obalem (viz Obrázek 10). V nedávné práci naší výzkumné skupiny Šišková a spol. [19] bylo prostřednictvím elektronové paramagnetické rezonance (EPR) prokázáno, že luminiscence AuNCs zanořených v BSA, vykazujících emisi u 655 nm (při excitaci u nižších vlnových délek), je jejich vnitřní vlastností a nejedná se v tomto případě o přenos náboje. Současně bylo v této práci zjištěno, že kromě oxidačního stavu Au^0 je přítomen též oxidační stav Au^{2+}.
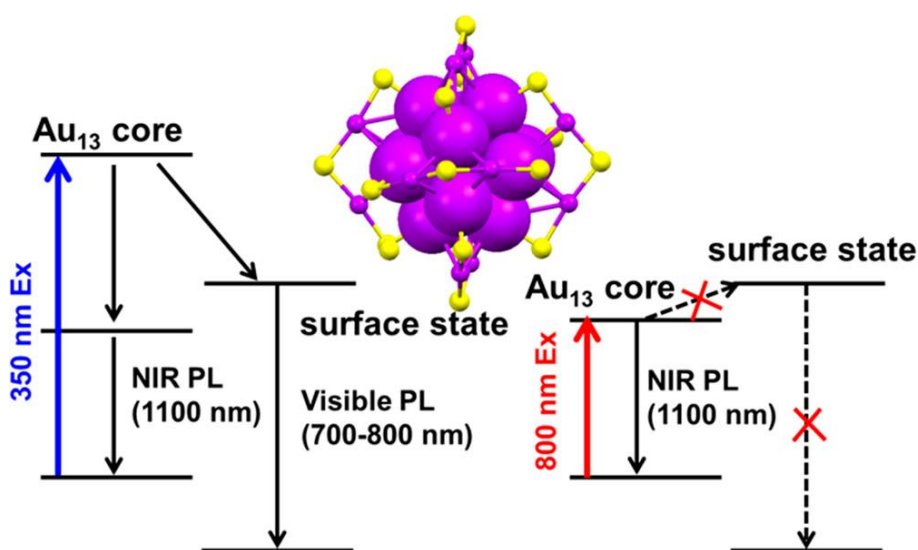
Obrázek 10: *Mechanismus fotoluminiscence (PL) $Au_{25}(SR)_{18}^-$. Převzato z [43].*

V porovnání s např. anorganickými kvantovými tečkami (II. B – VI. A skupin) je **intenzita PL** AuNCs poměrně slabá. Jednou z možností, jak navýšit intenzitu PL, je **výměna ligandů**. Wang a kol. (2006) [44] připravili $Au_{38}(SC_2H_4Ph)_{24}$ s průměrem jádra okolo 1,1 nm a $Au_{140}(SC_6H_{13})_{53}$ s průměrem okolo 1,6 nm. Intenzitu PL v infračervené

oblasti navýšili výměnou nepolárních ligandů za polární thiolátové ligandy. Zvýšení intenzity bylo větší v případě thiolátových ligandů majících větší množství substituentů přitahujících elektrony. V rámci některých thiofenolátových ligandů byla závislost mezi intenzitou PL a počtem vyměněných polárních ligandů dokonce přímo úměrná [44]. Závěry autorů Wang a kol. (2006) [44] podporují výsledky Wu a Jin (2010) [45], kteří připravili AuNCs s užitím různých thiolových ligandů a zjistili, že ligandy obsahující atomy či skupiny přitahující elektrony mohou značně zvýšit intenzitu PL. Autoři rovněž zmiňují 3 strategie navýšení intenzity PL: (i) zvýšení schopnosti ligandů poskytovat elektrony, (ii) zvýšení elektropozitivity kovového jádra, nebo (iii) použití ligandů obsahujících atomy či skupiny přitahující elektrony. Londoño-Larrea a kol. (2017) [46] připravili AuNCs pouze s využitím HAuCl$_4$ a NaOH, jež však nevykazovaly žádnou PL, nicméně obalením různými thiolovými ligandy a adenosin monofosfátem vedlo ke vzniku PL, již připisují interakcím mezi ligandem a povrchem nanoklastru.

Kromě intenzity PL může mít výměna ligandů vliv i na **pozici maxima emise**. Kundu a kol. (2020) [36] připravili AuNCs s využitím GSH, které následně modifikovali prostřednictvím leptání kovového jádra a výměny ligandu. Podařilo se jim připravit AuNCs s různými thiolovými ligandy na povrchu, kdy každý vykazuje odlišnou vlnovou délku maxima emise, přičemž s rostoucí délkou uhlíkatého řetězce ligandu docházelo k hypsochromnímu posunu, a to od 612 do 510 nm. Kromě vlnové délky maxima emise se připravené AuNCs odlišují v době životě excitovaného stavu a QY (hodnoty od 2,90 do 8,21 %). Tyto systémy poté užili jak k fluorescenčnímu značení buněk pozorovaných pod mikroskopem, tak ke sledování vzájemných interakcí proteinů *in vitro*, a to jednak s využitím mikroskopie na základě doby života excitovaného stavu, jednak pomocí fluorescenční korelační spektroskopie. Pozorovali, že právě **hydrofobicita** povrchu AuNCs může spustit jejich schopnost detekovat amyloidy bez nutnosti užití externích markerů. Hydrofobicita ovlivněná přídavkem kyseliny palmitové byla zkoumána pro systémy BSA-AuNCs v rámci naší výzkumné skupiny [47]. Byl prokázán pozitivní dopad přítomnosti kyseliny palmitové ve struktuře BSA na výslednou PL AuNCs.

Zhu a kol. (2021) [48] připravili AuNCs s využitím 11-merkaptoundekanové kyseliny (MUA), kterou následně nahradili ligandy s různou délkou uhlíkatého řetězce a pozorovali, že dochází ke změně intenzity PL a kinetiky dohasínání excitovaného stavu, ale nikoliv k posunu emisního maxima. S rostoucí délkou uhlíkatého řetězce (v rozsahu od 2 do 11 atomů C) docházelo k lineárnímu poklesu QY PL. Titíž autoři konjugovali

15

COOH skupinu MUA s aminoskupinou 3-(aminopropyl)trifenylfosfonium-bromidu nebo ethylendiaminu, což v obou případech vedlo ke zhášení PL. Uvádějí, že důvodem zhášení PL by mohlo být agregací indukované zhášení, kdy k agregaci může docházet z důvodu snižování velikosti povrchového náboje.

Další možností navýšení intenzity luminiscence je **změna oxidačního stavu** Au. Peng a kol. (2017) [49] připravili AuNCs s využitím acetyl-L-cysteinu a GSH, přičemž zjistili, že v obou případech může být intenzita **elektrochemiluminiscence** (ECL) navýšena buďto chemickou či elektrochemickou redukcí Au z Au^I na Au^0. Navýšení intenzity ECL je přímo úměrné stupni redukce Au [49]. Valenční stav Au může kromě intenzity ECL ovlivnit i polohu maxima emise. Kim a kol. (2018) [50] připravili AuNCs s využitím GSH jakožto thiolového ligandu, přičemž ECL v blízké infračervené oblasti při 800 nm přisuzují Au v oxidačním stavu I a naopak ECL ve viditelné oblasti při 610 nm přisuzují Au v oxidačním stavu 0. Huang a kol. (2021) [51] připravili AuNCs s využitím acetyl-L-cysteinu, které nanesli na elektrodu vyrobené ze skelného uhlíku a posléze chemicky redukovali pomocí $NaBH_4$. Tento systém využili k ECL detekci kanamycinu, která je založena na zhášení intenzity ECL při změně oxidačního stavu Au (z Au^0 na Au^I), ke které dochází díky redoxní reakci mezi Au^0 a kanamycinem v přítomnosti H_2O_2.

K navýšení intenzity luminiscence lze rovněž využít fotofyzikálního jevu nazývaného jako **agregací indukovaná emise**, během které materiál nevykazující luminiscenci (či vykazující slabou luminiscenci) začne po agregaci luminiscenci vykazovat (či emitovat záření s větší intenzitou), což lze vysvětlit omezením rotačních a vibračních pohybů ligandu ve vnějším obalu AuNCs, čímž dojde ke snížení disipace energie ve formě nezářivých procesů [38,52]. Agregací indukované emise lze dosáhnout přidáním určitého kationtu (Zn^{2+}, Al^{3+}, Gd^{3+}, Ce^{3+}, Y^{3+}, Tm^{3+}), polymeru či jiných biologických molekul, změnou pH roztoku, přidáním slabě polárního rozpouštědla do vodného roztoku AuNCs obalených hydrofilním ligandem nebo pomocí krystalizace [38,52]. Omezení rotačních a vibračních pohybů ligandu ve vnějším obalu AuNCs lze také efektivně dosáhnout imobilizací uvnitř matrice, a to například v hydrogelu nebo také v organokovovém rámci [38,52].

V neposlední řadě lze k navýšení luminiscence a/nebo posunu maxima emise též užít **nahrazování jednoho či více atomů Au heteroatomem/y**, jakými mohou například být Ag, Cu, Cd, Er, Pt a Zn [53–55]. Principem navýšení intenzity je modifikace

geometrické a/nebo elektronové struktury, nebo změny v přechodu zahrnujícím LMCT nebo LMMCT [56].

Kromě zmíněných optických vlastností mohou AuNCs vykazovat i **další unikátní fyzikálně-chemické vlastnosti**, jakými jsou kupříkladu magnetismus, vnitřní chiralita, katalytická aktivita či schopnost generace reaktivních forem kyslíku během interakce se zářením [38].

1.3. Metody syntézy a praktické využití AuNCs

K provedení syntézy AuNCs lze užít jednu ze dvou strategií: shora dolů, tedy z objemového materiálu směrem k NSs (anglicky top-down) (viz Obrázek 11A), nebo zdola nahoru, tudíž poskládáním jednotlivých atomů do NSs (anglicky bottom-up) (viz Obrázek 11B).
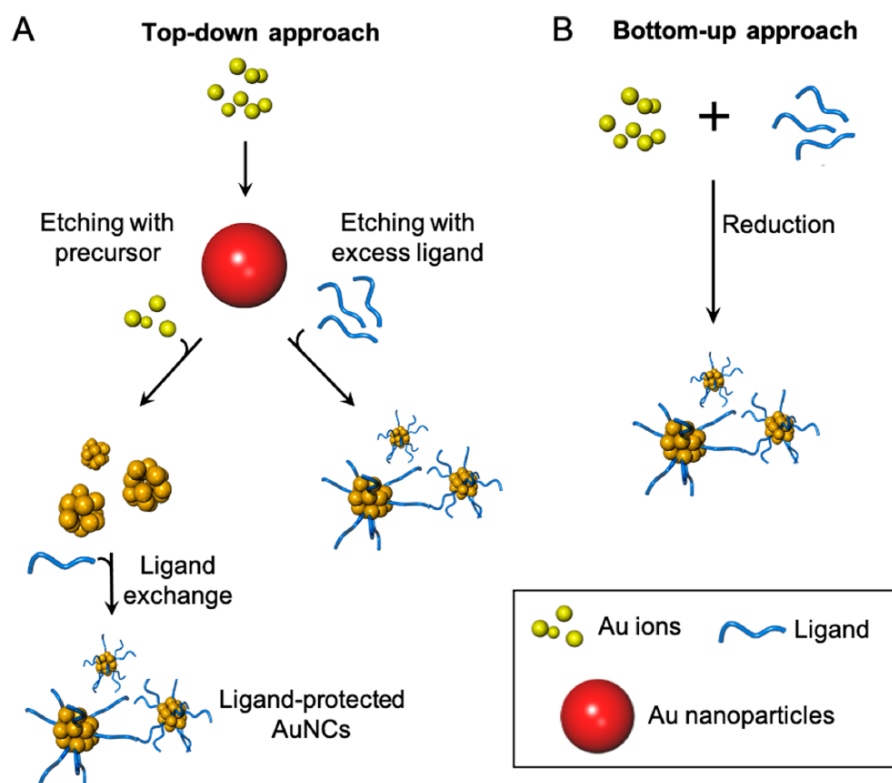
Obrázek 11: *Schéma představující dvě nejběžněji užívané strategie syntézy zlatých nanoklastrů. (A) Top-down (shora dolů) metoda spočívá v přípravě větších nanostruktur (například zlatých nanočástic) s následným chemickým leptáním buďto pomocí prekurzoru Au (a následnou výměnou ligandu) nebo užitím nadbytečného množství ligandu. (B) Bottom-up (zdola nahoru) metoda spočívá v redukci iontů prekurzoru Au redukčním činidlem v přítomnosti stabilizujícího ligandu. Převzato z [57] a upraveno.*

Top-down metoda zahrnuje především chemické leptání, kdy jsou materiály větších rozměrů, jakými mohou být například Au nanokrystaly [58], AuNPs [59] či větší AuNCs [60], leptány prostřednictvím nadbytku ligandů [61], nebo rovněž s využitím samotného prekurzoru Au [62] za vzniku AuNCs (viz Obrázek 11A). V případě leptání pomocí prekurzoru Au provedli Lin a kol. (2009) [62] následnou výměnu ligandu, která vedla k tvorbě systému emitujícím v červené oblasti spektra; zatímco před touto výměnou nevykazovaly připravené AuNCs žádnou fluorescenci. Mezi ligandy užívané k leptání patří různé thiolové sloučeniny [60,63], merkaptanové kyseliny [36], polyethylenimin [58], GSH [59,64], či dokonce BSA [65].

Princip **bottom-up** metody spočívá v redukci iontů Au (převážně Au^{3+}) na atomy Au^0 a následné nukleaci těchto atomů za vzniku AuNCs [66]. Mezi užívané formy redukce patří **redukce chemická** [18,67,68] a elektrochemická [69], fotoredukce [13,15,70] a redukce uvnitř biologického systému [71–73]. Mezi hojně využívaná chemická redukční činidla patří například tetrahydridoboritan sodný [18], kyselina askorbová [74], citrát trisodný [75], GSH [75] či BSA [67]. V této práci se autor zaměřil na využití redukčních účinků BSA na Au^{3+}. Je známo, že zvýšená teplota může usnadnit redukční reakce poskytnutím potřebné aktivační energie pro přeměnu prekurzorů obsahujících Au ionty na Au atomy či AuNCs [38]. Yan a kol. (2012) [76] byli první, kdo k syntéze AuNCs chráněných BSA využili mikrovlnné záření, čímž podstatně zkrátili reakční dobu z desítek hodin na několik minut.

Kromě výše uvedených forem redukce byly provedeny syntézy prostřednictvím **sonochemické metody** [12,16,77], přičemž chemické účinky ultrazvuku o vysoké intenzitě vyplývají především z tzv. akustické kavitace (tedy tvorby, růstu a implozivního kolapsu bublin v kapalinách), kdy lze dosáhnout extrémních podmínek, tj. velmi vysoké teploty, tlaku a rychlosti chlazení či ohřívání [12,78]. Další metody přípravy zahrnují **mikroemulzní proces** [79], kde mikroemulze je termodynamicky stabilní disperze obsahující dvě nemísitelné kapalné fáze (například olej dispergovaný ve vodě) [80]. Příklady některých výše uvedených metod jsou s výčtem užitých prekurzorů, templátů či ligandů, redukčních činidel a rozpouštědel a také s přehledem výsledných hodnot kvantového výtěžku (QY), vlnové délky maxima emise (λ_{max}) a průměru kovového jádra shrnuty v tabulce níže (viz Tabulka 4).

Tabulka 4: *Metody používané pro syntézu AuNCs s přehledem užitých prekurzorů, templátů či ligandů, redukčních činidel a rozpouštědel a také s přehledem výsledných hodnot kvantového výtěžku (QY), vlnové délky maxima emise (λ_{max}) a průměru kovového jádra.*

Autoři	Syntéza	Matrice nebo ligand	Redukční činidlo	Rozpouštědlo	QY [%]	λ_{max} [nm]	Průměr d [nm]	Metoda určení d
[69]	elektrochemická	PVP	-	acetonitril	12,5	315 335 350	-	-
[15]	fotoredukční (365 nm)	MPTS	-	THF	0,26 0,73 3,12	580 558 538	2,0 1,8 1,3	HRTEM
[13]	fotoredukční (365 nm)	PTMP-PMMA	-	H_2O	5,3	610	0,6 ± 0,4	TEM
[70]	fotoredukční (365 nm)	PTMP-PMMA PTMP-PBMA PTMP-PtBMA	-	THF	3,8 14,3 20,1	412 433	-	-
[67]	chemická, MW	BSA		H_2O	1,9	650	2,1 ± 0,3	TEM
[68]	chemická, MW	vaječný bílek		H_2O	2,37	648	2,7 ± 0,7	TEM
[18]	chemická, MW	lysozym	$NaBH_4$	H_2O	4,9	750	1,3 ± 0,3	TEM
[19]	chemická, MW	BSA		H_2O	6,7 ± 0,1	655	1,01 ± 0,24	TEM
[16]	sonochemická	GSH		H_2O	4,3	598	1,7 ± 0,3	TEM
[12]	sonochemická	BSA		H_2O	8	670	1,8	HRTEM
[77]	sonochemická	-	-	toluen	15,0 ± 2,5 17,4 ± 4,2 20,8 ± 2,3	450 490 475	< 1	AFM

Pozn.: AFM = mikroskopie atomárních sil, BSA = hovězí sérový albumin, GSH = glutathion, HRTEM = transmisní elektronová mikroskopie s vysokým rozlišením, MPTS = 3-(merkaptopropyl)trimethoxysilan, MW = syntéza s využitím mikrovlnného záření, PMMA = polymethylmethakrylát, PtBMA = poly(tert-butylmethakrylát), PTMP = poly(n-butylmethakrylát), PVP = polyvinylpyrrolidon, THF = tetrahydrofuran, TEM = transmisní elektronová mikroskopie.

Jak lze vypozorovat v tabulce výše (viz Tabulka 4), v rámci syntézy AuNCs se kromě samotných prekurzorů a redukčních činidel užívá téměř vždy nějaká templátová molekula či ligand. V případě syntézy bez této komponenty by mohlo dojít k interakcím mezi jednotlivými NCs, které by vedly k nevratné agregaci z důvodu snížení jejich povrchové energie [81]. Rovněž by mohlo postupně docházet k přerůstání AuNCs v AuNPs, jak bylo v naší skupině dříve pozorováno [47]. Ke stabilizaci AuNCs je možno užít širokou škálu ligandů, jakými jsou například: různé thiolové sloučeniny [82]; dendrimery [83,84], což jsou polymery s pravidelnou rozvětvenou strukturou, velmi dobře definovaným chemickým složením a molekulovou hmotností [85]; dále polymery [86,87]; proteiny [12,88]; peptidy [89,90]; různé sekvence DNA [91] a také jednotlivé nukleotidy [92,93]. Některé ligandy mohou současně sloužit jako stabilizující a redukční činidla, a to například MUA [94], BSA [19,95] a GSH [16,50].

Praktické **využití AuNCs** je poměrně rozmanité, počínaje **detekcí** iontů kovů, mezi které patří například ionty arsenité, chromité a chromové, kademnaté, kobaltnaté, měďnaté, olovnaté, rtuťnaté, stříbrné, zinečnaté a železité (viz Tabulka 5). Kromě kovů byly také detekovány různé anionty jako S^{2-}, CN^-, NO_2^- a malé molekuly jako například bilirubin, cystein, dopamin, glukóza, GSH, H_2O_2, H_2S, HClO a cholesterol (viz Tabulka 5).

Tabulka 5: *Přehled detekovaných kovových iontů, aniontů a malých molekul a princip jejich detekce.*

Detekované ionty/molekuly	Autoři	Princip detekce
Ionty kovů		
Ag^+	[96]	EN
As^{3+}	[97]	EN
Cd^{2+}	[98–100]	EN
	[101]	AIE
Co^{2+}	[102]	QU
Cr^{3+}	[94,103]	QU
Cr^{6+}	[103,104]	QU
Cu^{2+}	[99,100,102,105–111]	QU
	[112]	AIQ
Fe^{3+}	[113–116]	QU
Hg^{2+}	[99,105,110,117–126]	QU
Pb^{2+}	[95,99,127,128]	QU
	[129]	ECLC
	[123]	EN
Zn^{2+}	[108]	EN

Tabulka 5: *Pokračování.*

Detekované ionty/molekuly	Autoři	Princip detekce
Anionty		
CN^-	[130–132]	QU
NO^{2-}	[133–135]	QU
S^{2-}	[136–138]	QU
Malé molekuly		
bilirubin	[139]	QU
cystein	[140]	EN, DSI
dopamin	[141,142]	QU
	[143]	EN
glukóza	[144]	EQU
glutathion	[145]	EN
H_2O_2	[146,147]	QU
H_2S	[148,149]	QU
HClO	[150]	QU
cholesterol	[151]	EQU

Pozn.: *AIE = agregací indukované zvýšení intenzity fotoluminiscence, AIQ = agregací indukované zhášení fotoluminiscence, DSI = pokles intenzity Rayleighova rozptylu druhého řádu, ECLC = změna signálu elektrochemiluminiscence, EQU = enzymatické zhášení fotoluminiscence, EN = zvýšení intenzity fotoluminiscence, QU = zhášení fotoluminiscence.*

AuNCs lze rovněž s úspěchem využít k detekci enzymů [90,152–157], měření pH [103,148,158–160] a teploty [16,106,161–165], detekci patogenních bakterií [166–168] a metastází rakoviny [169]. Detekce bývá z převážné části založena na zhášení signálu PL (kupříkladu [104,116,125,132,147]) vlivem interakce AuNCs s ionty kovů, anionty či malými molekulami. Existují však také systémy, jejichž intenzita PL je vlivem interakce naopak navýšena (například [100,123,145]). V leckterých případech jsou AuNCs konjugovány s jinými entitami vykazujícími také luminiscenci [100,107], ale v jiné oblasti spektra. Tyto pak slouží jako reference, neboť jejich luminiscenční signál je oproti AuNCs konstantní. Mezi další principy detekce patří například agregací indukované zhášení [112], agregací indukovaná emise [101], změna signálu ECL [129] či změna v poloze maxima absorpce [157].

Mimo detekci lze AuNCs využít také ke **katalýze** chemických reakcí [170–173], regulace hladiny glukózy v krvi [174,175], *in vitro* nebo *in vivo* **zobrazování** s užitím výpočetní tomografie a/nebo PL [148,174,176–181], fototermální [182–186] a rovněž fotodynamické [37,183,185,187,188] **terapii**, **transportu léčiv** do nádorových buněk

[180,189–192] a v neposlední řadě jako teranostický systém [179,192], tj. kombinace diagnostiky a terapie [57].

1.4. SPIONs a jejich magnetické vlastnosti

NPs tvořené z feromagnetického či ferimagnetického materiálu mající velikost zhruba do 20 nm mohou vykazovat unikátní formu magnetismu nazývanou jako **superparamagnetismus** [193–195]. V případě SPIONs se nejčastěji jedná o magnetit (Fe_3O_4), maghemit (γ-Fe_2O_3) či ferity (oxid železa s příměsí jednoho či více přechodných kovů, například Ba, Co, Cu, Mn, Ni) [196,197].

Pro vysvětlení podstaty superparamagnetismu je potřeba začít s magnetickými materiály větších, okem viditelných, rozměrů. Magnetické materiály makroskopických velikostí jsou složeny z magnetických domén, což jsou oblasti uniformní magnetizace, které jsou od sebe odděleny doménovými stěnami, uvnitř kterých se směr magnetizace mění plynule od jedné domény ke druhé [198]. Když se velikost materiálu zmenšuje, počet magnetických domén klesá, přičemž jakmile je velikost částice srovnatelná se šířkou doménové stěny, vznik vícera domén není možný, a částice je tedy tvořena pouze jednou doménou [198,199]. Přesněji řečeno, materiál je tvořen pouze jednou magnetickou doménou, pokud energie nutná k tvorbě další domény je větší než pokles energie, ke kterému by došlo v důsledku snížení výsledného magnetického toku [193]. Se změnou velikosti materiálu se obecně mění také magnetická koercivita, která představuje intenzitu vnějšího magnetického pole potřebnou k odstranění zbytkové magnetizace (tzv. magnetické remanence) [195,200,201]. Její průběh v závislosti na velikosti pro NPs magnetitu (Fe_3O_4) mající krychlový tvar lze pozorovat na obrázku níže (viz Obrázek 12), kdy během přechodu z multidoménového charakteru částice na jednodoménový je koercivita maximální a s dalším snižováním velikosti částice klesá k nule.
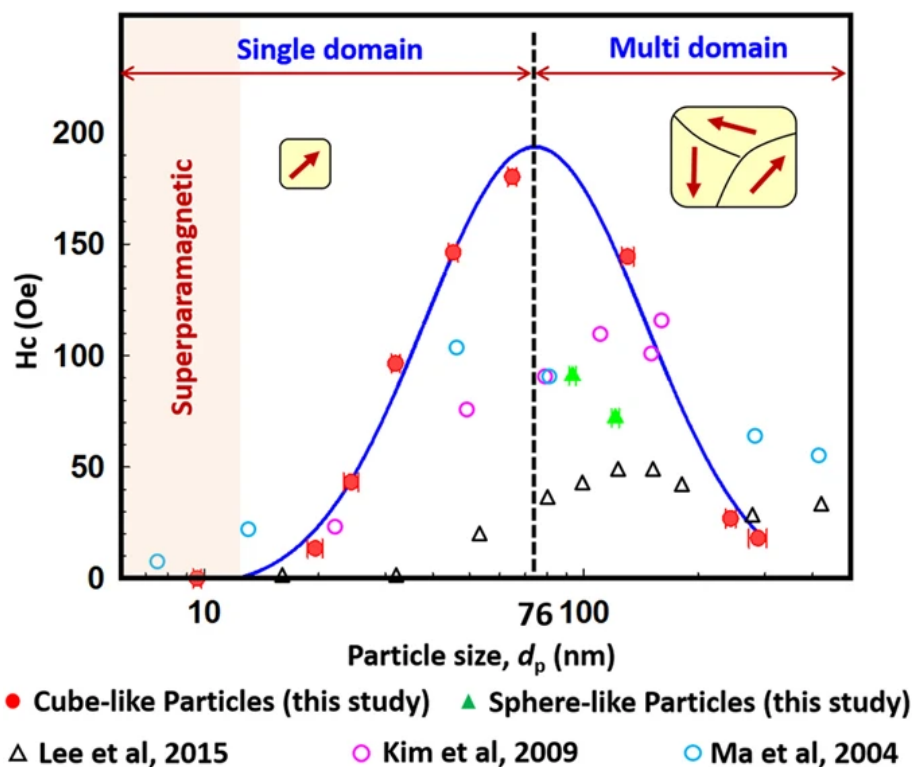
Obrázek 12: *Závislost magnetické koercivity nanočástic Fe₃O₄ na jejich velikosti při teplotě 300 K. Červené kruhové značky představují nanočástice s kubickou strukturou, zelené trojúhelníkové značky představují nanočástice se sférickou strukturou a černé trojúhelníkové, fialové kruhové a modré kruhové značky jsou postupně výsledky autorů Ma a kol. (2004) [202], Kim a kol. (2009) [203] a Lee a kol. (2015) [201]. Převzato z [195].*

Při dosažení určité hraniční velikosti částice, kdy je tepelná energie srovnatelná s energií potřebnou k reorientaci spinů (magnetická anizotropní energie), je koercivita nulová, a materiál se tedy nachází v superparamagnetickém režimu [200,201]. Tepelná energie tak umožňuje po odstranění působení vnějšího magnetického pole uskutečnit spontánní reorientaci spinů, která vede ke znáhodnění magnetických dipólů v určitém časovém intervalu, a tudíž k demagnetizaci materiálu není potřeba žádná dodatečná vnější energie [193,200]. Z důvodu potřeby dostatečné tepelné energie je poněkud zřejmé, že kromě velikosti částice je superparamagnetismus svázán také s její teplotou. Teplota, při které je tepelná energie $k_B T$ rovna magnetické anizotropní energií, se nazývá blokační teplota T_B [200]. V případě, kdy $T < T_B$, není tepelná energie potřebná ke spontánní reorientaci spinů dostatečná, a koercivita tak začíná být opět nenulová [193].

V superparamagnetickém režimu tedy materiál nevykazuje hysterezní chování, jinými slovy, vykazuje nulovou magnetickou remanenci a koercivitu (viz Obrázek 13) [193,200,204,205].
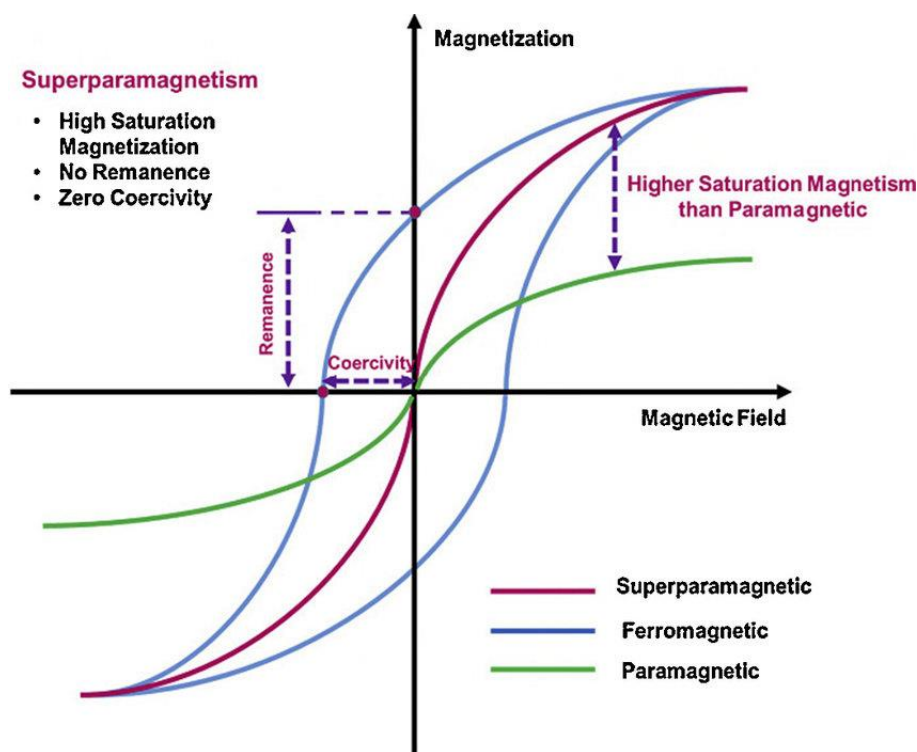
Obrázek 13: *Závislost magnetizace superparamagnetického (růžová), feromagnetického (modrá) a paramagnetického (zelená) materiálu na intenzitě vnějšího magnetického pole. Magnetická remanence (zbytková magnetizace při absenci vnějšího magnetického pole) a magnetická koercivita (intenzita vnějšího magnetického pole nutná k odstranění zbytkové magnetizace) jsou v případě superparamagnetického materiálu nulové. Převzato z [205], upraveno a přeloženo.*

Jak název tohoto jevu napovídá, hodnota saturační magnetizace superparamagnetických NPs je větší než v případě částic paramagnetických, nicméně je srovnatelná se saturační magnetizací feromagnetických a ferimagnetických částic (viz Obrázek 13) [193]. Saturační magnetizace SPIONs závisí jak na velikosti částic [195], tak na krystalové struktuře a typu obalujícího materiálu [206], dále také na tloušťce obalu [207], molárním poměru Fe^{2+}/Fe^{3+}, iontové síle, pH a na tom, zda byla při syntéze použita inertní (N_2) atmosféra [208].

1.5. Metody syntézy, popis vzniku a praktické využití SPIONs

Obdobně jako v případě AuNCs mohou být k **přípravě SPIONs** použity oba popisované přístupy: shora dolů či zdola nahoru [209]. Celkově lze využít mnoha různých strategií, které lze rozdělit na chemické, fyzikální a biologické, přičemž volbou syntézy lze dosáhnout různých tvarů, velikostí, struktury, koloidní stability a magnetických vlastností, čímž lze zajistit různé oblasti využití [210]. Mezi chemické metody lze zařadit tepelný rozklad, hydrotermální či solvotermální syntézu, syntézu s využitím polyolů, mikroemulzní a sol-gelovou syntézu a spolusrážení (koprecipitaci) [204]. K fyzikálním metodám patří kulové mletí, laserová ablace, pyrolýza či spalování [209]. V případě biologických metod lze k syntéze využít rostliny [211], zdravé či rakovinné buňky [212], plísně [213], řasy [214,215], bakterie [216], haloarchaea [217] či kvasinky [218]. Příklady některých výše uvedených metod lze nalézt v tabulce na další stránce (viz Tabulka 6). Lze si povšimnout, že přestože má koercivita v případě superparamagnetických částic být nulová, někteří autoři považují připravené částice za superparamagnetické, byť je jejich koercivita řádově v desítkách Oe.

Tabulka 6: *Metody syntézy SPIONs s uvedenými prekurzory, průměru kovového jádra d_{kj}, saturační magnetizace M_s, magnetické koercivity H_c a výsledné struktury.*

Autoři	Prekurzor kovu	Metoda syntézy	Vnější obal	d_{kj} (TEM) [nm]	M_s [emu·g⁻¹]	H_c [Oe]	Struktura kovu
[219]	FeCl$_2$·4H$_2$O	HT	-	15,4 – 31,1	53,0 – 97,5 (*)	NS	Fe$_3$O$_4$
[220]	Fe(NO$_3$)$_3$·9H$_2$O Zn(NO$_3$)$_2$·6H$_2$O	HT	OA	≈ 10	41,18 – 79,23	NS	Fe$_3$O$_4$
[221]	Fe(acac)$_3$	HT	PAA	6	39,0	NS	Fe$_3$O$_4$
[222]	FeCl$_2$ FeCl$_3$	KP	-	6,9 6,7	53,2 53,3	NS	Fe$_3$O$_4$ γ-Fe$_2$O$_3$
[223]	FeSO$_4$·7H$_2$O FeCl$_3$·6H$_2$O	KP SCH SCH	- PEG PEG	14 8 5	46,5 47,0 49,0	64,8 12,9 5,4	Fe$_3$O$_4$
[224]	FeSO$_4$·7H$_2$O FeCl$_3$·6H$_2$O	SCH	OA	15	83	NS	Fe$_3$O$_4$
[225]	FeSO$_4$·7H$_2$O FeCl$_3$·6H$_2$O	SCH	OLNa BPEI PAANa CIT	8 11 ± 3 10 ± 3 11 ± 3	59,27 70,98 71,51 77,36	34,27 33,21 35,26 33,90	Fe$_3$O$_4$
[226]	Fe(C$_2$H$_3$O$_2$)$_2$ Octan železnatý	SCH	-	10	< 1,25	NS	Fe$_3$O$_4$
[227]	Fe(acac)$_3$	TR	OA	7	59,1	NS	Fe$_3$O$_4$
[228]	Fe(acac)$_3$	TR	CIT	5,9 ± 1,4 5,7 ± 0,9	53 62	NS	Fe$_2$O$_3$
[229]	Fe(acac)$_3$	TR	PEG PEG-PEI (260 °C) PEG-PEI (200 °C)	6,8 ± 1,2 10,0 ± 1,7 9,0 ± 1,5	17 51 53	NS	Fe$_3$O$_4$
[230]	Fe(acac)$_3$	TR	PEG/PVP PLA/PEG/PVP	7,7 ± 1,1 8,0 ± 1,4	46,2 54,5	< 30	Fe$_3$O$_4$
[231]	FeCl$_2$	PR	DDA	9 13	60 70	NS	Fe$_3$O$_4$

Tabulka 6: *Pokračování.*

Autoři	Prekurzor kovu	Metoda syntézy	Vnější obal	d_{kj} (TEM) [nm]	M_s [emu·g^{-1}]	H_c [Oe]	Struktura kovu
[232]	FeSO$_4$·7H$_2$O FeCl$_3$·6H$_2$O	KP	-	16,9	69,1	NS	Fe$_3$O$_4$ γ-Fe$_2$O$_3$
	SPIONs	KP KM	Dextran	NS 11,8 – 13,5	5 56,4 – 65,5		
[233]	FeCl$_3$·6H$_2$O	KM	-	15 16,4 17,5	73,7 77,8 85,3	2,4 3,5 1,1	Fe$_3$O$_4$
[234]	Fe fólie	PLAB	-	3 a 12	124	76	Fe$_3$O$_4$ Fe$_3$C
[235]	Fe destička	PLAB	-	17 7	14,8 22,5	22 11,5	Fe$_3$O$_4$ FeO
[236]	Mg(NO$_3$)$_2$·6H$_2$O Fe(NO$_3$)$_3$·9H$_2$O	PYR	-	4,05 (XRD) 9,60 (XRD)	5,5 16,8	9,1 12,53	MgFe$_2$O$_4$
[237]	Pentakarbonyl železa	PYR	-	5,6 a 15,7 6,2 a 18	44,8 69,1	2,34 kA/m 13,9 kA/m	Fe$_3$O$_4$ γ-Fe$_2$O$_3$
[238]	Fe(acac)$_3$ Naftenát železitý	PYR	-	15,28 ± 4,02	97	< 30	Fe$_3$O$_4$ γ-Fe$_2$O$_3$
[239]	Fe(NO$_3$)$_3$·6H$_2$O	SP	TEOS	5	6 (*)	NS	α-Fe$_2$O$_3$
[240]	Fe(NO)$_3$	SP	-	3,4	21	20	α-Fe$_2$O$_3$

Pozn. 1: ** označuje, že hodnoty byly odečteny z grafu; BPEI = rozvětvený polyethylenimin, CIT = citrát trisodný, DDA = dodecylamin, HT = hydrotermální, KM = kulové mletí, KP = koprecipitace, NS = nespecifikováno, OA = olejová kyselina, OLNa = oleát sodný, PAA = polyakrylová kyselina, PAANa = polyakrylát sodný, PEG = polyethylenglykol, PEI = polyethylenimin, PLA = polymléčná kyselina, PLAB = pulzní laserová ablace, PR = precipitace, PVP = polyvinylpyrrolidon, PYR = pyrolýza, SCH = sonochemická, SP = spalování, TEM = transmisní elektronová mikroskopie, TEOS = tetraethoxysilan, TR = tepelný rozklad, XRD = rentgenová difrakce.* **Pozn. 2:** *Průměr kovového jádra je určen pomocí TEM, pokud není u hodnoty uvedeno jinak.*

Vznik materiálů s krystalovou strukturou je obvykle popisován pomocí teorie nukleace (vznik zárodků) a růstu, přičemž postupem času byly kromě teorie klasické popsány i teorie neklasické [241,242]. Proces nukleace spočívá v tvorbě zárodečných částic z roztoku užitého prekurzoru, přičemž může nastávat nukleace homogenní, během které dochází ke tvorbě zárodků uniformně v rámci celého roztoku, či heterogenní, kdy k nukleaci dochází na pevných substrátech, jakými jsou například povrchy nádob, nečistoty, či jiné zárodky [242–245]. Oproti klasické nukleační teorii dochází v případě nukleační teorie neklasické k výskytu několika přechodných metastabilních stavů nukleace před vznikem termodynamicky stabilní fáze [242]. Proces růstu zahrnuje depozice atomů či molekul na povrch zárodků v nasyceném roztoku [244,245].

Příkladem aplikace teorie nukleace a růstu budiž práce autorů LaMer a Dinegar (1950) [246]. Model, který prezentují, lze pozorovat na obrázku níže (viz Obrázek 14). Princip mechanismu spočívá v tom, že koncentrace prekurzoru narůstá, dokud nedosáhne určité kritické hodnoty, kdy začne docházet k náhlé a také rychlé nukleaci prekurzoru, přičemž postupně dochází ke snižování koncentrace prekurzoru, čímž dojde k zastavení procesu nukleace. Růst poté nastává díky difuzi prekurzoru v roztoku [247].
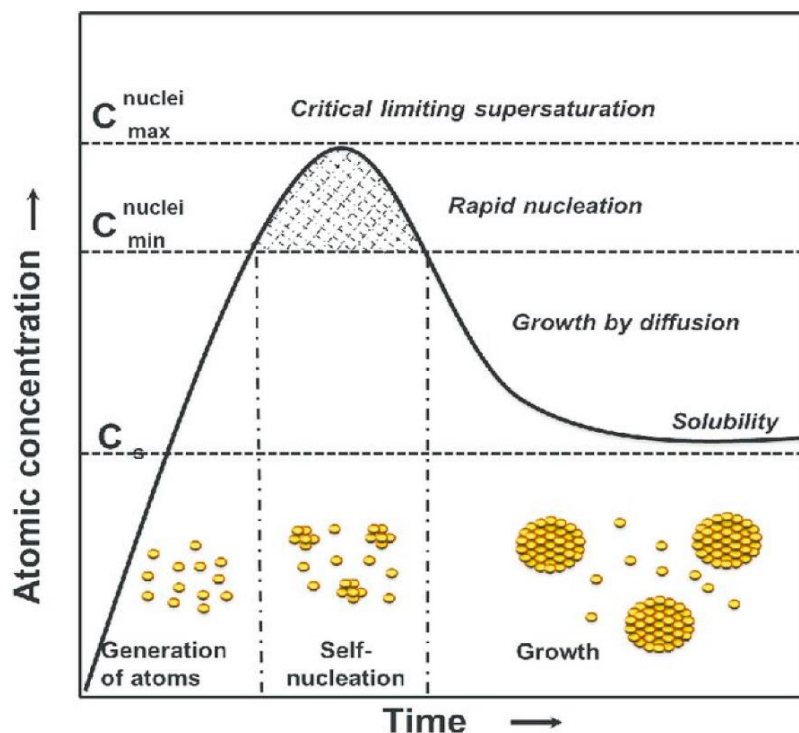
Obrázek 14: *Mechanismus nukleace a růstu dle LaMer a Dinegar (1950) [246]. Převzato z [248].*

Detailnější mechanismus vzniku nanočástic oxidů železa bude demonstrován na **koprecipitační metodě syntézy magnetitu**. Jedná se o velmi užívanou metodu syntézy SPIONs spočívající v přidání zásady (například NaOH nebo NH₄OH) k iontům Fe^{2+} a Fe^{3+} (obecně v molárním poměru 1:2) [249]. Na základě výsledků z infračervené spektroskopie s Fourierovou transformací, elektronové mikroskopie a také rentgenové difrakce Ahn a kol. (2012) [250] uvádějí, že NPs magnetitu vznikají spíše fázovou transformací oxohydroxidů železa, než přímou reakcí Fe^{2+} a Fe^{3+} iontů ve vodném roztoku. Zjistili, že pomalým, avšak nepřetržitým přidáváním zásady (NH₃) do roztoku obsahujícího FeCl₂ a FeCl₃ v molárním poměru 1:2 dochází postupně k nukleaci akaganeitu (β-FeOOH) a jeho fázové transformaci na magnetit skrze goethit (α-FeOOH) a pravděpodobně také skrze hematit (α-Fe₂O₃) a maghemit; zatímco náhlým přidáním báze dochází k nukleaci hydroxidu železnatého (Fe(OH)₂) a jeho transformaci na magnetit skrze lepidokrit (γ-FeOOH) (viz Obrázek 15). Proces sledovali a zjistili, že pomalou alkalizací se barva roztoku měnila pomalu, a to ze světle hnědé, přes tmavě hnědou až na černou indikující tvorbu NPs magnetitu [250].
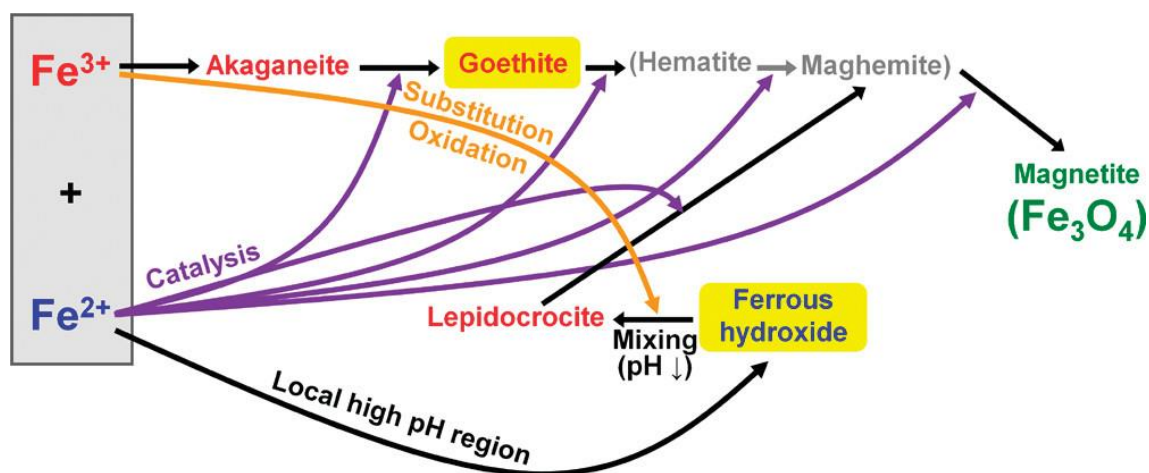
Obrázek 15: *Schéma vývoje nanočástic magnetitu připravených pomocí metody koprecipitace dle autorů Ahn a kol. (2012) [250]. Převzato z [250].*

Blanco-Andujar a kol. (2012) [251] do roztoku obsahujícího FeCl₂ a FeCl₃ v molárním poměru 1:2 postupně přikapávali ne hydroxid, ale zásaditou sůl alias sůl silné zásady a slabé kyseliny, Na₂CO₃. S využitím rentgenové difrakce zjistili, že při pokojové teplotě se jim jako první začal vytvářet goethit, který se pomalu postupně (během 24 hodin) transformoval na magnetit. Také LaGrow a kol. (2019) [252] užili Na₂CO₃ pro nastavení

zásaditého prostředí. Rychlým přidáváním a mísením prekurzorů Fe se zásadou, čehož bylo dosaženo díky průtokovému reaktoru, a analýzou s využitím transmisní elektronové mikroskopie, elektronové difrakce a Mössbauerovy spektroskopie tito autoři odhalili zřetelný přechod z amorfního ferihydritu ($Fe_{10}O_{14}(OH)_2$) na směs magnetitu a maghemitu (označeno jako $Fe_3O_4/\gamma\text{-}Fe_2O_3$). Synchrotronová rentgenová difrakce dále odhalila formování krystalických plátů $Fe_6(OH)_{12}CO_3$, které se formovaly před objevením výsledné směsi magnetitu a maghemitu. Jak se pláty $Fe_6(OH)_{12}CO_3$ rozpouštěly, docházelo ke zvětšování velikosti ferihydritových částic, a to až do doby, dokud tyto částice nevykrystalizovaly do směsi $Fe_3O_4/\gamma\text{-}Fe_2O_3$ (viz Obrázek 16). V kontrolním experimentu se bez přítomnosti Fe^{2+} nepovedlo dosáhnout růstu ferihydritu v magnetit. [252]
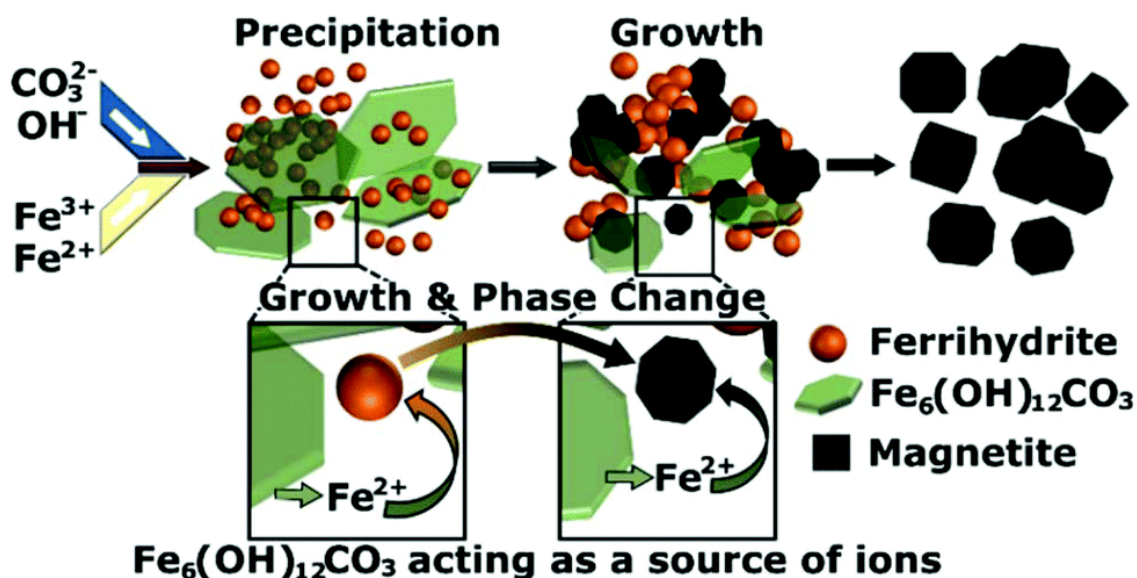
Obrázek 16: *Schéma vývoje nanočástic magnetitu připravených pomocí metody koprecipitace dle autorů LaGrow a kol. (2019) [252]. Převzato z [252].*

Autoři dále uvádějí, že množství zbytkového ferihydritu ve finálním produktu může být sníženo buďto ochranou Fe^{2+} iontů před oxidací, nebo zvýšením koncentrace těchto iontů v reakční směsi. S pomocí průtokového reaktoru, synchrotronové rentgenové difrakce a maloúhlového rozptylu rentgenového záření Besenhard a kol. (2020) [253] zjistili, že jediná fáze, která je přítomna 5 sekund po smíchání Fe^{2+} a Fe^{3+} iontů s NaOH, je směs $Fe_3O_4/\gamma\text{-}Fe_2O_3$ a že k následnému nárůstu velikosti částic dochází jen minimálně.

Povrch SPIONs je velice reaktivní z důvodu zvýšené plochy povrchu vůči objemu, tudíž se povrch SPIONs obvykle **obaluje** k zamezení aglomerace či agregace a modulace velikosti a tvaru [204]. Nicméně, tyto povrchové úpravy mohou **ovlivnit** jednak magnetické **vlastnosti** SPIONs v závislosti na množství, složení či šíře povrchové vrstvy [204], jednak například vstup NPs do buněk [254]. Liao a kol. (2011) [254] studovali vliv obalení SPIONs kyselinou listovou na jejich vstup do zdravých HEK293 a rakovinných HeLa buněk. V průběhu 4 hodin se do HeLa buněk dostalo více než 3x větší množství obalených SPIONs, kdežto v případě HEK293 buněk nebyl vliv obalení žádný. Důvodem by mohla být nadměrná exprese receptorů pro kyselinu listovou v případě HeLa buněk ve srovnání s buňkami HEK293 [254]. Mezi ligandy užívané k obalování SPIONs patří např. dextran [232], chitosan [255], 2,3-dimerkaptobutandiová kyselina (DMSA) [238], kyselina poly-γ-glutamová [256], polyethylenglykol [257] a polyvinylpyrrolidon [258].

Jedním ze směrů aplikovatelnosti **SPIONs** je jejich **uplatnění** jakožto kontrastní látky v rámci **zobrazování** magnetickou rezonancí (MRI) (například [259,260]). Jedná se o neinvazivní zobrazovací metodu s vysokým prostorovým rozlišením, během které není užíváno ionizující záření [261]. SPIONs jsou považovány za účinné T_2 kontrastní látky, jelikož dokážou zkrátit dobu transverzálního (neboli spin-spinového) relaxačního času magnetického momentu jednotlivých protonů, díky čemuž se ovlivněná oblast jeví jako tmavší [261,262]. Za určitých podmínek se však povedlo některým autorům získat i SPIONs s relativně vysokým T_1 kontrastem a nízkým poměrem relaxivit r_2/r_1 [263,264].

Dalším využitím SPIONs je magnetickým polem indukovaná **hypertermie**. Její fyzikální princip spočívá v generaci tepla NPs vlivem působení nestacionárního vnějšího magnetického pole [212]. Biologický účinek hypertermie je založen na skutečnosti, že zdravé buňky dokáží vydržet působení vyšších teplot, kdežto naopak rakovinné buňky při takovýchto teplotách podstupují apoptózu. Užití teplot vyšších než 46 °C již však může vést k potenciálně nebezpečné nekróze rakovinných buněk, která vede k vzniku zánětlivé reakce v okolí takto zemřelých buněk, a může negativním způsobem ovlivnit i buňky zdravé. [265]

SPIONs lze také využít k **cílenému transportu léčiv** do nádorových buněk, jenž může být aktivně zprostředkován jednak působením vnějšího magnetického pole [266–269], jednak konjugací SPIONs s látkou umožňující cílit na nádorové buňky [270–274]. Takovými látkami mohou být protilátky a jejich fragmenty, ligandy receptorů, peptidy

či aptamery [265]. Příkladem budiž hojně užívaná kyselina listová [270–273]. Mezi transportovaná léčiva patří různá chemoterapeutika jako například 5-fluorouracil [275], doxorubicin [268,270,274], kamptotecin [271], methotrexát [276] a paklitaxel [272]. Přidanou výhodou k cílenému transportu může být rovněž možnost kontrolovaného uvolňování transportovaného léčiva v reakci na určitý stimul, a to například působením blízkého infračerveného záření [277] či ultrazvuku [273] nebo změnou pH [278]. Kromě aktivního transportu může být použit i transport pasivní, kdy k nahromadění SPIONs uvnitř rakovinné tkáně dochází v důsledku efektu zvýšené permeability a retence rakovinných buněk. Nevýhodou této metody je obtížnost dosažení koncentrací SPIONs dostatečných k účinné léčbě, přičemž množství injektovaných SPIONs nelze neustále zvyšovat z důvodu nezanedbatelné toxicity v případě vyšších koncentrací [265]. Cílený transport léčiv lze kombinovat s hypertermií [276,279]. Mirzaghavami a kol. (2021) [275] dokonce připravili systém kombinující cílený transport léčiv, hypertermii a také možnost radioterapie, přičemž jejich spojením dosáhli signifikantně lepších terapeutických účinků.

Posledním příkladem využití SPIONs je **odstraňování iontů těžkých kovů** jako například Cd^{2+}, Co^{2+}, Cr^{6+}, Cu^{2+}, Pb^{2+} a Hg^{2+} [256,280–282].

1.6. Bimetalické NCPs složené z AuNCs a SPIONs nebo magnetických nanočástic oxidů železa, jejich syntéza a využití

Nanokompozit (NCP) je soustava složená ze dvou či více materiálů, přičemž minimálně jeden z jeho rozměrů je řádově v nanometrech [283]. **Bimetalický NCP** je pak NCP obsahující dva kovové materiály [284]. Existují dva různé přístupy přípravy NCPs, jejichž jednou ze součástí jsou kovové NCs: postsyntetická funkcionalizace a *in situ* syntéza [11]. Prvně zmiňovaný přístup spočívá v přípravě jednotlivých součástí NCP, jejich následné funkcionalizaci a propojení ve výsledný NCP. V případě *in situ* syntézy je NCP připraven postupným smísením všech prekurzorů v jednu reakční směs. Příklady těchto obou strategií budou demonstrovány výhradně na bimetalických NCPs tvořených současně jak AuNCs, tak SPIONs či případně magnetickými nanočásticemi oxidů železa.

Postsyntetická funkcionalizace bude v následujících odstavcích detailněji ukázána na jednotlivých metodách, kterými budou chemická konjugace [285,286],

metoda povrchové redukce [287], nekovalentní interakce [288–290] a samouspořádání [291].

Principem **chemické konjugace** je interakce mezi koncovými funkčními skupinami molekul, kterými jsou jednotlivé prvky konjugace modifikovány. Huang a kol. (2018) [286] připravili multifunkční bimetalický NCP složený z AuNCs a SPIONs se schopností duálního zobrazování a možností distribuce léčiv. Nejprve s využitím metody koprecipitace připravili SPIONs, jejichž povrch následně modifikovali prostřednictvím 3-aminopropyltriethoxysilanu. Poté připravili AuNCs s využitím kyseliny lipoové jako stabilizujícího činidla, které následně konjugovali s funkcionalizovanými SPIONs skrze amidové vazby. Nakonec konjugát uzavřeli do lipozomů a realizovali *in vitro* MRI a *in vivo* fluorescenční zobrazování (FI). S pomocí *ex vivo* optického zobrazování orgánů zjistili, že jejich NCP je primárně metabolizován v ledvinách.

Luo a kol. (2017) [285] připravili bimetalický NCP složený z AuNCs, SPIONs a SiO_2 vykazující peroxidázovou aktivitu. Nejprve připravili SPIONs pomocí metody koprecipitace a následně provedli aminaci pomocí 3-aminopropyltriethoxysilanu. Pak připravili AuNCs s využitím BSA jakožto stabilizujícího a redukčního činidla, kdy pro aktivaci COOH skupin BSA užili N-(3-dimethylaminopropyl)-N'-ethylkarbodiimid a také N-hydroxysukcinimid (NHS). Konjugací obou NSs vznikl výsledný NCP se schopností katalyzovat oxidaci substrátu peroxidázy 3,3',5,5'-tetramethylbenzidinu v přítomnosti H_2O_2 za vzniku 3,3',5,5'-tetramethylbenzidindiiminu, produktu modré barvy. Díky tomuto je možné tento systém použít pro citlivou kolorimetrickou detekci H_2O_2 s detekčním limitem 0,6 μM a glukózy s detekčním limitem 3 μM a navíc, díky emisi AuNCs v červené oblasti a jejího zhášení H_2O_2, je možné detekovat přítomnost glukózy také pomocí fluorescence. Kolorimetrická detekce glukózy je selektivní vůči analogům glukózy (laktóza, sacharóza a maltóza) a má velký potenciál pro detekci glukózy ve vzorcích lidského séra.

Metodou **povrchové redukce** připravili Zhao a kol. (2015) [287] bimetalický NCP složený z AuNCs a SPIONs se schopností *in vivo* zobrazování s využitím výpočetní tomografie a *in vivo* MRI, možností optického zobrazování buněk, a nakonec diagnózy různých onemocnění jater s potenciálem pro spolehlivé rozlišení stupně jaterního onemocnění. Stejně jako v předešlých případech, SPIONs byly připraveny pomocí koprecipitační metody, avšak tentokrát modifikovány prostřednictvím DMSA. K takto

funkcionalizovaným SPIONs byla poté přidána $HAuCl_4$ a redukcí Au thiolovými skupinami DMSA byly připraveny SPIONs pokryté AuNCs.

Jednou z **nekovalentních interakcí** je interakce elektrostatická, kterou Le Guével a kol. (2012) [288] využili k přípravě NCP složeného z AuNCs a superparamagnetického Mn-Zn feritu $Mn_{0,8}Zn_{0,2}Fe_2O_4$ s potenciálem využití jakožto nosiče léčiv a kontrastní látky pro duální zobrazování (FI a MRI). Nejprve pomocí koprecipitace připravili Mn-Zn ferit, který poté obalili několika vrstvami opačně nabitého polyallylamin hydrochloridu. Posléze připravili AuNCs s využitím BSA jakožto stabilizujícího a redukčního činidla. Syntetizované AuNCs byly nakonec adsorbovány na povrch modifikovaného feritu prostřednictvím elektrostatických interakcí.

Podobně Wang a kol. (2015) [289] využili elektrostatickou interakci k syntéze bimetalického NCP tvořeného AuNCs a SPIONs s potenciálem pro duální zobrazování (FI a MRI). Nejprve připravili AuNCs s využitím GSH jako stabilizujícího a redukčního činidla. Následně připravili magnetické nanočástice Fe_3O_4 s využitím metody termální dekompozice, které poté modifikovali bromidem hexadecyltrimethylamonným, jenž obsahuje kladně nabitý kvarterní dusík, díky kterému lze adsorbovat negativně nabité AuNCs na povrch funkcionalizovaných SPIONs.

Rovněž Cho a kol. (2017) [290] připravili bimetalický NCP prostřednictvím elektrostatické interakce, jenž je tvořený AuNCs a magnetickými Fe_3O_4 nanočásticemi, které výrazně vylepšují katalytickou aktivitu samotných AuNCs. Vylepšené vlastnosti využili ke kolorimetrickému stanovení glukózy ve vzorcích lidského séra s detekčním limitem 100 μM, vysokou selektivitou oproti močovině, fruktóze, laktóze a kyselině askorbové (tedy oproti molekulám, které se v krvi běžně vyskytují) a s potenciálem diagnostikování hyperglykémie v komplexních klinických vzorcích.

Shibu a kol. (2013) [291] nasyntetizovali bimetalický NCP tvořený AuNCs a magnetickými Fe_3O_4 nanočásticemi pomocí **metody samouspořádávání** (anglicky self-assembly), kdy využili silnou nekovalentní interakci mezi biotinem a avidinem [11]. Nejdříve připravili AuNCs s využitím BSA jakožto stabilizujícího a redukčního činidla. Prostřednictvím biotin-NHS esteru posléze biotinylovali aminoskupiny BSA, zatímco nanočástice funkcionalizovali streptavidinem. Konjugací obou funkcionalizovaných NSs získali NCP, který po konjugaci s epidermálním růstovým faktorem využili pro *in vitro* duální zobrazování (FI a MRI) živých buněk.

Příkladem druhého přístupu, tedy *in situ* **syntézy**, budiž příprava bimetalického NCP složeného z AuNCs a SPIONs, který byl využit jakožto kontrastní látka pro *in vitro* a *in vivo* duální zobrazování (FI a MRI) [292]. Bimetalický NCP byl připraven postupným smísením všech vstupních látek, přičemž schéma přípravy lze pozorovat na obrázku níže (viz Obrázek 17).
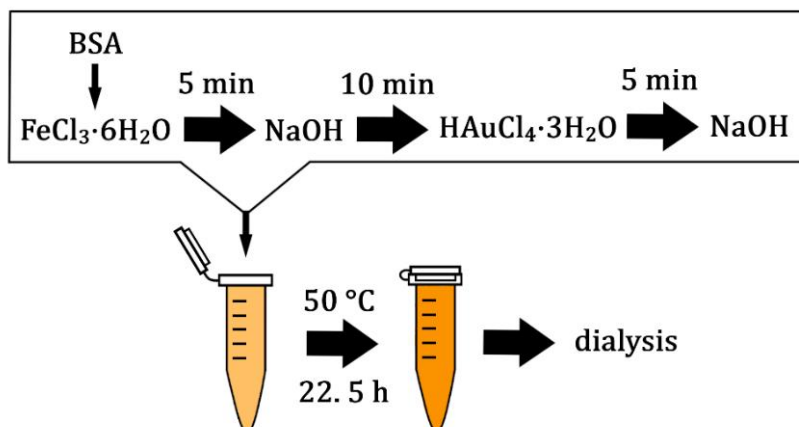
Obrázek 17: *Schematické znázornění přípravy bimetalického nanokompozitu dle [292].*

Obecně lze bimetalické NCPs syntetizovat i **pomocí dalších metod**, ke kterým patří například solvotermální a hydrotermální metoda, pyrolýza nebo elektrodepozice, jež spočívá v nanášení vodivého materiálu (kov nebo vodivý polymer) na pracovní elektrodu na základě redoxních dějů [11].

Jak bylo popsáno ve výčtu syntéz jednotlivých autorů výše, přidáním další kovové NSs lze vylepšit stávající vlastnosti monometalického NCP [285,290] a/nebo rozšířit jeho aplikovatelnost o další zobrazovací modalitu či jiné **využití** (například [286,289,291]). Zobrazování s využitím několika modalit současně může být velmi přínosné, neboť jejich užitečnou kombinací lze překonat omezení související s jejich samostatným používáním. Kupříkladu, vysoká citlivost optického zobrazování umožňuje sledování biologických dějů na molekulární úrovni v reálném čase, nicméně kvůli omezené propustnosti záření skrz tkáně neumožňuje získat její detailní 3D obraz. Na rozdíl od toho MRI poskytuje 3D obraz měkkých tkání s vysokým prostorovým rozlišením, ale bohužel citlivost této metody je nízká [289,293].

1.7. Proteinová matrice BSA

Albuminy jsou ve vodě rozpustné jednořetězcové globulární proteiny, které jsou díky své dostupnosti často využívány jako modelové proteiny v laboratorní praxi [294]. Jsou charakteristické nízkým obsahem tryptofanu a methioninu, a naopak vysokým obsahem nabitých aminokyselin (asparagová a glutamová kyselina, lysin a arginin) [295], kterých se v BSA nachází dohromady 181, z čehož 100 jich je nabitých negativně [296]. Sérové albuminy jsou v tělech obratlovců hojně zastoupené, podílejí se na udržování osmotického tlaku krve a hrají důležitou roli v distribuci mnoha metabolitů, hormonů, léčiv a přechodných kovů [294,297]. Většina albuminů savců (i BSA) obsahuje 4 vazebná místa pro kovy, které se však značně liší svou strukturou a specifitou [297]. Jmenovitě jde o N-koncové místo (známé jako NTS), Cys34 a jeho okolí, vazebné místo A, které bylo později ztotožněno s vícekovovým vazebným místem, a vazebné místo B [297].

Primární struktura BSA je dána sekvencí 583 aminokyselin, přičemž její podobnost se sekvencí lidského sérového albuminu je 75,6 % [298,299]. Je tvořen celkem 2 tryptofanovými rezidui, 20 tyrozinovými rezidui a 35 cysteinovými rezidui, z nichž 34 vytváří disulfidické můstky [295,298,299]. Jeho molekulová hmotnost byla stanovena mnoha autory, a to kupříkladu jako 66 500 Da [300], 66 267 Da [301], 66 600 Da [302], 66 509 ± 23 Da [303] a 66 465,8 Da [298]. Hirayama a kol. (1990) [298] opravili počet aminokyselin v BSA z dříve uváděných 582 [295] na 583 (chybějící tyrosin), díky čemuž se teoretická hodnota molekulové hmotnosti 66 430,3 Da přiblížila experimentálně určené hodnotě 66 431,5 ± 1,3 Da autory Feng a kol. (1991) [304].

Sekundární struktura BSA je převážně α-helikální, přičemž její procentuální zastoupení je uvedeno v tabulce níže (viz Tabulka 7).

Tabulka 7: *Procentuální zastoupení α-helikální struktury v hovězím sérovém albuminu v rozmezí hodnot pH 7 – 8.*

Autoři	pH	Zastoupení α-helikální struktury [%]
[305]	8	55
[306]	7,4	62,9 ± 2,9
[307]	7	67
[308]	7,4	59,6
[309]	7,4	59,3

Terciární struktura se skládá ze tří homologních domén (I, II a III), přičemž každá doména se skládá ze dvou subdomén (A a B) (viz Obrázek 18) [299].
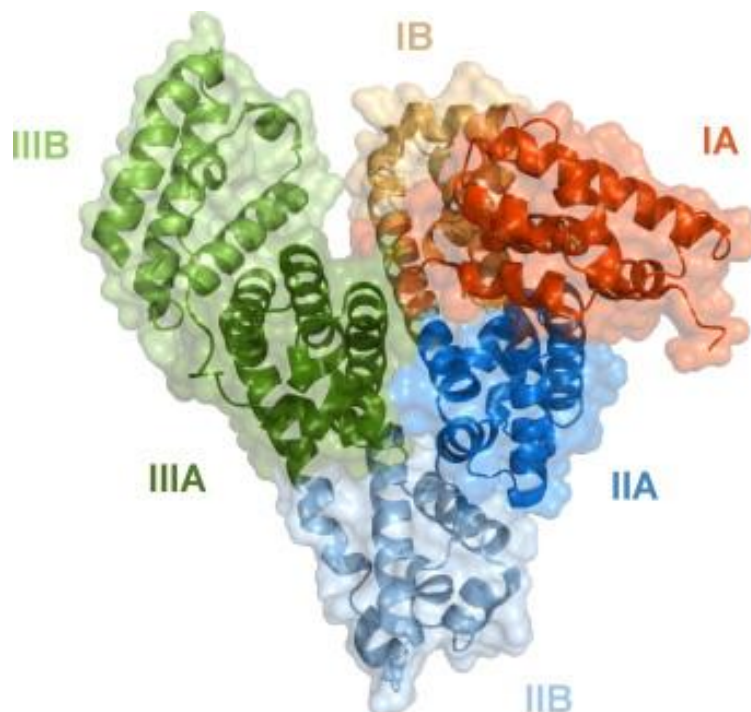
Obrázek 18: *Terciární struktura hovězího sérového albuminu sestává ze tří domén (I, II a III), přičemž každá doména se skládá ze dvou subdomén (A a B). Převzato z [299].*

Konformace BSA ve vodném roztoku je silně závislá na jeho pH, kdy během změny pH z oblasti kyselé do oblasti zásadité můžeme identifikovat celkem až 5 izomerních forem: E (pH < 2,7), F (2,7 < pH < 4,3), N (4,3 < pH < 8), B (8 < pH < 10) a A (pH > 10) [310–315]. V rozmezí pH od 4,3 do 8 má BSA svou nativní podobu, jež připomíná tvar srdce [311,316]. Denaturační teplota BSA v 0,1M NaCl je v rozmezí pH od 5,25 do 10,01 větší než 60 °C, přičemž maximální hodnota 64,3 °C je při pH 7 [317]. Kongraksawech a kol. (2007) [318] uvádějí hodnotu 70,6 °C při pH 7 (BSA v 0,01M fosfátovém pufru). Michnik a kol. (2006) [319] uvádějí, že po zahřátí BSA při pH 6,0 ± 0,5 na 60 °C je denaturace proteinu kompletně reverzibilní. Izoelektrický bod se nachází při pH 4,7 [307,320], nicméně Jachimska a Pajor (2012) [305] uvádějí hodnotu izoelektrického bodu 5,1 a Shi a kol. (2005) [321] uvádějí hodnotu 5,4.

UV-vis spektrum BSA vykazuje dva charakteristické píky v ultrafialové oblasti, přičemž jeden se nachází v rozsahu vlnových délek 205–220 nm a souvisí s absorpcí

polypeptidového řetězce BSA a druhý se nachází při 280 nm a je výsledkem absorpce aromatických aminokyselin (tryptofan, tyrosin, fenylalanin) [309,322,323]. Uvedené aminokyseliny jsou rovněž zodpovědné za fluorescenci BSA s maximem v rozsahu vlnových délek 340–350 nm, kde největší příspěvek tvoří tryptofan [308,322,324]. Ve spektru cirkulárního dichroismu BSA se vyskytuje jedno pozitivní maximum okolo 190–195 nm a dvě záporná minima při vlnových délkách 208 a 222 nm, což jsou píky charakteristické pro alfa-helikální strukturu proteinu [308,309,313,322,325].

2. Stručné shrnutí vědecké činnosti

Práci na bimetalických NCPs obsahujících jak AuNCs, tak SPIONs předcházela příprava a charakterizace monometalických NCPs sestávajících pouze z AuNCs. Tento systém je logicky jednodušší, jeho příprava je tvořena menším množstvím kroků a hlavně parametrů, což bylo pro následně uskutečněné optimalizace výhodnější. Monometalický systém sloužil také jako reference ke zmíněnému bimetalickému NCP. Příprava tohoto monometalického systému byla inspirována syntézou publikovanou autory Xie a kol. (2009) [88], přičemž místo konvenčního ohřevu byl pro urychlení vývoje AuNCs použit ohřev mikrovlnný dle autorů Yan a kol. (2012) [76]. Matricí obou výše zmíněných skupin autorů byl protein hovězí sérový albumin (BSA). Jeho význam spočívá v redukci iontů Au^{3+} a následné stabilizaci tvorby a růstu AuNCs [19]. Některé parametry syntézy (koncentrace, molární poměry a doba mezi přidáním jednotlivých vstupních látek, doba mikrovlnného ohřevu, výkon mikrovlnného záření a doba vývoje systému) však byly upraveny s přihlédnutím k výsledkům optimalizačních experimentů, jež byly provedeny z důvodu dosažení co největší hodnoty QY v rozumném čase vývoje systému. Část těchto výsledků, konkrétně vliv molárního poměru HAuCl₄ a NaOH (ovlivňující pH reakční směsi) na hodnotu QY a vlnovou délku maxima emise, je uvedena v konferenčním příspěvku autorů Ostruszka a Šišková (2022) [326].

Připravený monometalický NCP, značený jako AuBSA, vykazuje emisi v červené oblasti spektra s výskytem jednoho maxima při vlnové délce 655 ± 1 nm a hodnotou QY stanovenou jako $6{,}7 \pm 0{,}1$ % [19]. Průměrná velikost AuNCs určená pomocí transmisní elektronové mikroskopie je $1{,}01 \pm 0{,}24$ nm, kdežto v případě užití HRTEMu byla průměrná velikost větší než 2 nm, což bylo vysvětleno pozorováním *in situ* tvorby AuNPs pod fokusovaným svazkem elektronů při užití většího zvětšení a/nebo během mapování s využitím EDS. Pomocí EPR bylo jednak zjištěno, že okamžitě po zahájení ozařování systému AuBSA UVA zářením o vlnové délce 325 nm dochází k tvorbě thiylových (RS•), tryptofanových (Trp•) a také C-centrovaných (C•) radikálů, které s AuNCs magneticky neinteragují, ale při prodlouženém ozařování (nad 10 minut) vedou k nevratnému poškození proteinové matrice; jednak byla poprvé v rámci NCP tvořeného BSA a AuNCs prokázána přítomnost Au^{2+}, přičemž autoři většinou uvádějí výskyt oxidačních stavů Au^0 a Au^+, jež nejčastěji detekují pomocí rentgenové fotoelektronové spektroskopie (například [67,88,327,328]). Rovněž byla porovnáním EPR spekter systému AuBSA a prekurzoru Au, kterým byla kyselina tetrachlorozlatitá (HAuCl₄), potvrzena schopnost

BSA redukovat Au^{3+} na nižší oxidační stavy, přičemž s využitím absorpční spektroskopie byla pozorována redukce Au^{3+} na Au^0 za vzniku AuNPs (jejichž projevem je pík SPR) v případě, kdy byla $HAuCl_4$ inkubována s tyrosinem (aminokyselina, která je součástí BSA).

V návaznosti na monometalický systém AuBSA byl současně připraven jednak NCP bimetalický, značený jako AuBSA-Fe, jehož syntéza byla obohacena o prekurzory železa ($FeCl_2·4H_2O$ a $FeCl_3·6H_2O$), nicméně původní molární poměry pro ostatní reaktanty (tj. BSA: $HAuCl_4$ a $HAuCl_4$: NaOH) byly zachovány; jednak byl připraven další referenční NCP, označený jako BSA-Fe, jenž se od AuBSA liší tím, že neobsahuje AuNCs, ale naopak je tvořený SPIONs generovanými v přítomnosti BSA. Syntéza tohoto NCP je obdobou syntézy AuBSA-Fe s tím rozdílem, že $HAuCl_4$ byla nahrazena HCl tak, že bylo ponecháno stejné látkové množství Cl^-. Jak systém BSA-Fe, tak AuBSA-Fe byly opět zkoumány pomocí EPR spektroskopie a bylo experimentálně prokázáno, že v rámci obou systémů je Fe přítomno jednak ve formě jednojaderných komplexů, jednak ve formě SPIONs (jak bylo dříve prokázáno pomocí Mössbauerovy spektroskopie v [19]), přičemž v případě bimetalického NCP dochází k tvorbě SPIONs menších velikostí než v rámci systému monometalického BSA-Fe [329]. Také byla pozorována komunikace v podobě přenosu náboje mezi SPIONs (donor) a komplexy Fe (akceptor) po ozáření UVA zářením o vlnové délce 325 nm, avšak pouze v případě BSA-Fe (v rámci AuBSA-Fe nebyl tento přenos náboje pozorován). V neposlední řadě byl proveden experiment s užitím spinové pasti (anglicky spin trap), který odhalil přítomnost hydroxylových radikálů (˙OH) generovaných ve vodném roztoku po ozáření obou studovaných NCPs (BSA-Fe a AuBSA-Fe) UVA zářením po dobu 5 minut při pokojové teplotě.

AuNCs v systému AuBSA-Fe opět emitují v červené oblasti spektra s obdobnými hodnotami vlnové délky maxima emise a QY, jaké měly AuNCs v systému AuBSA [330]. Z průběhu mössbauerovských spekter při teplotách 300 a 5 K (u druhého též v externím magnetickém poli) bylo prokázáno, že nanočásticová forma Fe v systému AuBSA-Fe je superparamagnetický oxid železa v oxidačním stavu III. Výsledky z EDS poukazují na dominantní výskyt O v blízkosti Fe v nanočásticové formě a přítomnost S poblíž Au. Je známo, že AuNCs je k BSA vázáno přes S (například [331,332]) a SPIONs (a oxidy železa obecně) interagují snadno s COOH a/nebo OH skupinami [333,334]. Důsledkem této odlišné afinity je fakt, že jak AuNCs, tak SPIONs mohou být v rámci BSA lokalizovány poblíž odlišných aminokyselinových reziduí [329]. Také bylo provedeno

in vitro MRI s viditelným T_2 kontrastem a relaxometrie, kdy hodnoty relaxivity byly získány fitováním závislosti reciproké hodnoty relaxačního času na koncentraci Fe, přičemž ve zkoumaném rozsahu koncentrací byly identifikovány dvě lineární závislosti, a byly tedy získány dvě hodnoty relaxivity. V neposlední řadě byla stanovena viabilita nerakovinných RPE-1 buněk při jejich inkubaci se systémem AuBSA-Fe, která dosahovala hodnot okolo 80 % pro obě koncentrační oblasti, což dle ISO 10993 řadí tento NCP stále mezi netoxické látky [330].

V mezičase probíhaly četné optimalizace diskutovaného bimetalického systému, jednak na základě znalostí získaných z optimalizačních experimentů monometalického systému AuBSA, jednak byly některé experimenty inspirovány kupříkladu autory Babes a kol. (1999) [335], Andrade a kol. (2010) [336] a Ueno a kol. (2014) [337]. Optimalizace byly převážně zaměřeny na vylepšení magnetického kontrastu, jelikož uspokojivého kontrastu v případě systému AuBSA-Fe bylo dosaženo pouze po předchozím zakoncentrování vzorků, což mimo jiné vedlo ke zvýšení viskozity roztoku a snížení viability buněk zhruba na hraničních 80 %. Optimalizace bimetalického systému byla mnohem komplexnější, a to jednak proto, že zpočátku byla nepřekonatelnou překážkou jeho stabilita, jelikož docházelo k častým agregacím proteinové matrice nebo převážně agregacím Fe v mikročástice, jednak bylo potřeba najít takové podmínky, aby obě výsledné NSs (jak AuNCs, tak SPIONs) vykazovaly současně co možná nejlepší vlastnosti za daný čas jejich společného vývoje. Jedny z posledních experimentů byly inspirovány Jolivet a kol. (2004) [338], přičemž byly prováděny s myšlenkou, že zvýšení pH na hodnotu 7,4 před přidáním $HAuCl_4$, kdy se Fe^{3+} vyskytují převážně ve formě neutrálních komplexů [338], by mohlo vést ke zvýšení interakcí mezi komplexy Fe a proteinovou matricí, která by se navíc měla v tomto pH nacházet ve své přirozené konformaci [311,316]. Některé výsledky z těchto optimalizačních experimentů jsou uvedeny v Ostruszka a kol. (2024) [292].

Nakonec se povedlo připravit bimetalický NCP, označený jako APEBM, jehož syntéza respektuje principy „zelené chemie" (tj. práce ve vodném prostředí, použití netoxických látek a vyvarování se nadbytečnému množství chemikálií) [292]. Oproti syntéze AuBSA-Fe byly upraveny a/nebo nově zavedeny následující parametry: typ prekurzoru Fe, pořadí přidání jednotlivých reaktantů, jemná úprava pH před přidáním $HAuCl_4$, prodloužená doba mezi jednotlivými kroky syntézy, typ ohřevu pro urychlení obou chemických procesů (redukce Au^{3+} iontů a formace SPIONs) a delší doba dozrávání

vzorku, a to navíc při vyšší teplotě. Výsledkem je NCP velmi stabilní vůči agregaci jak v deionizované vodě, tak i v pufru PBS a kultivačním médiu, a to při různých teplotách inkubace (4, 20 a 37 °C). Teoretické molární poměry BSA: Au: Fe byly z původních hodnot 1: 10: 0,75 navýšeny na 1: 20: 20, přičemž experimentální poměry po dialýze jsou 1: 16: 18. Koncentrace Fe v optimalizovaném NCP byla tedy celkově navýšena více než dvacetinásobně. Bimetalický APEBM NCP vykazuje monomodální distribuci velikostí s hodnotou hydrodynamického průměru $d_H = 296 \pm 14$ nm a buněčné viability větší než 90 % pro nejvyšší koncentraci vzorku (tj. koncentrace přímo po dialýze, jež vzorek naředí vždy 1,5x deionizovanou vodou).

Nejprve bylo provedeno *in vitro* FI a MRI, avšak s přihlédnutím ke komplexnosti buněčné internalizace nanomateriálů, která je závislá na mnoha vzájemně propojených parametrech, bylo rovněž provedeno zobrazování *in vivo*. Totiž, hydrodynamický průměr a povrchový náboj (obecně reprezentován jako zeta potenciálem) sice hrají určitou roli v interakcích mezi nanomateriálem a buňkami [339–345], avšak mnoho jiných faktorů může mít také vliv na buněčnou internalizaci a/nebo cytotoxicitu studovaného materiálu. Mezi tyto faktory patří například tvar [346,347], složení kovového jádra a povrchu [346,348], elasticita [349,350], hydrofobicita [348,351] a rovněž i přítomnost a složení proteinové korony [346,352–354], která může být modulována fyzikálně-chemickými parametry, jakými mohou být pH, iontová síla, teplota, koncentrace plazmy, a dokonce také množství cholesterolu [354–358]. Z výsledných obrázků pořízených během *in vivo* MRI (viz Obrázek 19A a 19B) a FI (viz Obrázek 19C) je zřejmé, že prezentovaný NCP má schopnost sloužit jakožto efektivní inertní kontrastní látka pro duální zobrazování. Luminiscenční signál optimalizovaného NCP je nejméně 20x silnější než signál reference (tj. končetina injektovaná destilovanou vodou) a MR kontrast lze relativně dobře odlišit od okolní svalové tkáně.
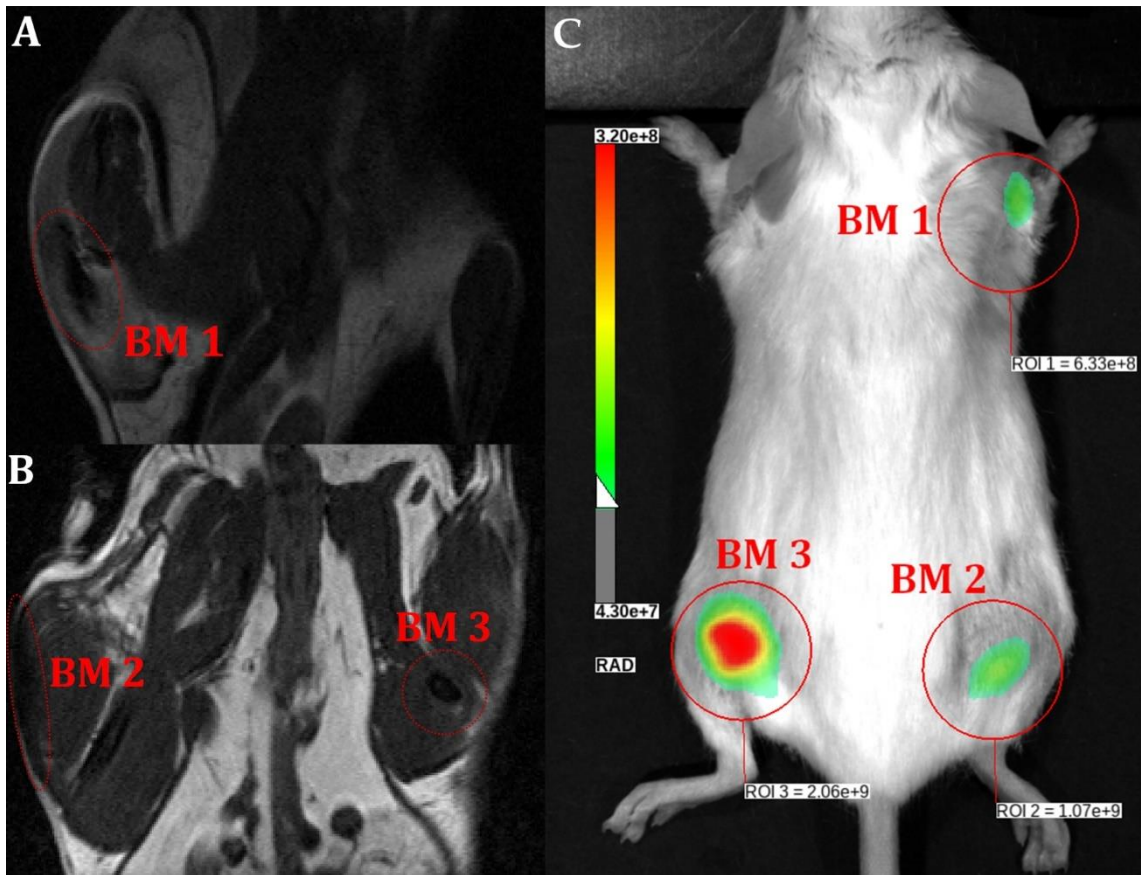
Obrázek 19: *In vivo (A, B) zobrazování magnetickou rezonancí a (C) fluorescenční zobrazování zdravé BALB/c myši pod anestézií. Triplikát bimetalického nanokompozitu APEBM (označené jako BM 1, BM 2 a BM 3) byl aplikován do jednotlivých končetin. Do neoznačené končetiny byla vpíchnuta destilovaná voda sloužící jako reference. Obrázky převzaty z [292] a zkombinovány.*

3. Závěr

Předložená dizertační práce se ze své převážné části soustředí na předání poznatků ohledně dvou zcela odlišných kovových NSs, AuNCs a SPIONs, které rozebírá z hlediska jejich optických (případ AuNCs) či magnetických (případ SPIONs) vlastností, strategií syntézy a rovněž možností praktického využití. Posléze se práce věnuje jednak systémům kombinujícím uvedené NSs, jednak proteinu BSA, jenž byl po celou dobu vědecké činnosti autora používán jako matrice pro syntézu těchto NSs. Druhá část práce se zaměřuje právě na zmíněnou vědeckou činnost autora, ve které jsou rozebírány jak NCPs monometalické (značené jako AuBSA, BSA-Fe) sloužící jako referenční systémy, tak NCPs bimetalické (označené jako AuBSA-Fe a APEBM). Díky relativně velkému množství postupných optimalizací syntézy bylo nakonec dosaženo přípravy systému APEBM, jenž je stabilní vůči agregaci v různých prostředích při různých teplotách, vysoce biokompatibilní a má schopnost sloužit jako inertní kontrastní látka pro *in vivo* **duální zobrazování** (FI a MRI). Důležité je zdůraznit, že APEBM nebylo nutné zakoncentrovat pro to, aby poskytoval dostatečný MRI signál, což je velký pokrok oproti systému AuBSA-Fe, jehož zakoncentrování vedlo k poklesu biokompatibility a nárůstu viskozity. Další potenciální využití systémů obsahujících SPIONs (ať už jde o systém monometalický či bimetalický) souvisí s generováním ˙OH (detekovaných pomocí EPR spektroskopie) ve vodném roztoku po ozáření daného systému UVA zářením po dobu 5 minut, čehož by se v budoucnu mohlo využít v environmentální oblasti k odstraňování polutantů ve vodě či k eliminaci mikroorganismů. V tomto směru je nicméně potřeba provést další experimenty. Mimo to lze samozřejmě pokračovat také v biomedicínské oblasti, kdy lze systém vylepšit například o možnost cílení do nádorových buněk, a tím umožnit jejich zobrazení a/nebo eliminaci. Nakonec je rovněž podstatné neopomenout roli referenčních monometalických systémů, díky kterým byly osvětleny mnohé vlastnosti nejen samotných monometalických, ale také bimetalických NCPs, což mimo jiné vedlo k přesnějším interpretacím získaných dat a k lepšímu pochopení těchto systémů.

4. Reference

[1]   Zhang L., Wang E. (2014) Metal nanoclusters: New fluorescent probes for sensors and bioimaging. *Nano Today* **9**, 132–157. DOI: 10.1016/j.nantod.2014.02.010.

[2]   Pan Y., Han Z., Chen S., Wei K., Wei X. (2023) Metallic nanoclusters: From synthetic challenges to applications of their unique properties in food contamination detection. *Coordination Chemistry Reviews* **478**, 214964. DOI: 10.1016/j.ccr.2022.214964.

[3]   Díez I., Ras R.H.A. (2010) Few-Atom Silver Clusters as Fluorescent Reporters. In: *Advanced Fluorescence Reporters in Chemistry and Biology II: Molecular Constructions, Polymers and Nanoparticles.*, pp. 307–332. DOI: 10.1007/978-3-642-04701-5_10.

[4]   Sonia, Komal, Kukreti S., Kaushik M. (2021) Gold nanoclusters: An ultrasmall platform for multifaceted applications. *Talanta* **234**, 122623. DOI: 10.1016/j.talanta.2021.122623.

[5]   Mooradian A. (1969) Photoluminescence of Metals. *Physical Review Letters* **22**, 185–187. DOI: 10.1103/PhysRevLett.22.185.

[6]   Olesiak-Banska J., Waszkielewicz M., Obstarczyk P., Samoc M. (2019) Two-photon absorption and photoluminescence of colloidal gold nanoparticles and nanoclusters. *Chemical Society Reviews* **48**, 4087–4117. DOI: 10.1039/C8CS00849C.

[7]   Liu Z., Zhu M., Meng X., Xu G., Jin R. (2011) Electron Transfer between $[Au_{25}(SC_2H_4Ph)_{18}]^-TOA^+$ and Oxoammonium Cations. *The Journal of Physical Chemistry Letters* **2**, 2104–2109. DOI: 10.1021/jz200925h.

[8]   Zhou M., Du X., Wang H., Jin R. (2021) The Critical Number of Gold Atoms for a Metallic State Nanocluster: Resolving a Decades-Long Question. *ACS Nano* **15**, 13980–13992. DOI: 10.1021/acsnano.1c04705.

[9]   Xu H., Suslick K.S. (2010) Water-Soluble Fluorescent Silver Nanoclusters. *Advanced Materials* **22**, 1078–1082. DOI: 10.1002/adma.200904199.

[10]   Zheng J., Nicovich P.R., Dickson R.M. (2007) Highly Fluorescent Noble-Metal Quantum Dots. *Annual Review of Physical Chemistry* **58**, 409–431. DOI: 10.1146/annurev.physchem.58.032806.104546.

[11]   Shang L., Xu J., Nienhaus G.U. (2019) Recent advances in synthesizing metal nanocluster-based nanocomposites for application in sensing, imaging and catalysis. *Nano Today* **28**, 100767. DOI: 10.1016/j.nantod.2019.100767.

[12]   Liu H., Zhang X., Wu X., Jiang L., Burda C., Zhu J.-J. (2011) Rapid sonochemical synthesis of highly luminescent non-toxic AuNCs and Au@AgNCs and Cu (II) sensing. *Chemical Communications* **47**, 4237. DOI: 10.1039/c1cc00103e.

[13]   Zhang H., Huang X., Li L., Zhang G., Hussain I., Li Z., Tan B. (2012) Photoreductive synthesis of water-soluble fluorescent metal nanoclusters. *Chem. Commun.* **48**, 567–569. DOI: 10.1039/C1CC16088E.

[14]   Negishi Y., Nakazaki T., Malola S., Takano S., Niihori Y., Kurashige W., Yamazoe S., Tsukuda T., Häkkinen H. (2015) A Critical Size for Emergence of Nonbulk Electronic and Geometric Structures in Dodecanethiolate-Protected Au Clusters. *Journal of the American Chemical Society* **137**, 1206–1212. DOI: 10.1021/ja5109968.

[15]   Zhou S., Duan Y., Wang F., Wang C. (2017) Fluorescent Au nanoclusters stabilized by silane: facile synthesis, color-tunability and photocatalytic properties. *Nanoscale* **9**, 4981–4988. DOI: 10.1039/C7NR01052D.

[16]   Jia Y., Sun T., Jiang Y., Sun W., Zhao Y., Xin J., Hou Y., Yang W. (2018) Green, fast, and large-scale synthesis of highly fluorescent Au nanoclusters for Cu^{2+} detection and temperature sensing. *The Analyst* **143**, 5145–5150. DOI: 10.1039/C8AN01617H.

[17]   Sakthivel N.A., Stener M., Sementa L., Fortunelli A., Ramakrishna G., Dass A. (2018) $Au_{279}(SR)_{84}$: The Smallest Gold Thiolate Nanocrystal That Is Metallic and the Birth of Plasmon. *The Journal of Physical Chemistry Letters* **9**, 1295–1300. DOI: 10.1021/acs.jpclett.8b00308.

[18]   Chuang C.-H., Chen W.-Y., Tseng W.-B., Lin A., Lu C.-Y., Tseng W.-L. (2022) Microwave-Mediated Synthesis of Near-Infrared-Emitting Silver Ion-Modified Gold Nanoclusters for Ratiometric Sensing of Hydrosulfide in Environmental Water and Hydrogen Sulfide in Live Cells. *ACS Sustainable Chemistry & Engineering* **10**, 2461–2472. DOI: 10.1021/acssuschemeng.1c07440.

[19]   Ostruszka R., Zoppellaro G., Tomanec O., Pinkas D., Filimonenko V., Šišková K. (2022) Evidence of Au(II) and Au(0) States in Bovine Serum Albumin-Au Nanoclusters Revealed by CW-EPR/LEPR and Peculiarities in HR-TEM/STEM Imaging. *Nanomaterials* **12**, 1425. DOI: 10.3390/nano12091425.

[20]   Varnavski O., Ramakrishna G., Kim J., Lee D., Goodson T. (2010) Critical Size for the Observation of Quantum Confinement in Optically Excited Gold Clusters. *Journal of the American Chemical Society* **132**, 16–17. DOI: 10.1021/ja907984r.

[21]   Philip R., Chantharasupawong P., Qian H., Jin R., Thomas J. (2012) Evolution of Nonlinear Optical Properties: From Gold Atomic Clusters to Plasmonic Nanocrystals. *Nano Letters* **12**, 4661–4667. DOI: 10.1021/nl301988v.

[22]   Zhou M., Zeng C., Chen Y., Zhao S., Sfeir M.Y., Zhu M., Jin R. (2016) Evolution from the plasmon to exciton state in ligand-protected atomically precise gold nanoparticles. *Nature Communications* **7**, 13240. DOI: 10.1038/ncomms13240.

[23]   Kwak K., Thanthirige V.D., Pyo K., Lee D., Ramakrishna G. (2017) Energy Gap Law for Exciton Dynamics in Gold Cluster Molecules. *The Journal of Physical Chemistry Letters* **8**, 4898–4905. DOI: 10.1021/acs.jpclett.7b01892.

[24]   Zhou M., Zeng C., Song Y., Padelford J.W., Wang G., Sfeir M.Y., Higaki T., Jin R. (2017) On the Non-Metallicity of 2.2 nm $Au_{246}(SR)_{80}$ Nanoclusters. *Angewandte Chemie* **129**, 16475–16479. DOI: 10.1002/ange.201709095.

[25]   Higaki T., Zhou M., Lambright K.J., Kirschbaum K., Sfeir M.Y., Jin R. (2018) Sharp Transition from Nonmetallic Au_{246} to Metallic Au_{279} with Nascent Surface Plasmon Resonance. *Journal of the American Chemical Society* **140**, 5691–5695. DOI: 10.1021/jacs.8b02487.

[26]   Zhou M., Higaki T., Li Y., Zeng C., Li Q., Sfeir M.Y., Jin R. (2019) Three-Stage Evolution from Nonscalable to Scalable Optical Properties of Thiolate-Protected Gold Nanoclusters. *Journal of the American Chemical Society* **141**, 19754–19764. DOI: 10.1021/jacs.9b09066.

[27]   Zhu M., Aikens C.M., Hollander F.J., Schatz G.C., Jin R. (2008) Correlating the Crystal Structure of A Thiol-Protected Au_{25} Cluster and Optical Properties. *Journal of the American Chemical Society* **130**, 5883–5885. DOI: 10.1021/ja801173r.

[28]   Nobusada K., Iwasa T. (2007) Oligomeric Gold Clusters with Vertex-Sharing Bi- and Triicosahedral Structures. *The Journal of Physical Chemistry C* **111**, 14279–14282. DOI: 10.1021/jp075509w.

[29]   Zhu M., Eckenhoff W.T., Pintauer T., Jin R. (2008) Conversion of Anionic $[Au_{25}(SCH_2CH_2Ph)_{18}]^-$ Cluster to Charge Neutral Cluster via Air Oxidation. *The Journal of Physical Chemistry C* **112**, 14221–14224. DOI: 10.1021/jp805786p.

[30]   Qian H., Zhu M., Wu Z., Jin R. (2012) Quantum Sized Gold Nanoclusters with Atomic Precision. *Accounts of Chemical Research* **45**, 1470–1479. DOI: 10.1021/ar200331z.

[31]   Devadas M.S., Bairu S., Qian H., Sinn E., Jin R., Ramakrishna G. (2011) Temperature-Dependent Optical Absorption Properties of Monolayer-Protected Au_{25} and Au_{38} Clusters. *The Journal of Physical Chemistry Letters* **2**, 2752–2758. DOI: 10.1021/jz2012897.

[32]   Ramakrishna G., Varnavski O., Kim J., Lee D., Goodson T. (2008) Quantum-Sized Gold Clusters as Efficient Two-Photon Absorbers. *Journal of the American Chemical Society* **130**, 5032–5033. DOI: 10.1021/ja800341v.

[33]   Liu C.-L. *et al.* (2009) Thiol-Functionalized Gold Nanodots: Two-Photon Absorption Property and Imaging *In Vitro*. *The Journal of Physical Chemistry C* **113**, 21082–21089. DOI: 10.1021/jp9080492.

[34]   Peng Y., Gao L., Pidamaimaiti G., Zhao D., Zhang L., Yin G., Wang F. (2022) Facile construction of highly luminescent and biocompatible gold nanoclusters by shell rigidification for two-photon pH-edited cytoplasmic and *in vivo* imaging. *Nanoscale* **14**, 8342–8348. DOI: 10.1039/D2NR01078J.

[35]   Xu J., Shang L. (2018) Emerging applications of near-infrared fluorescent metal nanoclusters for biological imaging. *Chinese Chemical Letters* **29**, 1436–1444. DOI: 10.1016/j.cclet.2017.12.020.

[36]   Kundu S., Ghosh B., Nandi S., Ghosh M., Pyne A., Chatterjee J., Sarkar N. (2020) Surface Ligand-Controlled Wavelength-Tunable Luminescence of Gold Nanoclusters: Cellular Imaging and Smart Fluorescent Probes for Amyloid Detection. *ACS Applied Bio Materials* **3**, 4282–4293. DOI: 10.1021/acsabm.0c00337.

[37]   Han R. *et al.* (2020) Super-efficient *in Vivo* Two-Photon Photodynamic Therapy with a Gold Nanocluster as a Type I Photosensitizer. *ACS Nano* **14**, 9532–9544. DOI: 10.1021/acsnano.9b05169.

[38]   Mussa Farkhani S., Dehghankelishadi P., Refaat A., Veerasikku Gopal D., Cifuentes-Rius A., Voelcker N.H. (2024) Tailoring gold nanocluster properties for biomedical applications: From sensing to bioimaging and theranostics. *Progress in Materials Science* **142**, 101229. DOI: 10.1016/j.pmatsci.2023.101229.

[39] Link S., Beeby A., FitzGerald S., El-Sayed M.A., Schaaff T.G., Whetten R.L. (2002) Visible to Infrared Luminescence from a 28-Atom Gold Cluster. *The Journal of Physical Chemistry B* **106**, 3410–3415. DOI: 10.1021/jp014259v.

[40] Devadas M.S., Kim J., Sinn E., Lee D., Goodson T., Ramakrishna G. (2010) Unique Ultrafast Visible Luminescence in Monolayer-Protected Au_{25} Clusters. *The Journal of Physical Chemistry C* **114**, 22417–22423. DOI: 10.1021/jp107033n.

[41] Wen X., Yu P., Toh Y.-R., Tang J. (2012) Structure-Correlated Dual Fluorescent Bands in BSA-Protected Au_{25} Nanoclusters. *The Journal of Physical Chemistry C* **116**, 11830–11836. DOI: 10.1021/jp303530h.

[42] Li Q. *et al.* (2019) A Mono-cuboctahedral Series of Gold Nanoclusters: Photoluminescence Origin, Large Enhancement, Wide Tunability, and Structure–Property Correlation. *Journal of the American Chemical Society* **141**, 5314–5325. DOI: 10.1021/jacs.8b13558.

[43] Zhou M., Song Y. (2021) Origins of Visible and Near-Infrared Emissions in $[Au_{25}(SR)_{18}]^{-}$ Nanoclusters. *The Journal of Physical Chemistry Letters* **12**, 1514–1519. DOI: 10.1021/acs.jpclett.1c00120.

[44] Wang G., Guo R., Kalyuzhny G., Choi J.-P., Murray R.W. (2006) NIR Luminescence Intensities Increase Linearly with Proportion of Polar Thiolate Ligands in Protecting Monolayers of Au_{38} and Au_{140} Quantum Dots. *The Journal of Physical Chemistry B* **110**, 20282–20289. DOI: 10.1021/jp0640528.

[45] Wu Z., Jin R. (2010) On the Ligand's Role in the Fluorescence of Gold Nanoclusters. *Nano Letters* **10**, 2568–2573. DOI: 10.1021/nl101225f.

[46] Londoño-Larrea P., Vanegas J.P., Cuaran-Acosta D., Zaballos-García E., Pérez-Prieto J. (2017) Water-Soluble Naked Gold Nanoclusters Are Not Luminescent. *Chemistry – A European Journal* **23**, 8137–8141. DOI: 10.1002/chem.201700913.

[47] Andrýsková P., Šišková K.M., Michetschlägerová Š., Jiráková K., Kubala M., Jirák D. (2020) The Effect of Fatty Acids and BSA Purity on Synthesis and Properties of Fluorescent Gold Nanoclusters. *Nanomaterials* **10**, 343. DOI: 10.3390/nano10020343.

[48] Zhu L. *et al.* (2021) Surface Engineering of Gold Nanoclusters Protected with 11-Mercaptoundecanoic Acid for Photoluminescence Sensing. *ACS Applied Nano Materials* **4**, 3197–3203. DOI: 10.1021/acsanm.1c00404.

[49] Peng H., Jian M., Deng H., Wang W., Huang Z., Huang K., Liu A., Chen W. (2017) Valence States Effect on Electrogenerated Chemiluminescence of Gold Nanocluster. *ACS Applied Materials & Interfaces* **9**, 14929–14934. DOI: 10.1021/acsami.7b02446.

[50] Kim J.M., Jeong S., Song J.K., Kim J. (2018) Near-infrared electrochemiluminescence from orange fluorescent Au nanoclusters in water. *Chemical Communications* **54**, 2838–2841. DOI: 10.1039/C7CC09394B.

[51] Huang Z., Li Z., Chen Y., Xu L., Xie Q., Deng H., Chen W., Peng H. (2021) Regulating Valence States of Gold Nanocluster as a New Strategy for the Ultrasensitive Electrochemiluminescence Detection of Kanamycin. *Analytical Chemistry* **93**, 4635–4640. DOI: 10.1021/acs.analchem.1c00063.

[52] Guo W., Zhao L., Jiang L., Nie Y., Zhou Y. (2024) Progress, enhancement mechanisms and applications of electrochemiluminescence and photoluminescence metal nanoclusters. *TrAC Trends in Analytical Chemistry* **170**, 117443. DOI: 10.1016/j.trac.2023.117443.

[53] Negishi Y., Iwai T., Ide M. (2010) Continuous modulation of electronic structure of stable thiolate-protected Au_{25} cluster by Ag doping. *Chemical Communications* **46**, 4713. DOI: 10.1039/c0cc01021a.

[54] Oh E., Delehanty J.B., Field L.D., Mäkinen A.J., Goswami R., Huston A.L., Medintz I.L. (2016) Synthesis and Characterization of PEGylated Luminescent Gold Nanoclusters Doped with Silver and Other Metals. *Chemistry of Materials* **28**, 8676–8688. DOI: 10.1021/acs.chemmater.6b03838.

[55] Liu H. *et al.* (2019) Atomic-Precision Gold Clusters for NIR-II Imaging. *Advanced Materials* **31**. DOI: 10.1002/adma.201901015.

[56] Qian S., Wang Z., Zuo Z., Wang X., Wang Q., Yuan X. (2022) Engineering luminescent metal nanoclusters for sensing applications. *Coordination Chemistry Reviews* **451**, 214268. DOI: 10.1016/j.ccr.2021.214268.

[57] Cifuentes-Rius A., Deepagan V.G., Xie J., Voelcker N.H. (2021) Bright Future of Gold Nanoclusters in Theranostics. *ACS Applied Materials & Interfaces* **13**, 49581–49588. DOI: 10.1021/acsami.1c14275.

[58] Duan H., Nie S. (2007) Etching Colloidal Gold Nanocrystals with Hyperbranched and Multivalent Polymers: A New Route to Fluorescent and Water-Soluble Atomic Clusters. *Journal of the American Chemical Society* **129**, 2412–2413. DOI: 10.1021/ja067727t.

[59] Bain D., Maity S., Paramanik B., Patra A. (2018) Core-Size Dependent Fluorescent Gold Nanoclusters and Ultrasensitive Detection of Pb^{2+} Ion. *ACS Sustainable Chemistry & Engineering* **6**, 2334–2343. DOI: 10.1021/acssuschemeng.7b03794.

[60] Qian H., Zhu Y., Jin R. (2009) Size-Focusing Synthesis, Optical and Electrochemical Properties of Monodisperse $Au_{38}(SC_2H_4Ph)_{24}$ Nanoclusters. *ACS Nano* **3**, 3795–3803. DOI: 10.1021/nn901137h.

[61] Cao Y., Liu T., Chen T., Zhang B., Jiang D., Xie J. (2021) Revealing the etching process of water-soluble Au_{25} nanoclusters at the molecular level. *Nature Communications* **12**, 3212. DOI: 10.1038/s41467-021-23568-0.

[62] Lin C.-A.J. *et al.* (2009) Synthesis, Characterization, and Bioconjugation of Fluorescent Gold Nanoclusters toward Biological Labeling Applications. *ACS Nano* **3**, 395–401. DOI: 10.1021/nn800632j.

[63] Ke C.-Y., Chen T.-H., Lu L.-C., Tseng W.-L. (2014) Understanding thiol-induced etching of luminescent gold nanoclusters. *RSC Adv.* **4**, 26050–26056. DOI: 10.1039/C4RA02111H.

[64] Habeeb Muhammed M.A., Ramesh S., Sinha S.S., Pal S.K., Pradeep T. (2008) Two distinct fluorescent quantum clusters of gold starting from metallic nanoparticles by pH-dependent ligand etching. *Nano Research* **1**, 333–340. DOI: 10.1007/s12274-008-8035-2.

[65] Habeeb Muhammed M.A., Verma P.K., Pal S.K., Retnakumari A., Koyakutty M., Nair S., Pradeep T. (2010) Luminescent Quantum Clusters of Gold in Bulk by Albumin-Induced Core Etching of Nanoparticles: Metal Ion Sensing, Metal-Enhanced Luminescence, and Biolabeling. *Chemistry – A European Journal* **16**, 10103–10112. DOI: 10.1002/chem.201000841.

[66] Hao D., Zhang X., Su R., Wang Y., Qi W. (2023) Biomolecule-protected gold nanoclusters: synthesis and biomedical applications. *Journal of Materials Chemistry B* **11**, 5051–5070. DOI: 10.1039/D3TB00651D.

[67] Hsu N.-Y., Lin Y.-W. (2016) Microwave-assisted synthesis of bovine serum albumin–gold nanoclusters and their fluorescence-quenched sensing of Hg^{2+} ions. *New Journal of Chemistry* **40**, 1155–1161. DOI: 10.1039/C5NJ02263K.

[68] Lin Y.-C., Wu T., Lin Y.-W. (2018) Fluorescence sensing of mercury(II) and melamine in aqueous solutions through microwave-assisted synthesis of egg-white-protected gold nanoclusters. *Analytical Methods* **10**, 1624–1632. DOI: 10.1039/C8AY00308D.

[69] Santiago González B., Rodríguez M.J., Blanco C., Rivas J., López-Quintela M.A., Martinho J.M.G. (2010) One Step Synthesis of the Smallest Photoluminescent and Paramagnetic PVP-Protected Gold Atomic Clusters. *Nano Letters* **10**, 4217–4221. DOI: 10.1021/nl1026716.

[70] Li L., Li Z., Zhang H., Zhang S., Majeed I., Tan B. (2013) Effect of polymer ligand structures on fluorescence of gold clusters prepared by photoreduction. *Nanoscale* **5**, 1986. DOI: 10.1039/c2nr33693f.

[71] Wang J., Zhang G., Li Q., Jiang H., Liu C., Amatore C., Wang X. (2013) *In vivo* self-bio-imaging of tumors through in situ biosynthesized fluorescent gold nanoclusters. *Scientific Reports* **3**, 1157. DOI: 10.1038/srep01157.

[72] Lai L., Zhao C., Li X., Liu X., Jiang H., Selke M., Wang X. (2016) Fluorescent gold nanoclusters for *in vivo* target imaging of Alzheimer's disease. *RSC Advances* **6**, 30081–30088. DOI: 10.1039/C6RA01027J.

[73] Ouyang X., Jia N., Luo J., Li L., Xue J., Bu H., Xie G., Wan Y. (2023) DNA Nanoribbon-Assisted Intracellular Biosynthesis of Fluorescent Gold Nanoclusters for Cancer Cell Imaging. *JACS Au* **3**, 2566–2577. DOI: 10.1021/jacsau.3c00365.

[74] Chen Y., Qiao J., Liu Q., Qi L. (2018) Ovalbumin-stabilized gold nanoclusters with ascorbic acid as reducing agent for detection of serum copper. *Chinese Chemical Letters* **29**, 366–370. DOI: 10.1016/j.cclet.2017.10.014.

[75] Ding W., Liu Y., Li Y., Shi Q., Li H., Xia H., Wang D., Tao X. (2014) Water-soluble gold nanoclusters with pH-dependent fluorescence and high colloidal stability over a wide pH range via co-reduction of glutathione and citrate. *RSC Adv.* **4**, 22651–22659. DOI: 10.1039/C4RA03363A.

[76] Yan L., Cai Y., Zheng B., Yuan H., Guo Y., Xiao D., Choi M.M.F. (2012) Microwave-assisted synthesis of BSA-stabilized and HSA-protected gold nanoclusters with red emission. *J. Mater. Chem.* **22**, 1000–1005. DOI: 10.1039/C1JM13457D.

[77] Li J.K.-J., Ke C.-J., Lin C.-A., Cai Z.-H., Chen C.-Y., Chang W.H. (2013) Facile Method for Gold Nanocluster Synthesis and Fluorescence Control Using Toluene and Ultrasound. *Journal of Medical and Biological Engineering* **33**, 23–28. DOI: 10.5405/jmbe.874.

[78] Suslick K.S., Flannigan D.J. (2008) Inside a Collapsing Bubble: Sonoluminescence and the Conditions During Cavitation. *Annual Review of Physical Chemistry* **59**, 659–683. DOI: 10.1146/annurev.physchem.59.032607.093739.

[79] Lemke K., Prietzel C., Koetz J. (2013) Fluorescent gold clusters synthesized in a poly(ethyleneimine) modified reverse microemulsion. *Journal of Colloid and Interface Science* **394**, 141–146. DOI: 10.1016/j.jcis.2012.11.057.

[80] Lu Y., Chen W. (2012) Sub-nanometre sized metal clusters: from synthetic challenges to the unique property discoveries. *Chemical Society Reviews* **41**, 3594. DOI: 10.1039/c2cs15325d.

[81] Yang T.-Q., Peng B., Shan B.-Q., Zong Y.-X., Jiang J.-G., Wu P., Zhang K. (2020) Origin of the Photoluminescence of Metal Nanoclusters: From Metal-Centered Emission to Ligand-Centered Emission. *Nanomaterials* **10**, 261. DOI: 10.3390/nano10020261.

[82] Yu Y., Chen X., Yao Q., Yu Y., Yan N., Xie J. (2013) Scalable and Precise Synthesis of Thiolated $Au_{10–12}$, Au_{15}, Au_{18}, and Au_{25} Nanoclusters via pH Controlled CO Reduction. *Chemistry of Materials* **25**, 946–952. DOI: 10.1021/cm304098x.

[83] Zheng J., Zhang C., Dickson R.M. (2004) Highly Fluorescent, Water-Soluble, Size-Tunable Gold Quantum Dots. *Physical Review Letters* **93**, 077402. DOI: 10.1103/PhysRevLett.93.077402.

[84] Bao Y., Zhong C., Vu D.M., Temirov J.P., Dyer R.B., Martinez J.S. (2007) Nanoparticle-Free Synthesis of Fluorescent Gold Nanoclusters at Physiological Temperature. *The Journal of Physical Chemistry C* **111**, 12194–12198. DOI: 10.1021/jp071727d.

[85] Lee C.C., MacKay J.A., Fréchet J.M.J., Szoka F.C. (2005) Designing dendrimers for biological applications. *Nature Biotechnology* **23**, 1517–1526. DOI: 10.1038/nbt1171.

[86] Schaeffer N. *et al.* (2008) Fluorescent or not? Size-dependent fluorescence switching for polymer-stabilized gold clusters in the 1.1–1.7 nm size range. *Chemical Communications* , 3986. DOI: 10.1039/b809876j.

[87] Chen Y., Zheng X., Wang X., Wang C., Ding Y., Jiang X. (2014) Near-Infrared Emitting Gold Cluster–Poly(acrylic acid) Hybrid Nanogels. *ACS Macro Letters* **3**, 74–76. DOI: 10.1021/mz4005748.

[88] Xie J., Zheng Y., Ying J.Y. (2009) Protein-Directed Synthesis of Highly Fluorescent Gold Nanoclusters. *Journal of the American Chemical Society* **131**, 888–889. DOI: 10.1021/ja806804u.

[89] Wang Y., Cui Y., Zhao Y., Liu R., Sun Z., Li W., Gao X. (2012) Bifunctional peptides that precisely biomineralize Au clusters and specifically stain cell nuclei. *Chem. Commun.* **48**, 871–873. DOI: 10.1039/C1CC15926G.

[90] Wen Q., Gu Y., Tang L.-J., Yu R.-Q., Jiang J.-H. (2013) Peptide-Templated Gold Nanocluster Beacon as a Sensitive, Label-Free Sensor for Protein Post-translational Modification Enzymes. *Analytical Chemistry* **85**, 11681–11685. DOI: 10.1021/ac403308b.

[91] Kennedy T.A.C., MacLean J.L., Liu J. (2012) Blue emitting gold nanoclusters templated by poly-cytosine DNA at low pH and poly-adenine DNA at neutral pH. *Chemical Communications* **48**, 6845. DOI: 10.1039/c2cc32841k.

[92] Liu G., Shao Y., Wu F., Xu S., Peng J., Liu L. (2013) DNA-hosted fluorescent gold nanoclusters: sequence-dependent formation. *Nanotechnology* **24**, 015503. DOI: 10.1088/0957-4484/24/1/015503.

[93] Jiang H., Zhang Y., Wang X. (2014) Single cytidine units-templated syntheses of multi-colored water-soluble Au nanoclusters. *Nanoscale* **6**, 10355–10362. DOI: 10.1039/C4NR02180K.

[94] Sun J., Zhang J., Jin Y. (2013) 11-Mercaptoundecanoic acid directed one-pot synthesis of water-soluble fluorescent gold nanoclusters and their use as probes for sensitive and selective detection of Cr^{3+} and Cr^{6+}. *J. Mater. Chem. C* **1**, 138–143. DOI: 10.1039/C2TC00021K.

[95] Li P., Li J., Bian M., Huo D., Hou C., Yang P., Zhang S., Shen C., Yang M. (2018) A redox route for the fluorescence detection of lead ions in sorghum, river water and tap water and a desk study of a paper-based probe. *Analytical Methods* **10**, 3256–3262. DOI: 10.1039/C8AY00892B.

[96] Duan B., Wang M., Li Y., Jiang S., Liu Y., Huang Z. (2019) Dual-emitting zein-protected gold nanoclusters for ratiometric fluorescence detection of Hg^{2+}/Ag^+ ions in both aqueous solution and self-assembled protein film. *New Journal of Chemistry* **43**, 14678–14683. DOI: 10.1039/C9NJ03524A.

[97] Roy S., Palui G., Banerjee A. (2012) The as-prepared gold cluster-based fluorescent sensor for the selective detection of As^{III} ions in aqueous solution. *Nanoscale* **4**, 2734. DOI: 10.1039/c2nr11786j.

[98] Peng Y., Wang M., Wu X., Wang F., Liu L. (2018) Methionine-Capped Gold Nanoclusters as a Fluorescence-Enhanced Probe for Cadmium(II) Sensing. *Sensors* **18**, 658. DOI: 10.3390/s18020658.

[99] Desai M.L., Basu H., Saha S., Singhal R.K., Kailasa S.K. (2021) Fluorescence enhancement of bovine serum albumin gold nanoclusters from La^{3+} ion: Detection of four divalent metal ions (Hg^{2+}, Cu^{2+}, Pb^{2+} and Cd^{2+}). *Journal of Molecular Liquids* **336**, 116239. DOI: 10.1016/j.molliq.2021.116239.

[100] Gao X., Ma Z., Sun M., Liu X., Zhong K., Tang L., Li X., Li J. (2022) A highly sensitive ratiometric fluorescent sensor for copper ions and cadmium ions in scallops based on nitrogen doped graphene quantum dots cooperating with gold nanoclusters. *Food Chemistry* **369**, 130964. DOI: 10.1016/j.foodchem.2021.130964.

[101] Wang H., Da L., Yang L., Chu S., Yang F., Yu S., Jiang C. (2020) Colorimetric fluorescent paper strip with smartphone platform for quantitative detection of cadmium ions in real samples. *Journal of Hazardous Materials* **392**, 122506. DOI: 10.1016/j.jhazmat.2020.122506.

[102] Sang F., Zhang X., Shen F. (2019) Fluorescent methionine-capped gold nanoclusters for ultra-sensitive determination of copper(II) and cobalt(II), and their use in a test strip. *Microchimica Acta* **186**, 373. DOI: 10.1007/s00604-019-3428-3.

[103] Zhang H., Liu Q., Wang T., Yun Z., Li G., Liu J., Jiang G. (2013) Facile preparation of glutathione-stabilized gold nanoclusters for selective determination of chromium (III) and chromium (VI) in environmental water samples. *Analytica Chimica Acta* **770**, 140–146. DOI: 10.1016/j.aca.2013.01.042.

[104] Liu F., Lai X., Zhao S., Lu Z., Han P., Chen L. (2023) A simple and feasible fluorescent approach for rapid detection of hexavalent chromium based on gold nanoclusters. *Food Chemistry* **402**, 134251. DOI: 10.1016/j.foodchem.2022.134251.

[105] Cao D., Fan J., Qiu J., Tu Y., Yan J. (2013) Masking method for improving selectivity of gold nanoclusters in fluorescence determination of mercury and copper ions. *Biosensors and Bioelectronics* **42**, 47–50. DOI: 10.1016/j.bios.2012.10.084.

[106] Kong L., Chu X., Ling X., Ma G., Yao Y., Meng Y., Liu W. (2016) Biocompatible glutathione-capped gold nanoclusters for dual fluorescent sensing and imaging of copper(II) and temperature in human cells and bacterial cells. *Microchimica Acta* **183**, 2185–2195. DOI: 10.1007/s00604-016-1854-z.

[107] Liu H., Jia L., Wang Y., Wang M., Gao Z., Ren X. (2019) Ratiometric fluorescent sensor for visual determination of copper ions and alkaline phosphatase based on carbon quantum dots and gold nanoclusters. *Analytical and Bioanalytical Chemistry* **411**, 2531–2543. DOI: 10.1007/s00216-019-01693-6.

[108] Desai M.L., Basu H., Saha S., Singhal R.K., Kailasa S.K. (2020) One pot synthesis of fluorescent gold nanoclusters from Curcuma longa extract for independent detection of Cd^{2+}, Zn^{2+} and Cu^{2+} ions with high sensitivity. *Journal of Molecular Liquids* **304**, 112697. DOI: 10.1016/j.molliq.2020.112697.

[109] Qian D., Wang Z., Xiao Z., Fang C.-J. (2021) A fluorescent probe for the detection of Cu(II) in water and tumor cells. *Inorganic Chemistry Communications* **126**, 108471. DOI: 10.1016/j.inoche.2021.108471.

[110] Saleh S.M., Almotiri M.K., Ali R. (2022) Green synthesis of highly luminescent gold nanoclusters and their application in sensing Cu(II) and Hg(II). *Journal of Photochemistry and Photobiology A: Chemistry* **426**, 113719. DOI: 10.1016/j.jphotochem.2021.113719.

[111] Sun X., Wen R., Zhang R., Guo Y., Li H., Lee Y.-I. (2022) Engineering a ratiometric-sensing platform based on a PTA-NH2@GSH-AuNCs composite for the visual detection of copper ions via RGB assay. *Microchemical Journal* **182**, 107877. DOI: 10.1016/j.microc.2022.107877.

[112] Ye C., Wang Y., Wang S., Wang Z. (2019) Fabrication of cefotaxime sodium-functionalized gold nanoclusters for the detection of copper ions in Chinese herbal medicines. *RSC Advances* **9**, 5037–5044. DOI: 10.1039/C8RA09987A.

[113] Dong W., Yu J., Gong X., Liang W., Fan L., Dong C. (2021) A turn-off-on near-infrared photoluminescence sensor for sequential detection of Fe^{3+} and ascorbic acid based on glutathione-capped gold nanoclusters. *Spectrochimica Acta Part A: Molecular and Biomolecular Spectroscopy* **247**, 119085. DOI: 10.1016/j.saa.2020.119085.

[114] Jiang J., Gao P., Zhang Y., Zhang G., Zhou Y., Dong C., Shuang S. (2017) Rapid one-pot synthesis of MMTA protected fluorescent gold nanoclusters for selective and sensitive detection of ferric ion. *Talanta* **174**, 44–51. DOI: 10.1016/j.talanta.2017.05.082.

[115] Halawa M.I., Wu F., Nsabimana A., Lou B., Xu G. (2018) Inositol directed facile "green" synthesis of fluorescent gold nanoclusters as selective and sensitive detecting probes of ferric ions. *Sensors and Actuators B: Chemical* **257**, 980–987. DOI: 10.1016/j.snb.2017.11.046.

[116] Luo W., Wang C., Min J., Luo H. (2023) Gold nanoclusters Cys-Au NCs as selective fluorescent probes for "on–off–on" detection of Fe^{3+} and ascorbic acid. *RSC Advances* **13**, 7425–7431. DOI: 10.1039/D3RA00410D.

[117] Qiao Y., Zhang Y., Zhang C., Shi L., Zhang G., Shuang S., Dong C., Ma H. (2016) Water-soluble gold nanoclusters-based fluorescence probe for highly selective and sensitive detection of Hg^{2+}. *Sensors and Actuators B: Chemical* **224**, 458–464. DOI: 10.1016/j.snb.2015.10.080.

[118] Niu Q., Gao P., Yuan M., Zhang G., Zhou Y., Dong C., Shuang S., Zhang Y. (2019) Development of sensing method for mercury ions and cell imaging based on highly fluorescent gold nanoclusters. *Microchemical Journal* **146**, 1140–1149. DOI: 10.1016/j.microc.2019.02.050.

[119] Yang J.-Y., Yang T., Wang X.-Y., Chen M.-L., Yu Y.-L., Wang J.-H. (2018) Mercury Speciation with Fluorescent Gold Nanocluster as a Probe. *Analytical Chemistry* **90**, 6945–6951. DOI: 10.1021/acs.analchem.8b01222.

[120] Yu X., Liu W., Deng X., Yan S., Su Z. (2018) Gold nanocluster embedded bovine serum albumin nanofibers-graphene hybrid membranes for the efficient detection and separation of mercury ion. *Chemical Engineering Journal* **335**, 176–184. DOI: 10.1016/j.cej.2017.10.148.

[121] Yang Y., Lu L., Tian X., Li Y., Yang C., Nie Y., Zhou Z. (2019) Ratiometric fluorescence detection of mercuric ions by sole intrinsic dual-emitting gold nanoclusters. *Sensors and Actuators B: Chemical* **278**, 82–87. DOI: 10.1016/j.snb.2018.09.072.

[122] Ru F., Du P., Lu X. (2020) Efficient ratiometric fluorescence probe utilizing silicon particles/gold nanoclusters nanohybrid for "on-off-on" bifunctional detection and cellular imaging of mercury (II) ions and cysteine. *Analytica Chimica Acta* **1105**, 139–146. DOI: 10.1016/j.aca.2020.01.020.

[123] Jiang X., Zhang H., Yang C., Xia J., Liu G., Luo X. (2022) A novel electrostatic drive strategy to prepare glutathione-capped gold nanoclusters embedded quaternized cellulose membranes fluorescent colorimetric sensor for Pb(II) and Hg(II) ions detection. *Sensors and Actuators B: Chemical* **368**, 132046. DOI: 10.1016/j.snb.2022.132046.

[124] Lu Z. *et al.* (2022) Deep learning-assisted smartphone-based ratio fluorescence for "on–off-on" sensing of Hg^{2+} and thiram. *Chemical Engineering Journal* **435**, 134979. DOI: 10.1016/j.cej.2022.134979.

[125] Wang Y. *et al.* (2023) A fluorescent probe based on aptamer gold nanoclusters for rapid detection of mercury ions. *Analytical Methods* **15**, 3893–3901. DOI: 10.1039/D3AY00967J.

[126] Xie R., Su D., Song Y., Sun P., Mao B., Tian M., Chai F. (2023) The synthesis of gold nanoclusters with high stability and their application in fluorometric detection for Hg^{2+} and cell imaging. *Talanta* **260**, 124573. DOI: 10.1016/j.talanta.2023.124573.

[127] Huang Y.-Q., Yang L.-N., Wang Y.-S., Xue J.-H., Chen S.-H. (2018) Protamine-stabilized gold nanoclusters as a fluorescent nanoprobe for lead(II) via Pb(II)–Au(I) interaction. *Microchimica Acta* **185**, 483. DOI: 10.1007/s00604-018-3019-8.

[128] Nath P., Chatterjee M., Chanda N. (2018) Dithiothreitol-Facilitated Synthesis of Bovine Serum Albumin–Gold Nanoclusters for Pb(II) Ion Detection on Paper Substrates and in Live Cells. *ACS Applied Nano Materials* **1**, 5108–5118. DOI: 10.1021/acsanm.8b01191.

[129] Jiang P., Luo L., Liu X., Zhao W., Bi X., Luo L., Li L., You T. (2023) A potential-resolved ratiometric electrochemiluminescence aptasensor for Pb^{2+}: Gold nanoclusters and amino-terminated perylene derivative as both emitters and resonance energy transfer donor-acceptor pair. *Sensors and Actuators B: Chemical* **386**, 133758. DOI: 10.1016/j.snb.2023.133758.

[130] Liu Y., Ai K., Cheng X., Huo L., Lu L. (2010) Gold-Nanocluster-Based Fluorescent Sensors for Highly Sensitive and Selective Detection of Cyanide in Water. *Advanced Functional Materials* **20**, 951–956. DOI: 10.1002/adfm.200902062.

[131] Lu D., Liu L., Li F., Shuang S., Li Y., Choi M.M.F., Dong C. (2014) Lysozyme-stabilized gold nanoclusters as a novel fluorescence probe for cyanide recognition. *Spectrochimica Acta Part A: Molecular and Biomolecular Spectroscopy* **121**, 77–80. DOI: 10.1016/j.saa.2013.10.009.

[132] Zhang G., Qiao Y., Xu T., Zhang C., Zhang Y., Shi L., Shuang S., Dong C. (2015) Highly selective and sensitive nanoprobes for cyanide based on gold nanoclusters with red fluorescence emission. *Nanoscale* **7**, 12666–12672. DOI: 10.1039/C5NR03033A.

[133] Liu H., Yang G., Abdel-Halim E.S., Zhu J.-J. (2013) Highly selective and ultrasensitive detection of nitrite based on fluorescent gold nanoclusters. *Talanta* **104**, 135–139. DOI: 10.1016/j.talanta.2012.11.020.

[134] Yue Q., Sun L., Shen T., Gu X., Zhang S., Liu J. (2013) Synthesis of Fluorescent Gold Nanoclusters Directed by Bovine Serum Albumin and Application for Nitrite Detection. *Journal of Fluorescence* **23**, 1313–1318. DOI: 10.1007/s10895-013-1265-z.

[135] Zhang J., Chen C., Xu X., Wang X., Yang X. (2013) Use of fluorescent gold nanoclusters for the construction of a NAND logic gate for nitrite. *Chemical Communications* **49**, 2691. DOI: 10.1039/c3cc38298b.

[136] Wang L. *et al.* (2015) Fluorescent sensing of sulfide ions based on papain-directed gold nanoclusters. *New Journal of Chemistry* **39**, 9306–9312. DOI: 10.1039/C5NJ01783A.

[137] Vasimalai N., Fernández-Argüelles M.T., Espiña B. (2018) Detection of Sulfide Using Mercapto Tetrazine-Protected Fluorescent Gold Nanodots: Preparation of Paper-Based Testing Kit for On-

Site Monitoring. *ACS Applied Materials & Interfaces* **10**, 1634–1645. DOI: 10.1021/acsami.7b11769.

[138] Nejad M.A.F., Bigdeli A., Hormozi-Nezhad M.R. (2020) Wide color-varying visualization of sulfide with a dual emissive ratiometric fluorescence assay using carbon dots and gold nanoclusters. *Microchemical Journal* **157**, 104960. DOI: 10.1016/j.microc.2020.104960.

[139] Santhosh M., Chinnadayyala S.R., Kakoti A., Goswami P. (2014) Selective and sensitive detection of free bilirubin in blood serum using human serum albumin stabilized gold nanoclusters as fluorometric and colorimetric probe. *Biosensors and Bioelectronics* **59**, 370–376. DOI: 10.1016/j.bios.2014.04.003.

[140] Hong L.-N., Cao H.-T., Feng Y.-X., Guo L.-Z., Liu M.-Q., Zhang K., Mai X., Li N. (2023) Aggregation-caused dual-signal response of gold nanoclusters for ratiometric optical detection of cysteine. *Analytical Sciences* **39**, 1719–1726. DOI: 10.1007/s44211-023-00385-7.

[141] Govindaraju S., Ankireddy S.R., Viswanath B., Kim J., Yun K. (2017) Fluorescent Gold Nanoclusters for Selective Detection of Dopamine in Cerebrospinal fluid. *Scientific Reports* **7**, 40298. DOI: 10.1038/srep40298.

[142] Halawa M.I., Wu F., Fereja T.H., Lou B., Xu G. (2018) One-pot green synthesis of supramolecular β-cyclodextrin functionalized gold nanoclusters and their application for highly selective and sensitive fluorescent detection of dopamine. *Sensors and Actuators B: Chemical* **254**, 1017–1024. DOI: 10.1016/j.snb.2017.07.201.

[143] Liu Y., Liu Y., Zhang J., Zheng J., Yuan Z., Lu C. (2022) Catechin-inspired gold nanocluster nanoprobe for selective and ratiometric dopamine detection via forming azamonardine. *Spectrochimica Acta Part A: Molecular and Biomolecular Spectroscopy* **274**, 121142. DOI: 10.1016/j.saa.2022.121142.

[144] Jin L., Shang L., Guo S., Fang Y., Wen D., Wang L., Yin J., Dong S. (2011) Biomolecule-stabilized Au nanoclusters as a fluorescence probe for sensitive detection of glucose. *Biosensors and Bioelectronics* **26**, 1965–1969. DOI: 10.1016/j.bios.2010.08.019.

[145] Tian D., Qian Z., Xia Y., Zhu C. (2012) Gold Nanocluster-Based Fluorescent Probes for Near-Infrared and Turn-On Sensing of Glutathione in Living Cells. *Langmuir* **28**, 3945–3951. DOI: 10.1021/la204380a.

[146] Jain V., Bhagat S., Singh S. (2021) Bovine serum albumin decorated gold nanoclusters: A fluorescence-based nanoprobe for detection of intracellular hydrogen peroxide. *Sensors and Actuators B: Chemical* **327**, 128886. DOI: 10.1016/j.snb.2020.128886.

[147] Lee M.J., Song J.A., Choi J.H., Shin J.H., Myeong J.W., Lee K.P., Kim T., Park K.E., Oh B.K. (2023) Horseradish Peroxidase-Encapsulated Fluorescent Bio-Nanoparticle for Ultra-Sensitive and Easy Detection of Hydrogen Peroxide. *Biosensors* **13**. DOI: 10.3390/bios13020289.

[148] Gao P., Li M., Zhang Y., Dong C., Zhang G., Shi L., Li G., Yuan M., Shuang S. (2019) Facile, rapid one-pot synthesis of multifunctional gold nanoclusters for cell imaging, hydrogen sulfide detection and pH sensing. *Talanta* **197**, 1–11. DOI: 10.1016/j.talanta.2018.12.078.

[149] Zhang Y., Li M., Niu Q., Gao P., Zhang G., Dong C., Shuang S. (2017) Gold nanoclusters as fluorescent sensors for selective and sensitive hydrogen sulfide detection. *Talanta* **171**, 143–151. DOI: 10.1016/j.talanta.2017.04.077.

[150] Li Y., Yi S., Lei Z., Xiao Y. (2021) Amphiphilic polymer-encapsulated Au nanoclusters with enhanced emission and stability for highly selective detection of hypochlorous acid. *RSC Advances* **11**, 14678–14685. DOI: 10.1039/D1RA01634B.

[151] Chen X., Baker G.A. (2013) Cholesterol determination using protein-templated fluorescent gold nanocluster probes. *The Analyst* **138**, 7299. DOI: 10.1039/c3an01548c.

[152] Hu L., Han S., Parveen S., Yuan Y., Zhang L., Xu G. (2012) Highly sensitive fluorescent detection of trypsin based on BSA-stabilized gold nanoclusters. *Biosensors and Bioelectronics* **32**, 297–299. DOI: 10.1016/j.bios.2011.12.007.

[153] Wang Y., Wang Y., Zhou F., Kim P., Xia Y. (2012) Protein-Protected Au Clusters as a New Class of Nanoscale Biosensor for Label-Free Fluorescence Detection of Proteases. *Small* **8**, 3769–3773. DOI: 10.1002/smll.201201983.

[154] Lin H., Li L., Lei C., Xu X., Nie Z., Guo M., Huang Y., Yao S. (2013) Immune-independent and label-free fluorescent assay for Cystatin C detection based on protein-stabilized Au nanoclusters. *Biosensors and Bioelectronics* **41**, 256–261. DOI: 10.1016/j.bios.2012.08.030.

[155] Xu S., Feng X., Gao T., Wang R., Mao Y., Lin J., Yu X., Luo X. (2017) A novel dual-functional biosensor for fluorometric detection of inorganic pyrophosphate and pyrophosphatase activity based on globulin stabilized gold nanoclusters. *Analytica Chimica Acta* **958**, 22–29. DOI: 10.1016/j.aca.2016.12.026.

[156] Li H., Yang M., Kong D., Jin R., Zhao X., Liu F., Yan X., Lin Y., Lu G. (2019) Sensitive fluorescence sensor for point-of-care detection of trypsin using glutathione-stabilized gold nanoclusters. *Sensors and Actuators B: Chemical* **282**, 366–372. DOI: 10.1016/j.snb.2018.11.077.

[157] Luo Q., Tian M., Luo F., Zhao M., Lin C., Qiu B., Wang J., Lin Z. (2023) Multicolor Biosensor for Trypsin Detection Based on the Regulation of the Peroxidase Activity of Bovine Serum Albumin-Coated Gold Nanoclusters and Etching of Gold Nanobipyramids. *Analytical Chemistry* **95**, 2390–2397. DOI: 10.1021/acs.analchem.2c04418.

[158] Bonanno A., Pérez-Herráez I., Zaballos-García E., Pérez-Prieto J. (2020) Gold nanoclusters for ratiometric sensing of pH in extremely acidic media. *Chemical Communications* **56**, 587–590. DOI: 10.1039/C9CC08539D.

[159] Chandirasekar S., You J.-G., Xue J.-H., Tseng W.-L. (2019) Synthesis of gold nanocluster-loaded lysozyme nanoparticles for label-free ratiometric fluorescent pH sensing: applications to enzyme–substrate systems and cellular imaging. *Journal of Materials Chemistry B* **7**, 3876–3883. DOI: 10.1039/C9TB00640K.

[160] Shen J., Xiao Q., Sun P., Feng J., Xin X., Yu Y., Qi W. (2021) Self-Assembled Chiral Phosphorescent Microflowers from Au Nanoclusters with Dual-Mode pH Sensing and Information Encryption. *ACS Nano* **15**, 4947–4955. DOI: 10.1021/acsnano.0c09766.

[161] Shang L., Stockmar F., Azadfar N., Nienhaus G.U. (2013) Intracellular Thermometry by Using Fluorescent Gold Nanoclusters. *Angewandte Chemie International Edition* **52**, 11154–11157. DOI: 10.1002/anie.201306366.

[162] Sun Y., Wu J., Wang C., Zhao Y., Lin Q. (2017) Tunable near-infrared fluorescent gold nanoclusters: temperature sensor and targeted bioimaging. *New Journal of Chemistry* **41**, 5412–5419. DOI: 10.1039/C7NJ00175D.

[163] Tian L., Zhao W., Li L., Tong Y., Peng G., Li Y. (2017) Multi-talented applications for cell imaging, tumor cells recognition, patterning, staining and temperature sensing by using egg white-encapsulated gold nanoclusters. *Sensors and Actuators B: Chemical* **240**, 114–124. DOI: 10.1016/j.snb.2016.08.147.

[164] Qiao J., Chen C., Shangguan D., Mu X., Wang S., Jiang L., Qi L. (2018) Simultaneous Monitoring of Mitochondrial Temperature and ATP Fluctuation Using Fluorescent Probes in Living Cells. *Analytical Chemistry* **90**, 12553–12558. DOI: 10.1021/acs.analchem.8b02496.

[165] Zhang H., Han W., Cao X., Gao T., Jia R., Liu M., Zeng W. (2019) Gold nanoclusters as a near-infrared fluorometric nanothermometer for living cells. *Microchimica Acta* **186**, 353. DOI: 10.1007/s00604-019-3460-3.

[166] Chan P.-H., Chen Y.-C. (2012) Human Serum Albumin Stabilized Gold Nanoclusters as Selective Luminescent Probes for *Staphylococcus aureus* and Methicillin-Resistant *Staphylococcus aureus*. *Analytical Chemistry* **84**, 8952–8956. DOI: 10.1021/ac302417k.

[167] Ji H., Wu L., Pu F., Ren J., Qu X. (2018) Point-of-Care Identification of Bacteria Using Protein-Encapsulated Gold Nanoclusters. *Advanced Healthcare Materials* **7**. DOI: 10.1002/adhm.201701370.

[168] Yan R. *et al.* (2018) On–Off–On Gold Nanocluster-Based Fluorescent Probe for Rapid *Escherichia coli* Differentiation, Detection and Bactericide Screening. *ACS Sustainable Chemistry & Engineering* **6**, 4504–4509. DOI: 10.1021/acssuschemeng.8b00112.

[169] Tan Y., He K., Tang B., Chen H., Zhao Z., Zhang C., Lin L., Liu J. (2020) Precisely Regulated Luminescent Gold Nanoparticles for Identification of Cancer Metastases. *ACS Nano* **14**, 13975–13985. DOI: 10.1021/acsnano.0c06388.

[170] Zhao S., Das A., Zhang H., Jin R., Song Y., Jin R. (2016) Mechanistic insights from atomically precise gold nanocluster-catalyzed reduction of 4-nitrophenol. *Progress in Natural Science: Materials International* **26**, 483–486. DOI: 10.1016/j.pnsc.2016.08.009.

[171] Feng A.-L., Jiang Q.-Y., Song G.-G., Xu Z., Liu X.-Q. (2022) DNA-templated NIR-emitting gold nanoclusters with peroxidase-like activity as a multi-signal probe for Hg^{2+} detection. *Chinese Journal of Analytical Chemistry* **50**, 100118. DOI: 10.1016/j.cjac.2022.100118.

[172] Shan H. *et al.* (2023) Modulating Catalytic Activity and Stability of Atomically Precise Gold Nanoclusters as Peroxidase Mimics via Ligand Engineering. *ACS Nano* **17**, 2368–2377. DOI: 10.1021/acsnano.2c09238.

[173] Huang Y., Yue N., Li Y., Han L., Fan A. (2021) One-step synthesis of cationic gold nanoclusters with high catalytic activity on luminol chemiluminescence reaction. *Luminescence* **36**, 85–93. DOI: 10.1002/bio.3916.

[174] Liu C. *et al.* (2011) Insulin-Directed Synthesis of Fluorescent Gold Nanoclusters: Preservation of Insulin Bioactivity and Versatility in Cell Imaging. *Angewandte Chemie International Edition* **50**, 7056–7060. DOI: 10.1002/anie.201100299.

[175] Zhang Y. *et al.* (2019) Gold nanoclusters for controlled insulin release and glucose regulation in diabetes. *Nanoscale* **11**, 6471–6479. DOI: 10.1039/C9NR00668K.

[176] Wang Y., Xu C., Zhai J., Gao F., Liu R., Gao L., Zhao Y., Chai Z., Gao X. (2015) Label-Free Au Cluster Used for *in Vivo* 2D and 3D Computed Tomography of Murine Kidneys. *Analytical Chemistry* **87**, 343–345. DOI: 10.1021/ac503887c.

[177] Chen Y., Montana D.M., Wei H., Cordero J.M., Schneider M., Le Guével X., Chen O., Bruns O.T., Bawendi M.G. (2017) Shortwave Infrared *in Vivo* Imaging with Gold Nanoclusters. *Nano Letters* **17**, 6330–6334. DOI: 10.1021/acs.nanolett.7b03070.

[178] Wang W. *et al.* (2020) Engineering the Protein Corona Structure on Gold Nanoclusters Enables Red-Shifted Emissions in the Second Near-infrared Window for Gastrointestinal Imaging. *Angewandte Chemie International Edition* **59**, 22431–22435. DOI: 10.1002/anie.202010089.

[179] Yang J. *et al.* (2020) Gold/alpha-lactalbumin nanoprobes for the imaging and treatment of breast cancer. *Nature Biomedical Engineering* **4**, 686–703. DOI: 10.1038/s41551-020-0584-z.

[180] Yang J., Li X., Tong Y., Yang Y., Zhao L., Zhou Q., Xu J., Dong L., Jiang Y. (2022) Targeting co-delivery of doxorubicin and gefitinib by biotinylated Au NCs for overcoming multidrug resistance in imaging-guided anticancer therapy. *Colloids and Surfaces B: Biointerfaces* **217**, 112608. DOI: 10.1016/j.colsurfb.2022.112608.

[181] Yu Z. *et al.* (2020) High-Resolution Shortwave Infrared Imaging of Vascular Disorders Using Gold Nanoclusters. *ACS Nano* **14**, 4973–4981. DOI: 10.1021/acsnano.0c01174.

[182] Cifuentes-Rius A., Ivask A., Das S., Penya-Auladell N., Fabregas L., Fletcher N.L., Houston Z.H., Thurecht K.J., Voelcker N.H. (2017) Gold Nanocluster-Mediated Cellular Death under Electromagnetic Radiation. *ACS Applied Materials & Interfaces* **9**, 41159–41167. DOI: 10.1021/acsami.7b13100.

[183] Liu P. *et al.* (2019) Concurrent photothermal therapy and photodynamic therapy for cutaneous squamous cell carcinoma by gold nanoclusters under a single NIR laser irradiation. *Journal of Materials Chemistry B* **7**, 6924–6933. DOI: 10.1039/C9TB01573F.

[184] Kim J. *et al.* (2020) Gold nanoparticle clusters for the investigation of therapeutic efficiency against prostate cancer under near-infrared irradiation. *Nano Convergence* **7**, 5. DOI: 10.1186/s40580-019-0216-z.

[185] Xie Y., Zheng W., Jiang X. (2020) Near-Infrared Light-Activated Phototherapy by Gold Nanoclusters for Dispersing Biofilms. *ACS Applied Materials & Interfaces* **12**, 9041–9049. DOI: 10.1021/acsami.9b21777.

[186] Zhu S., Wang X., Liu L., Li L. (2020) Gold nanocluster grafted conjugated polymer nanoparticles for cancer cell imaging and photothermal killing. *Colloids and Surfaces A: Physicochemical and Engineering Aspects* **597**, 124764. DOI: 10.1016/j.colsurfa.2020.124764.

[187] Kawasaki H., Kumar S., Li G., Zeng C., Kauffman D.R., Yoshimoto J., Iwasaki Y., Jin R. (2014) Generation of Singlet Oxygen by Photoexcited $Au_{25}(SR)_{18}$ Clusters. *Chemistry of Materials* **26**, 2777–2788. DOI: 10.1021/cm500260z.

[188] Poderys V., Jarockyte G., Bagdonas S., Karabanovas V., Rotomskis R. (2020) Protein-stabilized gold nanoclusters for PDT: ROS and singlet oxygen generation. *Journal of Photochemistry and Photobiology B: Biology* **204**, 111802. DOI: 10.1016/j.jphotobiol.2020.111802.

[189] Chen T., Xu S., Zhao T., Zhu L., Wei D., Li Y., Zhang H., Zhao C. (2012) Gold nanocluster-conjugated amphiphilic block copolymer for tumor-targeted drug delivery. *ACS Applied Materials and Interfaces* **4**, 5766–5774. DOI: 10.1021/am301223n.

[190] Chattoraj S., Amin A., Jana B., Mohapatra S., Ghosh S., Bhattacharyya K. (2016) Selective Killing of Breast Cancer Cells by Doxorubicin-Loaded Fluorescent Gold Nanoclusters: Confocal Microscopy and FRET. *ChemPhysChem* **17**, 253–259. DOI: 10.1002/cphc.201500982.

[191] Kong Y. *et al.* (2021) A NIR-II-emitting gold nanocluster-based drug delivery system for smartphone-triggered photodynamic theranostics with rapid body clearance. *Materials Today* **51**, 96–107. DOI: 10.1016/j.mattod.2021.09.022.

[192] Li W., Zhou T., Sun W., Liu M., Wang X., Wang F., Zhang G., Zhang Z. (2023) A conjugated aptamer and oligonucleotides-stabilized gold nanoclusters nanoplatform for targeted fluorescent imaging and efficient drug delivery. *Colloids and Surfaces A: Physicochemical and Engineering Aspects* **657**, 130521. DOI: 10.1016/j.colsurfa.2022.130521.

[193] Huber D.L. (2005) Synthesis, Properties, and Applications of Iron Nanoparticles. *Small* **1**, 482–501. DOI: 10.1002/smll.200500006.

[194] Mahmoudi M., Simchi A., Milani A.S., Stroeve P. (2009) Cell toxicity of superparamagnetic iron oxide nanoparticles. *Journal of Colloid and Interface Science* **336**, 510–518. DOI: 10.1016/j.jcis.2009.04.046.

[195] Li Q., Kartikowati C.W., Horie S., Ogi T., Iwaki T., Okuyama K. (2017) Correlation between particle size/domain structure and magnetic properties of highly crystalline Fe_3O_4 nanoparticles. *Scientific Reports* **7**, 9894. DOI: 10.1038/s41598-017-09897-5.

[196] Wahajuddin, Arora. (2012) Superparamagnetic iron oxide nanoparticles: magnetic nanoplatforms as drug carriers. *International Journal of Nanomedicine* **7**, 3445. DOI: 10.2147/IJN.S30320.

[197] Houbi A., Aldashevich Z.A., Atassi Y., Bagasharova Telmanovna Z., Saule M., Kubanych K. (2021) Microwave absorbing properties of ferrites and their composites: A review. *Journal of Magnetism and Magnetic Materials* **529**, 167839. DOI: 10.1016/j.jmmm.2021.167839.

[198] Dickson D.P.E., Frankel R.B. (1992) Magnetic Fine Particles in Biological Systems. In: *Magnetic Properties of Fine Particles.*, pp. 393–402. Elsevier. DOI: 10.1016/B978-0-444-89552-3.50047-5.

[199] Teja A.S., Koh P.-Y. (2009) Synthesis, properties, and applications of magnetic iron oxide nanoparticles. *Progress in Crystal Growth and Characterization of Materials* **55**, 22–45. DOI: 10.1016/j.pcrysgrow.2008.08.003.

[200] Jeong U., Teng X., Wang Y., Yang H., Xia Y. (2007) Superparamagnetic Colloids: Controlled Synthesis and Niche Applications. *Advanced Materials* **19**, 33–60. DOI: 10.1002/adma.200600674.

[201] Sung Lee J., Myung Cha J., Young Yoon H., Lee J.-K., Keun Kim Y. (2015) Magnetic multi-granule nanoclusters: A model system that exhibits universal size effect of magnetic coercivity. *Scientific Reports* **5**, 12135. DOI: 10.1038/srep12135.

[202] Ma M., Wu Y., Zhou J., Sun Y., Zhang Y., Gu N. (2004) Size dependence of specific power absorption of Fe_3O_4 particles in AC magnetic field. *Journal of Magnetism and Magnetic Materials* **268**, 33–39. DOI: 10.1016/S0304-8853(03)00426-8.

[203] Kim D., Lee N., Park M., Kim B.H., An K., Hyeon T. (2009) Synthesis of Uniform Ferrimagnetic Magnetite Nanocubes. *Journal of the American Chemical Society* **131**, 454–455. DOI: 10.1021/ja8086906.

[204] Kandasamy G., Maity D. (2015) Recent advances in superparamagnetic iron oxide nanoparticles (SPIONs) for *in vitro* and *in vivo* cancer nanotheranostics. *International Journal of Pharmaceutics* **496**, 191–218. DOI: 10.1016/j.ijpharm.2015.10.058.

[205] Mohammed L., Gomaa H.G., Ragab D., Zhu J. (2017) Magnetic nanoparticles for environmental and biomedical applications: A review. *Particuology* **30**, 1–14. DOI: 10.1016/j.partic.2016.06.001.

[206] Dadfar S.M. *et al.* (2020) Size-isolation of superparamagnetic iron oxide nanoparticles improves MRI, MPI and hyperthermia performance. *Journal of Nanobiotechnology* **18**, 22. DOI: 10.1186/s12951-020-0580-1.

[207] Tadic M., Kralj S., Kopanja L. (2019) Synthesis, particle shape characterization, magnetic properties and surface modification of superparamagnetic iron oxide nanochains. *Materials Characterization* **148**, 123–133. DOI: 10.1016/j.matchar.2018.12.014.

[208] Alp E., Aydogan N. (2016) A comparative study: Synthesis of superparamagnetic iron oxide nanoparticles in air and N_2 atmosphere. *Colloids and Surfaces A: Physicochemical and Engineering Aspects* **510**, 205–212. DOI: 10.1016/j.colsurfa.2016.06.033.

[209] Niculescu A.-G., Chircov C., Grumezescu A.M. (2022) Magnetite nanoparticles: Synthesis methods – A comparative review. *Methods* **199**, 16–27. DOI: 10.1016/j.ymeth.2021.04.018.

[210] Samrot A. V., Sahithya C.S., Selvarani A J., Purayil S.K., Ponnaiah P. (2021) A review on synthesis, characterization and potential biological applications of superparamagnetic iron oxide nanoparticles. *Current Research in Green and Sustainable Chemistry* **4**, 100042. DOI: 10.1016/j.crgsc.2020.100042.

[211] Rahmani R., Gharanfoli M., Gholamin M., Darroudi M., Chamani J., Sadri K., Hashemzadeh A. (2020) Plant-mediated synthesis of superparamagnetic iron oxide nanoparticles (SPIONs) using aloe vera and flaxseed extracts and evaluation of their cellular toxicities. *Ceramics International* **46**, 3051–3058. DOI: 10.1016/j.ceramint.2019.10.005.

[212] Kaushik S., Thomas J., Panwar V., Ali H., Chopra V., Sharma A., Tomar R., Ghosh D. (2020) In Situ Biosynthesized Superparamagnetic Iron Oxide Nanoparticles (SPIONS) Induce Efficient Hyperthermia in Cancer Cells. *ACS Applied Bio Materials* **3**, 779–788. DOI: 10.1021/acsabm.9b00720.

[213] Chatterjee S., Mahanty S., Das P., Chaudhuri P., Das S. (2020) Biofabrication of iron oxide nanoparticles using manglicolous fungus Aspergillus niger BSC-1 and removal of Cr(VI) from aqueous solution. *Chemical Engineering Journal* **385**, 123790. DOI: 10.1016/j.cej.2019.123790.

[214] Khaleelullah M.M.S.I., Murugan M., Radha K. V, Thiyagarajan D., Shimura Y., Hayakawa Y. (2017) Synthesis of super-paramagnetic iron oxide nanoparticles assisted by brown seaweed *Turbinaria decurrens* for removal of reactive navy blue dye. *Materials Research Express* **4**, 105038. DOI: 10.1088/2053-1591/aa9131.

[215] Parandhaman T., Pentela N., Ramalingam B., Samanta D., Das S.K. (2017) Metal Nanoparticle Loaded Magnetic-Chitosan Microsphere: Water Dispersible and Easily Separable Hybrid Metal Nano-biomaterial for Catalytic Applications. *ACS Sustainable Chemistry & Engineering* **5**, 489–501. DOI: 10.1021/acssuschemeng.6b01862.

[216] Abouelkheir S.S., Ibrahim H.A.H., Beltagy E.A. (2023) Functionalized maghemite superparamagnetic iron oxide nanoparticles (γ-Fe$_2$O$_3$-SPIONs)-amylase enzyme hybrid in biofuel production. *Scientific Reports* **13**, 11117. DOI: 10.1038/s41598-023-37826-2.

[217] Salem N.F.A., Abouelkheir S.S., Yousif A.M., Meneses-Brassea B.P., Sabry S.A., Ghozlan H.A., El-Gendy A.A. (2021) Large scale production of superparamagnetic iron oxide nanoparticles by the haloarchaeon Halobiforma sp. N1 and their potential in localized hyperthermia cancer therapy. *Nanotechnology* **32**, 09LT01. DOI: 10.1088/1361-6528/abc851.

[218] Rajesh Kumar S., Jayavignesh V., Selvakumar R., Swaminathan K., Ponpandian N. (2016) Facile synthesis of yeast cross-linked Fe$_3$O$_4$ nanoadsorbents for efficient removal of aquatic environment contaminated with As(V). *Journal of Colloid and Interface Science* **484**, 183–195. DOI: 10.1016/j.jcis.2016.08.081.

[219] Ge S., Shi X., Sun K., Li C., Uher C., Baker J.R., Banaszak Holl M.M., Orr B.G. (2009) Facile Hydrothermal Synthesis of Iron Oxide Nanoparticles with Tunable Magnetic Properties. *The Journal of Physical Chemistry C* **113**, 13593–13599. DOI: 10.1021/jp902953t.

[220] Chen F., Bu W., Lu C., Chen G., Chen M., Shen X., Liu R., Shi J. (2011) Hydrothermal Synthesis of a Highly Sensitive T$_2$-Weigthed MRI Contrast Agent: Zinc-Doped Superparamagnetic Iron Oxide Nanocrystals. *Journal of Nanoscience and Nanotechnology* **11**, 10438–10443. DOI: 10.1166/jnn.2011.3934.

[221] Yang X., Jiang W., Liu L., Chen B., Wu S., Sun D., Li F. (2012) One-step hydrothermal synthesis of highly water-soluble secondary structural Fe$_3$O$_4$ nanoparticles. *Journal of Magnetism and Magnetic Materials* **324**, 2249–2257. DOI: 10.1016/j.jmmm.2012.02.111.

[222] Saxena N., Agraval H., Barick K.C., Ray D., Aswal V.K., Singh A., Yadav U.C.S., Dube C.L. (2020) Thermal and microwave synthesized SPIONs: Energy effects on the efficiency of nano drug carriers. *Materials Science and Engineering: C* **111**, 110792. DOI: 10.1016/j.msec.2020.110792.

[223] El-Dek S.I., Ali M.A., El-Zanaty S.M., Ahmed S.E. (2018) Comparative investigations on ferrite nanocomposites for magnetic hyperthermia applications. *Journal of Magnetism and Magnetic Materials* **458**, 147–155. DOI: 10.1016/j.jmmm.2018.02.052.

[224] Hee Kim E., Sook Lee H., Kook Kwak B., Kim B.-K. (2005) Synthesis of ferrofluid with magnetic nanoparticles by sonochemical method for MRI contrast agent. *Journal of Magnetism and Magnetic Materials* **289**, 328–330. DOI: 10.1016/j.jmmm.2004.11.093.

[225] Neto D.M.A. *et al.* (2017) Rapid Sonochemical Approach Produces Functionalized Fe$_3$O$_4$ Nanoparticles with Excellent Magnetic, Colloidal, and Relaxivity Properties for MRI Application. *The Journal of Physical Chemistry C* **121**, 24206–24222. DOI: 10.1021/acs.jpcc.7b04941.

[226] Vijayakumar R., Koltypin Yu., Felner I., Gedanken A. (2000) Sonochemical synthesis and characterization of pure nanometer-sized Fe$_3$O$_4$ particles. *Materials Science and Engineering: A* **286**, 101–105. DOI: 10.1016/S0921-5093(00)00647-X.

[227] Cano M., Núñez-Lozano R., Dumont Y., Larpent C., Cueva-Méndez G. de la. (2016) Synthesis and characterization of multifunctional superparamagnetic iron oxide nanoparticles (SPION)/C$_{60}$ nanocomposites assembled by fullerene–amine click chemistry. *RSC Advances* **6**, 70374–70382. DOI: 10.1039/C6RA14047E.

[228] Gonzalez-Moragas L., Yu S.-M., Murillo-Cremaes N., Laromaine A., Roig A. (2015) Scale-up synthesis of iron oxide nanoparticles by microwave-assisted thermal decomposition. *Chemical Engineering Journal* **281**, 87–95. DOI: 10.1016/j.cej.2015.06.066.

[229] Wang J., Zhang B., Wang L., Wang M., Gao F. (2015) One-pot synthesis of water-soluble superparamagnetic iron oxide nanoparticles and their MRI contrast effects in the mouse brains. *Materials Science and Engineering: C* **48**, 416–423. DOI: 10.1016/j.msec.2014.12.026.

[230] Yang G., Zhang B., Wang J., Wang M., Xie S., Li X. (2016) Synthesis and characterization of poly(lactic acid)-modified superparamagnetic iron oxide nanoparticles. *Journal of Sol-Gel Science and Technology* **77**, 335–341. DOI: 10.1007/s10971-015-3858-2.

[231] Aslam M., Schultz E.A., Sun T., Meade T., Dravid V.P. (2007) Synthesis of Amine-Stabilized Aqueous Colloidal Iron Oxide Nanoparticles. *Crystal Growth & Design* **7**, 471–475. DOI: 10.1021/cg060656p.

[232] Chen B., Hatamie S., Garu P., Heravi P., Chen J., Liu B., Wei Z., Yao D. (2020) Synthesis of iron-oxide magnetic nanoparticles coated with dextran of varied molecular mass using a facile ball-milling method. *Micro & Nano Letters* **15**, 645–650. DOI: 10.1049/mnl.2019.0811.

[233] Iwasaki T., Sato N., Nakamura H., Watano S. (2013) Mechanochemical formation of superparamagnetic magnetite nanoparticles from ferrihydrite over a wide range of pH environments. *Materials Chemistry and Physics* **140**, 596–601. DOI: 10.1016/j.matchemphys.2013.04.011.

[234] Franzel L., Bertino M.F., Huba Z.J., Carpenter E.E. (2012) Synthesis of magnetic nanoparticles by pulsed laser ablation. *Applied Surface Science* **261**, 332–336. DOI: 10.1016/j.apsusc.2012.08.010.

[235] Vahabzadeh E., Torkamany M.J. (2014) Iron Oxide Nanocrystals Synthesis by Laser Ablation in Water: Effect of Laser Wavelength. *Journal of Cluster Science* **25**, 959–968. DOI: 10.1007/s10876-013-0676-y.

[236] Das H., Sakamoto N., Aono H., Shinozaki K., Suzuki H., Wakiya N. (2015) Investigations of superparamagnetism in magnesium ferrite nano-sphere synthesized by ultrasonic spray pyrolysis technique for hyperthermia application. *Journal of Magnetism and Magnetic Materials* **392**, 91–100. DOI: 10.1016/j.jmmm.2015.05.029.

[237] Dumitrache F. *et al.* (2015) Highly magnetic Fe_2O_3 nanoparticles synthesized by laser pyrolysis used for biological and heat transfer applications. *Applied Surface Science* **336**, 297–303. DOI: 10.1016/j.apsusc.2014.12.098.

[238] Estévez M. *et al.* (2023) Large-scale production of superparamagnetic iron oxide nanoparticles by flame spray pyrolysis: *In vitro* biological evaluation for biomedical applications. *Journal of Colloid and Interface Science* **650**, 560–572. DOI: 10.1016/j.jcis.2023.07.009.

[239] Kopanja L., Milosevic I., Panjan M., Damnjanovic V., Tadic M. (2016) Sol–gel combustion synthesis, particle shape analysis and magnetic properties of hematite (α-Fe_2O_3) nanoparticles embedded in an amorphous silica matrix. *Applied Surface Science* **362**, 380–386. DOI: 10.1016/j.apsusc.2015.11.238.

[240] Manukyan K. V. *et al.* (2014) Ultrasmall α-Fe_2O_3 Superparamagnetic Nanoparticles with High Magnetization Prepared by Template-Assisted Combustion Process. *The Journal of Physical Chemistry C* **118**, 16264–16271. DOI: 10.1021/jp504733r.

[241] Baumgartner J., Dey A., Bomans P.H.H., Le Coadou C., Fratzl P., Sommerdijk N.A.J.M., Faivre D. (2013) Nucleation and growth of magnetite from solution. *Nature Materials* **12**, 310–314. DOI: 10.1038/nmat3558.

[242] Jun Y.-S., Zhu Y., Wang Y., Ghim D., Wu X., Kim D., Jung H. (2022) Classical and Nonclassical Nucleation and Growth Mechanisms for Nanoparticle Formation. *Annual Review of Physical Chemistry* **73**, 453–477. DOI: 10.1146/annurev-physchem-082720-100947.

[243] Thanh N.T.K., Maclean N., Mahiddine S. (2014) Mechanisms of Nucleation and Growth of Nanoparticles in Solution. *Chemical Reviews* **114**, 7610–7630. DOI: 10.1021/cr400544s.

[244] Wu K.-J., Tse E.C.M., Shang C., Guo Z. (2022) Nucleation and growth in solution synthesis of nanostructures – From fundamentals to advanced applications. *Progress in Materials Science* **123**, 100821. DOI: 10.1016/j.pmatsci.2021.100821.

[245] Yakasai F., Jaafar M.Z., Bandyopadhyay S., Agi A., Sidek M.A. (2022) Application of iron oxide nanoparticles in oil recovery – A critical review of the properties, formulation, recent advances and prospects. *Journal of Petroleum Science and Engineering* **208**, 109438. DOI: 10.1016/j.petrol.2021.109438.

[246] LaMer V.K., Dinegar R.H. (1950) Theory, Production and Mechanism of Formation of Monodispersed Hydrosols. *Journal of the American Chemical Society* **72**, 4847–4854. DOI: 10.1021/ja01167a001.

[247] Finney E.E., Finke R.G. (2008) Nanocluster nucleation and growth kinetic and mechanistic studies: A review emphasizing transition-metal nanoclusters. *Journal of Colloid and Interface Science* **317**, 351–374. DOI: 10.1016/j.jcis.2007.05.092.

[248] Khan, Rehman, Hayat, Andreescu. (2019) Magnetic Particles-Based Analytical Platforms for Food Safety Monitoring. *Magnetochemistry* **5**, 63. DOI: 10.3390/magnetochemistry5040063.

[249] Kara G., Ozpolat B. (2024) SPIONs: Superparamagnetic iron oxide-based nanoparticles for the delivery of microRNAi-therapeutics in cancer. *Biomedical Microdevices* **26**, 16. DOI: 10.1007/s10544-024-00698-y.

[250] Ahn T., Kim J.H., Yang H.-M., Lee J.W., Kim J.-D. (2012) Formation Pathways of Magnetite Nanoparticles by Coprecipitation Method. *The Journal of Physical Chemistry C* **116**, 6069–6076. DOI: 10.1021/jp211843g.

[251] Blanco-Andujar C., Ortega D., Pankhurst Q.A., Thanh N.T.K. (2012) Elucidating the morphological and structural evolution of iron oxide nanoparticles formed by sodium carbonate in aqueous medium. *Journal of Materials Chemistry* **22**, 12498. DOI: 10.1039/c2jm31295f.

[252] LaGrow A.P., Besenhard M.O., Hodzic A., Sergides A., Bogart L.K., Gavriilidis A., Thanh N.T.K. (2019) Unravelling the growth mechanism of the co-precipitation of iron oxide nanoparticles with

the aid of synchrotron X-Ray diffraction in solution. *Nanoscale* **11**, 6620–6628. DOI: 10.1039/C9NR00531E.

[253] Besenhard M.O. *et al.* (2020) Co-precipitation synthesis of stable iron oxide nanoparticles with NaOH: New insights and continuous production via flow chemistry. *Chemical Engineering Journal* **399**, 125740. DOI: 10.1016/j.cej.2020.125740.

[254] Liao Z., Wang H., Lv R., Zhao P., Sun X., Wang S., Su W., Niu R., Chang J. (2011) Polymeric Liposomes-Coated Superparamagnetic Iron Oxide Nanoparticles as Contrast Agent for Targeted Magnetic Resonance Imaging of Cancer Cells. *Langmuir* **27**, 3100–3105. DOI: 10.1021/la1050157.

[255] Javid A., Ahmadian S., Saboury A.A., Kalantar S.M., Rezaei-Zarchi S. (2013) Chitosan-Coated Superparamagnetic Iron Oxide Nanoparticles for Doxorubicin Delivery: Synthesis and Anticancer Effect Against Human Ovarian Cancer Cells. *Chemical Biology & Drug Design* **82**, 296–306. DOI: 10.1111/cbdd.12145.

[256] Inbaraj S., Chen B.H. (2012) *In vitro* removal of toxic heavy metals by poly(γ-glutamic acid)-coated superparamagnetic nanoparticles. *International Journal of Nanomedicine* **7**, 4419. DOI: 10.2147/IJN.S34396.

[257] Karaagac O., Köçkar H. (2022) Improvement of the saturation magnetization of PEG coated superparamagnetic iron oxide nanoparticles. *Journal of Magnetism and Magnetic Materials* **551**, 169140. DOI: 10.1016/j.jmmm.2022.169140.

[258] Karimzadeh I., Aghazadeh M., Ganjali M.R., Norouzi P., Shirvani-Arani S., Doroudi T., Kolivand P.H., Marashi S.A., Gharailou D. (2016) A novel method for preparation of bare and poly(vinylpyrrolidone) coated superparamagnetic iron oxide nanoparticles for biomedical applications. *Materials Letters* **179**, 5–8. DOI: 10.1016/j.matlet.2016.05.048.

[259] Wang Y., Xu C., Chang Y., Zhao L., Zhang K., Zhao Y., Gao F., Gao X. (2017) Ultrasmall Superparamagnetic Iron Oxide Nanoparticle for T_2-Weighted Magnetic Resonance Imaging. *ACS Applied Materials & Interfaces* **9**, 28959–28966. DOI: 10.1021/acsami.7b10030.

[260] Chee H.L., Gan C.R.R., Ng M., Low L., Fernig D.G., Bhakoo K.K., Paramelle D. (2018) Biocompatible Peptide-Coated Ultrasmall Superparamagnetic Iron Oxide Nanoparticles for *In Vivo* Contrast-Enhanced Magnetic Resonance Imaging. *ACS Nano* **12**, 6480–6491. DOI: 10.1021/acsnano.7b07572.

[261] Chen C., Ge J., Gao Y., Chen L., Cui J., Zeng J., Gao M. (2022) Ultrasmall superparamagnetic iron oxide nanoparticles: A next generation contrast agent for magnetic resonance imaging. *Wiley Interdiscip Rev Nanomed Nanobiotechnol.* **14**. DOI: 10.1002/wnan.1740.

[262] Frantellizzi V., Conte M., Pontico M., Pani A., Pani R., De Vincentis G. (2020) New Frontiers in Molecular Imaging with Superparamagnetic Iron Oxide Nanoparticles (SPIONs): Efficacy, Toxicity, and Future Applications. *Nuclear Medicine and Molecular Imaging* **54**, 65–80. DOI: 10.1007/s13139-020-00635-w.

[263] Rui Y.-P., Liang B., Hu F., Xu J., Peng Y.-F., Yin P.-H., Duan Y., Zhang C., Gu H. (2016) Ultra-large-scale production of ultrasmall superparamagnetic iron oxide nanoparticles for T_1-weighted MRI. *RSC Advances* **6**, 22575–22585. DOI: 10.1039/C6RA00347H.

[264] Du C., Liu X., Hu H., Li H., Yu L., Geng D., Chen Y., Zhang J. (2020) Dual-targeting and excretable ultrasmall SPIONs for T_1-weighted positive MR imaging of intracranial glioblastoma cells by targeting the lipoprotein receptor-related protein. *Journal of Materials Chemistry B* **8**, 2296–2306. DOI: 10.1039/C9TB02391G.

[265] Hervault A., Thanh N.T.K. (2014) Magnetic nanoparticle-based therapeutic agents for thermo-chemotherapy treatment of cancer. *Nanoscale* **6**, 11553–11573. DOI: 10.1039/C4NR03482A.

[266] Jeon H. *et al.* (2016) Poly-paclitaxel/cyclodextrin-SPION nano-assembly for magnetically guided drug delivery system. *Journal of Controlled Release* **231**, 68–76. DOI: 10.1016/j.jconrel.2016.01.006.

[267] Zhuang M., Chen X., Du D., Shi J., Deng M., Long Q., Yin X., Wang Y., Rao L. (2020) SPION decorated exosome delivery of TNF-α to cancer cell membranes through magnetism. *Nanoscale* **12**, 173–188. DOI: 10.1039/C9NR05865F.

[268] Luque-Michel E., Lemaire L., Blanco-Prieto M.J. (2021) SPION and doxorubicin-loaded polymeric nanocarriers for glioblastoma theranostics. *Drug Delivery and Translational Research* **11**, 515–523. DOI: 10.1007/s13346-020-00880-8.

[269] Tan L.K.S., How C.W., Low L.E., Ong B.H., Loh J.S., Lim S.-Y., Ong Y.S., Foo J.B. (2023) Magnetic-guided targeted delivery of zerumbone/SPION co-loaded in nanostructured lipid carrier into breast cancer cells. *Journal of Drug Delivery Science and Technology* **87**, 104830. DOI: 10.1016/j.jddst.2023.104830.

[270]   Huang Y., Mao K., Zhang B., Zhao Y. (2017) Superparamagnetic iron oxide nanoparticles conjugated with folic acid for dual target-specific drug delivery and MRI in cancer theranostics. *Materials Science and Engineering: C* **70**, 763–771. DOI: 10.1016/j.msec.2016.09.052.

[271]   Al-Musawi S., Albukhaty S., Al-Karagoly H., Sulaiman G.M., Jabir M.S., Naderi-Manesh H. (2020) Dextran-coated superparamagnetic nanoparticles modified with folate for targeted drug delivery of camptothecin. *Advances in Natural Sciences: Nanoscience and Nanotechnology* **11**, 045009. DOI: 10.1088/2043-6254/abc75b.

[272]   Al-Obaidy R., Haider A.J., Al-Musawi S., Arsad N. (2023) Targeted delivery of paclitaxel drug using polymer-coated magnetic nanoparticles for fibrosarcoma therapy: *in vitro* and *in vivo* studies. *Scientific Reports* **13**, 3180. DOI: 10.1038/s41598-023-30221-x.

[273]   Samani R.K., Maghsoudinia F., Asgari M., Atarod M., Mehrgardi M.A., Tavakoli M.B. (2023) Superparamagnetic iron oxide nanoparticle-loaded nanodroplets for dual-modal ultrasound/magnetic resonance imaging-guided drug delivery. *New Journal of Chemistry* **47**, 20193–20203. DOI: 10.1039/D3NJ02856A.

[274]   Nguyen M.P., Thuy V.T.T., Kim D. (2020) Integration of iron oxide nanoparticles and polyaspartamide biopolymer for MRI image contrast enhancement and an efficient drug-delivery system in cancer therapy. *Nanotechnology* **31**, 335712. DOI: 10.1088/1361-6528/ab8f49.

[275]   Mirzaghavami P.S., Khoei S., Khoee S., Shirvalilou S., Mahdavi S.R., Pirhajati Mahabadi V. (2021) Radio-sensitivity enhancement in HT29 cells through magnetic hyperthermia in combination with targeted nano-carrier of 5-Flourouracil. *Materials Science and Engineering: C* **124**, 112043. DOI: 10.1016/j.msec.2021.112043.

[276]   Ong Y.S., Bañobre-López M., Costa Lima S.A., Reis S. (2020) A multifunctional nanomedicine platform for co-delivery of methotrexate and mild hyperthermia towards breast cancer therapy. *Materials Science and Engineering: C* **116**, 111255. DOI: 10.1016/j.msec.2020.111255.

[277]   Wu L., Chen L., Liu F., Qi X., Ge Y., Shen S. (2017) Remotely controlled drug release based on iron oxide nanoparticles for specific therapy of cancer. *Colloids and Surfaces B: Biointerfaces* **152**, 440–448. DOI: 10.1016/j.colsurfb.2017.01.015.

[278]   Tu Z., Zhang B., Yang G., Wang M., Zhao F., Sheng D., Wang J. (2013) Synthesis of poly(ethylene glycol) and poly(vinyl pyrrolidone) co-coated superparamagnetic iron oxide nanoparticle as a pH-sensitive release drug carrier. *Colloids and Surfaces A: Physicochemical and Engineering Aspects* **436**, 854–861. DOI: 10.1016/j.colsurfa.2013.08.019.

[279]   Khan A., Kumar Sahu N. (2020) Folate encapsulation in PEG-diamine grafted mesoporous Fe_3O_4 nanoparticles for hyperthermia and *in vitro* assessment. *IET Nanobiotechnology* **14**, 881–888. DOI: 10.1049/iet-nbt.2020.0101.

[280]   Wanna Y., Chindaduang A., Tumcharern G., Phromyothin D., Porntheerapat S., Nukeaw J., Hofmann H., Pratontep S. (2016) Efficiency of SPIONs functionalized with polyethylene glycol bis(amine) for heavy metal removal. *Journal of Magnetism and Magnetic Materials* **414**, 32–37. DOI: 10.1016/j.jmmm.2016.04.064.

[281]   Samrot A. V, Sahithya C.S., Selvarani A J., Pachiyappan S., Kumar S S. (2019) Surface-Engineered Super-Paramagnetic Iron Oxide Nanoparticles For Chromium Removal. *International Journal of Nanomedicine* **Volume 14**, 8105–8119. DOI: 10.2147/IJN.S214236.

[282]   Bilgic A., Cimen A. (2023) Synthesis, characterisation, adsorption studies and comparison of superparamagnetic iron oxide nanoparticles (SPION) with three different amine groups functionalised with BODIPY for the removal of Cr(VI) metal ions from aqueous solutions. *International Journal of Environmental Analytical Chemistry* **103**, 1866–1891. DOI: 10.1080/03067319.2021.1884240.

[283]   Sharma G., Kumar A., Sharma S., Naushad Mu., Prakash Dwivedi R., ALOthman Z.A., Mola G.T. (2019) Novel development of nanoparticles to bimetallic nanoparticles and their composites: A review. *Journal of King Saud University - Science* **31**, 257–269. DOI: 10.1016/j.jksus.2017.06.012.

[284]   Stephanie R., Kim M.W., Kim S.H., Kim J.-K., Park C.Y., Park T.J. (2021) Recent advances of bimetallic nanomaterials and its nanocomposites for biosensing applications. *TrAC Trends in Analytical Chemistry* **135**, 116159. DOI: 10.1016/j.trac.2020.116159.

[285]   Luo S., Liu Y., Rao H., Wang Y., Wang X. (2017) Fluorescence and magnetic nanocomposite $Fe_3O_4@SiO_2@Au$ MNPs as peroxidase mimetics for glucose detection. *Analytical Biochemistry* **538**, 26–33. DOI: 10.1016/j.ab.2017.09.006.

[286]   Huang C.-L., Hsieh W.-J., Lin C.-W., Yang H.-W., Wang C.-K. (2018) Multifunctional liposomal drug delivery with dual probes of magnetic resonance and fluorescence imaging. *Ceramics International* **44**, 12442–12450. DOI: 10.1016/j.ceramint.2018.04.034.

[287]   Zhao H.Y., Liu S., He J., Pan C.C., Li H., Zhou Z.Y., Ding Y., Huo D., Hu Y. (2015) Synthesis and application of strawberry-like Fe_3O_4-Au nanoparticles as CT-MR dual-modality contrast agents

in accurate detection of the progressive liver disease. *Biomaterials* **51**, 194–207. DOI: 10.1016/j.biomaterials.2015.02.019.

[288] Le Guével X., Prinz E.-M., Müller R., Hempelmann R., Schneider M. (2012) Synthesis and characterization of superparamagnetic nanoparticles coated with fluorescent gold nanoclusters. *Journal of Nanoparticle Research* **14**, 727. DOI: 10.1007/s11051-012-0727-6.

[289] Wang C., Yao Y., Song Q. (2015) Gold nanoclusters decorated with magnetic iron oxide nanoparticles for potential multimodal optical/magnetic resonance imaging. *Journal of Materials Chemistry C* **3**, 5910–5917. DOI: 10.1039/C5TC00290G.

[290] Cho S., Shin H.Y., Kim M. Il. (2017) Nanohybrids consisting of magnetic nanoparticles and gold nanoclusters as effective peroxidase mimics and their application for colorimetric detection of glucose. *Biointerphases* **12**, 01A401. DOI: 10.1116/1.4974198.

[291] Shibu E.S., Sugino S., Ono K., Saito H., Nishioka A., Yamamura S., Sawada M., Nosaka Y., Biju V. (2013) Singlet-Oxygen-Sensitizing Near-Infrared-Fluorescent Multimodal Nanoparticles. *Angewandte Chemie International Edition* **52**, 10559–10563. DOI: 10.1002/anie.201304264.

[292] Ostruszka R., Halili A., Pluháček T., Rárová L., Jirák D., Šišková K. (2024) Advanced protein-embedded bimetallic nanocomposite optimized for *in vivo* fluorescence and magnetic resonance bimodal imaging. *Journal of Colloid and Interface Science* **663**, 467–477. DOI: 10.1016/j.jcis.2024.02.116.

[293] Chen H., Wang Y., Wang T., Shi D., Sun Z., Xia C., Wang B. (2016) Application prospective of nanoprobes with MRI and FI dual-modality imaging on breast cancer stem cells in tumor. *Journal of Nanobiotechnology* **14**, 52. DOI: 10.1186/s12951-016-0195-8.

[294] Tankovskaia S.A., Abrosimova K. V., Paston S. V. (2018) Spectral demonstration of structural transitions in albumins. *Journal of Molecular Structure* **1171**, 243–252. DOI: 10.1016/j.molstruc.2018.05.100.

[295] Peters T. (1985) Serum Albumin. In: *Advances in Protein Chemistry*., pp. 161–245. Academic Press. DOI: 10.1016/S0065-3233(08)60065-0.

[296] Peters T. (1995) The Albumin Molecule: Its Structure and Chemical Properties. In: *All About Albumin*., pp. 9–II. Elsevier. DOI: 10.1016/B978-012552110-9/50004-0.

[297] Bal W., Sokołowska M., Kurowska E., Faller P. (2013) Binding of transition metal ions to albumin: Sites, affinities and rates. *Biochimica et Biophysica Acta (BBA) - General Subjects* **1830**, 5444–5455. DOI: 10.1016/j.bbagen.2013.06.018.

[298] Hirayama K., Akashi S., Furuya M., Fukuhara K. (1990) Rapid confirmation and revision of the primary structure of bovine serum albumin by ESIMS and frit-FAB LC/MS. *Biochemical and Biophysical Research Communications* **173**, 639–646. DOI: 10.1016/S0006-291X(05)80083-X.

[299] Majorek K.A., Porebski P.J., Dayal A., Zimmerman M.D., Jablonska K., Stewart A.J., Chruszcz M., Minor W. (2012) Structural and immunologic characterization of bovine, horse, and rabbit serum albumins. *Molecular Immunology* **52**, 174–182. DOI: 10.1016/j.molimm.2012.05.011.

[300] Baldwin R.L. (1957) Boundary spreading in sedimentation-velocity experiments. 5. Measurement of the diffusion coefficient of bovine albumin by Fujita's equation. *Biochemical Journal* **65**, 503–512. DOI: 10.1042/bj0650503.

[301] Reed R.G., Putnam F.W., Peters T. (1980) Sequence of residues 400–403 of bovine serum albumin. *Biochemical Journal* **191**, 867–868. DOI: 10.1042/bj1910867.

[302] Loo J.A., Udseth H.R., Smith R.D. (1989) Peptide and protein analysis by electrospray ionization-mass spectrometry and capillary electrophoresis-mass spectrometry. *Analytical Biochemistry* **179**, 404–412. DOI: 10.1016/0003-2697(89)90153-X.

[303] Chowdhury S.K., Katta V., Chait B.T. (1990) An electrospray-ionization mass spectrometer with new features. *Rapid Communications in Mass Spectrometry* **4**, 81–87. DOI: 10.1002/rcm.1290040305.

[304] Feng R., Konishi Y., Bell A.W. (1991) High Accuracy Molecular Weight Determination and Variation Characterization of Proteins Up To 80 ku by Ionspray Mass Spectrometry. *Journal of the American Society for Mass Spectrometry* **2**, 387–401. DOI: 10.1016/1044-0305(91)85005-Q.

[305] Jachimska B., Pajor A. (2012) Physico-chemical characterization of bovine serum albumin in solution and as deposited on surfaces. *Bioelectrochemistry* **87**, 138–146. DOI: 10.1016/j.bioelechem.2011.09.004.

[306] Baler K., Martin O.A., Carignano M.A., Ameer G.A., Vila J.A., Szleifer I. (2014) Electrostatic Unfolding and Interactions of Albumin Driven by pH Changes: A Molecular Dynamics Study. *The Journal of Physical Chemistry B* **118**, 921–930. DOI: 10.1021/jp409936v.

[307] Li R., Wu Z., Wangb Y., Ding L., Wang Y. (2016) Role of pH-induced structural change in protein aggregation in foam fractionation of bovine serum albumin. *Biotechnology Reports* **9**, 46–52. DOI: 10.1016/j.btre.2016.01.002.

[308] Ju P., Fan H., Liu T., Cui L., Ai S. (2011) Probing the interaction of flower-like CdSe nanostructure particles targeted to bovine serum albumin using spectroscopic techniques. *Journal of Luminescence* **131**, 1724–1730. DOI: 10.1016/j.jlumin.2011.03.070.

[309] Zhao X., Liu R., Chi Z., Teng Y., Qin P. (2010) New Insights into the Behavior of Bovine Serum Albumin Adsorbed onto Carbon Nanotubes: Comprehensive Spectroscopic Studies. *The Journal of Physical Chemistry B* **114**, 5625–5631. DOI: 10.1021/jp100903x.

[310] Curvale R., Masuelli M., Padilla A.P. (2008) Intrinsic viscosity of bovine serum albumin conformers. *International Journal of Biological Macromolecules* **42**, 133–137. DOI: 10.1016/j.ijbiomac.2007.10.007.

[311] Cao X.-L., Li H.-W., Yue Y., Wu Y. (2013) pH-Induced conformational changes of BSA in fluorescent AuNCs@BSA and its effects on NCs emission. *Vibrational Spectroscopy* **65**, 186–192. DOI: 10.1016/j.vibspec.2013.01.004.

[312] Varga N., Hornok V., Sebők D., Dékány I. (2016) Comprehensive study on the structure of the BSA from extended-to aged form in wide (2–12) pH range. *International Journal of Biological Macromolecules* **88**, 51–58. DOI: 10.1016/j.ijbiomac.2016.03.030.

[313] Chi Z., Hong B., Ren X., Cheng K., Lu Y., Liu X. (2018) Investigation on the conformational changes of bovine serum albumin in a wide pH range from 2 to 12. *Spectroscopy Letters* **51**, 279–286. DOI: 10.1080/00387010.2018.1471092.

[314] Fehér B., Lyngsø J., Bartók B., Mihály J., Varga Z., Mészáros R., Pedersen J.S., Bóta A., Varga I. (2020) Effect of pH on the conformation of bovine serume albumin - gold bioconjugates. *Journal of Molecular Liquids* **309**, 113065. DOI: 10.1016/j.molliq.2020.113065.

[315] Chen L., Gharib M., Zeng Y., Roy S., Nandi C.K., Chakraborty I. (2023) Advances in bovine serum albumin-protected gold nanoclusters: from understanding the formation mechanisms to biological applications. *Mater Today Chem.* **29**. DOI: 10.1016/j.mtchem.2023.101460.

[316] Russell B.A., Kubiak-Ossowska K., Mulheran P.A., Birch D.J.S., Chen Y. (2015) Locating the nucleation sites for protein encapsulated gold nanoclusters: a molecular dynamics and fluorescence study. *Physical Chemistry Chemical Physics* **17**, 21935–21941. DOI: 10.1039/C5CP02380G.

[317] Yamasaki M., Yano H., Aoki K. (1990) Differential scanning calorimetric studies on bovine serum albumin: I. Effects of pH and ionic strength. *International Journal of Biological Macromolecules* **12**, 263–268. DOI: 10.1016/0141-8130(90)90007-W.

[318] Kongraksawech T., Vázquez-Landaverde P., Huerta-Ruelas J., Torres J.A. (2007) IONIC STRENGTH AND pH EFFECTS ON OPTICAL THERMOGRAPHS FOR BOVINE SERUM ALBUMIN (BSA) EFECTOS DE LA FUERZA IÓNICA Y EL pH SOBRE LOS TERMOGRAMAS ÓPTICOS DE LA SEROALBUMINA BOVINA (BSA). *Ciencia y Tecnologia Alimentaria* **5**, 259–264. DOI: 10.1080/11358120709487699.

[319] Michnik A., Michalik K., Kluczewska A., Drzazga Z. (2006) Comparative DSC study of human and bovine serum albumin. *Journal of Thermal Analysis and Calorimetry* **84**, 113–117. DOI: 10.1007/s10973-005-7170-1.

[320] Peng Z.G., Hidajat K., Uddin M.S. (2004) Adsorption of bovine serum albumin on nanosized magnetic particles. *Journal of Colloid and Interface Science* **271**, 277–283. DOI: 10.1016/j.jcis.2003.12.022.

[321] Shi Q., Zhou Y., Sun Y. (2008) Influence of pH and Ionic Strength on the Steric Mass-Action Model Parameters around the Isoelectric Point of Protein. *Biotechnology Progress* **21**, 516–523. DOI: 10.1021/bp049735o.

[322] Liu X.-H., Xi P.-X., Chen F.-J., Xu Z.-H., Zeng Z.-Z. (2008) Spectroscopic studies on binding of 1-phenyl-3-(coumarin-6-yl)sulfonylurea to bovine serum albumin. *Journal of Photochemistry and Photobiology B: Biology* **92**, 98–102. DOI: 10.1016/j.jphotobiol.2008.04.008.

[323] Xu H., Yao N., Xu H., Wang T., Li G., Li Z. (2013) Characterization of the Interaction between Eupatorin and Bovine Serum Albumin by Spectroscopic and Molecular Modeling Methods. *International Journal of Molecular Sciences* **14**, 14185–14203. DOI: 10.3390/ijms140714185.

[324] Zhang Y.-Z., Zhou B., Liu Y.-X., Zhou C.-X., Ding X.-L., Liu Y. (2008) Fluorescence Study on the Interaction of Bovine Serum Albumin with P-Aminoazobenzene. *Journal of Fluorescence* **18**, 109–118. DOI: 10.1007/s10895-007-0247-4.

[325] Güler G., Vorob'ev M.M., Vogel V., Mäntele W. (2016) Proteolytically-induced changes of secondary structural protein conformation of bovine serum albumin monitored by Fourier transform infrared (FT-IR) and UV-circular dichroism spectroscopy. *Spectrochimica Acta Part A: Molecular and Biomolecular Spectroscopy* **161**, 8–18. DOI: 10.1016/j.saa.2016.02.013.

[326] Ostruszka R., Šišková K. (2022) Optimization of Synthesis of Bovine Serum Albumin-Encapsulated Fluorescent Gold Nanoclusters. In: *The 3rd International Online-Conference on Nanomaterials.*, p. 15. Basel Switzerland: MDPI. DOI: 10.3390/materproc2022009015.

[327] Li H.-W., Yue Y., Liu T.-Y., Li D., Wu Y. (2013) Fluorescence-Enhanced Sensing Mechanism of BSA-Protected Small Gold-Nanoclusters to Silver(I) Ions in Aqueous Solutions. *The Journal of Physical Chemistry C* **117**, 16159–16165. DOI: 10.1021/jp403466b.

[328] Lin H., Imakita K., Fujii M., Sun C., Chen B., Kanno T., Sugimoto H. (2017) New insights into the red luminescent bovine serum albumin conjugated gold nanospecies. *Journal of Alloys and Compounds* **691**, 860–865. DOI: 10.1016/j.jallcom.2016.08.300.

[329] Zoppellaro G., Ostruszka R., Siskova K. (2024) Engineered protein-iron and/or gold-protein-iron nanocomposites in aqueous solutions upon UVA light: Photo-induced electron transfer possibilities and limitations. *Journal of Photochemistry and Photobiology A: Chemistry* **450**, 115415. DOI: 10.1016/j.jphotochem.2023.115415.

[330] Ostruszka R., Půlpánová D., Pluháček T., Tomanec O., Novák P., Jirák D., Šišková K. (2023) Facile One-Pot Green Synthesis of Magneto-Luminescent Bimetallic Nanocomposites with Potential as Dual Imaging Agent. *Nanomaterials* **13**, 1027. DOI: 10.3390/nano13061027.

[331] Simms G.A., Padmos J.D., Zhang P. (2009) Structural and electronic properties of protein/thiolate-protected gold nanocluster with "staple" motif: A XAS, L-DOS, and XPS study. *The Journal of Chemical Physics* **131**. DOI: 10.1063/1.3268782.

[332] Weerawardene K.L.D.M., Aikens C.M. (2016) Theoretical Insights into the Origin of Photoluminescence of $Au_{25}(SR)_{18}^-$ Nanoparticles. *Journal of the American Chemical Society* **138**, 11202–11210. DOI: 10.1021/jacs.6b05293.

[333] Siskova K., Tucek J., Machala L., Otyepkova E., Filip J., Safarova K., Pechousek J., Zboril R. (2012) Air-stable nZVI formation mediated by glutamic acid: solid-state storable material exhibiting 2D chain morphology and high reactivity in aqueous environment. *Journal of Nanoparticle Research* **14**, 805. DOI: 10.1007/s11051-012-0805-9.

[334] Šišková K., Machala L., Tuček J., Kašlík J., Mojzeš P., Zbořil R. (2013) Mixtures of l-Amino Acids as Reaction Medium for Formation of Iron Nanoparticles: The Order of Addition into a Ferrous Salt Solution Matters. *International Journal of Molecular Sciences* **14**, 19452–19473. DOI: 10.3390/ijms141019452.

[335] Babes L., Denizot B., Tanguy G., Le Jeune J.J., Jallet P. (1999) Synthesis of Iron Oxide Nanoparticles Used as MRI Contrast Agents: A Parametric Study. *Journal of Colloid and Interface Science* **212**, 474–482. DOI: 10.1006/jcis.1998.6053.

[336] Andrade Â.L., Souza D.M., Pereira M.C., Fabris J.D., Domingues R.Z. (2010) pH effect on the synthesis of magnetite nanoparticles by the chemical reduction-precipitation method. *Química Nova* **33**, 524–527. DOI: 10.1590/S0100-40422010000300006.

[337] Ueno H.M., Urazono H., Kobayashi T. (2014) Serum albumin forms a lactoferrin-like soluble iron-binding complex in presence of hydrogen carbonate ions. *Food Chemistry* **145**, 90–94. DOI: 10.1016/j.foodchem.2013.07.143.

[338] Jolivet J.-P., Chanéac C., Tronc E. (2004) Iron oxide chemistry. From molecular clusters to extended solid networks. *Chem. Commun.* **4**, 477–483. DOI: 10.1039/B304532N.

[339] He C., Hu Y., Yin L., Tang C., Yin C. (2010) Effects of particle size and surface charge on cellular uptake and biodistribution of polymeric nanoparticles. *Biomaterials* **31**, 3657–3666. DOI: 10.1016/j.biomaterials.2010.01.065.

[340] Ayala V., Herrera A.P., Latorre-Esteves M., Torres-Lugo M., Rinaldi C. (2013) Effect of surface charge on the colloidal stability and *in vitro* uptake of carboxymethyl dextran-coated iron oxide nanoparticles. *Journal of Nanoparticle Research* **15**, 1874. DOI: 10.1007/s11051-013-1874-0.

[341] Hühn D. *et al.* (2013) Polymer-Coated Nanoparticles Interacting with Proteins and Cells: Focusing on the Sign of the Net Charge. *ACS Nano* **7**, 3253–3263. DOI: 10.1021/nn3059295.

[342] Liu X., Huang N., Li H., Jin Q., Ji J. (2013) Surface and Size Effects on Cell Interaction of Gold Nanoparticles with Both Phagocytic and Nonphagocytic Cells. *Langmuir* **29**, 9138–9148. DOI: 10.1021/la401556k.

[343] Choi J.-S., Cao J., Naeem M., Noh J., Hasan N., Choi H.-K., Yoo J.-W. (2014) Size-controlled biodegradable nanoparticles: Preparation and size-dependent cellular uptake and tumor cell growth inhibition. *Colloids and Surfaces B: Biointerfaces* **122**, 545–551. DOI: 10.1016/j.colsurfb.2014.07.030.

[344] Jiang Y. *et al.* (2015) The Interplay of Size and Surface Functionality on the Cellular Uptake of Sub-10 nm Gold Nanoparticles. *ACS Nano* **9**, 9986–9993. DOI: 10.1021/acsnano.5b03521.

[345] Donahue N.D., Acar H., Wilhelm S. (2019) Concepts of nanoparticle cellular uptake, intracellular trafficking, and kinetics in nanomedicine. *Advanced Drug Delivery Reviews* **143**, 68–96. DOI: 10.1016/j.addr.2019.04.008.

[346] Carnovale C., Bryant G., Shukla R., Bansal V. (2019) Identifying Trends in Gold Nanoparticle Toxicity and Uptake: Size, Shape, Capping Ligand, and Biological Corona. *ACS Omega* **4**, 242–256. DOI: 10.1021/acsomega.8b03227.

[347] Lee Y.J., Ahn E.-Y., Park Y. (2019) Shape-dependent cytotoxicity and cellular uptake of gold nanoparticles synthesized using green tea extract. *Nanoscale Research Letters* **14**, 129. DOI: 10.1186/s11671-019-2967-1.

[348] Bai X. *et al.* (2020) Regulation of Cell Uptake and Cytotoxicity by Nanoparticle Core under the Controlled Shape, Size, and Surface Chemistries. *ACS Nano* **14**, 289–302. DOI: 10.1021/acsnano.9b04407.

[349] Anselmo A.C., Zhang M., Kumar S., Vogus D.R., Menegatti S., Helgeson M.E., Mitragotri S. (2015) Elasticity of Nanoparticles Influences Their Blood Circulation, Phagocytosis, Endocytosis, and Targeting. *ACS Nano* **9**, 3169–3177. DOI: 10.1021/acsnano.5b00147.

[350] Guo P., Liu D., Subramanyam K., Wang B., Yang J., Huang J., Auguste D.T., Moses M.A. (2018) Nanoparticle elasticity directs tumor uptake. *Nature Communications* **9**, 130. DOI: 10.1038/s41467-017-02588-9.

[351] Samadi Moghaddam M., Heiny M., Shastri V.P. (2015) Enhanced cellular uptake of nanoparticles by increasing the hydrophobicity of poly(lactic acid) through copolymerization with cell-membrane-lipid components. *Chemical Communications* **51**, 14605–14608. DOI: 10.1039/C5CC06397C.

[352] Francia V., Yang K., Deville S., Reker-Smit C., Nelissen I., Salvati A. (2019) Corona Composition Can Affect the Mechanisms Cells Use to Internalize Nanoparticles. *ACS Nano* **13**, 11107–11121. DOI: 10.1021/acsnano.9b03824.

[353] Aliyandi A., Reker-Smit C., Bron R., Zuhorn I.S., Salvati A. (2021) Correlating Corona Composition and Cell Uptake to Identify Proteins Affecting Nanoparticle Entry into Endothelial Cells. *ACS Biomaterials Science & Engineering* **7**, 5573–5584. DOI: 10.1021/acsbiomaterials.1c00804.

[354] Mahmoudi M., Landry M.P., Moore A., Coreas R. (2023) The protein corona from nanomedicine to environmental science. *Nature Reviews Materials* **8**, 422–438. DOI: 10.1038/s41578-023-00552-2.

[355] Walkey C.D., Olsen J.B., Song F., Liu R., Guo H., Olsen D.W.H., Cohen Y., Emili A., Chan W.C.W. (2014) Protein Corona Fingerprinting Predicts the Cellular Interaction of Gold and Silver Nanoparticles. *ACS Nano* **8**, 2439–2455. DOI: 10.1021/nn406018q.

[356] Liu N., Tang M., Ding J. (2020) The interaction between nanoparticles-protein corona complex and cells and its toxic effect on cells. *Chemosphere* **245**, 125624. DOI: 10.1016/j.chemosphere.2019.125624.

[357] Oberländer J., Champanhac C., da Costa Marques R., Landfester K., Mailänder V. (2022) Temperature, concentration, and surface modification influence the cellular uptake and the protein corona of polystyrene nanoparticles. *Acta Biomaterialia* **148**, 271–278. DOI: 10.1016/j.actbio.2022.06.028.

[358] Tang H. *et al.* (2023) Cholesterol modulates the physiological response to nanoparticles by changing the composition of protein corona. *Nature Nanotechnology* **18**, 1067–1077. DOI: 10.1038/s41565-023-01455-7.

5. Seznam přiložených publikací

I   **Ostruszka R.**, Zoppellaro G., Tomanec O., Pinkas D., Filimonenko V., Šišková K. (2022) Evidence of Au(II) and Au(0) States in Bovine Serum Albumin-Au Nanoclusters Revealed by CW-EPR/LEPR and Peculiarities in HR-TEM/STEM Imaging. *Nanomaterials*, **12**:1425. DOI: https://doi.org/10.3390/nano12091425.

II   **Ostruszka R.**, Půlpánová D., Pluháček T., Tomanec O., Novák P., Jirák D., Šišková K. (2023) Facile One-Pot Green Synthesis of Magneto-Luminescent Bimetallic Nanocomposites with Potential as Dual Imaging Agent. *Nanomaterials*, **13**:1027. DOI: https://doi.org/10.3390/nano13061027.

III   Zoppellaro G., **Ostruszka R.**, Šišková K. (2024) Engineered protein-iron and/or gold-protein-iron nanocomposites in aqueous solutions upon UVA light: Photo-induced electron transfer possibilities and limitations. *Journal of Photochemistry & Photobiology A: Chemistry* **450**:115415. DOI: https://doi.org/10.1016/j.jphotochem.2023.115415.

IV   **Ostruszka R.**, Halili A., Pluháček T., Rárová L., Jirák D., Šišková K. (2024) Advanced protein-embedded bimetallic nanocomposite optimized for *in vivo* fluorescence and magnetic resonance bimodal imaging. *Journal of Colloid And Interface Science* **663**, 467-477. DOI: https://doi.org/10.1016/j.jcis.2024.02.116.

I

Evidence of Au(II) and Au(0) States in Bovine Serum Albumin-Au Nanoclusters Revealed by CW-EPR/LEPR and Peculiarities in HR-TEM/STEM Imaging	
Ostruszka R., Zoppellaro G., Tomanec O., Pinkas D., Filimonenko V., Šišková K.	*Nanomaterials*, **12**:1425
	2022

Article

Evidence of Au(II) and Au(0) States in Bovine Serum Albumin-Au Nanoclusters Revealed by CW-EPR/LEPR and Peculiarities in HR-TEM/STEM Imaging

Radek Ostruszka [1] , Giorgio Zoppellaro [2,*] , Ondřej Tomanec [2], Dominik Pinkas [3], Vlada Filimonenko [3] and Karolína Šišková [1,*]

[1] Department of Experimental Physics, Faculty of Science, Palacký University, tř. 17. Listopadu 12, 77900 Olomouc, Czech Republic; radek.ostruszka@upol.cz

[2] Regional Centre of Advanced Technologies and Materials, Faculty of Science, Palacký University, tř. 17. Listopadu 12, 77900 Olomouc, Czech Republic; ondrej.tomanec@upol.cz

[3] Institute of Molecular Genetics of the Czech Academy of Sciences, Microscopy Centre, Electron Microscopy Core Facility, Vídeňská 1083, 14220 Prague, Czech Republic; dominik.pinkas@img.cas.cz (D.P.); vlada.filimonenko@img.cas.cz (V.F.)

[*] Correspondence: giorgio.zoppellaro@upol.cz (G.Z.); karolina.siskova@upol.cz (K.Š.)

Abstract: Bovine serum albumin-embedded Au nanoclusters (BSA-AuNCs) are thoroughly probed by continuous wave electron paramagnetic resonance (CW-EPR), light-induced EPR (LEPR), and sequences of microscopic investigations performed via high-resolution transmission electron microscopy (HR-TEM), scanning transmission electron microscopy (STEM), and energy dispersive X-ray analysis (EDS). To the best of our knowledge, this is the first report analyzing the BSA-AuNCs by CW-EPR/LEPR technique. Besides the presence of Au(0) and Au(I) oxidation states in BSA-AuNCs, the authors observe a significant amount of Au(II), which may result from a disproportionation event occurring within NCs: $2Au(I) \rightarrow Au(II) + Au(0)$. Based on the LEPR experiments, and by comparing the behavior of BSA versus BSA-AuNCs under UV light irradiation (at 325 nm) during light off-on-off cycles, any energy and/or charge transfer event occurring between BSA and AuNCs during photoexcitation can be excluded. According to CW-EPR results, the Au nano assemblies within BSA-AuNCs are estimated to contain 6–8 Au units per fluorescent cluster. Direct observation of BSA-AuNCs by STEM and HR-TEM techniques confirms the presence of such diameters of gold nanoclusters in BSA-AuNCs. Moreover, in situ formation and migration of Au nanostructures are observed and evidenced after application of either a focused electron beam from HR-TEM, or an X-ray from EDS experiments.

Keywords: gold nanostructures; fluorescent nanoprobe; noble metal nanocrystal; protein nanocomposite

1. Introduction

Fluorescent gold nanoclusters (AuNCs) embedded in bovine serum albumin (BSA) have been extensively studied in the literature since 2009, following the publication of Xie et al. [1] However, many open questions remain unsolved, especially for the witnessed dependence of the fluorescent properties with the sizes of Au nanostructures. [2–42]. The discussion remains controversial because many reports describe fluorescent AuNCs where the origin of such phenomenon is linked to the small size of the nanoparticles (NPs) (e.g., Burt et al. [37], Zhang and Wang [38], Zheng et al. [39]), while other reports suggest that the key to the fluorescence properties is intimately associated to the oxidation state of the gold cluster, Au(III)- [3] and/or Au(I)-complexes [40]. In Table 1, examples of selected BSA-AuNCs preparations are given, including their synthetic parameters, as reported in literature, in conjunction with the AuNCs size, oxidation state of Au when known, and maximum (maxima) of their fluorescence emissions.

Table 1. Details of selected BSA-AuNCs preparations and properties as reported in literature.

Reference Number	Oxidation State of Au	Size of BSA-AuNCs [nm]	Emission Wavelength Maximum [nm]	Quantum Yield [%]	Synthesis Conditions (X = BSA + HAuCl4)
[1]	Au^0, Au^+ XPS	≈0.8 TEM	640	6	X –(2 min)> NaOH → incubation at 37 °C for 12 h
[2]	n.a.	≈1 TEM	n.a.	n.a.	X → NaBH$_4$ → incubation at RT for 1 h
[3]	n.a.	6.3 ± 2.9 (pH 12) * 3.3 ± 1.4 (pH 10) * 1.6 ± 0.7 (pH 9) *	640 (pH 12) n.a. (pH 10) 440 (pH 9)	n.a.	same as [1], NaBH$_4$ used in later steps
[4]	Au^0, Au^+ XPS	4.2 ± 0.5 TEM	676	4.14	X → NaOH → MW (incubation at 80 °C for 4 min)
[4]	Au^0 XPS + FQ	3.1 ± 0.4 TEM	436	1.94	X → NaOH → MW (incubation at 135 °C for 4 min)
[7]	n.a.	n.a.	640, 710	n.a.	X → incubation at 37 °C overnight
[15]	Au^0, Au^+ XPS	2.1 ± 0.3 TEM	650	1.9	X → NaOH → MW (120 W, 2 min)
[16]	Au^0, Au^+ XPS	n.a.	656	n.a.	same as [1]
[27]	n.a.	n.a.	705	n.a.	X –(1 h) > NaOH → incubation at 45 °C for 4 h
[30]	Au^0, Au^+ XPS	n.a.	635	n.a.	same as [1]
[32]	Au^0, Au^+ XPS	4–6 TEM	650	≈8	X –(30 min)> NaOH → incubation at 50 °C for 3–4 h
[34]	Au^0, Au^+ XPS	n.a.	685	≈5.5	X → ascorbic acid → NaOH → incubation at 37 °C for 5 h
[35]	Au^0, Au^+ XPS	1.6 HR-TEM	604	n.a.	X –(2 min)> NaOH → MW and then incubation at 37 °C for 12 h X –(10 min)> NaOH → incubation at 37 °C for 24 h
[36]	Au^0, Au^+ XPS	n.a.	620	n.a.	X → NaOH → incubation at 37 °C for 12 h + dialysis for 48 h
[37]	n.a.	average < 2 TEM 1.5–1.8 HAADF-STEM	n.a.	n.a.	X → NaBH$_4$ → incubation for 3 h
[41]	n.a.	3.6 DLS	650	6.2	X –(90 s)> NaOH → MW (150 W, 10 s)
[42]	n.a.	≈5 TEM, HR-TEM	645	n.a.	X → NaOH → MW (300 W, 6 min)

Notes: n.a. = not available, * = sizes obtained after the reduction performed by addition of NaBH$_4$ to Au(III)-BSA systems which were generated at given pH values, MW = microwave radiation heating, XPS = X-ray photoelectron spectroscopy, FQ = fluorescence quenching, TEM = transmission electron microscopy, HAADF-STEM = high-angle annular dark-field scanning transmission electron microscopy, HR-TEM = high resolution transmission electron microscopy.

From the size perspectives, AuNCs are considered intermediate systems, falling between dimensions of isolated Au atoms (0D, zero dimensional) and Au nanoparticles (3D dimensional). The fluorescent properties emerge and are tuned by the presence of discrete energy levels that mirror the nanoparticle size variance, which approach the Fermi wavelength of free electrons (e.g., [38,43]). More detailed descriptions of different types of luminescent Au nanostructures and the related emission mechanisms, including not only

the free-electron model, but also surface ligand effects, are thoroughly discussed in recent reviews (e.g., [39,44–46]).

The oxidation state of Au is undoubtedly an important parameter to unveil for understanding the physical basis of the fluorescence phenomenon. [44] In this context, analysis of the fluorescent properties of Au clusters entrapped by proteins, such as bovine serum albumin (BSA), is particularly debated. Mostly, Au(0) and Au(I) oxidation states are observed and screened by XPS (X-ray photoelectron spectroscopy) in BSA-AuNCs [1,2,4,15,16,30,32,34–36]. The pseudo-polymeric structure, such as SR-(Au-SR)x- (x = 1 or 2) motif, is envisioned to be present, and from XPS results the authors [2] demonstrated that Au-Au and Au-S bonds form in the BSA-AuNCs system. It should be noted that the occurrence of the staple motif arrangement (-S-Au(I)-S-Au(I)-S-) determined in BSA-AuNCs (as in e.g., [7]) shares similarities with the arrangement observed in thiol-protected $Au_{25}(SR)_{18}$ clusters prepared by Zhu M. et al. [47,48]. Based on XRD analysis, a core-shell structure of the thiol-protected Au_{25} cluster was determined in [47]. The same group of researchers revealed the intrinsic magnetism of these thiolate-protected Au_{25} super atoms in 2009 [49]. On the contrary, the magnetic properties of BSA-AuNCs have not been investigated so far, to the best of our knowledge. Therefore, the presence of such a property represents one of the aims tackled in this study.

Importantly, the oxidation state of Au in the final AuNCs is closely related to the experimental conditions. There are obvious differences in the presence and/or absence of a strong reduction agent in the course of AuNCs formation as shown in Table 1. In synthetic procedures where $NaBH_4$ is used, BSA represents solely a template (matrix) that prevents the occurrence of coalescence processes in AuNCs at room temperature. On the contrary, when the use of $NaBH_4$ is avoided (as in our previous work [41]), BSA acts as a reducing agent (probably due to tyrosine residues [1] at increased pH above its pK_a value) and, simultaneously, as a capping agent for AuNCs. Interestingly, even syntheses exploiting solely BSA as the reducing agent can lead to different fluorescent properties of resulting AuNCs, as shown in Table 1. The reason for such differences in fluorescent characteristics may be either the type of heating (incubator at 37 °C vs. MW heating), or the initial concentration of BSA—see Table 1.

Several literature reports that describe organometallic complexes containing Au(I) sites show the existence of strong Au–Au bonds and the term "aurophilicity" was therefore introduced in 1989 to describe the unusual bond properties [50]. Aurophilic interaction is thought to be as strong as a hydrogen bond and shows the presence of bond length as shorter than the sum of two van der Waals radii of gold (3.80 Å). This bond characteristic is suggested to be one of the relevant factors promoting the fluorescence effect of Au(I) complexes in the UV-vis region, when investigated in the solid state [50]. The fluorescent property may then vanish in the solution, but there are scenarios where the luminescence is restored, at least for high concentrations, when a suitable solvent is used [51,52] and/or increases in the solution when AuNCs undergo self-assembly into nanoribbon structures [53]. Importantly, many Au(I) ions, being complexed with thiols and/or compounds containing other functional groups, such as carboxylates and amides, show fluorescent effects when they are partially ordered (from aurophillic interactions) [51,52]. This might also be the case of Au(I) in BSA-AuNCs.

Concerning another oxidation state of Au (besides Au(I) and Au(0)) being evidenced in BSA-AuNCs, however implicitly (i.e., based on additional chemical reduction using $NaBH_4$ and not directly by XPS), Dixon and Egusa [3] reported the presence of a significant amount of Au(III) in 2018. Terminologically, they label the systems as BSA-Au(III) complexes, but, simultaneously, they admit that there is no disproval of the existence of neutral Au(0) NCs in BSA-Au samples [3]. They [3] summarized that the red fluorescence that emerged due to Au(III) cations complexed with BSA at or above the pH value (9.7 +/− 0.2), which was responsible for the conformational change of BSA structure from normal (N) to aged (A) conformation. Therefore, they [3] concluded that upon BSA conformational change, some Cys–Cys bonds were expected to be sufficiently exposed and solvent-accessible and

might interact with Au(III). They also experimentally proved multiple specific Au(III) binding sites in BSA and postulated that the UV-excitable red fluorescence of the BSA-Au(III) complex is due to the internal and potentially cascaded energy transfers among chromophores [3]. Alternatively, they admit strong electron delocalization as a source of the red fluorescence [3].

Furthermore, based on Table 1, it is obvious that sizes of AuNCs, the oxidation state of Au, and consequently their luminescent properties are strongly dependent, among others, on the exact conditions of their synthesis. Moreover, purification (if applied), storage conditions, and time elapsed before the characterization of AuNCs is completed, may represent other factors influencing the fluorescence of the final NCs as demonstrated in our previous work [41]. Obviously (Table 1), visualization of tiny AuNCs is usually performed by TEM and HR-TEM (high-resolution transmission electron microscopy). Particularly, STEM (scanning transmission electron microscopy) using High-Angle Annular Dark Field (HAADF) mode is necessary to be employed in the case of BSA-AuNCs [37]; otherwise, the TEM resolution is obscured by the enveloping protein (BSA) and the accurate size distribution cannot be obtained as stated in [2]. Interestingly, in many research papers (e.g., [3,4,42,54]), the TEM images of AuNCs exceed the size characteristic for their fluorescent properties (maximum of 2 nm in diameter). Besides HR-TEM/STEM, the determination of BSA-AuNCs sizes is often based on mass spectrometry measurements (MS) [55,56]. This is an indirect method where the MS size of BSA is subtracted from the MS size of the BSA-AuNCs system. However, this leads to the determination of the number of Au atoms per BSA. Such estimation does not provide any information about the real size of AuNCs because Au atoms are not localized on a single place in BSA; indeed, they can be spread on different cysteine and other residues of the protein [3,41]. Therefore, it seems that direct visualization of AuNCs as well as determination of individual AuNCs sizes within BSA represent challenging tasks.

As above mentioned, the magnetic properties of BSA-AuNCs have not been investigated so far and, therefore, it is one of the aims of the present study. From the analysis of literature results [57–66], many NPs (mostly prepared using thiolate residues) comprising engineered Au(0) metal clusters give a wide range of magnetic behaviors (diamagnetic, Pauli paramagnetism, antiferro-, and ferromagnetic responses) that depend on the system size (1.8–4.4 nm), the metal's local symmetry, metal coordination environments, and unbalanced/charged states (neutral, positive, and negative metal–organic clusters). For example, the 25 gold (Au(0)) atoms NC stabilized by 18 thiolate ligands prepared by Zhu and co-authors ($Au_{25}(SR)_{18}$, with R = phenylethyl) shows, in frozen CH_2Cl_2/toluene solution at T = 8 K an EPR (Electron Paramagnetic Resonance) signal characteristic for $S = \frac{1}{2}$ systems with g-values consistent with an orthorhombic symmetry at 2.56(x), 2.36(y), and 1.82(z) [49]. Similarly, Agrachev and co-authors reported the phenylethanethiolate Au complex (neutral), $Au_{25}(SC_2Ph)_{18}$, encoding a radius of 13.2 Å, which also exhibits EPR signatures associated to spin $S = \frac{1}{2}$. The EPR spectrum of the complex at T = 5 K is rather broad (~200 mT) for $Au_{25}(SR)_{18}$ and anisotropic, with g-tensor components at 2.53 (x), 2.36 (y), and 1.82 (z) [67].

In this report, the authors used CW-EPR (Continuous Wave EPR), light-induced EPR (LEPR), HR-TEM, and STEM to thoroughly investigate the formation of BSA-AuNCs in a solution, which were intentionally prepared by Xie's type of synthesis [1]. So far, EPR has been employed for the investigation of the emerging magnetism of atomically precise AuNCs of different sizes (e.g., $Au_{25}(SR)_{18}$, $Au_{133}(TBBT)_{52}$), which were prepared by a multistep synthesis involving $NaBH_4$ as a reduction agent [5,6,49]. The EPR/LEPR study of BSA-AuNCs (further labelled as AuBSA in the present study to be directly distinguished from the other published results for BSA-AuNCs) is more complicated than the previous EPR studies of atomically precise AuNCs [5,6,49] because BSA alone reveals photochemically induced radicals' generation, which results in damages of the BSA structure and oxidation of cysteine and tryptophan residues [68,69]. Several years ago, Lassmann and coworkers [68] analyzed, using the LEPR technique, the formation of C and S radical centers

in BSA by UV-photolysis, especially thiyl (R-CH2-S•) and perthiyl radicals (R-CH2-S-S•), revealing that radiation damages are produced in the amino acid chain in a dose-dependent manner, i.e., the number of radicals increases by increasing the UV light irradiation time. The authors found that in bovine serum albumin (BSA) the thiyl radical (R-CH2-S•) exhibits axial anisotropy, with $g_{//} = 2.17$, $g_\perp = 2.008$, $\Delta B_{pp} = 1.8$ mT, pH = 7, $T = 80$ K) and the cysteine × HCl radical (phosphate buffer, pH = 3) shows similar features, with $g_{//} = 2.11$, $g_\perp = 2.011$, $\Delta B_{pp} = 3.2$ mT, $T = 80$ K). The $g_{//}$ component was always found to be very broad and weak, to the point that it becomes barely detectable, while the $g_\perp$ component gives the dominating, most intense signal. Together with the thiyl radicals, other types of radical species were demonstrated to form as well, which include perthiyl centres (R-CH2-S-S•) that exhibits rhombic character, and likewise, C-radical centers. In BSA (pH = 7, $T = 80$ K), EPR signals for the perthiyl specie show resonances at $g_1 = 2.057$, $g_2 = 2.027$, and $g_3 = 2.002$, while the C-radical species have $g_{avg} \sim 2.000$ [68].

Therefore, the main aim of this study is to thoroughly investigate the properties of the AuBSA system with the aid of selected techniques (EPR/LEPR, HR-TEM/STEM). The following key findings are presented: (i) redox processes take place upon entrapment of Au(III) in BSA, in which the protein backbone, in absence of other reducing equivalents, provide the electrons needed for Au(III) reduction; (ii) the Au uptake process by BSA in the solution occurs on two types of sites, i.e., cysteine (Cys) and oxygen/carboxylate donor residues (e.g., tyrosine, Tyr); (iii) the magnetic interaction among cationic forms of Au arises from an admixture of Au(0), Au(I), and Au(II); and (iv) UV irradiation of the AuBSA system induces irreversible damages, and radicals are generated in BSA upon UV light irradiation. It is disclosed that no energy transfer between entrapped Au clusters and the BSA protein occurs under photoexcitation, thus the photoluminescence phenomenon is governed by the intrinsic properties of the Au system (its size and the presence of various spin active redox states) and both variables equally matter. On the other hand, in view of the extended application of these materials in biomedical scenarios, correlation between their experimental parameters (e.g., concentration in solution) and cell's toxicity (with and upon photoexcitation) should be analyzed with great caution, because observation of an enhancement of toxic effects on cells by light irradiation might be hampered by light-induced radical's formation on the protein itself and not solely to the photoexcited states of the gold nanoassembly.

2. Materials and Methods

2.1. Chemicals

Bovine serum albumin (>98%, BSA), gold(III) chloride trihydrate ($HAuCl_4 \cdot 3H_2O$), and sodium hydroxide (NaOH) were purchased from Sigma-Aldrich (Saint Louis, MO, USA) and used as received (without any further purification) for all experiments. Deionized (DI) water prepared by purging Milli-Q purified water (Millipore Corp., Bedford, MA, USA) was used in all experiments.

2.2. Synthesis of AuBSA System

The procedure of our AuBSA system preparation was a slightly modified version of a method published by Xie et al. [1]. In a typical experiment, BSA solution (1 mL, 1 mM) was mixed with aqueous $HAuCl_4$ solution (1 mL, 10 mM) under vigorous stirring (600 rpm). After 90 s, NaOH solution (1 M) was added to obtain a basic environment (pH ≈ 12), which induced the reduction capability of BSA. Ninety seconds later, the mixed solution was heated up in a microwave oven for 10 s (power was set to 150 W). After 2 h of ageing at room temperature, the samples were dialyzed with a 12 kDa cut-off dialysis membrane against DI water. Dialysis was performed at room temperature for 24 h, with DI water being changed twice: once after one hour and then again after the second hour. Dialyzed samples were stored in the dark at room temperature.

2.3. Characterization of AuBSA System

Fluorescence measurements of AuNCs were performed on a JASCO F8500 (Jasco, Tokyo, Japan) spectrofluorometer using a 1 cm quartz cuvette and 2.5 nm slits. Emission spectra were measured in the range of 500–850 nm with the data interval of 1 nm and a scan speed of 100 nm/min. The excitation wavelength was set to 480 nm. Excitation-emission 3D maps were measured in the excitation range of 250–500 nm with the data interval of 2 nm and in the emission range of 250–850 nm with the data interval of 1 nm and a scan speed of 5000 nm/min (Figure 1). All spectra were corrected to avoid any deviations of instrumental components. Samples were diluted with DI water so that the protein concentration was 2 mg/mL for emission spectra and 0.25 mg/mL for excitation-emission 3D maps.
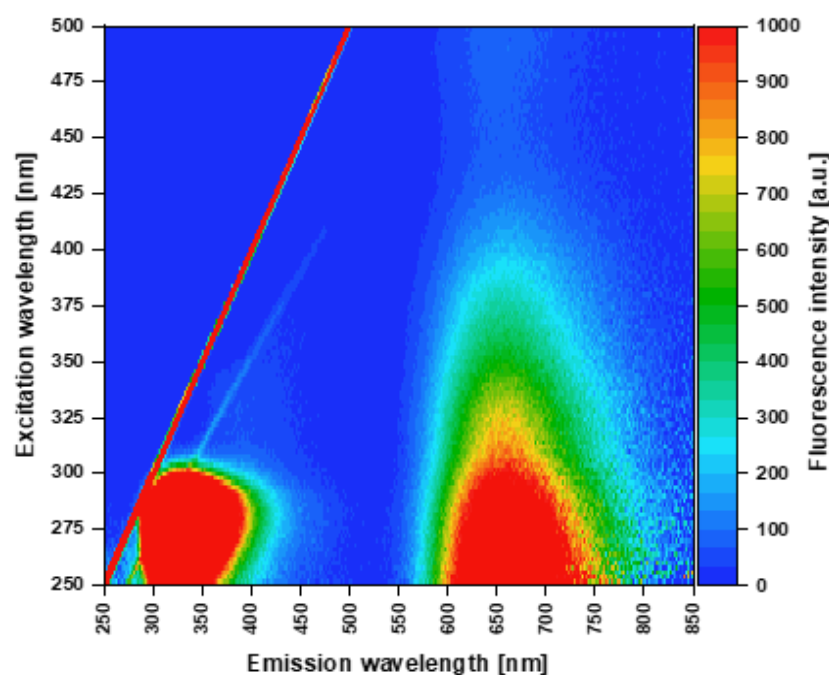
Figure 1. Fluorescence 3D excitation-emission map of AuBSA. Note: Strong Rayleigh (red line) and weak Raman (blue line) scattering first-order maxima are visible as straight lines in the map and represent artifacts that do not belong to AuBSA.

The quantum yield of fluorescence (QY, Φ) was calculated by the following equation:

$$\Phi = \Phi_s \cdot \frac{F \cdot \left(1 - 10^{-A_s}\right) \cdot n^2}{F_s \cdot \left(1 - 10^{-A}\right) \cdot n_s^2} \tag{1}$$

where F is the integrated fluorescence intensity, A is the absorbance, n is the index of refraction, and subscript s indicates the standard. DCM, 4-(dicyanomethylene)-2-methyl-6-(4-dimethylaminostyryl)-4H-pyran, dissolved in ethanol (99,8%, Lach-Ner, Neratovice, Czech Republic) was used as a standard ($\Phi_s = 0.437 \pm 0.024$) [70].

Absorbance was measured on a Specord 250 Plus—223G1032 (Analytik Jena, Jena, Germany) using a 1 cm quartz cuvette and double beam arrangement. As a reference, a 1 cm quartz cuvette filled with DI water was used.

CW-EPR spectra were recorded on a JEOL JES-X-320 spectrometer (JEOL, Tokyo, Japan) operating at the X-band frequency (~9.0–9.1 GHz) equipped with a variable-temperature controller (He, N2) ES-CT470 apparatus. The cavity quality factor (Q) was kept above 6000 in all measurements. Highly pure quartz tubes were employed (Suprasil, Wilmad, ≤0.5 OD), and accuracy on g-values was obtained against the Mn(II)/MgO standard (JEOL standard). The spectra were acquired by carefully monitoring that signal saturation from the applied microwave power did not occur during signal's acquisition. In situ light

excitation EPR experiments (LEPR) were performed using a HeCd laser source operating @325 nm (max cw power of 200 mW) from Kimmon Koha Co. Ltd. (Tokyo, Japan). The UV-light was shined directly onto the sample, kept frozen inside the cavity EPR resonator, through its dedicated optical window. The light-off to light-on process was operated by an on-off light-shutter mechanism. Filling factors were kept the same (200 μL) in all experiments. Experimental parameters used for all the EPR traces shown in Figure 2A:
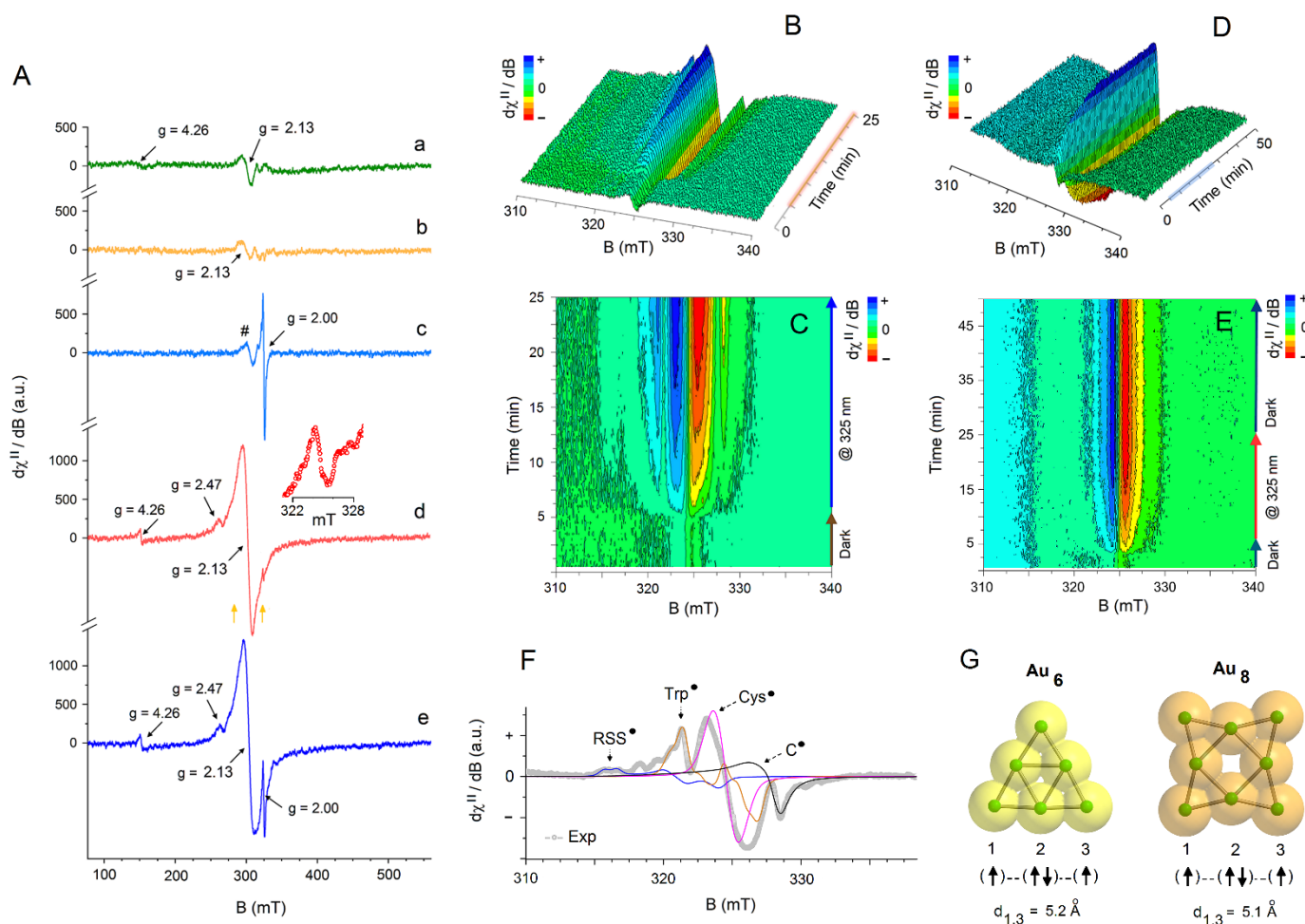
Figure 2. Panel (**A**) CW X-band Electron Paramagnetic Resonance (EPR) spectra recorded in water at *T* = 90 K under dark conditions of (a) HAuCl$_4$, (b) BSA, and (d) AuBSA. The LEPR spectra obtained under in situ UV irradiation (@325 nm, for 10 min) of the frozen matrix solutions for the various samples (*T* = 90 K) are given as trace (c) for BSA and trace (e) for AuBSA. Note that in trace (c), the symbol (#) indicates the region in which the g$_x$ component of the thyil radical (Cys•) in BSA is expected to be observed. The in situ 3D/2D LEPR experiment (*T* = 90 K, water) for BSA is shown in panel (**B**) and panel (**C**); panel (**D**) and panel (**E**) show the 3D/2D LEPR experiment for AuBSA. Panel (**F**) gives the experimental EPR spectrum (*T* = 90 K) together with computer simulations of the individual spin components obtained for neat BSA in water after 20 min of continuous UV irradiation. Panel (**G**) shows the structural organization of gold nanoclusters (Au$_6$ and Au$_8$) derived from DFT theory (neutral forms, coordinate files taken from ref. [67]) encoding the minimum dimensions for the Au nano-assemblies in BSA that are compatible with the distances calculated by EPR for a pair of spin–spin interacting Au(II)/Au(0) centers (labelled as 1,3).

9.0821–9.0878 GHz frequency, 100 kHz modulation frequency, 0.03 s time constant, 2.00 mW applied power, 1.0 mT modulation width, 4 min sweep time, and 3 scans accumulated and averaged. Cavity background was subtracted. Experimental parameters for the dark to light sequential EPR spectra shown in Figure 2B,C: *T* = 90 K, 9.0802 GHz

frequency, 100 kHz modulation frequency, 0.03 s time constant, 1.60 mW applied power, 0.5 mT modulation width, 30 s sweep time, and 5 min under dark followed by 20 min under light irradiation. Experimental parameters for the dark to light sequential EPR spectra shown in Figure 2D,E: *T* = 90 K, 9.0808 GHz frequency, 100 kHz modulation frequency, 0.03 s time constant, 1.60 mW applied power, 0.5 mT modulation width, 30 s sweep time, 5 min under dark conditions followed by 20 min under light irradiation, and then another 25 min under dark conditions. Experimental parameters for the EPR spectrum shown in Figure 2F: *T* = 90 K, 9.0802 GHz frequency, 100 kHz modulation frequency, 0.03 s time constant, 1.60 mW applied power, 0.5 mT modulation width, 1 min sweep time, and 5 scans accumulated and averaged. Cavity background subtracted.

HR-TEM measurements were independently performed by two different operators on two working places: (i) in the Regional Centre of Advanced Technologies and Materials (RCPTM) in Olomouc (Czech Republic) and (ii) in the Institute of Molecular Genetics (IMG) in Prague (Czech Republic). In both cases, AuBSA (the final protein concentration of 1 mg/mL) was drop-casted (2–4 μL) on glow discharged TEM copper grids covered with either a continuous 4-nm-thick carbon foil or lacey carbon and allowed them to dry spontaneously at room temperature. It is worth noting that for successful measurements, lacey carbon-copper grids (300 mesh) were used similarly as in ref. [37], and an electron beam was focused within the holes of the carbon film to obtain images of the protein-conjugated Au nanostructures without the interference of the carbon support (i.e., the measurements of samples deposited on 4-nm-thick carbon films were not successful). Then, the samples were measured by HR-TEM Titan G2 60–300 (FEI, Hillsboro, OR, USA) with an image corrector with an accelerating voltage of 300 kV in RCPTM. Images were taken with a BM UltraScan CCD camera (Gatan, Pleasanton, CA, USA). Energy Dispersive Spectrometry (EDS) was performed in STEM mode by a Super-X system with four silicon drift detectors (Bruker, Billerica, MA, USA). STEM images were taken with an HAADF detector 3000 (Fishione, Export, PA, USA). HAADF mode of STEM is intentionally used to better visualize NCs because heavier elements appear bright, while lighter elements appear dark. Imaging and data acquisition in IMG were performed with JEM-F200 TEM (JEOL, Tokyo, Japan) operated at 200 kV. TEM Images were acquired using an XF 416 CMOS camera (TVIPS, Gauting, Germany) and STEM images were acquired using the HAADF detector with a detecting angle of 24.4–89.4 mrad at a camera length set to 250 mm. EDS data were acquired using a JED 2300 X-ray spectrometer (JEOL, Tokyo, Japan) with a single 100 mm^2 (0.98 sr) windowless SDD detector. Presented elemental maps are calculated from the raw spectra using a standardless Zeta factor method embedded in the Jeol Analysis Station software.

3. Results and Discussion

3.1. Fluorescent Properties of AuBSA

Figure 1 displays characteristic fluorescent properties of AuBSA samples. According to the 3D excitation-emission fluorescence map (Figure 1), two distinct asymmetric excitation-emission maxima (EX/EM) with bathochromic tails appeared in the ultraviolet-visible (UV-vis) spectral region: 275/345 nm (EX/EM) and 275/655 nm (EX/EM). This is in accordance with our previous work [41] as well as with the fluorescent features of NCs prepared in a similar manner (see Table 1), i.e., using BSA simultaneously as a reductant of Au(III) precursors and a template for AuNCs formation. While the former EX/EM maximum and its bathochromic tail of a low intensity (being located at around 325/400 nm EX/EM) could be attributed to Trp and oxidized Tyr residues of BSA and/or blue-emissive small AuNCs, respectively; the latter intensive EX/EM maximum can stem from Au(x)-BSA, where x represents the oxidation state of gold reaching the values of 0, I, II, (proved in this study for the first time), and III. Obviously, AuBSA can be excited by employing any wavelength in the range of 250–500 nm, as clearly demonstrated in Figure 1.

The characteristic fluorescent spectrum of AuBSA (EX 480 nm) where the center of emission (positioned at 655 nm) is marked off is shown in Figure S1 in Supporting Information for the sake of a direct comparison with fluorescence spectra of AuNCs being

prepared by other authors using similar synthetic procedures (see Table 1). Namely, the visible excitations of fluorescent species serving as bio-imaging probes are preferred in practical applications because of the tissue optical window [71]. Fluorescence quantum yield (QY) of AuBSA was determined according to equation (1) and revealed the mean value of $6.7 \pm 0.1\%$ (details presented in Table S1 in Supporting Information) with respect to DCM dissolved in ethanol.

3.2. CW-EPR and LEPR Experiments and Analysis

To address in more details the electronic/magnetic characteristics of AuBSA, without and under in situ UV-light irradiation (@325 nm), CW-EPR and LEPR spectroscopic techniques were employed. In addition, as reference systems, the resonance fingerprints of $HAuCl_4$ (Au(III) precursor) dissolved in DI water, as well as the neat BSA protein (in DI water), were recorded under identical experimental conditions to unveil the electronic changes that might occur in the BSA protein after decoration/entrapment of Au; see Figure 2.

3.2.1. CW-EPR and LEPR Analysis of Precursors ($HAuCl_4$ and BSA)

Figure 2A (trace a) shows the X-band resonance signal acquired at $T = 90$ K in dark conditions of the aqueous solution of $HAuCl_4$ (8.1 mg/0.2 mL). As expected, the Au^{3+} cation does not show any strong EPR resonance signals, which agrees with the diamagnetic nature of its ground state electronic configuration ($[Xe]4f^{14}5d^8$). Only a very weak derivative signal emerges at $g_{iso} = 2.13$, which is superimposed to a broad dispersion signal extending over 100 mT that becomes visible above the background noise at a magnetic field higher than 300 mT. These weak resonances suggest that a small fraction of Au is present in the reduced forms, Au^0 ($[Xe]4f^{14}5d^{10}6s^1$) and/or Au^{2+} ($[Xe]4f^{14}5d^9$), in the hydrated Au^{3+} cations [72]. The additional resonance signal that appears in the low field region (Figure 2A, trace a), at $g = 4.26$, indicates that the reduced Au centers, Au^0 or Au^{2+}, are magnetically interacting, either via a direct or super-exchange pathway (e.g., O or OH- bridged $Au^{0/2+}$ dimers), forming aggregates with dimensions <1 nm, and giving an effective integer spin system in which the resonance signal at $g = 4.26$ represents the half-field transition ($\Delta m_s = 2$). Upon in situ irradiation by UV-light of the frozen $HAuCl_4$ aqueous solution at $T = 90$ K, no changes in the overall resonance envelope were observed (spectrum not shown).

Different behavior is recorded for BSA in water. The EPR resonance signal observed under dark conditions is shown in Figure 2A (trace b) ($T = 90$ K, neat BSA, 7.0 mg/0.2 mL in DI water). A cluster of very weak resonances develop just above the background noise at $g_{avg} = 2.13$. No other detectable high or low field resonance components are observed. These resonance signal originate from either not fully compensated cavity background noise, even after its subtraction from the sample resonance signal, or from the presence of the very minute inclusion of metal impurities in BSA, such as Cu^{2+} or low spin Fe^{3+}. During UV-light irradiation (Figure 2A, trace c) a strong signal immediately appears at $g_{iso} = 2.00$, which arises from radiation damages induced in the BSA protein. These spin containing sites are based on cysteine (Cys●), tryptophan (Trp●) moieties and other C-centred radicals (C●) [68,69].

In full agreement with previous literature reports [68], the authors observed the dynamic formation of the radical species in BSA during an UV light-off (5 min) to UV light-on (20 min) EPR signal acquisition sequence, as shown in the 3D reconstructed CW-EPR/LEPR resonance plot given in Figure 2B and in the 2D CW-EPR/LEPR plot in Figure 2C. Individual CW-EPR spectra were acquired under fast-scan detection mode (30 s acquisition time for each sequential resonance spectrum). The authors noticed that formation of thiyl, tryptophan and C-centered radicals represent the early oxidation events in BSA and start to form as soon as the UV light is applied to the frozen sample kept inside the cavity resonator. The perthiyl radicals (RSS●), on the other hand, develop much later in a slower process, after application of a much longer UV irradiation time (e.g., detected after 8 min of UV irradiation in the frozen water matrix at $T = 90$ K). Figure 2F shows a well-resolved EPR resonance signal recorded for BSA in water irradiated in situ

at 325 nm for 20 min at 90 K, which unveils the resonance features of the perthiyl radical (RSS•, g_x = 2.052, g_y = 2.018 g_z = 2.002) overlapped to tryptophan-based radicals (Trp•, $g_{y,z}$ = 2.003, g_x = 2.002, $A_N(xx,yy,zz)$ = 2.0 G, 2.0 G, 10.0 G; $A_{H\beta1}(xx,yy,zz)$ = 28.3 G, 28.3 G, 28.3 G; $A_{H\beta2}(xx,yy,zz)$ = 13.0 G, 13.0 G, 13.0 G). Note that the region around g = 2.000 clearly contains the overlapped resonance contributions of various spin species, but it is dominated by the $g_{y,z}$ components of the thiyl radical (Cys•, g_y = 2.003, g_z = 2.002) [68]. Unfortunately, the g_x component of this radical specie is expected to fall around 2.16–2.17 and it is known to be rather weak and broad; thus, its resonance feature remains obscured by the presence of clustered signals seen already in EPR spectrums recorded under dark conditions (see Figure 2A, trace b). Additional resonances are observed in the spectrum and originate from the hyperfine interactions of the electron spin moments of the radical species with the nuclear spin moments of hydrogen (^{1}H, I = 1/2, natural abundance 99.98%), nitrogen (^{14}N, I = 1, natural abundance 99.60%) and sulfur nuclei (^{33}S, I = 3/2, natural abundance 0.76%) present in cysteine (Cys) and tryptophan (Trp) amino acid residues. For simplicity, the detailed EPR simulation parameters used for plotting the various resonance envelopes of these spin species in BSA, shown in Figure 2F, are given in the Supporting Information (Figure S2). Therefore, a threshold of 10 min under UV-light irradiation time was used in the following analysis of AuBSA during photoexcitation, in agreement with the suggested irradiation time employed by Lassman and co-authors [68].

3.2.2. CW-EPR and LEPR Analysis of AuBSA

The resonance features of the AuBSA system are much different from those observed in neat BSA. Figure 2A (trace d) shows the EPR spectrum of the AuBSA recorded under dark conditions in DI water at T = 90 K (7.2 mg/0.2 mL). Unlike the EPR signatures shown earlier by neat BSA recorded under dark conditions (Figure 2A, trace b), AuBSA exhibits a strong derivative signal at g_{avg} = 2.13 (ΔB$_{pp}$ = 13 mT) with clear shoulders developing rather symmetrically at low and high magnetic fields: one absorption component at a g-value of 2.47 and a derivative component at low field, with a g-value of 4.26. All these resonance signals arise from spin containing Au centers. The intensity of the EPR resonances coming from Au centers in AuBSA (Figure 2A, trace d) significantly increased in comparison to those seen in the EPR spectrum of HAuCl$_4$ (Figure 2A, trace a); thus, a reduction process of Au(III) promoted by BSA takes place during protein incubation with the gold precursor, either to Au(I), Au(II), or to Au(0), in agreement with literature reports [1,10,16,41,73,74]. However, Au(I) is a diamagnetic cation and cannot produce the resonance features seen in the EPR spectrum. Moreover, the EPR spectrum shown in Figure 2A, trace (d), differs substantially from those reported for thiolate Au^0 nanoclusters [5,6,49,57–66].

According to literature data, the reduction process of Au(III) by BSA leads to the formation of gold nanoparticles (AuNCs) in which the BSA protein is directly interacting with metal centers through cysteine (Cys) and methionine (Met) residues. [3,74]. Furthermore, it is also expected that Tyr residues of BSA are the moieties that provide the electron equivalents needed for driving the Au(III) reduction process [1,41], and thus, these are the amino acids that undergo oxidation. Although very weak, at g ~ 2.00, the presence of organic radical signals in AuBSA emerges in the EPR spectrum, but its resolution could not be improved (Figure 2A, trace d, inset). In this framework, the authors performed a set of test-experiments where either Tyr and/or Cys molecules were incubated with Au(III) salt under the same experimental conditions used in AuBSA synthesis and the resulting systems (denoted as Au-Tyr, Au-Cys) were characterized by UV-vis extinction measurements and TEM imaging. The appearance of surface plasmon resonance (SPR) peak (around 525 nm), which is characteristic for AuNPs—see Figure S3A in Supporting Information—in the Au-Tyr system confirms the following results: (i) direct reduction of Au(III) to Au(0) by Tyr and (ii) key function of the BSA protein as a matrix/template in limiting the growth of the gold nanocluster during AuBSA synthesis. No SPR was detected in the UV-vis spectrum of Au-Cys. TEM images (Figure S3B,C in Supporting Information) give further evidence that AuNPs, of various sizes, are formed in the Au-Tyr system.

Based on the EPR results, it is suggested that while small, nanosized Au aggregates are indeed formed during the incubation and redox process between Au and BSA (size of Au nano-assembly estimated ~ 1 nm), an admixture of oxidation states of entrapped and clustered Au cations is indeed present. The authors speculate that the presence of both Au^{2+} and Au^0, together with the dominant Au^+ specie, is generated during the entrapment process of Au in BSA, in which a disproportionation event might occur in the nanocluster (NC), $2Au^+ \rightarrow Au^{2+} + Au^0$, following the initial electron delivery by BSA to Au^{3+} and reorganization of the electron distribution within the Au cluster in response to its anisotropic interactions with the BSA protein backbone. Thus, the weak signal at $g = 2.47$ and the more intense signal at $g = 2.13$ can be associated with the co-existence of two gold-based spin active species, Au^{2+} and Au^0. Moreover, the observed EPR features cannot simply be described, in our opinion, in terms of isolated $S = 1/2$ states, but rather to an admixture of doublets and triplet states. Simulated CW-EPR spectra of AuBSA in dark conditions are shown in Figure S4 in the Supporting Information. The transition observed at $g = 4.26$ may thus represent the half-field component ($\Delta m_s = 2$) of the $S = 1$ $Au^{0/2+}$ interacting species, having for the $\Delta m_s = 1$ transition a g_{eff} value of 2.13, as observed here. Assuming an axial zero-field-splitting for the high spin component of ~20.5 mT (see Figure 2A, trace d, the orange arrows indicate the estimated 2D), from a simple point dipole approximation [75], $|D|$ (MHz) $= 77{,}924 (g_{obs}/g_e)/r^3$, the through-space distance (r) between interacting $S = 1/2$ centers should fall at ~5.1 Å. The through-space distance derived from EPR analysis translates into the smallest dimension for the entrapped Au cluster in BSA of Au_6-Au_8 gold units. Figure 2G shows the density functional theory (DFT) calculated structures (neutral forms) [67] for an Au_6 (triangular) and Au_8 (4-fold edge-capped square) assemblies. From the EPR results, it is suggested that the Au(II)/Au(0) centers that are magnetically interacting to form the $S = 1$ system adopt the spin exchange coupling pathway Au(II)-Au(I)-Au(0), thus the spin containing sites Au(II)/Au(0) are located at the corners of the Au_6 or Au_8 nano assemblies. Such an assumption corresponds well with the early observations of Dixon and Egusa [3] who discovered that the maximum number of Au being incorporated into BSA is less than approximately 30 per BSA, but the minimum number of Au per BSA to yield red fluorescence is less than 7.

Upon in situ irradiation of AuBSA (10 min of UV-light irradiation) at $T = 90$ K, the overall EPR signatures addressable to the Au system did not change, both in intensity and overall signal-shape. However, the clear appearance of a resonance signal around $g = 2.00$ (Figure 2A, trace e) points towards the formation of radical species, as described above, in BSA. Most importantly, these spin containing centers that formed during UV irradiation do not appear to magnetically interact with the Au NCs; in fact, the intensity of the half-field component did not increase at all, and no other additional signals arising from a new admixture of high spin species become evident in the EPR spectrum. Therefore, these BSA radical centers (Cys•, Trp•, C•) formed during photoexcitation must involve sites that are far from the amino acid (Cys) residues that directly interact with the Au nano assemblies.

Further validation of the present findings was obtained upon following (via LEPR measurements) the in situ variation of the entire resonance line of AuBSA using an irradiation cycle of light-off to light-on and back to light-off cycle, as shown in the 3D reconstructed CW-EPR/LEPR resonance plot given in Figure 2D and in the 2D CW-EPR/LEPR plot in Figure 2E. Individual CW-EPR spectra were acquired similarly to those employed for neat BSA under fast-field scan detection mode (30 s acquisition time for each sequential resonance spectrum). The authors observed that after application of UV light, the radiation damages induced in the protein backbone in AuBSA are quickly triggered, likewise in the neat BSA system, but there is no clear impact on the EPR signals associated with the EPR signal associated to the gold species. Then, when UV light is turned off, no significant changes are observed in the radical canters of BSA (hence the protein damages are not reversible), nor changes in the EPR resonance features of the gold centers are seen. Therefore, there is no charge or energy transfer processes involved between AuNCs and

the BSA protein (at 90 K), although it is a process that, sometimes, becomes observable in BSA-AuNCs, as stated in literature reports [3,9,10]. Our finding supports the results of Yamamoto et al. [40], who discussed a high photo-stability of their BSA-Au$_{25}$NCs, albeit the authors are dealing with much smaller AuNCs (Au$_{6-8}$) in AuBSA as derived from EPR spectra analysis.

3.3. HR-TEM, STEM, and EDS Analysis of AuBSA

To directly visualize our NCs in AuBSA samples, HR-TEM and STEM analysis were performed. These techniques exploit electrons that represent reduction species par excellence. Therefore, by using electrons in studies of cationic metal-organic compounds (obviously our case), irreversible transformation (i.e., reduction) may occur. Consequently, the results of visualization cannot report on the initial nanomaterial, but on the transformed one, as already known from the literature [76].

EDS was performed on the places of holes in the lacey-carbon Cu grid covered by an AuBSA sample, similarly as in ref. [37]. It turned out that Au is well distributed along with S elements being attributed to the protein (Figure 3a). Figure 3b,c demonstrates STEM images of the same area on the AuBSA sample prior and after the scanning of EDS for several occasions, respectively. Red circles pinpoint the areas where the changes are the most apparent. Similarly, Figure 3d,e shows the same area of AuBSA prior and after the HR-TEM measurement being performed by using a higher magnification (i.e., higher density of electron beam). White ellipses emphasize different spots on the AuBSA sample in these two images—see Figure 3d,e. The authors can sum up that Au nanoparticles (NPs, sizes exceeding 2 nm) are formed by the focused electron beam if working with a higher magnification of HR-TEM and/or if using EDS mapping. Our observation can be a clue and indirectly confirms why there are discrepancies in sizes of fluorescent NCs presented in the literature (e.g., [3,4,42,54]) and summarized in Table 1. Another set of STEM images taken on the same AuBSA sample using a different HR-TEM/STEM machine (located at IMG in Prague) is shown in Figure S5 in Supporting Information. Independently, these additional measurements confirmed that it is possible to visualize NCs of sizes well below 2 nm without inducing their size modification. Moreover, based on TEM, HR-TEM, and STEM images, particle size distributions (PSD) were determined, and appropriate histograms are shown in Figure S6 in Supporting Information. The average AuNC sizes of 1.01 ± 0.24 nm and 1.18 ± 0.21 nm were derived from TEM and STEM images of AuBSA samples, respectively. On the other hand, the average AuNC size in the same AuBSA sample increased to 2.28 ± 0.63 nm after HR-TEM and/or EDS measurements. This corroborates the above-discussed observation about NPs in situ formation. Lattice planes of Au(111) and Au(200) were detected in NCs of AuBSA sample in a particular HR-TEM image as provided in Figure S7 in Supporting Information.

Furthermore, HR-TEM and STEM images of the same spot on the AuBSA sample are compared in Figure 3f,g. Indeed, the HR-TEM image (Figure 3f) was taken first, followed by STEM imaging (being recorded for a better contrast, Figure 3g). Red circles demonstrate the shifts of Au nanostructures, which migrated right after HR-TEM imaging. The observed Au NPs formation and their further migration upon HR-TEM imaging can be explained by considering the cationic state of Au in AuBSA (as determined by EPR measurements here) and reduction ability of electrons employed during TEM imaging. Indeed, Au(I) as well as Au(II) being attached to BSA, most probably through sulfur atoms (as evidenced by EPR and EDS in this study), can be reduced to Au(0). Since this Au(0) may be less strongly connected with the protein backbone than cationic Au in AuBSA, it can migrate on the carbon support of the TEM grid (which is more pronounced in cases of lacey-carbon rather than on 4-nm carbon coating of the Cu grid). By meeting other Au(0) atoms, they can coalesce and form larger Au nanostructures than NCs, i.e., NPs as evidenced in Figure 3c,e,g, and confirmed also by an increased value of average AuNC size (2.28 ± 0.63 nm). The above-mentioned observation of Au NPs formation and their migration during HR-TEM imaging could also explain why the difference in size of red and blue emitting systems in

ref. [4] was not as clear as expected. Logically, this supports the idea that AuNCs samples might be influenced by the interaction with the focused electron beam and the resulting images do not show the real structure of AuNCs. In other words, the presence of any cationic Au center (Au^+ and/or Au^{2+} and/or Au^{3+}) in BSA-AuNCs render such systems as being much more sensitive to techniques that use high energy electrons and/or X-ray irradiation and can explain the size and oxidation state discrepancies of Au nanoassembly in BSA-AuNCs found within the scientific literature (compared in Table 1).
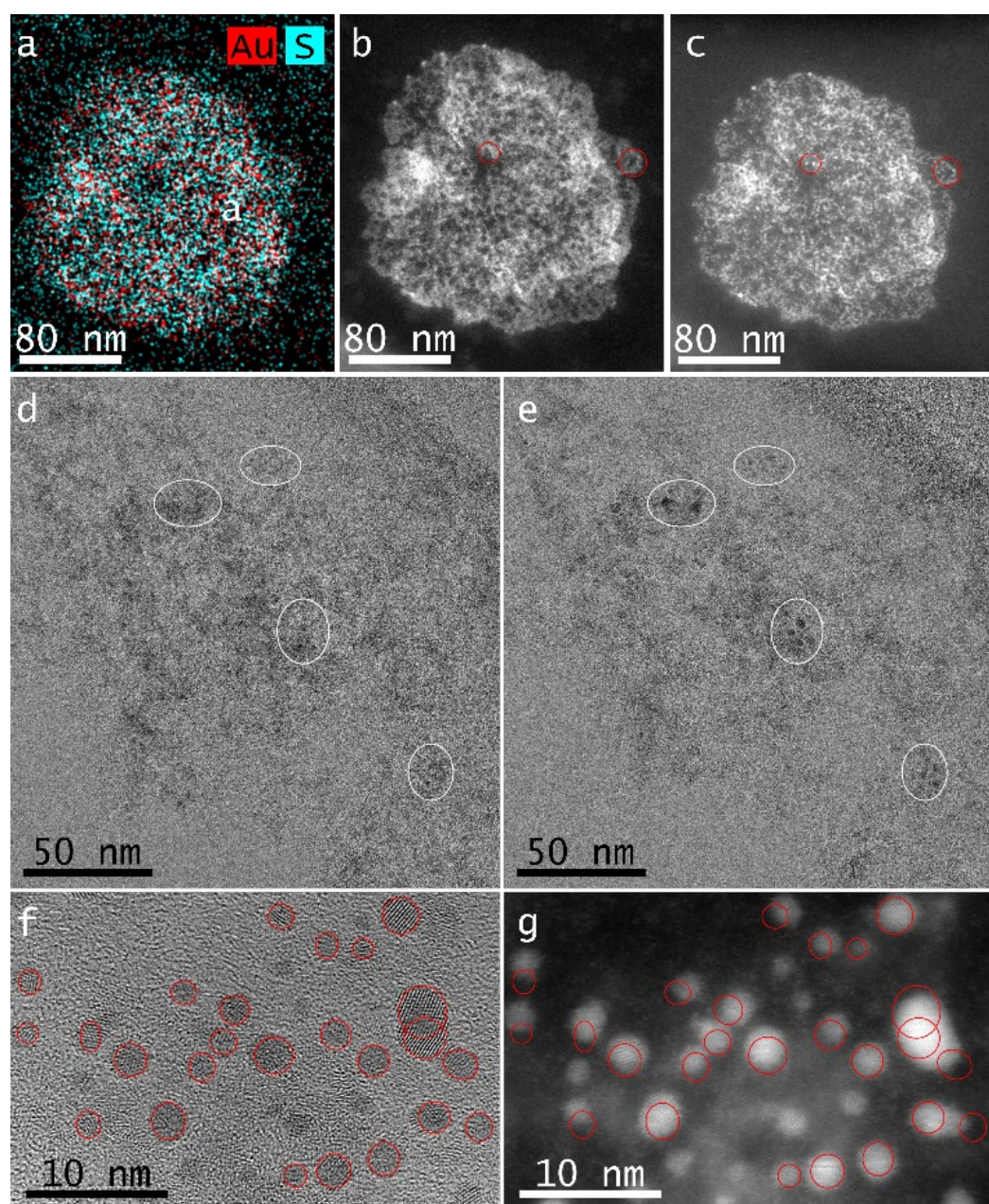
Figure 3. (**a**) Elemental map of Au and S distributions in AuBSA determined by EDS. STEM images of AuBSA prior (**b**) and after (**c**) the performed EDS analysis. HR-TEM images of the same area of AuBSA prior (**d**) and after (**e**) the exploitation of a higher magnification. HR-TEM (**f**) and STEM (**g**) images of the same spot on AuBSA. Colored and/or white circles indicate appearance of new NPs in (**b**–**e**) and/or migration of NPs in (**f**,**g**).

Based on our results, the authors would like to emphasize that results strongly depend on the type of experimental techniques employed for AuNCs characterization and

subsequent data interpretation. Many powerful experimental techniques frequently used for nanomaterials' characterization exploit electrons and/or are working with strong irradiation (X ray), thus affecting the electronic structure of the studied material, e.g., TEM, XAS, EDS, etc., respectively. On the contrary, EPR represents a mild technique which uses the magnetic field and microwave irradiation and, thus, can be envisaged as a very powerful technique suitable for probing AuBSA systems in particular, as well as BSA-AuNCs in general, because it does not physically alter the oxidation state of the nanomaterial in the course of data acquisition. Moreover, by using LEPR, any changes in the electronic structure of a particular nanomaterial exposed to electromagnetic irradiation (UV in our case here) can be investigated and evidenced in situ.

4. Conclusions

The present work demonstrates that a redox process that leads to an admixture of Au(0), Au(I), and Au(II) is taking place upon entrapment of Au(III) in BSA and several Au atoms of AuNCs are directly interacting through Cys and Tyr residues with BSA. The authors observed that Tyr molecules are able to reduce Au(III) to Au(0) in the form of AuNPs, while Cys did not provide the electron equivalents needed for the Au(III) reduction. It is also demonstrated that UV irradiation induces irreversible damages in AuBSA and radical species are generated during photoexcitation in the protein backbone. Since there is no evidence of electronic communication between AuNCs and BSA according to the LEPR experiments (in situ off-on-off cycles under UV light, at 90 K), any energy and/or charge transfer can be excluded as a key mechanism for expressing the bright fluorescence phenomenon observed, with maximum emission at 655 nm, in AuBSA. Furthermore, evidence was given for the in situ growth of AuNCs to AuNPs and migration of Au nanostructures during HR-TEM and EDS data acquisition. This work further reinforces the knowledge that results obtained by using sophisticated techniques exploiting electrons and/or X-ray irradiation in the investigation of gold nanostructures embedded in protein matrixes must be considered carefully, because the experimental evidence might be severely hampered by induced radiation damages on the protein structure.

Abbreviations

AuNCs: gold nanoclusters; AuBSA: abbreviation used in this study for the particular AuNCs embedded in BSA being prepared by the described synthetic procedure; BSA: bovine serum albumin; BSA-AuNCs: general abbreviation for AuNCs embedded in BSA being published within the scientific literature, i.e., regardless the consideration of the exact experimental conditions; CW-EPR: continuous wave electron paramagnetic resonance; DFT: density functional theory; EDS: energy dispersive X-ray analysis; EX/EM: excitation/emission; EXAFS: extended X-ray absorption fine structure; HAADF: high-angle annular dark field; HR-TEM: high resolution transmission electron microscopy; l-DOS: local density of states; LEPR: light-induced electron paramagnetic resonance; MS: mass spectrometry; MW: microwaves; NCs: nanoclusters; SPR: surface plasmon resonance; STEM: scanning transmission electron microscopy; UV: ultraviolet; vis: visible; XANES: X-ray absorption near-edge structure; XAS: X-ray absorption spectroscopy; XPS: X-ray photoelectron spectroscopy; XRD: X-ray diffraction.

References

1. Xie, J.; Zheng, Y.; Ying, J.Y. Protein-Directed Synthesis of Highly Fluorescent Gold Nanoclusters. *J. Am. Chem. Soc.* **2009**, *131*, 888–889. [CrossRef] [PubMed]
2. Simms, G.A.; Padmos, J.D.; Zhang, P. Structural and Electronic Properties of Protein/Thiolate-Protected Gold Nanocluster with "Staple" Motif: A XAS, L-DOS, and XPS Study. *J. Chem. Phys.* **2009**, *131*, 214703. [CrossRef]
3. Dixon, J.M.; Egusa, S. Conformational Change-Induced Fluorescence of Bovine Serum Albumin-Gold Complexes. *J. Am. Chem. Soc.* **2018**, *140*, 2265–2271. [CrossRef] [PubMed]
4. Chuang, K.T.; Lin, Y.W. Microwave-Assisted Formation of Gold Nanoclusters Capped in Bovine Serum Albumin and Exhibiting Red or Blue Emission. *J. Phys. Chem. C* **2017**, *121*, 26997–27003. [CrossRef]
5. Antonello, S.; Perera, N.V.; Ruzzi, M.; Gascón, J.A.; Maran, F. Interplay of Charge State, Lability, and Magnetism in the Molecule-like Au$_{25}$(SR)$_{18}$ Cluster. *J. Am. Chem. Soc.* **2013**, *135*, 15585–15594. [CrossRef] [PubMed]
6. Zeng, C.; Weitz, A.; Withers, G.; Higaki, T.; Zhao, S.; Chen, Y.; Gil, R.R.; Hendrich, M.; Jin, R. Controlling Magnetism of Au133(TBBT)52 Nanoclusters at Single Electron Level and Implication for Nonmetal to Metal Transition. *Chem. Sci.* **2019**, *10*, 9684–9691. [CrossRef] [PubMed]
7. Wen, X.; Yu, P.; Toh, Y.R.; Tang, J. Structure-Correlated Dual Fluorescent Bands in BSA-Protected Au$_{25}$ Nanoclusters. *J. Phys. Chem. C* **2012**, *116*, 11830–11836. [CrossRef]
8. Wen, X.; Yu, P.; Toh, Y.R.; Hsu, A.C.; Lee, Y.C.; Tang, J. Fluorescence Dynamics in BSA-Protected Au$_{25}$ Nanoclusters. *J. Phys. Chem. C* **2012**, *116*, 19032–19038. [CrossRef]
9. Raut, S.; Chib, R.; Butler, S.; Borejdo, J.; Gryczynski, Z.; Gryczynski, I. Evidence of Energy Transfer from Tryptophan to BSA/HSA Protected Gold Nanoclusters. *Methods Appl. Fluoresc.* **2014**, *2*, 035004. [CrossRef]
10. Russell, B.A.; Kubiak-Ossowska, K.; Mulheran, P.A.; Birch, D.J.S.; Chen, Y. Locating the Nucleation Sites for Protein Encapsulated Gold Nanoclusters: A Molecular Dynamics and Fluorescence Study. *Phys. Chem. Chem. Phys.* **2015**, *17*, 21935–21941. [CrossRef]
11. Chang, H.; Karan, N.S.; Shin, K.; Bootharaju, M.S.; Nah, S.; Chae, S.I.; Baek, W.; Lee, S.; Kim, J.; Son, Y.J.; et al. Highly Fluorescent Gold Cluster Assembly. *J. Am. Chem. Soc.* **2021**, *143*, 326–334. [CrossRef] [PubMed]
12. Cao, X.L.; Li, H.W.; Yue, Y.; Wu, Y. PH-Induced Conformational Changes of BSA in Fluorescent AuNCs@BSA and Its Effects on NCs Emission. *Vib. Spectrosc.* **2013**, *65*, 186–192. [CrossRef]
13. Cui, M.; Zhao, Y.; Song, Q. Synthesis, Optical Properties and Applications of Ultra-Small Luminescent Gold Nanoclusters. *TrAC—Trends Anal. Chem.* **2014**, *57*, 73–82. [CrossRef]
14. Bhowal, A.C.; Pandit, S.; Kundu, S. Fluorescence Emission and Interaction Mechanism of Protein-Coated Gold and Copper Nanoclusters as Ion Sensors in Different Ionic Environments. *J. Phys. D. Appl. Phys.* **2019**, *52*, 015302. [CrossRef]
15. Hsu, N.Y.; Lin, Y.W. Microwave-Assisted Synthesis of Bovine Serum Albumin-Gold Nanoclusters and Their Fluorescence-Quenched Sensing of Hg2+ Ions. *New J. Chem.* **2016**, *40*, 1155–1161. [CrossRef]

16. Lin, H.; Imakita, K.; Fujii, M.; Sun, C.; Chen, B.; Kanno, T.; Sugimoto, H. New Insights into the Red Luminescent Bovine Serum Albumin Conjugated Gold Nanospecies. *J. Alloys Compd.* **2017**, *691*, 860–865. [CrossRef]
17. Chib, R.; Butler, S.; Raut, S.; Shah, S.; Borejdo, J.; Gryczynski, Z.; Gryczynski, I. Effect of Quencher, Denaturants, Temperature and PH on the Fluorescent Properties of BSA Protected Gold Nanoclusters. *J. Lumin.* **2015**, *168*, 62–68. [CrossRef]
18. Kawasaki, H.; Hamaguchi, K.; Osaka, I.; Arakawa, R. Ph-Dependent Synthesis of Pepsin-Mediated Gold Nanoclusters with Blue Green and Red Fluorescent Emission. *Adv. Funct. Mater.* **2011**, *21*, 3508–3515. [CrossRef]
19. Liu, J.; Duchesne, P.N.; Yu, M.; Jiang, X.; Ning, X.; Vinluan, R.D., III; Zhang, P.; Zheng, J. Luminescent Gold Nanoparticles with Size-Independent Emission. *Angew. Chem.* **2016**, *128*, 9040–9044. [CrossRef]
20. Liu, C.; Zhang, X.; Han, X.; Fang, Y.; Liu, X.; Wang, X.; Waterhouse, G.I.N.; Xu, C.; Yin, H.; Gao, X. Polypeptide-Templated Au Nanoclusters with Red and Blue Fluorescence Emissions for Multimodal Imaging of Cell Nuclei. *ACS Appl. Bio Mater.* **2020**, *3*, 1934–1943. [CrossRef]
21. Shang, L.; Stockmar, F.; Azadfar, N.; Nienhaus, G.U. Intracellular Thermometry by Using Fluorescent Gold Nanoclusters. *Angew. Chem. Int. Ed.* **2013**, *52*, 11154–11157. [CrossRef] [PubMed]
22. Wei, Z.; Pan, Y.; Hou, G.; Ran, X.; Chi, Z.; He, Y.; Kuang, Y.; Wang, X.; Liu, R.; Guo, L. Excellent Multiphoton Excitation Fluorescence with Large Multiphoton Absorption Cross Sections of Arginine-Modified Gold Nanoclusters for Bioimaging. *ACS Appl. Mater. Interfaces* **2022**, *14*, 2452–2463. [CrossRef] [PubMed]
23. Wen, F.; Dong, Y.; Feng, L.; Wang, S.; Zhang, S.; Zhang, X. Horseradish Peroxidase Functionalized Fluorescent Gold Nanoclusters for Hydrogen Peroxide Sensing. *Anal. Chem.* **2011**, *83*, 1193–1196. [CrossRef] [PubMed]
24. Wu, Z. Anti-Galvanic Reduction of Thiolate-Protected Gold and Silver Nanoparticles. *Angew. Chem.* **2012**, *51*, 2934–2938. [CrossRef] [PubMed]
25. Wu, Z.; Jin, R. On the Ligand's Role in the Fluorescence of Gold Nanoclusters. *Nano Lett.* **2010**, *10*, 2568–2573. [CrossRef]
26. Wu, Y.T.; Shanmugam, C.; Tseng, W.B.; Hiseh, M.M.; Tseng, W.L. A Gold Nanocluster-Based Fluorescent Probe for Simultaneous PH and Temperature Sensing and Its Application to Cellular Imaging and Logic Gates. *Nanoscale* **2016**, *8*, 11210–11216. [CrossRef]
27. Xu, Y.; Sherwood, J.; Qin, Y.; Crowley, D.; Bonizzoni, M.; Bao, Y. The Role of Protein Characteristics in the Formation and Fluorescence of Au Nanoclusters. *Nanoscale* **2014**, *6*, 1515–1524. [CrossRef]
28. Yue, Y.; Liu, T.Y.; Li, H.W.; Liu, Z.; Wu, Y. Microwave-Assisted Synthesis of BSA-Protected Small Gold Nanoclusters and Their Fluorescence-Enhanced Sensing of Silver(i) Ions. *Nanoscale* **2012**, *4*, 2251–2254. [CrossRef]
29. Yue, Y.; Li, H.W.; Liu, T.Y.; Wu, Y. Exploring the Role of Ligand-BSA in the Response of BSA-Protected Gold-Nanoclusters to Silver (I) Ions by FT-IR and Circular Dichroism Spectra. *Vib. Spectrosc.* **2014**, *74*, 137–141. [CrossRef]
30. Zhang, M.; Dang, Y.Q.; Liu, T.Y.; Li, H.W.; Wu, Y.; Li, Q.; Wang, K.; Zou, B. Pressure-Induced Fluorescence Enhancement of the BSA-Protected Gold Nanoclusters and the Corresponding Conformational Changes of Protein. *J. Phys. Chem. C* **2013**, *117*, 639–647. [CrossRef]
31. Zhou, M.; Du, X.; Wang, H.; Jin, R. The Critical Number of Gold Atoms for a Metallic State Nanocluster: Resolving a Decades-Long Question. *ACS Nano* **2021**, *15*, 13980–13992. [CrossRef] [PubMed]
32. Govindaraju, S.; Ankireddy, S.R.; Viswanath, B.; Kim, J.; Yun, K. Fluorescent Gold Nanoclusters for Selective Detection of Dopamine in Cerebrospinal Fluid. *Sci. Rep.* **2017**, *7*, 1–12. [CrossRef] [PubMed]
33. Chang, T.K.; Cheng, T.M.; Chu, H.L.; Tan, S.H.; Kuo, J.C.; Hsu, P.H.; Su, C.Y.; Chen, H.M.; Lee, C.M.; Kuo, T.R. Metabolic Mechanism Investigation of Antibacterial Active Cysteine-Conjugated Gold Nanoclusters in Escherichia Coli. *ACS Sustain. Chem. Eng.* **2019**, *7*, 15479–15486. [CrossRef]
34. Le Guével, X.; Hötzer, B.; Jung, G.; Hollemeyer, K.; Trouillet, V.; Schneider, M. Formation of Fluorescent Metal (Au, Ag) Nanoclusters Capped in Bovine Serum Albumin Followed by Fluorescence and Spectroscopy. *J. Phys. Chem. C* **2011**, *115*, 10955–10963. [CrossRef]
35. Li, H.W.; Yue, Y.; Liu, T.Y.; Li, D.; Wu, Y. Fluorescence-Enhanced Sensing Mechanism of BSA-Protected Small Gold-Nanoclusters to Silver(I) Ions in Aqueous Solutions. *J. Phys. Chem. C* **2013**, *117*, 16159–16165. [CrossRef]
36. Wang, X.; Wu, P.; Hou, X.; Lv, Y. An Ascorbic Acid Sensor Based on Protein-Modified Au Nanoclusters. *Analyst* **2013**, *138*, 229–233. [CrossRef]
37. Burt, J.L.; Gutiérrez-Wing, C.; Miki-Yoshida, M.; José-Yacamán, M. Noble-Metal Nanoparticles Directly Conjugated to Globular Proteins. *Langmuir* **2004**, *20*, 11778–11783. [CrossRef]
38. Zhang, L.; Wang, E. Metal Nanoclusters: New Fluorescent Probes for Sensors and Bioimaging. *Nano Today* **2014**, *9*, 132–157. [CrossRef]
39. Zheng, J.; Zhou, C.; Yu, M.; Liu, J. Different Sized Luminescent Gold Nanoparticles. *Nanoscale* **2012**, *4*, 4073–4083. [CrossRef]
40. Yamamoto, M.; Osaka, I.; Yamashita, K.; Hasegawa, H.; Arakawa, R.; Kawasaki, H. Effects of Ligand Species and Cluster Size of Biomolecule-Protected Au Nanoclusters on Eff Iciency of Singlet-Oxygen Generation. *J. Lumin.* **2016**, *180*, 315–320. [CrossRef]
41. Andrýsková, P.; Šišková, K.M.; Michetschlägerová, Š.; Jiráková, K.; Kubala, M.; Jirák, D. The Effect of Fatty Acids and Bsa Purity on Synthesis and Properties of Fluorescent Gold Nanoclusters. *Nanomaterials* **2020**, *10*, 343. [CrossRef] [PubMed]
42. Yan, L.; Cai, Y.; Zheng, B.; Yuan, H.; Guo, Y.; Xiao, D.; Choi, M.M.F. Microwave-Assisted Synthesis of BSA-Stabilized and HSA-Protected Gold Nanoclusters with Red Emission. *J. Mater. Chem.* **2012**, *22*, 1000–1005. [CrossRef]
43. Shang, L.; Dong, S.; Nienhaus, G.U. Ultra-Small Fluorescent Metal Nanoclusters: Synthesis and Biological Applications. *Nano Today* **2011**, *6*, 401–418. [CrossRef]

44. Sonia; Komal; Kukreti, S.; Kaushik, M. Gold Nanoclusters: An Ultrasmall Platform for Multifaceted Applications. *Talanta* **2021**, *234*, 122623. [CrossRef]

45. Nienhaus, K.; Wang, H.; Nienhaus, G.U. Nanoparticles for Biomedical Applications: Exploring and Exploiting Molecular Interactions at the Nano-Bio Interface. *Mater. Today Adv.* **2020**, *5*, 100036. [CrossRef]

46. Zheng, Y.; Lai, L.; Liu, W.; Jiang, H.; Wang, X. Recent Advances in Biomedical Applications of Fluorescent Gold Nanoclusters. *Adv. Colloid Interface Sci.* **2017**, *242*, 1–16. [CrossRef] [PubMed]

47. Zhu, M.; Aikens, C.M.; Hollander, F.J.; Schatz, G.C.; Jin, R. Correlating the Crystal Structure of A Thiol-Protected Au$_{25}$ Cluster and Optical Properties. *J. Am. Chem. Soc.* **2008**, *130*, 5883–5885. [CrossRef]

48. Zhu, M.; Lanni, E.; Garg, N.; Bier, M.E.; Jin, R. Kinetically Controlled, High-Yield Synthesis of Au$_{25}$ Clusters. *J. Am. Chem. Soc.* **2008**, *130*, 1138–1139. [CrossRef]

49. Zhu, M.; Aikens, C.M.; Hendrich, M.P.; Gupta, R.; Qian, H.; Schatz, G.C.; Jin, R. Reversible Switching of Magnetism in Thiolate-Protected Au$_{25}$ Superatoms. *J. Am. Chem. Soc.* **2009**, *131*, 2490–2492. [CrossRef]

50. Schmidbaur, H. The Aurophilicity Phenomenon: A Decade of Experimental Findings, Theoretical Concepts and Emerging Applications. *Gold Bull.* **2000**, *33*, 3–10. [CrossRef]

51. Schmidbaur, H.; Schier, A. A Briefing on Aurophilicity. *Chem. Soc. Rev.* **2008**, *37*, 1931–1951. [CrossRef] [PubMed]

52. Schmidbaur, H.; Schier, A. Aurophilic Interactions as a Subject of Current Research: An up-Date. *Chem. Soc. Rev.* **2012**, *41*, 370–412. [CrossRef] [PubMed]

53. Wu, Z.; Du, Y.; Liu, J.; Yao, Q.; Chen, T.; Cao, Y.; Zhang, H.; Xie, J. Aurophilic Interactions in the Self-Assembly of Gold Nanoclusters into Nanoribbons with Enhanced Luminescence. *Angew. Chem. Int. Ed.* **2019**, *58*, 8139–8144. [CrossRef] [PubMed]

54. Rehman, F.U.; Du, T.; Shaikh, S.; Jiang, X.; Chen, Y.; Li, X.; Yi, H.; Hui, J.; Chen, B.; Selke, M.; et al. Nano in Nano: Biosynthesized Gold and Iron Nanoclusters Cargo Neoplastic Exosomes for Cancer Status Biomarking. *Nanomed. Nanotechnol. Biol. Med.* **2018**, *14*, 2619–2631. [CrossRef]

55. Fernández-Iglesias, N.; Bettmer, J. Synthesis, Purification and Mass Spectrometric Characterisation of a Fluorescent Au9@BSA Nanocluster and Its Enzymatic Digestion by Trypsin. *Nanoscale* **2014**, *6*, 716–721. [CrossRef]

56. Mathew, M.S.; Baksi, A.; Pradeep, T.; Joseph, K. Choline-Induced Selective Fluorescence Quenching of Acetylcholinesterase Conjugated Au@BSA Clusters. *Biosens. Bioelectron.* **2016**, *81*, 68–74. [CrossRef]

57. Hori, H.; Teranishi, T.; Nakae, Y.; Seino, Y.; Miyake, M.; Yamada, S. Anomalous Magnetic Polarization Effect of Pd and Au Nano-Particles. *Phys. Lett. Sect. A Gen. At. Solid State Phys.* **1999**, *263*, 406–410. [CrossRef]

58. Brust, M.; Walker, M.; Bethell, D.; Schiffrin, D.J.; Whyman, R. Synthesis of Thiol-Derivatised Gold Nanoparticles in a Two-Phase Liquid-Liquid System. *J. Chem. Soc. Chem. Commun.* **1994**, *7*, 801–802. [CrossRef]

59. Gréget, R.; Nealon, G.; Vileno, B.; Turek, P.; Mény, C.; Ott, F.; Derory, A.; Voirin, E.; Rivière, E.; Rogalev, A.; et al. Magnetic Properties of Gold Nanoparticles A Room-Temperature Quantum Effect. *ChemPhysChem* **2012**, *13*, 3092–3097. [CrossRef]

60. Muñoz-Márquez, M.A.; Guerrero, E.; Fernández, A.; Crespo, P.; Hernando, A.; Lucena, R.; Conesa, J.C. Permanent Magnetism in Phosphine- and Chlorine-Capped Gold: From Clusters to Nanoparticles. *J. Nanoparticle Res.* **2010**, *12*, 1307–1318. [CrossRef]

61. Crespo, P.; García, M.A.; Fernández Pinel, E.; Multigner, M.; Alcántara, D.; De La Fuente, J.M.; Penadés, S.; Hernando, A. Fe Impurities Weaken the Ferromagnetic Behavior in Au Nanoparticles. *Phys. Rev. Lett.* **2006**, *97*, 1–4. [CrossRef] [PubMed]

62. Cirri, A.; Silakov, A.; Jensen, L.; Lear, B.J. Probing Ligand-Induced Modulation of Metallic States in Small Gold Nanoparticles Using Conduction Electron Spin Resonance. *Phys. Chem. Chem. Phys.* **2016**, *18*, 25443–25451. [CrossRef] [PubMed]

63. Donnio, B.; García-Vázquez, P.; Gallani, J.-L.; Guillon, D.; Terazzi, E. Dendronized Ferromagnetic Gold Nanoparticles Self-Organized in a Thermotropic Cubic Phase. *Adv. Mater.* **2007**, *19*, 3534–3539. [CrossRef]

64. Cirri, A.; Silakov, A.; Lear, B.J. Ligand Control over the Electronic Properties within the Metallic Core of Gold Nanoparticles. *Angew. Chem. Int. Ed.* **2015**, *54*, 11750–11753. [CrossRef] [PubMed]

65. Yamamoto, Y.; Miura, T.; Suzuki, M.; Kawamura, N.; Miyagawa, H.; Nakamura, T.; Kobayashi, K.; Teranishi, T.; Hori, H. Direct Observation of Ferromagnetic Spin Polarization in Gold Nanoparticles. *Phys. Rev. Lett.* **2004**, *93*, 1–4. [CrossRef] [PubMed]

66. Cirri, A.; Silakov, A.; Jensen, L.; Lear, B.J. Chain Length and Solvent Control over the Electronic Properties of Alkanethiolate-Protected Gold Nanoparticles at the Molecule-to-Metal Transition. *J. Am. Chem. Soc.* **2016**, *138*, 15987–15993. [CrossRef]

67. Agrachev, M.; Antonello, S.; Dainese, T.; Ruzzi, M.; Zoleo, A.; Aprà, E.; Govind, N.; Fortunelli, A.; Sementa, L.; Maran, F. Magnetic Ordering in Gold Nanoclusters. *ACS Omega* **2017**, *2*, 2607–2617. [CrossRef]

68. Lassmann, G.; Kolberg, M.; Bleifuss, G.; Gräslund, A.; Sjöberg, B.M.; Lubitz, W. Protein Thiyl Radicals in Disordered Systems: A Comparative Epr Study at Low Temperature. *Phys. Chem. Chem. Phys.* **2003**, *5*, 2442–2453. [CrossRef]

69. Silvester Julie, A.; Timmins Graham, S.D. Photodynamically Generated Bovine Serum Albumin Radicals: Evidence for Damage Transfer and Oxidation at Cysteine and Tryptophan Residues. *Free Radic. Biol. Med.* **1998**, *24*, 754–766. [CrossRef]

70. Rurack, K.; Spieles, M. Fluorescence Quantum Yields of a Series of Red and Near-Infrared Dyes Emitting at 600–1000 Nm. *Anal. Chem.* **2011**, *83*, 1232–1242. [CrossRef]

71. Lyons, S.K.; Patrick, P.S.; Brindle, K.M. Imaging Mouse Cancer Models in Vivo Using Reporter Transgenes. *Cold Spring Harb. Protoc.* **2013**, *2013*, 685–699. [CrossRef] [PubMed]

72. Nealon, G.L.; Donnio, B.; Greget, R.; Kappler, J.P.; Terazzi, E.; Gallani, J.L. Magnetism in Gold Nanoparticles. *Nanoscale* **2012**, *4*, 5244–5258. [CrossRef] [PubMed]

73. Chevrier, D.M.; Thanthirige, V.D.; Luo, Z.; Driscoll, S.; Cho, P.; Macdonald, M.A.; Yao, Q.; Guda, R.; Xie, J.; Johnson, E.R.; et al. Structure and Formation of Highly Luminescent Protein-Stabilized Gold Clusters. *Chem. Sci.* **2018**, *9*, 2782–2790. [CrossRef] [PubMed]
74. Hsu, Y.C.; Hung, M.J.; Chen, Y.A.; Wang, T.F.; Ou, Y.R.; Chen, S.H. Identifying Reducing and Capping Sites of Protein-Encapsulated Gold Nanoclusters. *Molecules* **2019**, *24*, 1630. [CrossRef] [PubMed]
75. Anderson, P.W. New Approach to the Theory of Superexchange Interactions. *Career Theor. Phys. A 2nd Ed.* **2005**, *115*, 100–111. [CrossRef]
76. Andres, J.; Longo, E.; Gouveia, A.F.; Gracia, L.; Oliveira, M.C. In Situ Formation of Metal Nanoparticles through Electron Beam Irradiation: Modeling Real Materials from First-Principles Calculations. *J. Mater. Sci. Eng.* **2018**, *7*, 3. [CrossRef]

Evidence of Au(II) and Au(0) States in Bovine Serum Albumin-Au Nanoclusters Revealed by CW-EPR/LEPR and Peculiarities in HR-TEM/STEM Imaging

Radek Ostruszka [1], Giorgio Zoppellaro [2,*], Ondřej Tomanec [2], Dominik Pinkas [3], Vlada Filimonenko [3] and Karolína Šišková [1,*]

[1] Department of Experimental Physics, Faculty of Science, Palacký University, tř. 17.listopadu 12, 77900 Olomouc, Czech Republic; radek.ostruszka@upol.cz

[2] Regional Centre of Advanced Technologies and Materials, Faculty of Science, Palacký University, tř. 17.listopadu 12, 77900 Olomouc, Czech Republic; ondrej.tomanec@upol.cz

[3] Institute of Molecular Genetics of the Czech Academy of Sciences, Microscopy Centre, Electron Microscopy Core Facility, Vídeňská 1083, 142 20 Prague 4, Czech Republic; dominik.pinkas@img.cas.cz (D.P.); vlada.filimonenko@img.cas.cz (V.F.)

*   Correspondence: giorgio.zoppellaro@upol.cz (G.Z.); karolina.siskova@upol.cz (K.Š.)
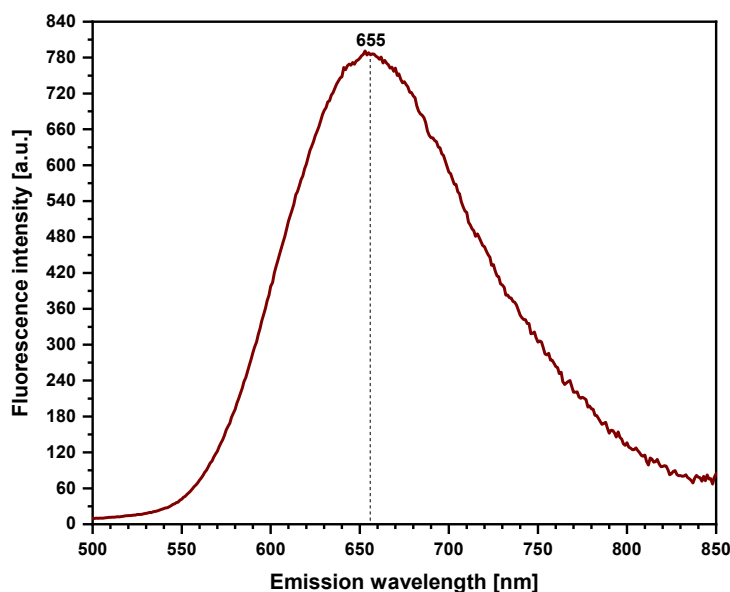
Figure S1. Corrected emission spectrum of AuBSA in deionized water.

Table S1. Quantum yield and wavelength of fluorescence maximum of AuBSA.

Sample	Absorbance	Quantum Yield [%]	Wavelength of Fluorescence Maximum [nm]
AuBSA I	0.0425	6.72	655
AuBSA II	0.0453	6.57	654
AuBSA III	0.0435	6.68	655
Average	0.0438	6.7	655
Standard Deviation	0.0014	0.1	1

Note: Quantum yields were calculated from corrected emission spectra and with respect to DCM dissolved in ethanol. DCM in ethanol was chosen as a standard due to the fact that it reveals a very similar excitation wavelength and fluorescence emission profile as AuBSA.

EPR Data treatments. Simulation of the powder EPR spectrum was performed with the WinEPR SimFonia software (V.1.25, EPR Division, Bruker Instruments, Inc., Billerica, USA) using second-order perturbation theory and spherical integration (grid) of 200 (theta), 200 (phi).
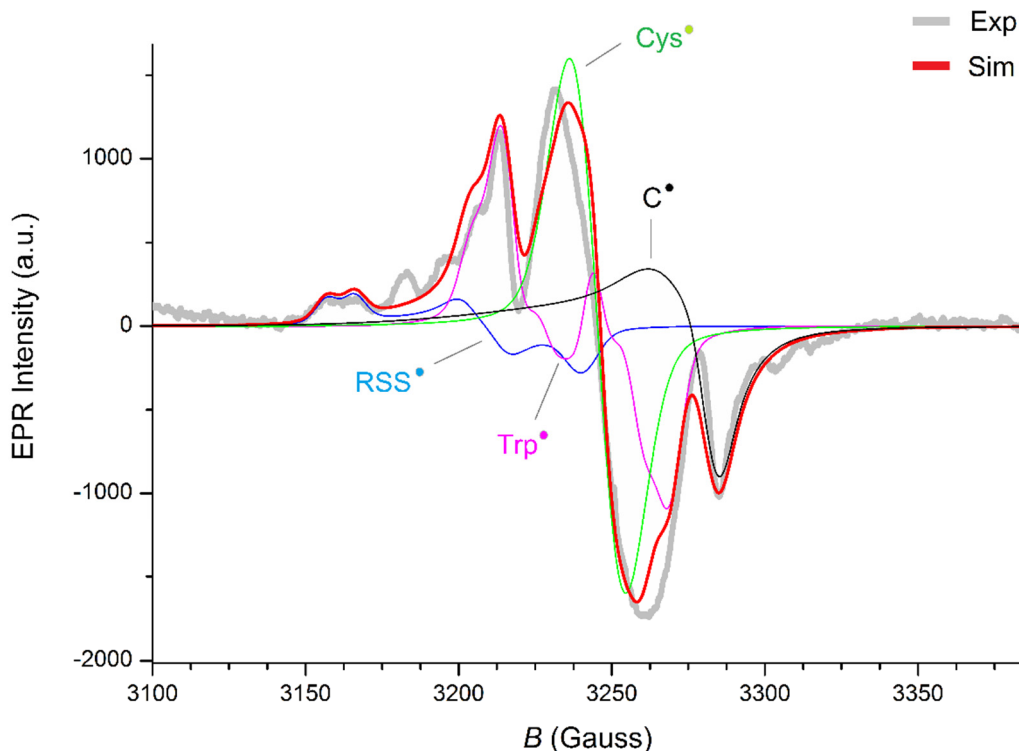
Figure S2. CW-EPR spectrum obtained after 20 min of UV irradiation of BSA in water. Experimental parameters: $T = 90$ K, 9.0802 GHz frequency, 100kHz modulation frequency, 0.03 s time constant, 1.60 mW applied power, 0.5 mT modulation width, 6 × 100 Gain, 1 min sweep time, and 5 scans accumulated and averaged. The simulation of the various spin components is shown together with their sum (red-line).

Doublet specie, $S = 1/2$, tryptophan radical (Trp•). $g_x = 2.002$, $g_y = 2.003$, $g_z = 2.003$. A_N (xx,yy,zz) = 2.0, G, 2.0 G, 10.0 G; $A_{H\beta1}$ (xx,yy,zz) = 28.3, G, 28.3 G, 28.3 G; $A_{H\beta2}$ (xx,yy,zz) = = 13.0, G, 13.0 G, 13.0 G Line-width tensor (x,y,z) = 9.0 G, 9.0 G, 9.0 G. Lorentzian/Gaussian ratio = 0.8. Relative intensity weight = 30.1%

Doublet specie, $S = 1/2$, perthiyl radical (RSS•). $g_x = 2.052$, $g_y = 2.018$, $g_z = 2.002$. Line-width tensor (x,y,z) = 7.0 G, 9.0 G, 9.0 G. Lorentzian/Gaussian ratio = 0.8. Relative intensity weight = 7.1%

Doublet specie, $S = 1/2$, thiyl radical (Cys•). $g_x = 2.17$, $g_y = 2.003$, $g_z = 2.002$. Line-width tensor (x,y,z) = 16.0 G, 16.0 G, 16.0 G. Lorentzian/Gaussian ratio = 0.8. Relative intensity weight = 40.2%

Doublet specie, $S = 1/2$, C-based radical (C•). $g_x = 2.012$, $g_y = 1.984$, $g_z = 1.977$, $g_{avg} = 1.991$. Line-width tensor (x,y,z) = 60.0 G, 16.0 G, 6.0 G. Lorentzian/Gaussian ratio = 0.8. Relative intensity weight = 22.6%

Preparation of Au-Tyr and Au-Cys: 1 mL solutions of Tyr and/or Cys (12.6 mM and/or 21.1 mM, respectively) were mixed with $HAuCl_4$ (10 mM, 1 mL) under vigorous stirring (600 rpm) after 90 s followed by NaOH addition (1 M, 200 μL), and after another 90 s, microwave heating was applied (10 s, power set to 150 W) as in the case of AuBSA preparation.

UV-vis absorption spectra of Au-Tyr and Au-Cys were then recorded, and the kinetics of potential surface plasmon resonance peak at around 525 nm was followed in the period ranging between 0 and 61.75 mins elapsed from the microwave heating application.
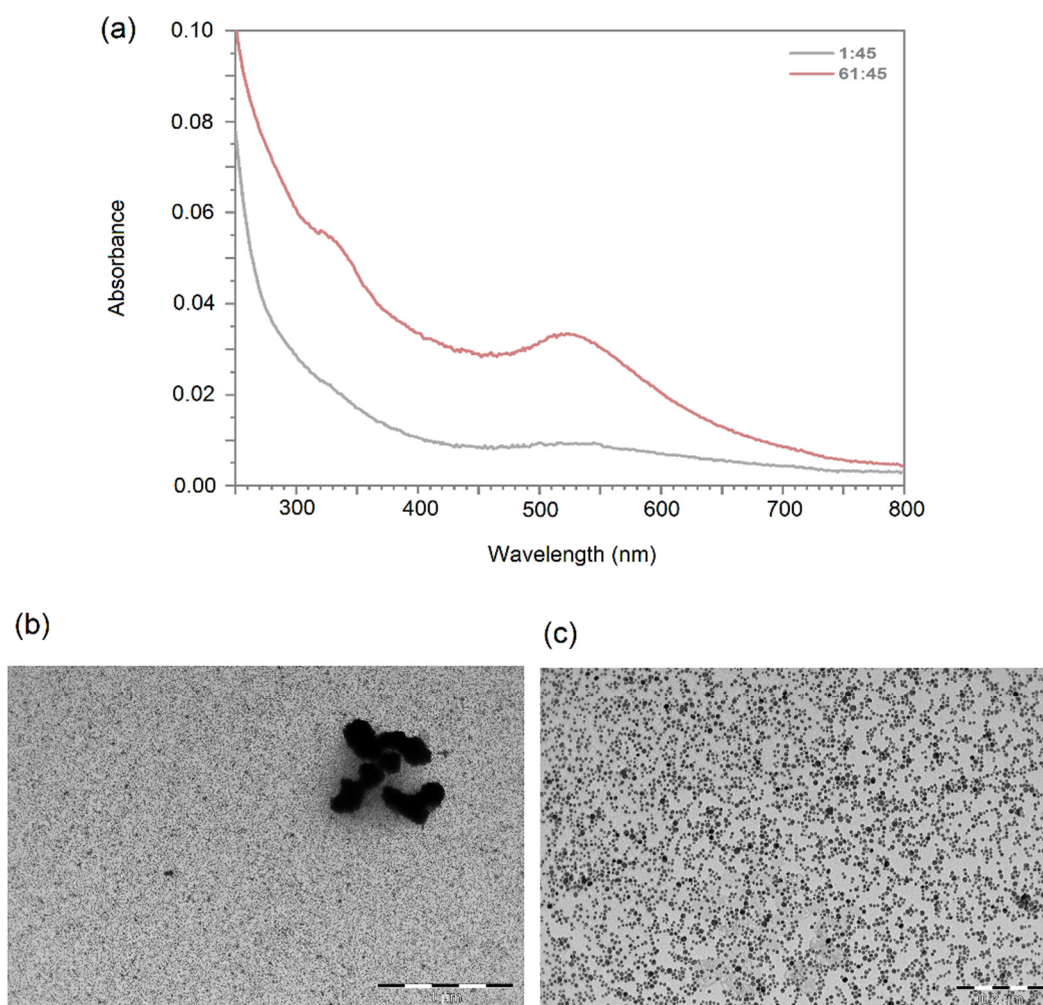
Figure S3. (a) Extinction spectra of Au-Tyr in deionized water recorded at 1 minute and 45 seconds after synthesis (grey line) and 61 minutes and 45 seconds after synthesis (red line). Panels **(b)** and **(c)** show the TEM images of Au-Tyr recorded at different magnifications. Scale bar in panel **(b)** equals to 1 μm, and in panel **(c)** equals to 0.2 μm.
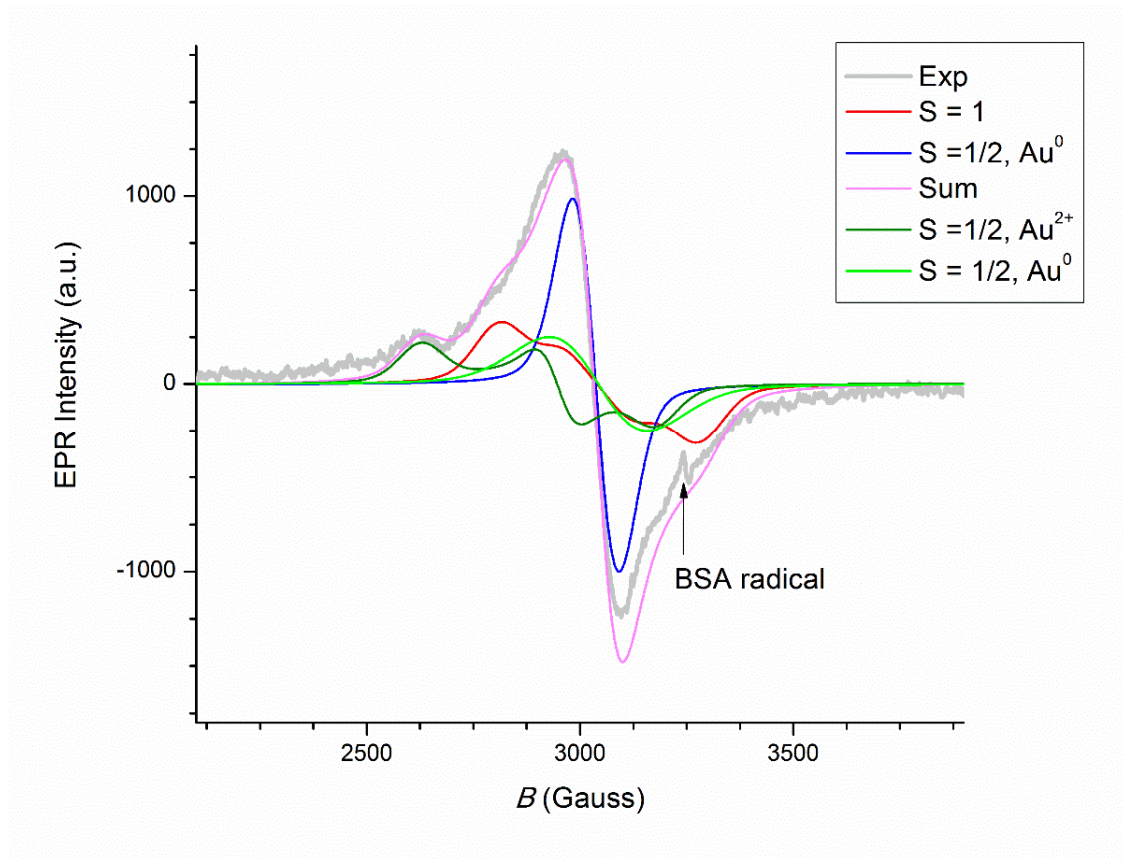
Figure S4. CW-EPR spectrum of <u>AuBSA</u> in water recorded at *T* = 90 K <u>in dark conditions</u> with the EPR simulation of the diverse spin-components associated to the Au nanoclusters.

Doublet specie, *S* =1/2, dark green line, Au^{2+}. g_x = 2.47, g_y = 2.20, g_z = 2.04. Line-width tensor (x,y,z) = 100 G, 80 G, 100 G. Lorentzian/Gaussian ratio = 0.63. Relative intensity weight = 12.8%

Doublet specie, *S* =1/2, blue line, Au^0. g_x = 2.13, g_y = 2.13, g_z = 2.13. Line-width tensor (x,y,z) = 180 G, 100 G, 100 G. Lorentzian/Gaussian ratio = 0.63. Relative intensity weight = 55.2% and *S* =1/2, green line, Au^0. g_x = 2.13, g_y = 2.13, g_z = 2.13. Line-width tensor (x,y,z) = 230 G, 230 G, 230 G. Lorentzian/Gaussian ratio = 0.63. Relative intensity weight = 13.8%

Triplet specie, *S* =1, red line. g_x = 2.13, g_y = 2.13, g_z = 2.13. Line-width tensor (x,y,z) = 100 G, 100 G, 100 G. *D* = 205 G, *E* = 60 G. Lorentzian/Gaussian ratio = 0.63. Relative intensity weight = 18.2%
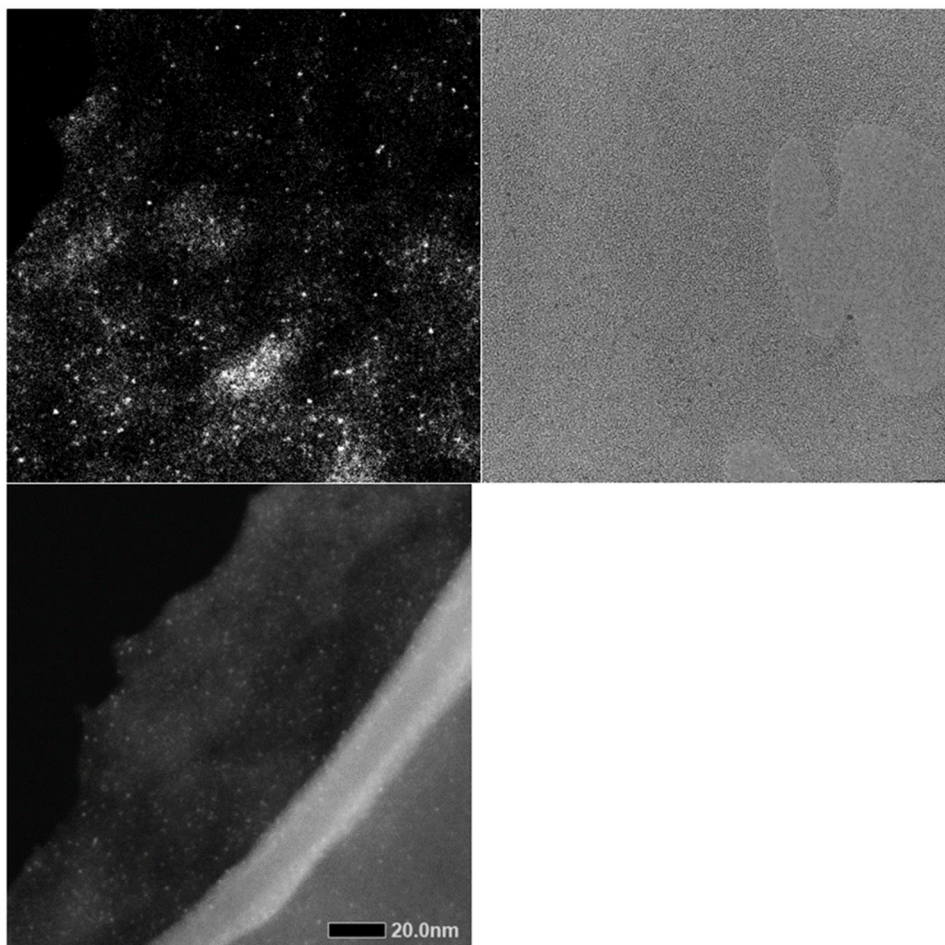
Figure S5. Further STEM images of AuBSA.
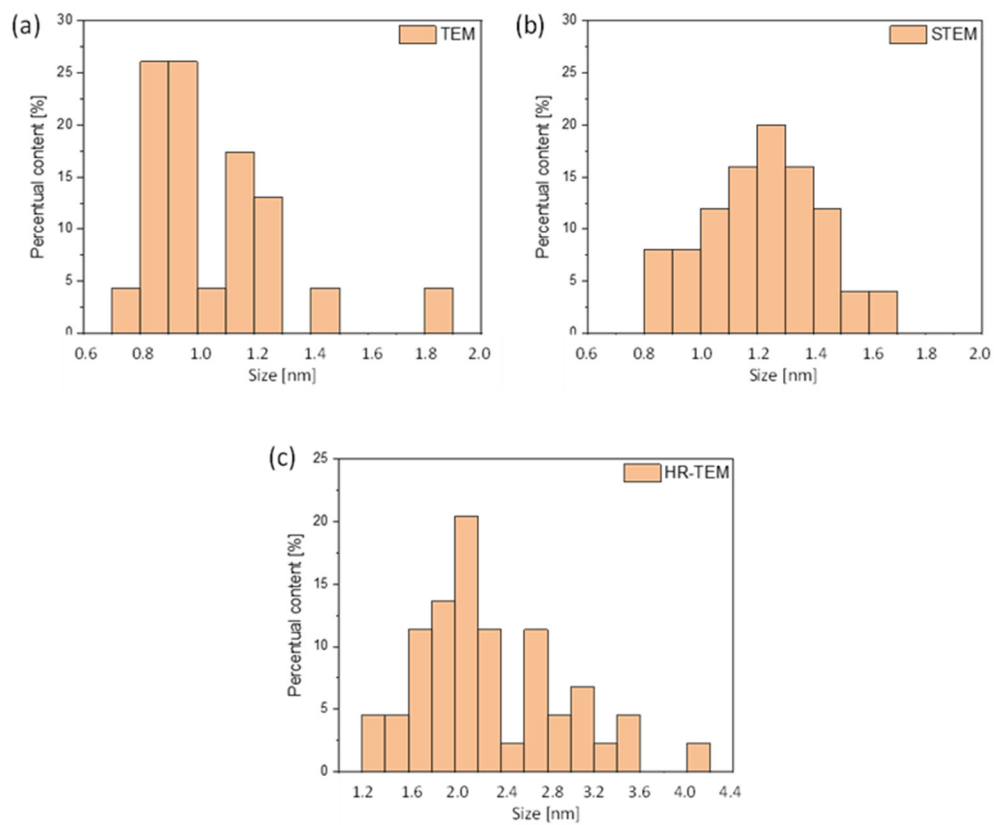
Figure S6. Particle size distributions derived from (**a**) TEM, (**b**) STEM, and/or (**c**) HR-TEM images.
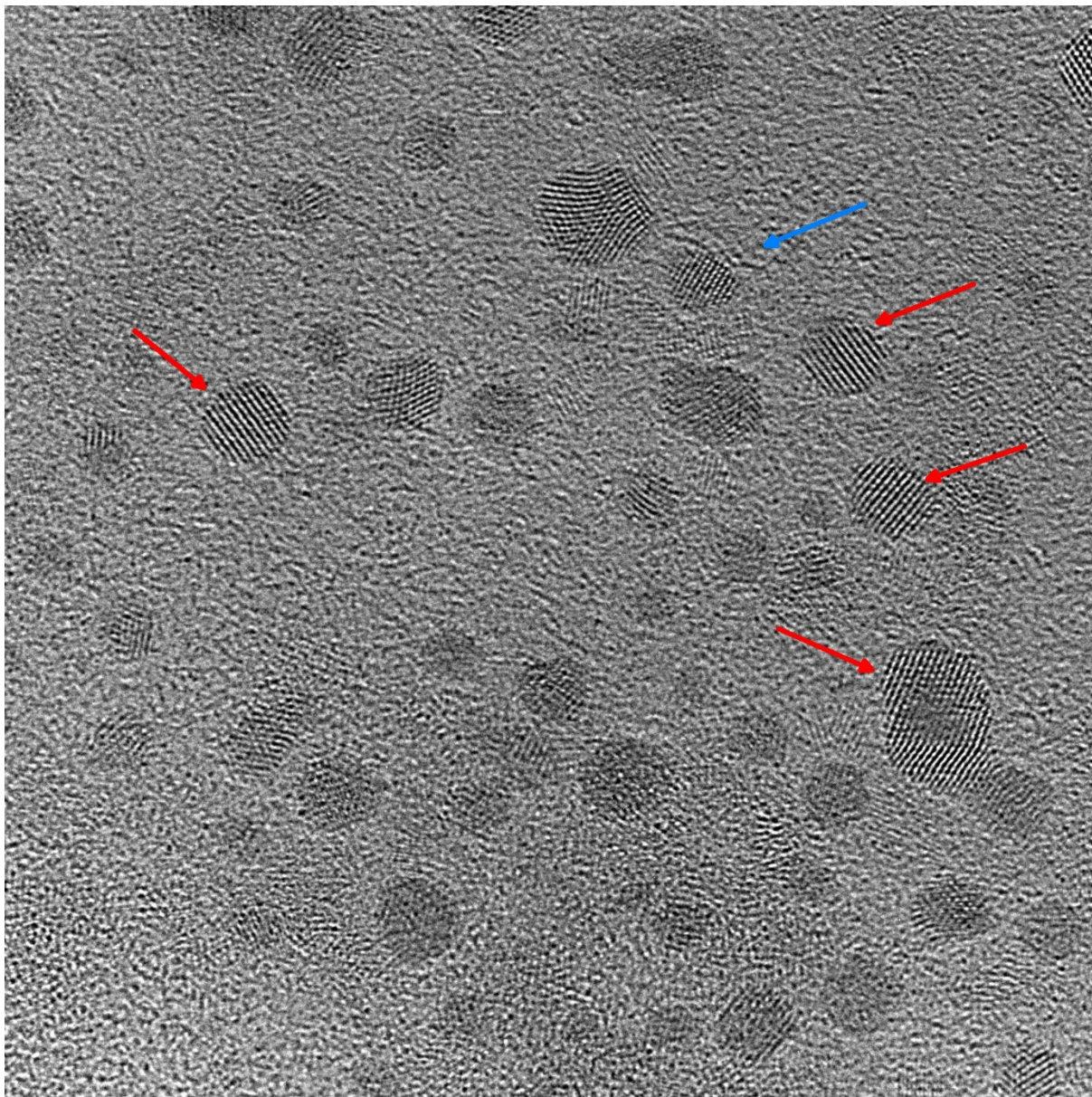
Figure S7. Lattice planes determined for several AuNCs of AuBSA in a particular HR-TEM image. Red arrows indicate Au(111), while the blue arrow represents Au(200).

Facile One-Pot Green Synthesis of Magneto-Luminescent Bimetallic Nanocomposites with Potential as Dual Imaging Agent

Ostruszka R., Půlpánová D., Pluháček T., Tomanec O., Novák P., Jirák D., Šišková K.	*Nanomaterials*, **13**:1027
	2023

Article

Facile One-Pot Green Synthesis of Magneto-Luminescent Bimetallic Nanocomposites with Potential as Dual Imaging Agent

Radek Ostruszka [1], Denisa Půlpánová [2], Tomáš Pluháček [3], Ondřej Tomanec [4], Petr Novák [1], Daniel Jirák [2,5] and Karolína Šišková [1,*]

1 Department of Experimental Physics, Faculty of Science, Palacký University Olomouc, 77900 Olomouc, Czech Republic
2 Faculty of Health Studies, Technical University of Liberec, 46117 Liberec, Czech Republic
3 Department of Analytical Chemistry, Faculty of Science, Palacký University Olomouc, 77900 Olomouc, Czech Republic
4 Regional Centre of Advanced Technologies and Materials, Czech Advanced Technology and Research Institute, Palacký University Olomouc, 77900 Olomouc, Czech Republic
5 Radiodiagnostic and Interventional Radiology Department, Institute for Clinical and Experimental Medicine, 14021 Prague, Czech Republic
* Correspondence: karolina.siskova@upol.cz

Abstract: Nanocomposites serving as dual (bimodal) probes have great potential in the field of bio-imaging. Here, we developed a simple one-pot synthesis for the reproducible generation of new luminescent and magnetically active bimetallic nanocomposites. The developed one-pot synthesis was performed in a sequential manner and obeys the principles of green chemistry. Briefly, bovine serum albumin (BSA) was exploited to uptake Au (III) and Fe (II)/Fe (III) ions simultaneously. Then, Au (III) ions were transformed to luminescent Au nanoclusters embedded in BSA (AuNCs-BSA) and majority of Fe ions were bio-embedded into superparamagnetic iron oxide nanoparticles (SPIONs) by the alkalization of the reaction medium. The resulting nanocomposites, AuNCs-BSA-SPIONs, represent a bimodal nanoprobe. Scanning transmission electron microscopy (STEM) imaging visualized nanostructures with sizes in units of nanometres that were arranged into aggregates. Mössbauer spectroscopy gave direct evidence regarding SPION presence. The potential applicability of these bimodal nanoprobes was verified by the measurement of their luminescent features as well as magnetic resonance (MR) imaging and relaxometry. It appears that these magneto-luminescent nanocomposites were able to compete with commercial MRI contrast agents as MR displays the beneficial property of bright luminescence of around 656 nm (fluorescence quantum yield of $6.2 \pm 0.2\%$). The biocompatibility of the AuNCs-BSA-SPIONs nanocomposite has been tested and its long-term stability validated.

Keywords: nanocomposite material; imaging; gold nanocluster; luminescence material; MRI assessment; SPION; bovine serum albumin

1. Introduction

Today, nanocomposites that are simultaneously luminescent and magnetically active are the focus of many research groups due to their applications in nanomedicine (for instance, [1–5]). Several approaches can be used to combine luminescent and magnetic features within one nanocomposite: (i) luminescent nanostructures (NSs) (e.g., quantum dots and/or AuNSs) connected with magnetic NSs [6–12]; (ii) fluorescent (organic) dyes and magnetic NSs [13,14]; (iii) luminescent NSs and magnetic complexes (e.g., containing Gd^{3+}) [3,15,16]; and (iv) fluorescent dyes and magnetic complexes [17,18]. Here, we deal with the first approach (luminescent NSs and magnetic NSs) to achieve magneto-luminescent nanocomposites serving as dual (bimodal) probes.

Typical synthetic strategies for the fabrication of such magneto-luminescent nanocomposites can include: (a) complex multi-step synthesis via a series of sequential synthetic procedures with separately optimized steps (e.g., [6,7]); (b) one-pot method from as-prepared or commercially available structures (e.g., post-synthetic modifications) [13,14,16,17]; and/or (c) a one-pot method without the previous preparation of NSs components (e.g., [15,18]). Here, a straightforward synthesis of the (c) type with a high yield is presented.

Aside from the complexity of the preparation, the individual syntheses of NSs also differ in the total preparation time, ranging from a few minutes (in the case of microwave-assisted synthesis) [19–21] to tens of hours [7,15,18]. Today, simplicity, reproducibility, and green chemistry in NSs preparation are beneficial and highly recommended and are therefore applied in this work. Indeed, we have chosen a protein templated synthesis of luminescent Au nanoclusters based on our previous experience [19,22]. Bovine serum albumin (BSA), a transportation protein which is structurally analogous to human serum albumin, is successfully employed as a matrix for the formation of non-toxic luminescent Au nanoclusters embedded in BSA [19,22].

Furthermore, the same protein, BSA, has also been used by other authors in the generation of superparamagnetic iron oxide nanoparticles (SPIONs), which play a special role in the *in vivo* visualization of cells or biological tissues by ^{1}H MRI (magnetic resonance imaging) [23,24]. BSA in conjunction with SPIONs are exploited for two reasons: (i) achieving a better *in vivo* biocompatibility (e.g., [25–28]) and (ii) prolonging the blood circulation lifetime of SPIONs, representing MRI nanoprobes (e.g., [29–33]). Both properties are superior in SPIONs in comparison to, for instance, Gd (III) species, which are exhaustively reported in the literature, even in combination with AuNSs (e.g., [15,16]). Since Gd (III) species are toxic and represent potential risk to environment and human health [34], we instead decided to exploit SPIONs as MRI contrast agents in our nanocomposites. Wang Y. and co-authors [29] generated ultrasmall SPIONs directly in the presence of BSA under alkaline pH, i.e., using a one-step bio-mineralization method. In the works of other authors, BSA created only a part of the modification layers of SPIONs [30–33,35–37]. Nevertheless, none of these SPIONs-BSA nanocomposites manifested fluorescent properties in the visible region of the electromagnetic spectrum.

In the present study, a one-pot simultaneous bio-mineralization method of gold and iron ions in the presence of BSA under alkaline medium was developed to create new magneto-luminescent probes (further abbreviated as AuBSA-Fe). We demonstrate here that an easy, reproducible, highly efficient synthesis of new functional bimodal probes can be achieved by performing the one-pot sequential preparation procedure. Importantly, in comparison to most of the related literature [12], no abundant chemical agents are necessary and the use of organic solvents was totally avoided by us. Therefore, the synthesis can be regarded as a green one.

Several basic, as well as sophisticated experimental techniques, were exploited for the characterization of our bimodal AuBSA-Fe probes, such as steady-state fluorescence, dynamic light scattering (DLS), UV–Vis absorption measurements, scanning transmission electron microscopy (STEM), energy dispersive spectroscopy (EDS), Mössbauer spectroscopy, inductively coupled plasma mass spectrometry (ICP-MS), relaxation rates determination, and magnetic resonance imaging (MRI). Moreover, cell viability tests were performed by using Alamar blue assay (resazurin) and the long-term stability of AuBSA-Fe nanocomposites was verified by X-ray photoelectron spectroscopy (XPS), among others.

Our results clearly demonstrate that our AuBSA-Fe probes prepared by a simple one-pot sequential green synthetic procedure are superior to commercial MRI contrast agents owing to their bright luminescence at 656 nm when excited in the visible region (e.g., using 480 nm excitation wavelength).

2. Materials and Methods

2.1. Chemicals for Syntheses

Bovine serum albumin (BSA; >98%), gold(III) chloride trihydrate (HAuCl$_4$·3H$_2$O, $\geq$99.9%), iron(II) chloride tetrahydrate (FeCl$_2$·4H$_2$O; containing 93.4% of FeCl$_2$ and 6.6% of FeOOH according to Mössbauer spectroscopy), iron(III) chloride hexahydrate (FeCl$_3$·6H$_2$O; $\geq$99%), and sodium hydroxide (NaOH; $\geq$98.0%) were purchased from Sigma-Aldrich (Saint Louis, MO, USA) and used as received (without any further purification) for all experiments. Nitric acid (69%, Analpure), hydrochloric acid (36%, Analpure), acid-certified reference materials of the calibration standard solution ASTASOL$^®$ of Au, Fe (1000 $\pm$ 2 mg·L^{-1}), and INT-MIX 1 (10.0 $\pm$ 0.1 mg·L^{-1}) were purchased from Analytika, Ltd., Prague, Czech Republic, and used only for ICP-MS analyses. Deionized (DI) water prepared by purging Milli-Q purified water (Millipore Corp., Bedford, MA, USA) was used in all experiments.

2.2. Chemicals for Alamar Blue Assay

Foetal bovine serum (FBS), L-glutamine, Penicillin-Streptomycin, sodium chloride (NaCl; $\geq$99.0%), potassium chloride (KCl; $\geq$99.0%), potassium dihydrogen phosphate (KH$_2$PO$_4$; $\geq$99.0%), disodium hydrogen phosphate (Na$_2$HPO$_4$; $\geq$99.0%), and trypsin (from the porcine pancreas) were purchased from Sigma-Aldrich (Saint Louis, MO, USA). Resazurin sodium salt ($\geq$75%) was purchased from VWR International (Radnor, PA, USA). Dulbecco's modified Eagle's medium (DMEM, 11054) was purchased from Thermo Fisher Scientific (Waltham, MA, USA).

2.3. Syntheses of AuBSA and AuBSA-Fe—Their Purification, Concentrate Formation, and Storage

The synthetic procedure of AuBSA system follows the one used in our previous manuscript [22]. Briefly, DI water (0.2 mL) was added to an aqueous HAuCl$_4$ solution (0.8 mL, 12.5 mM) and, subsequently, BSA solution (1 mL, 1 mM) was introduced under vigorous stirring (600 rpm). After 90 s, NaOH solution (0.2 mL, 1 M) was added to obtain a basic environment (pH $\approx$ 12). Ninety seconds later, the mixed solution was heated up in a microwave oven for 10 s (power was set to 150 W). The preparation of the AuBSA-Fe system differs only in the gradual addition of DI water (0.05 mL), FeCl$_2$ (0.05 mL, 5 mM) and FeCl$_3$ (0.1 mL, 5 mM) to an aqueous HAuCl$_4$ solution instead of DI water volume (0.2 mL) alone.

After two hours of maturing at room temperature, the samples were dialyzed with a 14 kDa cut-off dialysis membrane (regenerated cellulose, Membra-Cel^{TM}) against DI water. Dialysis was performed at room temperature for 24 h, with DI water being changed twice: once after the first hour and then again after the second hour. Concentrated forms of samples were prepared using a centrifugal concentrator (30 kDa). The rotational speed was set to 5000 rpm and the centrifugation lasted for 5 min. This process was performed repeatedly until the desired concentration was reached. Dialyzed and concentrated samples were stored in the dark at 4 °C.

2.4. Characterization Techniques

2.4.1. Fluorescence Spectroscopy

The fluorescence measurements of AuBSA and AuBSA-Fe systems were performed on a JASCO F8500 (Jasco, Tokyo, Japan) spectrofluorometer using a 1 cm quartz cuvette. Excitation–emission 3D maps were measured in the excitation range of 250–850 nm with a data interval of 5 nm and in an emission range of 250–850 nm with a data interval of 1 nm and a scan speed of 5000 nm·min^{-1}. Emission spectra were measured in the range of 500–850 nm with a data interval of 1 nm and a scan speed of 100 nm·min^{-1}. The excitation wavelength was set to 480 nm. All spectra were corrected to avoid any deviations induced by instrumental components.

The quantum yield of fluorescence (Φ) was then calculated by Equation (1):

$$\Phi = \Phi_\text{s} \cdot \frac{F \cdot \left(1 - 10^{-A_s}\right) \cdot n^2}{F_\text{s} \cdot \left(1 - 10^{-A}\right) \cdot n_\text{s}^2},\tag{1}$$

where F is the integrated fluorescence intensity, A is the absorbance, n is the index of refraction, and the subscript s indicates the standard. DCM, 4-(dicyanomethylene)-2-methyl-6-(4-dimethylaminostyryl)-4H-pyran, dissolved in ethanol (99.8%, Lach-Ner, Neratovice, Czech Republic) was used as a standard ($\Phi_\text{s} = 0.437 \pm 0.024$) [38].

Absorbance was measured on a Specord 250 Plus—223G1032 (Analytik Jena, Jena, Germany) with a double beam arrangement using a 1 cm quartz cuvette. As a reference, a 1 cm quartz cuvette filled with DI water was used.

The hydrodynamic diameter of both systems was determined by dynamic light scattering using Zetasizer Nano ZS (Malvern Instruments Ltd., Malvern, UK) equipped with a He-Ne laser ($\lambda = 633$ nm) at 22 ± 1 °C. For fluorescence, absorbance, and hydrodynamic diameter measurements, the ratio of the sample dilution with DI water was the same.

2.4.2. HR-TEM, STEM, and EDS

The AuBSA-Fe samples were measured by HR-TEM Titan G2 60–300 (FEI, Hillsboro, OR, USA) with an image corrector at an accelerating voltage of 300 kV. Images were taken with a BM UltraScan CCD camera (Gatan, Pleasanton, CA, USA). Energy Dispersive Spectrometry (EDS) was performed in STEM mode by a Super-X system with four silicon drift detectors (Bruker, Billerica, MA, USA). STEM images were taken with an HAADF detector 3000 (Fishione, Export, PA, USA).

2.4.3. Mössbauer Spectroscopy

A home-made Mössbauer spectrometer was used to determine the oxidation and spin state of iron atoms within AuBSA-Fe samples. A representative as-prepared and centrifuged AuBSA-Fe sample was measured with an OLTWINS Mössbauer spectrometer in the transmission mode [39], using a constant acceleration rate and ^{57}Co (Rh) source. The isomer shift values were related to the 28 μm α-Fe foil (Ritverc) measured at room temperature. By using measurements in magnetic field at low temperature, average sizes of SPIONs within AuBSA-Fe samples could be roughly estimated. The acquired Mössbauer spectra were processed using MossWinn 4.0 software [40].

2.4.4. XPS

The X-ray photoelectron spectroscopy (XPS) measurements were carried out with the PHI 5000 VersaProbe II XPS system (Physical Electronics) with a monochromatic Al-Ka source (15 kV, 50 W) and a photon energy of 1486.7 eV. All the spectra were measured in a vacuum of 1.1×10^{-7} Pa and at a room temperature of 20 °C. Dual beam charge compensation was used for all measurements. The spectra were evaluated with MultiPak software, version 9 (Ulvac—PHI, Inc., Chanhassen, MN, USA).

2.4.5. ICP-MS

To accurately determine the total Au and Fe concentrations, the validated ICP-MS method was employed. Prior to ICP-MS analysis, each sample was sonicated and consequently digested using MLS 1200 mega closed vessel microwave digestion unit (Milestone, Italy). The organic matrix was decomposed by a mixture of 4 mL of nitric acid (69%, Analpure) and hydrochloric acid (36%, Analpure) in 1:1 ratio. The digests were allowed to cool down to laboratory temperature, diluted with the ultrapure water to 25 mL in volumetric flasks, and stored at 4 °C until ICP-MS analysis. The detailed ICP-MS method description and the corresponding validation in terms of the limit of detection (LOD), the limit of quantification (LOQ), trueness, and precision are presented in the Supplementary Materials. All ICP-MS measurements were performed in six replicates, and the results are expressed as an average $\pm$ standard deviation (SD).

2.4.6. MR Relaxometry and Imaging

The MR relaxometry was used to determine the relaxivities $r_{1,2}$ of AuBSA-Fe nanocomposites (M1–M4). The relaxation times T_1 and T_2 were measured on relaxometer Bruker Minispec mq 60 (Bruker Biospin, Ettlingen, Germany) at 1.5 T, at a stabilized temperature of 37 °C throughout the whole experiment. MR sequence for T_1 measurement: Inversion recovery (IR), 20 points for fitting, 1 excitation, time of repetition (TR) = 0.01–10,000 ms, recycle delay 2 s. T_2 relaxation times were measured with Carr-Purcell-Meiboom-Gill (CPMG), TR = 5000 ms, 20,000 echoes, 1 excitation, echo time (TE) = 0.05 ms, recycle delay 2 s. The relaxivities $r_{1,2}$ were calculated via the least-squares curve fitting of R_1 and R_2 relaxation rates [s^{-1}] versus iron concentration (mM). The experimentally determined solvent relaxation rate R was subtracted as a starting value from the nanoparticle relaxation rates prior to the linear regression analysis.

The MR imaging experiments were performed on a Bruker Biospec 47/20 (Bruker, Ettlingen, Germany) at 4.7 T. T_1- and T_2-weighted MR images of M1–M4 and water (served as a control) samples in tubes were acquired. Rapid acquisition with relaxation enhancement (RARE) multi-spin echo MR sequence were used with the following parameters: T_1-weighted sequence: effective echo time (TE) = 11.6 ms, time of repetition (TR) = 587.0 ms, turbo factor (TF) = 1, scan time = 10.5 min, plane resolution (PR) = 234 × 195 µm^2, slice thickness = 0.6 mm. T_2-weighted sequence: RARE, TE = 36 ms, TR = 3300 ms, TF = 8, scan time = 11.0 min, PR = 234 × 195 µm^2, slice thickness = 0.6 mm. MR image processing and quantification were performed using ImageJ software. The signal-to-noise ratio (SNR) was calculated from images as $0.655 \times S_{sample}/\sigma_{noise}$ and contrast-to-noise ratio (CNR) was calculated from images as $0.655 \times |S_{sample} - S_{water}|/\sigma_{noise}$, where S is signal intensity in the region of interest, σ is the standard deviation of background noise, and the constant 0.655 reflects the Rician distribution of background noise in a magnitude MR image.

2.4.7. Alamar Blue Assay (Resazurin Assay)

In a typical experiment, 80 µL of cultivation medium (second column) or cell (RPE-1) suspension was added to a 96-well plate, which was afterward plaved inside the incubator (37 °C, 5% CO$_2$). After 24 h, 20 µL of DI water (second and third column), two different concentrations of gold and iron precursors, or AuBSA-Fe nanocomposites were added in the form of tri/hexaplicates. Another 24 h later, 20 µL of resazurin was introduced to each well. After 3 h of incubation, fluorescence intensity was measured on a microplate reader Synergy Mx (BioTek^{TM}, Winooski, VT, USA). The excitation and emission wavelengths were set to 540 nm and 590 nm, respectively. Cell viability (*CV*) was calculated according to Equation (2):

$$CV = 100 \times \frac{F_{sample} - F_{medium}}{F_{cells} - F_{medium}}, \qquad (2)$$

where *F* is the averaged fluorescence intensity and the subscripts sample, cells, and medium indicate the measurement of fluorescence in the suspensions of sample-treated cells, non-treated cells, and the solution of cultivation medium alone, respectively.

3. Results and Discussion

The samples of AuBSA-Fe were prepared by an easy one-pot synthetic procedure performed in a sequential manner, which was newly developed by us, as described in detail in the Materials and Methods section. Essentially, ferrous and ferric ions were mixed together in the ratio of 1:2, added to Au (III) aqueous solution and then allowed to interact with BSA for a certain period. The reaction mixture was alkalized in the next step to set up conditions for simultaneous and spontaneous Au (III) reduction and SPIONs formation (i.e., precipitation of Fe ions under alkaline medium in the presence of BSA); the subsequent heating accelerated both bio-mineralization reactions. As a reference, the AuBSA sample was prepared by using the same amount of Au (III) and BSA as in AuBSA-Fe system. Thus, AuBSA and AuBSA-Fe systems differ only in the absence/presence of iron ions in their

synthetic procedures, respectively. The procedures of both nanocomposite syntheses are schematically depicted in Figure 1.
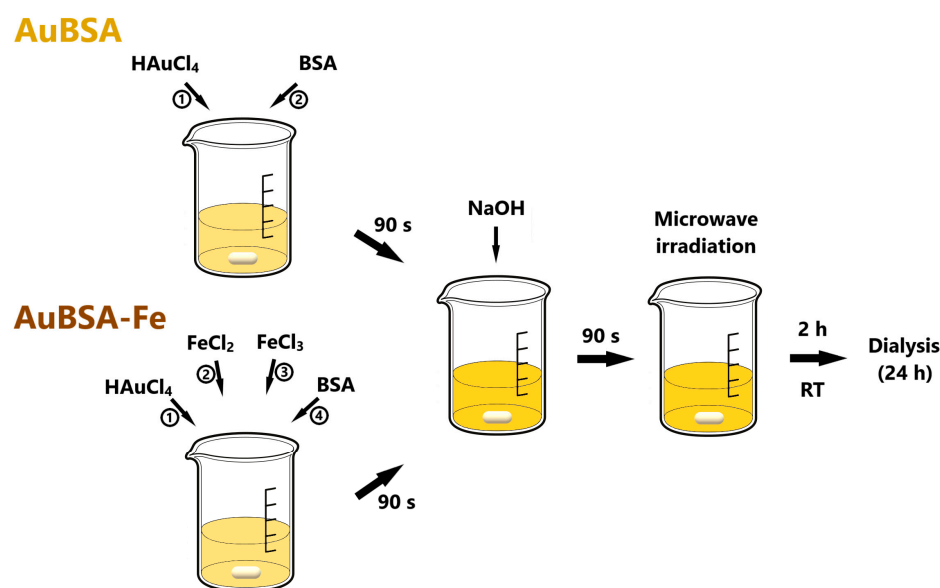

Figure 1. Schematic depiction of AuBSA and AuBSA-Fe nanocomposites.

3.1. Luminescent Properties of AuBSA-Fe in Comparison to AuBSA

There might be concerns about luminescence quenching induced by iron cations, since luminescent AuNCs have been used as sensors of Fe (III) in solution [41–43]. However, in the cited studies, BSA is not used as the template for luminescent AuNCs formation. Moreover, there is a big difference between (i) Fe cations being present in the course of luminescent AuNCs formation within BSA (this study) and (ii) Fe cations being added to well-formed luminescent AuNCs [41–43].

Prompted by this issue, we first focused our attention on the validation of luminescent properties of AuNCs in the AuBSA-Fe system inherited from AuBSA—see Figure 2 for emission spectra in the region of 500–850 nm and Figure S1 for the whole-range 3D excitation–emission maps. Obviously, the average position of the emission maximum of AuNCs remained almost unchanged when iron ions were present: 657 ± 2 nm for AuBSA and 656 ± 1 nm for AuBSA-Fe (Tables S1 and S2, respectively). The intensity of luminescence decreased slightly in AuBSA-Fe in comparison to AuBSA (Figure 2). The fluorescent quantum yield reflects this fact and is of virtually the same average value for AuBSA-Fe, 6.2 ± 0.2 (Table S2), as for AuBSA, 6.4 ± 0.1 (Table S1). This is a good sign that qualitative and quantitative luminescent features of AuNCs are not affected by the presence of iron atoms in AuBSA-Fe samples. Furthermore, one can assume that sizes and numbers of AuNCs within AuBSA-Fe and AuBSA nanocomposites are approximately the same.

3.2. Investigation of Morphology and Particle Size Distribution in Luminescent AuBSA-Fe

According to STEM image in Figure 3A, one can see relatively large aggregates exceeding several hundreds of nanometres in size; however, they consist of individual particles with sizes in units of nanometres and are frequently encountered in AuBSA-Fe systems. EDS data shown in Figure 3B,C further demonstrate that oxygen dominates in the close vicinity of iron in nanoparticulate form (e.g., Fe_xO_y), while sulphur can be co-located together with gold atoms, respectively. This supports previous results of many researchers (including us, [22]) concerning Au–S interactions within AuBSA. It also correlates well with the observation that the luminescent features of AuNCs are not severely hampered by the presence of Fe_xO_y in AuBSA-Fe. Thus, we anticipate that the same type of amino-acid residues creates the closest nano-environment of luminescent AuNCs in AuBSA-Fe as that in AuBSA systems. Since the samples for STEM/EDS are prepared by drying on a support

(lacey carbon-coated Cu grid), the real particle size distribution (PSD) in the solution may differ from that observed by STEM. Therefore, it is reasonable to determine PSD directly by measuring the aqueous solutions of the samples by DLS. The average values of the hydrodynamic diameters of particles in AuBSA and AuBSA-Fe nanocomposite solutions along with polydispersity values (PDI) determined by DLS are compared in Table 1. Both samples (AuBSA as well as AuBSA-Fe) represent proper solutions without any obvious aggregate formation visible by the naked eye.
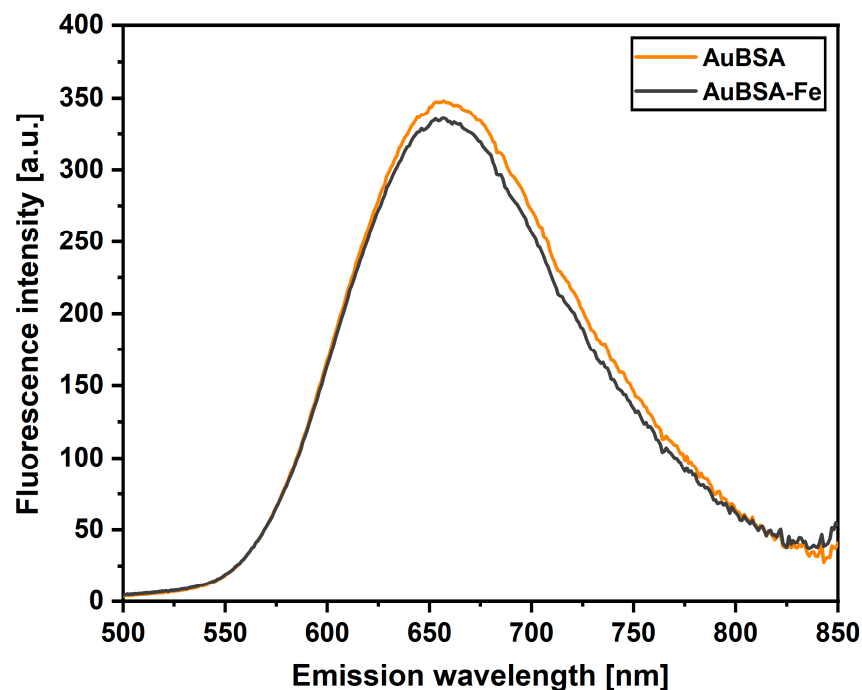
Figure 2. Comparison of fluorescence emission spectra of AuBSA (orange curve) and AuBSA-Fe (black curve) samples when excited at 480 nm. Average fluorescence spectra are shown as a result of seven independent sample preparations and their measurements.
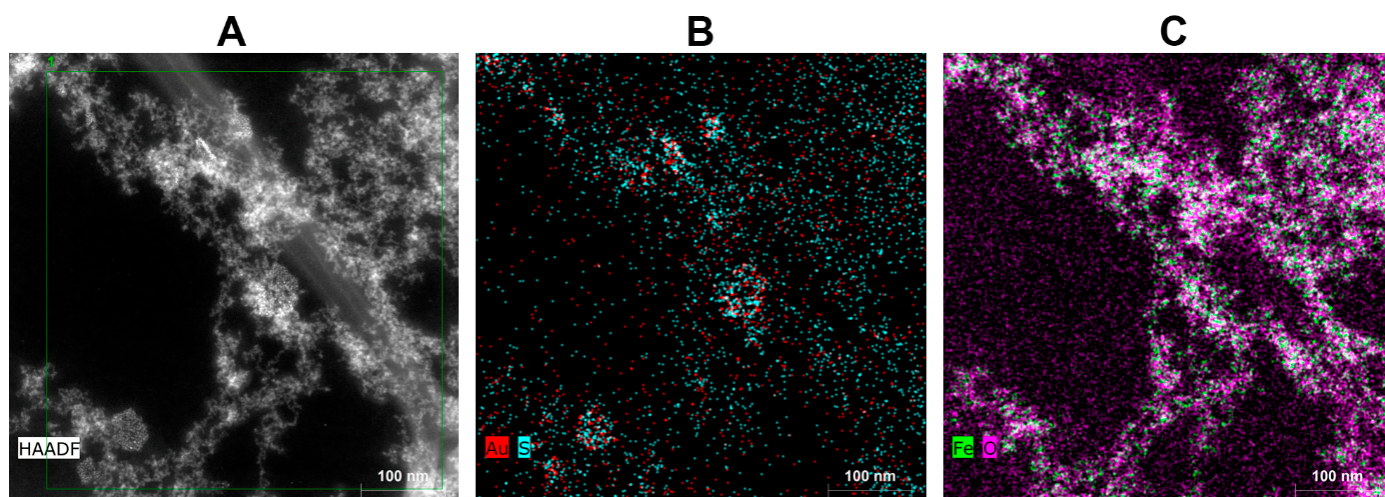
Figure 3. Scanning transmission electron microscopy (STEM) and energy dispersive spectroscopic (EDS) analysis of a representative AuBSA-Fe sample: (**A**) STEM image, scale bar of 100 nm; (**B**) Au and S spatial distribution map; and (**C**) Fe and O spatial distribution map.

Table 1. Hydrodynamic diameter (represented by Z-average) and polydispersity (PDI) of nanocomposites determined by DLS measurements.

Sample	Z-Average [nm]	PDI
AuBSA	23.9 ± 10.8	0.4 ± 0.1
AuBSA-Fe	71.2 ± 8.0	1.0 ± 0.0

Obviously, both the hydrodynamic diameter and PDI increased in AuBSA-Fe in comparison to AuBSA (Table 1). These increases in the average values (from approx. 24 nm in diameter and 0.4 polydispersity in AuBSA to 71 nm and 1.0 in AuBSA-Fe) can be ascribed to the presence of iron oxide particles and their aggregates in AuBSA-Fe because these are the only differences between the two compared systems. Further details of DLS data are shown and discussed in the Supplementary Materials (Figures S2–S4); whereas appropriate values for AuBSA and AuBSA-Fe are listed in Tables S3 and S4, respectively. Although influenced by sample drying to some extent, the STEM images of AuBSA-Fe in dried state (Figure 3A) correlate with the PSD determined for the same system by DLS measured directly in aqueous solution (liquid state).

3.3. Evidence of SPIONs in Luminescent AuBSA-Fe via Mössbauer Spectroscopy

Mössbauer spectroscopy as an iron-sensitive method has been selected to give direct evidence regarding the type of iron oxide present in AuBSA-Fe. Since relatively high concentrations of iron are required in this spectroscopy and, simultaneously, by knowing (from STEM-EDS) that iron is most dominantly distributed in nanoparticulate form at the surface of BSA, we centrifuged the AuBSA-Fe samples, a rusty pellet was carefully dried under nitrogen atmosphere and then measured. The Mössbauer spectrum of AuBSA-Fe recorded at room temperature, shown in Figure 4A, manifested itself as a doublet with an isomer shift value of 0.33 ± 0.01 mm$\cdot$s^{-1} and the quadrupole splitting of 0.68 ± 0.01 mm$\cdot$s^{-1}. By measuring the Mössbauer spectrum at 5 K and 5 T, as seen Figure 4B, a sextet with an isomer shift value of 0.43 ± 0.01 mm$\cdot$s^{-1}, a quadrupole splitting of -0.08 ± 0.01 mm$\cdot$s^{-1}, and an effective hyperfine magnetic field of 46.4 ± 0.3 T was revealed. Based on these parameters and our previous knowledge [44], the nanoparticulate form of iron in AuBSA-Fe samples can be assigned to superparamagnetic Fe (III) oxide. Furthermore, the measurements at low temperatures and under external magnetic fields showed a symmetrical environment with no preferential orientation; therefore, very small superparamagnetic iron oxide particles (SPIONs) are present in AuBSA-Fe, generally in units of nanometres. This coincides well with STEM imaging and DLS analysis.

3.4. Application of Luminescent AuBSA-Fe as MRI Contrast Agents

SPIONs are well-known as negative or T_2-weighted MRI contrast agents [23]. Therefore, we assessed MRI performance of our AuBSA-Fe samples. In Figure 5, we show the T_2-weighted MR images of four independently prepared AuBSA-Fe samples (denoted as M1–M4), containing different (increasing) concentrations of gold and iron, as determined by ICP-MS (Table S6), but keeping the same molar ratio of these metals (10:0.75). Intentionally, four independently prepared samples were concentrated to verify the reproducibility and to increase the T_2-weighted signal. Obviously, the T_2-weighted MR images of water phantoms were affected by the presence of AuBSA-Fe samples and the clear decrease in the MR signal was observed; on the other hand, and as expected, the only negligible effect was observed in T_1-weighted MR images, where the MR signal increase was low (Figure 5). The values of signal-to-noise ratio (SNR) as well as contrast-to-noise ratio (CNR) for the quantitative comparison of M1–M4 samples are listed in Figure 5. Both SNR and CNR reached values above 37 in the T_2-weighted MR images of all four variants of AuBSA-Fe samples; simultaneously, low SNR and CNR values in T_1-weighted MR images were achieved. This means that AuBSA-Fe samples represent "negative" contrast agents due to the presence of SPIONs. This is in full accordance with the literature [29,30].
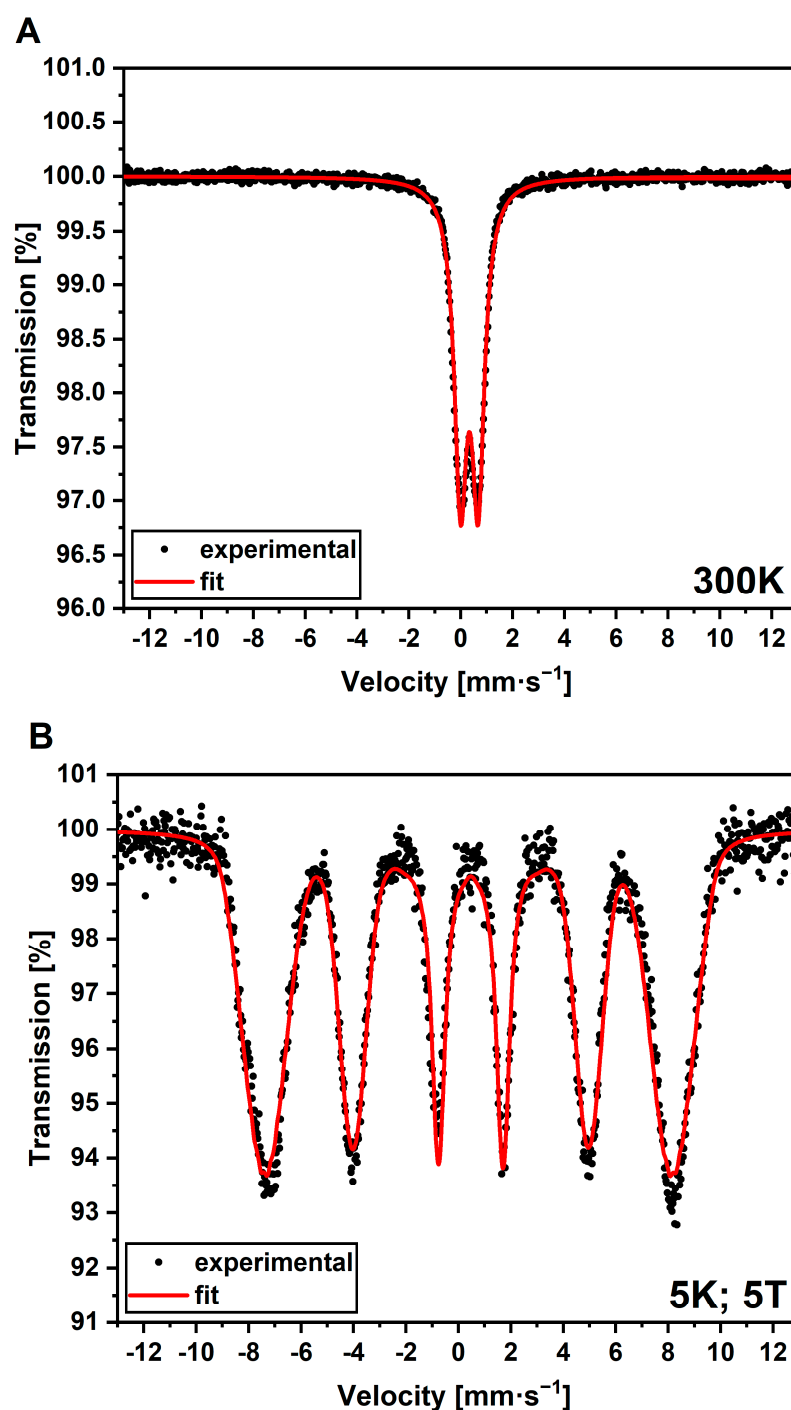
Figure 4. Mössbauer spectra of AuBSA-Fe recorded (**A**) at room temperature and (**B**) at the 5 K and 5 T external magnetic field.

Aside from the MRI imaging of water phantoms containing AuBSA-Fe samples (M1–M4), MR relaxometry was performed. The relaxation rates R_1 and R_2 were calculated as $1/T_1$ and $1/T_2$, respectively, for concentrated and diluted M1–M4 samples. Note that the real concentrations of Fe in concentrated and diluted M1–M4 samples together with the corresponding values of R_1, R_2 relaxation rates are listed in Table S7 in the Supporting Materials. Plotting the relaxation rates as a function of real iron concentration in AuBSA-Fe samples (determined by ICP-MS) resulted in the determination of relaxivities r_1 and r_2 from graphs shown in Figure 6. Evidently, the experimental R_1 values could be best fitted with a linear function (although it can be separated in two parts, according to R_2 dependence).

On the other hand, two linear functions with two different slopes are best able to fit the experimental R_2 values: 3.44 ± 0.36 L·mmol^{-1}·s^{-1} for iron concentrations equal and above 0.52 mM; 2.68 ± 0.11 L·mmol^{-1}·s^{-1} for iron concentrations below this value (Table 2). These slopes represent the characteristic r_2 relaxivity of AuBSA-Fe samples and, as such, can be compared with the relaxivity values of the commercial MRI contrast agents (e.g., in [45]). From this direct comparison, it is obvious that the r_2 relaxivity values of AuBSA-Fe samples closely approach those of several commercially available contrast agents. Importantly, the commercial MRI contrast agents do not possess luminescent properties, while AuBSA-Fe samples do. Therefore, AuBSA-Fe samples could serve as bimodal (dual) probes for MRI and fluorescence measurements.
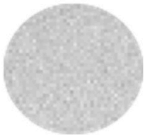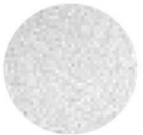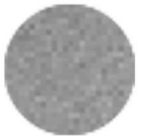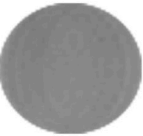
Figure 5. Magnetic resonance (MR) images of AuBSA-Fe phantoms (denoted as M1–M4) containing different Fe concentrations (807 μM Fe in M1, 1020 μM Fe in M2, 1193 μM Fe in M3, and 1249 μM Fe in M4) and water phantom (H$_2$O), measured at 4.7 T external magnetic field. T$_1$- and T$_2$-weighted MR images are shown. Note: the signal-to-noise ratio (SNR) was calculated using SNR $= 0.655 \times$ S/σ, where S is signal intensity in the region of interest (ROI), σ is the standard deviation of background noise, and the constant 0.655 reflects the Rician distribution of background noise in a magnitude MR image. Eight averages were used.

Interestingly, R_2 values may be even fitted with a quadratic function as shown for concentrated samples in Figure S5. The quadratic dependence of relaxation rates on concentration of contrast agents was observed in previous studies by different authors [46–51]. In our opinion, two plausible explanations may be adopted in the case of AuBSA-Fe samples: either the aggregation of SPIONs and the consequent inhomogeneity of magnetic fields as in [52] or the small sizes of SPIONs (evidenced for our AuBSA-Fe samples through direct visualization using STEM and/or spectroscopically through the Mössbauer effect), thus falling in a range of quadratic relaxation [53].

3.5. Stability and Biocompatibility of AuBSA-Fe Nanocomposites

An important issue in any sample applicability is their stability in time if stored under relevant conditions. Since AuBSA-Fe samples contain inorganic parts, being responsible for luminescent and MR features as well as protein (although denatured during the synthesis), generally, we stored our samples in a fridge. However, for the sake of curiosity, a sample of AuBSA-Fe was stored at room temperature over 1 year, and its X-ray photoelectron spectroscopic (XPS) spectrum measured and directly compared with that of freshly prepared AuBSA-Fe. The XPS results, shown in Figure S6 and discussed in the Supplementary Materials, confirmed the degradation of organic part, while preserving Au (0) content even in the AuBSA-Fe sample stored at room temperature. Thus, the stability of the newly developed AuBSA-Fe dual probes was verified. It can be summed up that

AuBSA-Fe, representing a stable system when stored in a fridge, could potentially be applied as fluorescent and MRI contrast agents.
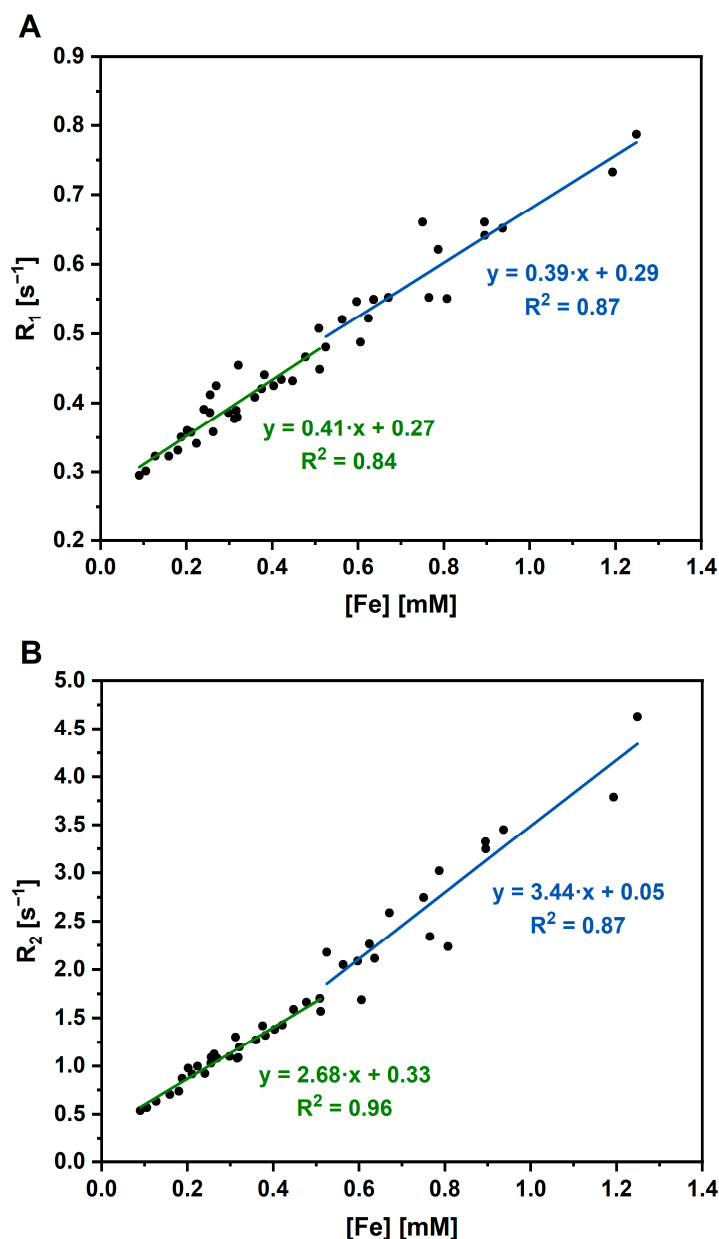

Figure 6. (**A**) Relaxation rate R_1 and (**B**) relaxation rate R_2 as functions of real iron concentrations in AuBSA-Fe samples, as determined by ICP-MS (values are listed in Table S7).

Table 2. The values of r_1 and r_2 relaxivities assessed for AuBSA-Fe samples, depending on real iron concentrations, as determined by ICP-MS. Two linear regimes are recognized by a jump around the value of 0.52 mM in Fe concentrations.

Fe Concentration [mM]	Relaxivity r_1 [L·mmol^{-1}·s^{-1}]	Relaxivity r_2 [L·mmol^{-1}·s^{-1}]
<0.52	0.41 ± 0.04	2.68 ± 0.11
$\geq$0.52	0.39 ± 0.04	3.44 ± 0.36

Another very important issue of AuBSA-Fe nanocomposite application as a potential contrast agent is its biocompatibility. Since AuBSA-Fe nanocomposites are prepared by a synthetic approach obeying the principles of green chemistry (i.e., non-toxic reactants

and aqueous environments, no abundant chemicals used), their biocompatibility can be presumed. Moreover, AuBSA nanocomposites have been tested by many authors, including us [19], for potential cytotoxicity, which was revealed to be negligible. Similarly, SPIONs were tested by several authors and manifested almost zero cytotoxicity (e.g., [25–28]). It would be thus very unusual if AuBSA-Fe nanocomposites were cytotoxic. However, the assumption of the low cytotoxicity of AuBSA-Fe was validated by using Alamar blue assay (exploiting resazurin and fluorescence measurements) in the present study. The average cell viabilities for AuBSA-Fe nanocomposites with different iron concentrations (below and/or above 0.52 mM Fe content, in correlation with MRI data) are shown in Table 3, and an example of the resazurin assay is given in Table S8.

Table 3. Results of cell viability tests.

AuBSA-Fe	Average Viability [%]
Iron concentration < 0.52 mM	78 ± 3
Iron concentration $\geq$ 0.52 mM	80 ± 2

Surprisingly, the average cell viability was determined to be around 80% (only) in all AuBSA-Fe nanocomposites. This value still falls in the range of non-toxic species according to ISO 10993. However, it should be pointed out that the cytotoxicity results may be false negatives because resazurin is able to interact with serum albumin, especially at elevated protein concentrations, as revealed in [54]. In which case, the final values of cell viability (here evaluated around 80%) could be underestimated with respect to reality, i.e., the biocompatibility of AuBSA-Fe nanocomposites could be much better than determined by the Alamar blue assay. It should be also noted that the MTT assay and CCK-8 kit were not employed because both are able to provide false-positive results, as discussed in [55,56]. Further experiments assessing the real cytotoxicity of AuBSA-Fe nanocomposites are in progress.

4. Conclusions

We developed an easy, reproducible, one-pot, green synthesis of a new type of potential bimodal probe, labelled as AuBSA-Fe. These AuBSA-Fe probes are based on non-toxic luminescent AuNCs (embedded in BSA), which are generated together with SPIONs simply through the alkalization of the reaction mixture. Luminescent features of AuNCs are preserved in AuBSA-Fe samples, i.e., emission maxima and quantum yields are comparable within experimental errors with those of AuBSA (serving here as a reference). Furthermore, MRI experiments confirmed the effect of AuBSA-Fe on T_2 contrast in MR images. The relaxivity values of AuBSA-Fe approach those of commercial contrast agents. The great benefit of AuBSA-Fe probes, serving as MR alternatives, lies in their simultaneous luminescent feature. Therefore, AuBSA-Fe nanocomposites (stable when stored in a fridge) represent promising bimodal probes and could be potentially applied as fluorescent and MRI contrast agents. Further experiments with AuBSA-Fe nanocomposites are envisaged, leading to the increased possibility of their use as MRI alternatives and testing their biocompatibility and stability, performed not only *in vitro* but also *in vivo*.

PSD of several independently measured AuBSA samples determined by DLS based on intensity and number. Average and standard deviation (SD) values are then calculated; Table S4: PSD of several independently measured AuBSA-Fe determined by DLS based on intensity and number. Average and standard deviation (SD) values are then calculated; Figure S3: Histograms of PSD of several independently measured AuBSA; Figure S4: Histograms of PSD of several independently measured AuBSA-Fe; Table S5: Validation results for ICP-MS; Table S6: Contents of Au and Fe in many independently prepared AuBSA-Fe samples as determined by ICP-MS and calculation of Au:Fe ratios in real samples; Table S7: Values of relaxation times T_1, T_2 and relaxation rates R_1, R_2 together with real iron concentrations (as determined by ICP-MS for concentrated samples, while derived from these values for diluted samples); Figure S5: Relaxation rates as a function of iron concentration in AuBSA-Fe samples (100% concentration, any dilution is omitted). Comparison of linear and nonlinear (quadratic) fits; Figure S6: (A) XPS signal of fresh AuBSA-Fe sample, Au4f region; (B) XPS signal of one-year aged AuBSA-Fe sample, Au4f region; (C) XPS signal of fresh AuBSA-Fe sample, N1s region; (D) XPS signal of one-year aged AuBSA-Fe sample, N1s region; (E) XPS signal of fresh AuBSA-Fe sample, S2p region; (F) XPS signal of one-year aged AuBSA-Fe sample, S2p region; (G) XPS signal of fresh AuBSA-Fe sample, C1s region; (H) XPS signal of one-year aged AuBSA-Fe sample, C1s region; (I) XPS signal of fresh AuBSA-Fe sample, O1s region; (J) XPS signal of one-year aged AuBSA-Fe sample, O1s region; Table S8: Table showing values of fluorescence in each well of the titration plate when cell viability tests of AuBSA-Fe nanocomposites and their precursors (HAuCl$_4$, mixture of FeCl$_2$ and FeCl$_3$) were performed in two representative iron concentrations (below and above 0.52 mM).

Author Contributions: R.O.: investigation, methodology, formal analysis, original draft—review and editing. T.P.: investigation, original draft—review and editing. O.T.: investigation. D.P.: investigation. P.N.: investigation. D.J.: funding acquisition, original draft—review and editing. K.Š.: conceptualization, resources, methodology, funding acquisition, supervision, original draft—writing and editing, original draft—review and editing. All authors have read and agreed to the published version of the manuscript.

Data Availability Statement: The raw/processed data required to reproduce these findings can be requested from the authors directly.

Conflicts of Interest: The authors declare no conflict of interest.

References

1. Han, X.; Xu, K.; Taratula, O.; Farsad, K. Applications of Nanoparticles in Biomedical Imaging. *Nanoscale* **2019**, *11*, 799–819. [CrossRef]
2. Nienhaus, K.; Wang, H.; Nienhaus, G.U. Nanoparticles for Biomedical Applications: Exploring and Exploiting Molecular Interactions at the Nano-Bio Interface. *Mater. Today Adv.* **2020**, *5*, 100036. [CrossRef]
3. Xu, C.; Wang, Y.; Zhang, C.; Jia, Y.; Luo, Y.; Gao, X. AuGd Integrated Nanoprobes for Optical/MRI/CT Triple-Modal in Vivo Tumor Imaging. *Nanoscale* **2017**, *9*, 4620–4628. [CrossRef]
4. Pan, U.N.; Khandelia, R.; Sanpui, P.; Das, S.; Paul, A.; Chattopadhyay, A. Protein-Based Multifunctional Nanocarriers for Imaging, Photothermal Therapy, and Anticancer Drug Delivery. *ACS Appl. Mater. Interfaces* **2017**, *9*, 19495–19501. [CrossRef] [PubMed]
5. Zhao, C.; Du, T.; ur Rehman, F.; Lai, L.; Liu, X.; Jiang, X.; Li, X.; Chen, Y.; Zhang, H.; Sun, Y.; et al. Biosynthesized Gold Nanoclusters and Iron Complexes as Scaffolds for Multimodal Cancer Bioimaging. *Small* **2016**, *12*, 6255–6265. [CrossRef]
6. Pahari, S.K.; Olszakier, S.; Kahn, I.; Amirav, L. Magneto-Fluorescent Yolk–Shell Nanoparticles. *Chem. Mater.* **2018**, *30*, 775–780. [CrossRef]
7. Su, X.; Xu, Y.; Che, Y.; Liao, X.; Jiang, Y. A Type of Novel Fluorescent Magnetic Carbon Quantum Dots for Cells Imaging and Detection. *J. Biomed. Mater. Res. A* **2015**, *103*, 3956–3964. [CrossRef] [PubMed]

8. Wang, C.; Yao, Y.; Song, Q. Gold Nanoclusters Decorated with Magnetic Iron Oxide Nanoparticles for Potential Multimodal Optical/Magnetic Resonance Imaging. *J. Mater. Chem. C Mater.* **2015**, *3*, 5910–5917. [CrossRef]

9. Huang, C.-L.; Hsieh, W.-J.; Lin, C.-W.; Yang, H.-W.; Wang, C.-K. Multifunctional Liposomal Drug Delivery with Dual Probes of Magnetic Resonance and Fluorescence Imaging. *Ceram. Int.* **2018**, *44*, 12442–12450. [CrossRef]

10. Binaymotlagh, R.; Hajareh Haghighi, F.; Aboutalebi, F.; Mirahmadi-Zare, S.Z.; Hadadzadeh, H.; Nasr-Esfahani, M.-H. Selective Chemotherapy and Imaging of Colorectal and Breast Cancer Cells by a Modified MUC-1 Aptamer Conjugated to a Poly(Ethylene Glycol)-Dimethacrylate Coated Fe$_3$O$_4$–AuNCs Nanocomposite. *New J. Chem.* **2019**, *43*, 238–248. [CrossRef]

11. Sheng, J.; Jiang, X.; Wang, L.; Yang, M.; Liu, Y.-N. Biomimetic Mineralization Guided One-Pot Preparation of Gold Clusters Anchored Two-Dimensional MnO2 Nanosheets for Fluorometric/Magnetic Bimodal Sensing. *Anal. Chem.* **2018**, *90*, 2926–2932. [CrossRef]

12. Xu, Y.; Palchoudhury, S.; Qin, Y.; Macher, T.; Bao, Y. Make Conjugation Simple: A Facile Approach to Integrated Nanostructures. *Langmuir* **2012**, *28*, 8767–8772. [CrossRef]

13. Meng, L.; Ma, X.; Jiang, S.; Ji, G.; Han, W.; Xu, B.; Tian, J.; Tian, W. High-Efficiency Fluorescent and Magnetic Multimodal Probe for Long-Term Monitoring and Deep Penetration Imaging of Tumors. *J. Mater. Chem. B* **2019**, *7*, 5345–5351. [CrossRef] [PubMed]

14. Li, D.-L.; Tan, J.-E.; Tian, Y.; Huang, S.; Sun, P.-H.; Wang, M.; Han, Y.-J.; Li, H.-S.; Wu, H.-B.; Zhang, X.-M.; et al. Multifunctional Superparamagnetic Nanoparticles Conjugated with Fluorescein-Labeled Designed Ankyrin Repeat Protein as an Efficient HER2-Targeted Probe in Breast Cancer. *Biomaterials* **2017**, *147*, 86–98. [CrossRef]

15. Le, W.; Cui, S.; Chen, X.; Zhu, H.; Chen, B.; Cui, Z. Facile Synthesis of Gd-Functionalized Gold Nanoclusters as Potential MRI/CT Contrast Agents. *Nanomaterials* **2016**, *6*, 65. [CrossRef]

16. Liang, G.; Xiao, L. Gd 3+-Functionalized Gold Nanoclusters for Fluorescence–Magnetic Resonance Bimodal Imaging. *Biomater. Sci.* **2017**, *5*, 2122–2130. [CrossRef]

17. Dong, D.; Jing, X.; Zhang, X.; Hu, X.; Wu, Y.; Duan, C. Gadolinium(III)–Fluorescein Complex as a Dual Modal Probe for MRI and Fluorescence Zinc Sensing. *Tetrahedron* **2012**, *68*, 306–310. [CrossRef]

18. Guan, S.; Liang, R.; Li, C.; Wei, M. A Supramolecular Material for Dual-Modal Imaging and Targeted Cancer Therapy. *Talanta* **2017**, *165*, 297–303. [CrossRef]

19. Andrýsková, P.; Šišková, K.M.; Michetschlägerová, Š.; Jiráková, K.; Kubala, M.; Jirák, D. The Effect of Fatty Acids and BSA Purity on Synthesis and Properties of Fluorescent Gold Nanoclusters. *Nanomaterials* **2020**, *10*, 343. [CrossRef] [PubMed]

20. Hsu, N.-Y.; Lin, Y.-W. Microwave-Assisted Synthesis of Bovine Serum Albumin–Gold Nanoclusters and Their Fluorescence-Quenched Sensing of Hg^{2+} Ions. *New J. Chem.* **2016**, *40*, 1155–1161. [CrossRef]

21. Yan, L.; Cai, Y.; Zheng, B.; Yuan, H.; Guo, Y.; Xiao, D.; Choi, M.M.F. Microwave-Assisted Synthesis of BSA-Stabilized and HSA-Protected Gold Nanoclusters with Red Emission. *J. Mater. Chem.* **2012**, *22*, 1000–1005. [CrossRef]

22. Ostruszka, R.; Zoppellaro, G.; Tomanec, O.; Pinkas, D.; Filimonenko, V.; Šišková, K. Evidence of Au(II) and Au(0) States in Bovine Serum Albumin-Au Nanoclusters Revealed by CW-EPR/LEPR and Peculiarities in HR-TEM/STEM Imaging. *Nanomaterials* **2022**, *12*, 1425. [CrossRef] [PubMed]

23. Zhou, Z.; Yang, L.; Gao, J.; Chen, X. Structure-Relaxivity Relationships of Magnetic Nanoparticles for Magnetic Resonance Imaging. *Adv. Mater.* **2019**, *31*, 1804567. [CrossRef] [PubMed]

24. Babes, L.; Denizot, B.; Tanguy, G.; le Jeune, J.J.; Jallet, P. Synthesis of Iron Oxide Nanoparticles Used as MRI Contrast Agents: A Parametric Study. *J. Colloid Interface Sci.* **1999**, *212*, 474–482. [CrossRef]

25. Bajaj, A.; Samanta, B.; Yan, H.; Jerry, D.J.; Rotello, V.M. Stability, Toxicity and Differential Cellular Uptake of Protein Passivated-Fe$_3$O$_4$ Nanoparticles. *J. Mater. Chem.* **2009**, *19*, 6328. [CrossRef]

26. Li, D.; Hua, M.; Fang, K.; Liang, R. BSA Directed-Synthesis of Biocompatible Fe$_3$O$_4$ Nanoparticles for Dual-Modal T1 and T2 MR Imaging in Vivo. *Anal. Methods* **2017**, *9*, 3099–3104. [CrossRef]

27. Nosrati, H.; Sefidi, N.; Sharafi, A.; Danafar, H.; Kheiri Manjili, H. Bovine Serum Albumin (BSA) Coated Iron Oxide Magnetic Nanoparticles as Biocompatible Carriers for Curcumin-Anticancer Drug. *Bioorg. Chem.* **2018**, *76*, 501–509. [CrossRef]

28. Xu, S.; Wang, J.; Wei, Y.; Zhao, H.; Tao, T.; Wang, H.; Wang, Z.; Du, J.; Wang, H.; Qian, J.; et al. In Situ One-Pot Synthesis of Fe$_2$O$_3$@BSA Core-Shell Nanoparticles as Enhanced T1-Weighted Magnetic Resonance Imagine Contrast Agents. *ACS Appl. Mater. Interfaces* **2020**, *12*, 56701–56711. [CrossRef]

29. Wang, Y.; Xu, C.; Chang, Y.; Zhao, L.; Zhang, K.; Zhao, Y.; Gao, F.; Gao, X. Ultrasmall Superparamagnetic Iron Oxide Nanoparticle for T2-Weighted Magnetic Resonance Imaging. *ACS Appl. Mater. Interfaces* **2017**, *9*, 28959–28966. [CrossRef]

30. Li, H.; Yan, K.; Shang, Y.; Shrestha, L.; Liao, R.; Liu, F.; Li, P.; Xu, H.; Xu, Z.; Chu, P.K. Folate-Bovine Serum Albumin Functionalized Polymeric Micelles Loaded with Superparamagnetic Iron Oxide Nanoparticles for Tumor Targeting and Magnetic Resonance Imaging. *Acta Biomater.* **2015**, *15*, 117–126. [CrossRef]

31. Vismara, E.; Bongio, C.; Coletti, A.; Edelman, R.; Serafini, A.; Mauri, M.; Simonutti, R.; Bertini, S.; Urso, E.; Assaraf, Y.; et al. Albumin and Hyaluronic Acid-Coated Superparamagnetic Iron Oxide Nanoparticles Loaded with Paclitaxel for Biomedical Applications. *Molecules* **2017**, *22*, 1030. [CrossRef]

32. An, L.; Yan, C.; Mu, X.; Tao, C.; Tian, Q.; Lin, J.; Yang, S. Paclitaxel-Induced Ultrasmall Gallic Acid-Fe@BSA Self-Assembly with Enhanced MRI Performance and Tumor Accumulation for Cancer Theranostics. *ACS Appl. Mater. Interfaces* **2018**, *10*, 28483–28493. [CrossRef]

33. Tian, Q.; An, L.; Tian, Q.; Lin, J.; Yang, S. Ellagic Acid-Fe@BSA Nanoparticles for Endogenous H2S Accelerated Fe(III)/Fe(II) Conversion and Photothermal Synergistically Enhanced Chemodynamic Therapy. *Theranostics* **2020**, *10*, 4101–4115. [CrossRef]

34. Harini, G.; Balasurya, S.; Khan, S.S. Recent Advances on Gadolinium-Based Nano-Photocatalysts for Environmental Remediation and Clean Energy Production: Properties, Fabrication, Defect Engineering and Toxicity. *J. Clean Prod.* **2022**, *345*, 131139. [CrossRef]

35. Gao, F.; Qu, H.; Duan, Y.; Wang, J.; Song, X.; Ji, T.; Cao, L.; Nie, G.; Sun, S. Dopamine Coating as a General and Facile Route to Biofunctionalization of Superparamagnetic Fe_3O_4 Nanoparticles for Magnetic Separation of Proteins. *RSC Adv.* **2014**, *4*, 6657. [CrossRef]

36. Nosrati, H.; Davaran, S.; Kheiri Manjili, H.; Rezaeejam, H.; Danafar, H. Bovine Serum Albumin Stabilized Iron Oxide and Gold Bimetallic Heterodimers: Synthesis, Characterization and Stereological Study. *Appl. Organomet. Chem.* **2019**, *33*, e5155. [CrossRef]

37. Nosrati, H.; Baghdadchi, Y.; Abbasi, R.; Barsbay, M.; Ghaffarlou, M.; Abhari, F.; Mohammadi, A.; Kavetskyy, T.; Bochani, S.; Rezaeejam, H.; et al. Iron Oxide and Gold Bimetallic Radiosensitizers for Synchronous Tumor Chemoradiation Therapy in 4T1 Breast Cancer Murine Model. *J. Mater. Chem. B* **2021**, *9*, 4510–4522. [CrossRef] [PubMed]

38. Rurack, K.; Spieles, M. Fluorescence Quantum Yields of a Series of Red and Near-Infrared Dyes Emitting at 600−1000 nm. *Anal. Chem.* **2011**, *83*, 1232–1242. [CrossRef]

39. Procházka, V.; Novák, P.; Stejskal, A. Department of Experimental Physics. Mössbauer Spectrometers OLTWINS. Available online: http://oltwins.upol.cz/ (accessed on 6 February 2023).

40. Klencsár, Z.; Kuzmann, E.; Vértes, A. User-Friendly Software for Mössbauer Spectrum Analysis. *J. Radioanal. Nucl. Chem. Artic.* **1996**, *210*, 105–118. [CrossRef]

41. Zhang, J.; Cai, C.; Razzaque, S.; Hussain, I.; Lu, Q.-W.; Tan, B. Synthesis of Water-Soluble and Highly Fluorescent Gold Nanoclusters for Fe^{3+} Sensing in Living Cells Using Fluorescence Imaging. *J. Mater. Chem. B* **2017**, *5*, 5608–5615. [CrossRef]

42. Zhang, Y.; Chen, Y.; Jiang, H.; Wang, X. Selective and Sensitive Detection of Fe^{3+} Ion in Drinking Water Using L-Glutathione Stabilized Red Fluorescent Gold Nanoclusters. *J. Nanosci. Nanotechnol.* **2016**, *16*, 12179–12186. [CrossRef]

43. Ungor, D.; Csapó, E.; Kismárton, B.; Juhász, Á.; Dékány, I. Nucleotide-Directed Syntheses of Gold Nanohybrid Systems with Structure-Dependent Optical Features: Selective Fluorescence Sensing of Fe^{3+} Ions. *Colloids Surf B Biointerfaces* **2017**, *155*, 135–141. [CrossRef] [PubMed]

44. Šišková, K.; Machala, L.; Tuček, J.; Kašlík, J.; Mojžeš, P.; Zbořil, R. Mixtures of L-Amino Acids as Reaction Medium for Formation of Iron Nanoparticles: The Order of Addition into a Ferrous Salt Solution Matters. *Int. J. Mol. Sci.* **2013**, *14*, 19452–19473. [CrossRef]

45. Rohrer, M.; Bauer, H.; Mintorovitch, J.; Requardt, M.; Weinmann, H.-J. Comparison of Magnetic Properties of MRI Contrast Media Solutions at Different Magnetic Field Strengths. *Investig. Radiol.* **2005**, *40*, 715–724. [CrossRef] [PubMed]

46. Stanisz, G.J.; Henkelman, R.M. Gd-DTPA Relaxivity Depends on Macromolecular Content. *Magn. Reson. Med.* **2000**, *44*, 665–667. [CrossRef]

47. Bjørnerud, A.; Johansson, L.O.; Briley-Saebø, K.; Ahlström, H.K. Assessment of T1 and T2* Effects in Vivo and Ex Vivo Using Iron Oxide Nanoparticles in Steady State-Dependence on Blood Volume and Water Exchange. *Magn. Reson. Med.* **2002**, *47*, 461–471. [CrossRef]

48. Van Osch, M.J.P.; Vonken, E.P.A.; Viergever, M.A.; van der Grond, J.; Bakker, C.J.G. Measuring the Arterial Input Function with Gradient Echo Sequences. *Magn. Reson. Med.* **2003**, *49*, 1067–1076. [CrossRef]

49. Zhao, J.M.; Clingman, C.S.; Närväinen, M.J.; Kauppinen, R.A.; van Zijl, P.C.M. Oxygenation and Hematocrit Dependence of Transverse Relaxation Rates of Blood at 3T. *Magn. Reson. Med.* **2007**, *58*, 592–597. [CrossRef]

50. Calamante, F.; Connelly, A.; van Osch, M.J.P. Nonlinear ΔR2* Effects in Perfusion Quantification Using Bolus-Tracking MRI. *Magn. Reson. Med.* **2009**, *61*, 486–492. [CrossRef]

51. Patil, V.; Jensen, J.H.; Johnson, G. Intravascular Contrast Agent T2* Relaxivity in Brain Tissue. *NMR Biomed.* **2013**, *26*, 392–399. [CrossRef]

52. Ta, H.T.; Li, Z.; Wu, Y.; Cowin, G.; Zhang, S.; Yago, A.; Whittaker, A.K.; Xu, Z.P. Effects of Magnetic Field Strength and Particle Aggregation on Relaxivity of Ultra-Small Dual Contrast Iron Oxide Nanoparticles. *Mater. Res. Express* **2017**, *4*, 116105. [CrossRef]

53. Weisskoff, R.; Zuo, C.S.; Boxerman, J.L.; Rosen, B.R. Microscopic Susceptibility Variation and Transverse Relaxation: Theory and Experiment. *Magn. Reson. Med.* **1994**, *31*, 601–610. [CrossRef] [PubMed]

54. Goegan, P.; Johnson, G.; Vincent, R. Effects of Serum Protein and Colloid on the AlamarBlue Assay in Cell Cultures. *Toxicol. In Vitr.* **1995**, *9*, 257–266. [CrossRef] [PubMed]

55. Funk, D.; Schrenk, H.-H.; Frei, E. Serum Albumin Leads to False-Positive Results in the XTT and the MTT Assay. *Biotechniques* **2007**, *43*, 178–186. [CrossRef]

56. Neufeld, B.H.; Tapia, J.B.; Lutzke, A.; Reynolds, M.M. Small Molecule Interferences in Resazurin and MTT-Based Metabolic Assays in the Absence of Cells. *Anal. Chem.* **2018**, *90*, 6867–6876. [CrossRef] [PubMed]

Facile One-Pot Green Synthesis of Magneto-Luminescent Bimetallic Nanocomposites with Potential as Dual Imaging Agent

Radek Ostruszka [1], Denisa Půlpánová [2], Tomáš Pluháček [3], Ondřej Tomanec [4], Petr Novák [1], Daniel Jirák [2,5] and Karolína Šišková [1,*]

[1] Department of Experimental Physics, Faculty of Science, Palacký University Olomouc, 77900 Olomouc, Czech Republic

[2] Faculty of Health Studies, Technical University of Liberec, 46117 Liberec, Czech Republic

[3] Department of Analytical Chemistry, Faculty of Science, Palacký University Olomouc, 77900 Olomouc, Czech Republic

[4] Regional Centre of Advanced Technologies and Materials, Czech Advanced Technology and Research Institute, Palacký University Olomouc, 77900 Olomouc, Czech Republic

[5] Radiodiagnostic and Interventional Radiology Department, Institute for Clinical and Experimental Medicine, 14021 Prague, Czech Republic

[*] Correspondence: karolina.siskova@upol.cz

Table of contents:

1. 3D-fluorescence maps and average quantum yield determination of AuBSA and AuBSA-Fe
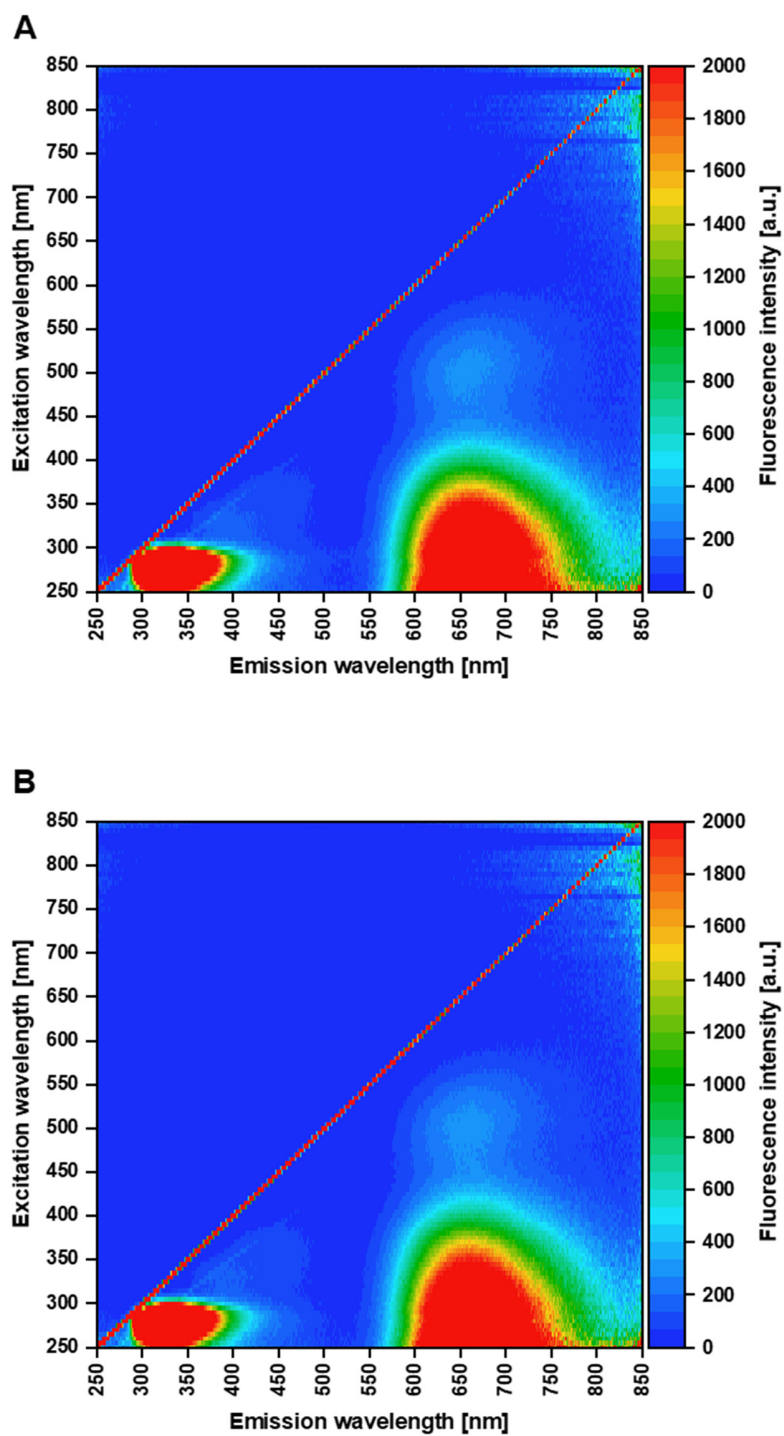
Figure S1. 3D excitation-emission maps of AuBSA (A) and AuBSA-Fe (B).

Table S1. Quantum yield and position of emission maxima of AuBSA (7 independent sample preparations).

AuBSA	I	II	III	IV	V	VI	VII	Average	SD
Absorbance	0.0196	0.0211	0.0204	0.0207	0.0205	0.0205	0.0206	0.0205	0.0005
Quantum yield [%]	6.4	6.1	6.4	6.4	6.4	6.5	6.4	6.4	0.1
Maximum at [nm]	659	654	656	656	658	659	656	657	2

Table S2. Quantum yield and position of emission maxima of AuBSA-Fe (7 independent sample preparations).

AuBSA-Fe	I	II	III	IV	V	VI	VII	Average	SD
Absorbance	0.0197	0.0202	0.0205	0.0200	0.0201	0.0207	0.0204	0.0202	0.0003
Quantum yield [%]	6.5	6.1	6.1	6.3	6.2	6.0	6.2	6.2	0.2
Maximum at [nm]	658	655	656	655	656	655	658	656	1

2. *Particle size distribution determined by DLS*

Particle size distribution (PSD) within a liquid sample can be determined by dynamic light scattering (DLS), i.e., by measuring changes of the scattered light intensity as a function of time. The instrument (Zetasizer Malvern) enables to determine PSD based on intensity, number, and volume. The former is the only value, which is measured experimentally; the two others are calculated from the former under certain assumptions (spherical, isolated, identical particles). Average PSD histograms of AuBSA and AuBSA-Fe nanocomposites are shown in Figure SI-2 for the sake of a direct comparison and for explanation of polydispersity (PDI) increase in AuBSA-Fe in comparison to AuBSA as shown and discussed in the main text. However, keep in mind that contents of big particles in PSD based on intensity changes of scattered light are overestimated because the bigger particles, the higher contribution of their scattering.
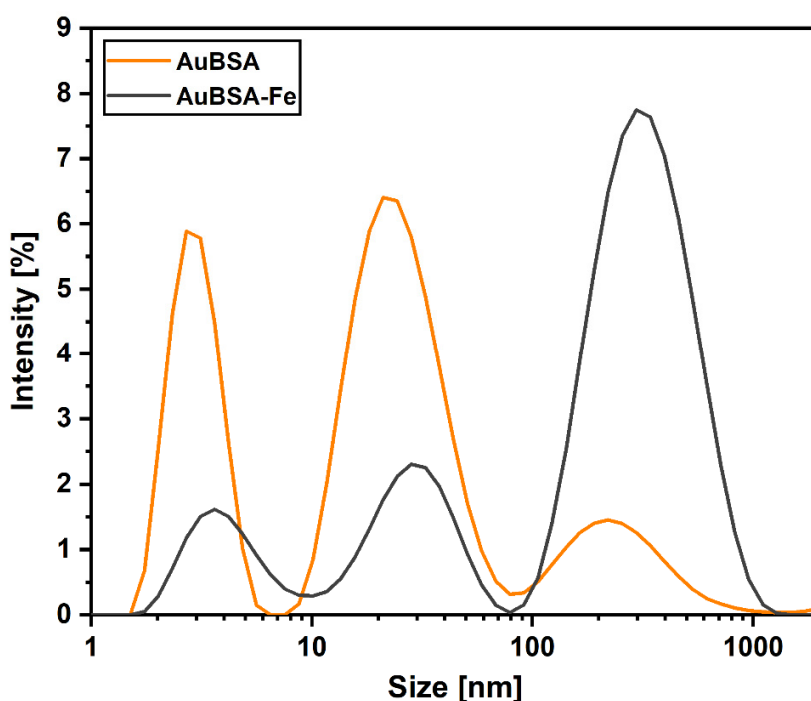
Figure S2. Particle size distribution (PSD) histograms of AuBSA (orange curve) and AuBSA-Fe (black curve) based on the changes in intensity of scattered light (633 nm laser line) measured by dynamic light scattering. Trimodal PSD is observed in both samples, however, with different average values and percentage (in brackets): 266.1 ± 38.0 nm (12.9 ± 2.1 %), 26.8 ± 2.4 nm (50.8 ± 1.2 %), 3.0 ± 0.1 nm (27.7 ± 0.8 %) for AuBSA; 351.2 ± 21. 0 nm (68.7 ± 1.4 %), 30.0 ± 2.9 nm (16.7 ± 0.9 %), 4.4 ± 0.3 nm (10.6 ± 0.8 %) for AuBSA-Fe.

Three different types of NP sizes are thus present in both aqueous systems AuBSA and AuBSA-Fe (representing proper solutions, i.e., without any aggregates visible by naked eyes): several units, tens, and hundreds of nanometers, which well explains the relatively large PDI values. Obviously, there is a more significant contribution of the largest particles (around 351 nm in average) in PSD of AuBSA-Fe in comparison to PSD of AuBSA (Figure SI-2). However, their sizes

are still in hundreds of nanometers, which means that these nanoparticles could be internalized by cells (which are 10-100 μm in size for most animal and plant cells).

Reproducibility of PSD data is demonstrated in Figures SI-3 and SI-4 and in Tables SI-3 and SI-4. By assuming spherical isolated particles, PSD based on number can be also calculated as seen in Tables SI-3 and SI-4. However, it should be reminded that PSD based on particle number is the calculated value obtained under the above-mentioned assumptions of identical, spherical, isolated particles.

Table S3. PSD of several independently measured AuBSA samples determined by DLS based on intensity (Int) and number (Num). Average and standard deviation (SD) values are then calculated.

AuBSA	Int 1 [nm]	Int 2 [nm]	Int 3 [nm]	Num 1 [nm]	Area Int 1 [%]	Area Int 2 [%]	Area Int 3 [%]	Area Num 1 [%]	Z-Average [nm]	PDI
I	243.6	26.4	3.0	2.2	13.1	52.6	27.9	100.0	42.86	0.236
II	246.2	25.0	2.9	2.2	12.0	50.7	27.7	100.0	16.08	0.438
III	303.3	27.1	3.0	2.3	13.4	49.5	27.8	100.0	21.15	0.389
IV	227.2	24.9	3.0	2.2	10.1	49.9	28.7	100.0	20.62	0.327
V	310.4	30.8	3.2	2.4	15.9	51.3	26.5	100.0	18.92	0.494
Average	266.1	26.8	3.0	2.3	12.9	50.8	27.7	100.0	23.9	0.4
SD	38.0	2.4	0.1	0.1	2.1	1.2	0.8	0.0	10.8	0.1

Table S4. PSD of several independently measured AuBSA-Fe determined by DLS based on intensity (Int) and number (Num). Average and standard deviation (SD) values are then calculated.

| AuBSA-Fe	Int 1 [nm]	Int 2 [nm]	Int 3 [nm]	Num 1 [nm]	Area Int 1 [%]	Area Int 2 [%]	Area Int 3 [%]	Area Num 1 [%]	Z-Average [nm]	PDI
I	361.2	34.4	4.7	2.2	67.7	17.2	11.2	100.0	83.61	1.000
II	331.5	26.8	4.2	2.8	70.3	15.4	9.8	100.0	71.59	1.000
III	382.3	30.4	3.9	2.6	68.8	17.8	9.8	100.0	71.28	1.000
IV	334.1	28.5	4.6	2.5	67.0	16.4	11.3	100.0	68.13	1.000
V	347.0	30.0	4.5	2.4	69.8	16.9	11.1	100.0	61.61	1.000
Average	351.2	30.0	4.4	2.5	68.7	16.7	10.6	100.0	71.2	1.0
SD	21.0	2.9	0.3	0.2	1.4	0.9	0.8	0.0	8.0	0.0
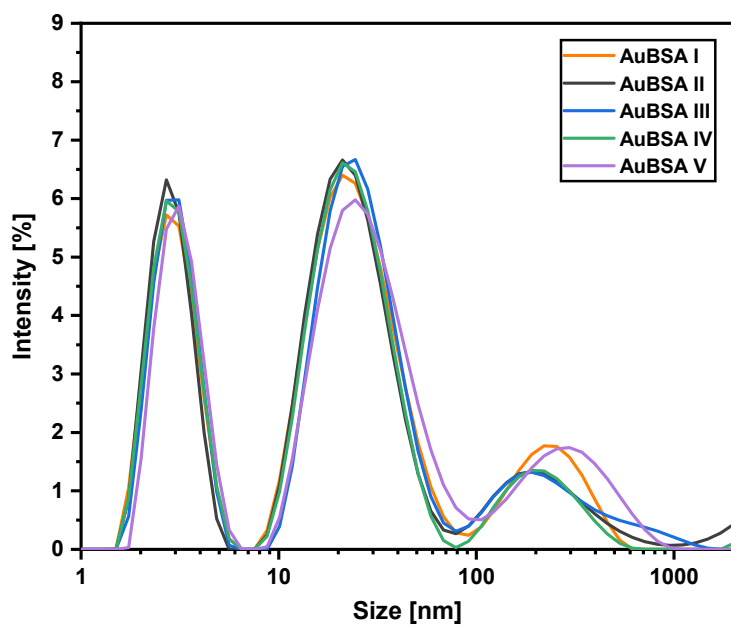
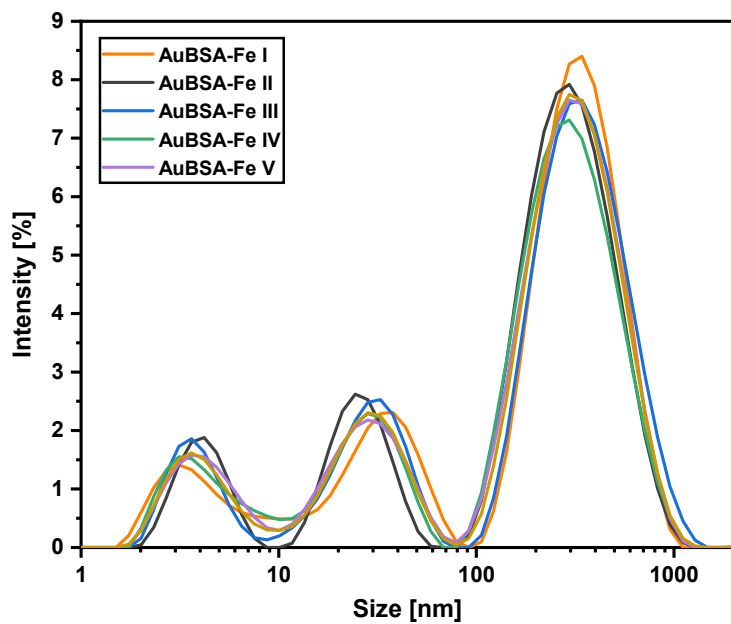**Figure S3.** Histograms of PSD of several independently measured AuBSA.

Figure S4. Histograms of PSD of several independently measured AuBSA-Fe.

3. ICP-MS method validation and determination of Au and Fe concentrations

The total gold and iron concentrations were determined by an Agilent 7700x ICP-MS (Agilent Technologies Ltd., Japan) fitted with ASX-520 autosampler, MicroMist concentric nebulizer, a Scott-type double pass spray chamber, and an octopole reaction system working in helium mode was used for all analyses. The optimized ICP-MS operating conditions were as follows: RF power of 1550 W, plasma gas flow rate of 15.0 L·min^{-1}, an auxiliary gas flow rate of 0.9 L·min^{-1}, nebulizer gas flow rate of 1.05 L·min^{-1}, collision gas He flow rate of 4.3 mL·min^{-1} and a dwell time of 100 ms for ^{56}Fe, ^{197}Au, ^{45}Sc, ^{209}Bi isotopes (last two served as internal standards).

The ICP-MS method validation covered the evaluation of limit of detection (LOD), the limit of quantification (LOQ), trueness, precision (repeatability). Moreover, the quality control sample at the concentration level of 50 mg·L^{-1} for Fe, and 500 mg·L^{-1} for Au was analysed every ten samples to ensure the quality of the routinely acquired results.

Linearities of calibration curves were evaluated within a range from 10 to 2 000 µg·L^{-1} for Fe and 100 to 10 000 µg·L^{-1} for Au, respectively. LODs and LOQs were calculated using the equations: LOD = 3.3 SD/s and LOQ = 10 SD/s, where SD is the standard deviation of the signal intensity (standard deviation of the intercept) and s is the slope of the calibration curve. Trueness and precision were assessed by analyses of 6 independently prepared spiked samples at the concentration level of 500 µg·L^{-1} for Fe, and 5 000 µg·L^{-1} for Au. Calculated recoveries for Fe, and Au in repeatedly measured QC samples (n=9) were 101.7 %, 101.8 %. The validation results are summarized in Table SI-5.

Table S5. Validation results for ICP-MS.

Parameter	Analyte	
	Fe	Au
Calibration range [µg·L^{-1}]	10 – 2 000	100 – 10 000
Correlation coefficient	0.9999	0.9999
LOD [µg·L^{-1}]	9	2
LOQ [µg·L^{-1}]	27	6
Trueness [%]	96.3	101.1
Precision [%]	0.6	0.5

Table S6. Contents of Au and Fe in many independently prepared AuBSA-Fe samples as determined by ICP-MS and calculation of Au:Fe ratios in real samples.

Sample	[Au] [mM]	[Au] [mg·mL⁻¹]	[Fe] [μM]	[Fe] [μg·mL⁻¹]	Au:Fe		
M-8	3.9	0.8	321.1	17.9	12.2		
M-7	4.9	1.0	359.6	20.1	13.5		
M-6	5.9	1.2	421.5	23.5	14.0		
M-5	7.0	1.4	508.8	28.4	13.8		
M-4	8.3	1.6	636.4	35.5	13.1		
M-3	10.6	2.1	750.2	41.9	14.2		
M-2	11.7	2.3	894.4	49.9	13.0		
M-1	13.9	2.7	1049.2	58.6	13.2		
M1	10.9	2.2	807.0	45.1	13.6		
M2	14.0	2.8	1020.4	57.0	13.7		
M3	16.1	3.2	1193.3	66.6	13.5		
M4	17.1	3.4	1248.5	69.7	13.7		
				Average	13.5	13.3	Theory
				SD	0.5		

Note: Average Au:Fe ratio in real samples coincides well with the theoretical ratio of these metals (theoretical Au:Fe ratio derived from BSA:Au:Fe = 1:10:0.75 => 10/0.75 ≐ 13.3)

4. MRI for AuBSA-Fe samples

Table S7: Values of relaxation times T_1, T_2 and relaxation rates R_1, R_2 together with real iron concentrations (as determined by ICP-MS for concentrated samples, while derived from these values for diluted samples).

Sample	Sample concentration [%]	Fe concentration [mM]	T_1 [ms]	R_1 [s^{-1}]	T_2 [ms]	R_2 [s^{-1}]
M-8	100	0.321	2200	0.455	835	1.198
	75	0.241	2560	0.391	1085	0.922
	50	0.161	2285	0.438	809.5	1.235
	25	0.080	1490	0.671	492.2	2.032
M-7	100	0.360	2450	0.408	787	1.271
	75	0.270	2355	0.425	926.2	1.080
	50	0.180	3020	0.331	1360	0.735
	25	0.090	3390	0.295	1869.2	0.535
M-6	100	0.421	2305	0.434	700	1.429
	75	0.316	2570	0.389	926.2	1.080
	50	0.211	2800	0.357	1092	0.916
	25	0.105	3320	0.301	1765.3	0.566
M-5	100	0.509	1970	0.508	587.6	1.702
	75	0.382	2270	0.441	757.1	1.321
	50	0.254	2590	0.386	973.4	1.027
	25	0.127	3100	0.323	1579.4	0.633
M-4	100	0.636	1820	0.549	473	2.114
	75	0.477	2145	0.466	602.1	1.661
	50	0.318	2635	0.380	920.4	1.086
	25	0.159	3100	0.323	1420.8	0.704
M-3	100	0.750	1515	0.660	364	2.747
	75	0.563	1920	0.521	487.7	2.050
	50	0.375	2379	0.420	704.3	1.420
	25	0.188	2855	0.350	1151.2	0.869
M-2	100	0.894	1515	0.660	301.1	3.321
	75	0.671	1810	0.552	386.3	2.589
	50	0.447	2315	0.432	629.7	1.588
	25	0.224	2930	0.341	1003.1	0.997

Table S7. Cont.

M-1	100	1.049	1305	0.766	213.4	4.686
	75	0.787	1610	0.621	331.133	3.020
	50	0.525	2080	0.481	459	2.179
	25	0.262	2795	0.358	889.73	1.124
M1	100	0.807	1815	0.551	447	2.237
	75	0.605	2050	0.488	593	1.686
	50	0.404	2355	0.425	723	1.383
	25	0.202	2780	0.360	1023	0.978
M2	100	1.020	1655	0.604	379	2.639
	75	0.765	1810	0.552	427	2.342
	50	0.510	2230	0.448	638	1.567
	25	0.255	2430	0.412	918	1.089
M3	100	1.193	1365	0.733	264	3.788
	75	0.895	1560	0.641	308	3.247
	50	0.597	1830	0.546	479	2.088
	25	0.298	2590	0.386	911	1.098
M4	100	1.249	1271	0.787	216	4.630
	75	0.936	1535	0.651	290	3.448
	50	0.624	1915	0.522	442	2.262
	25	0.312	2655	0.377	767	1.304

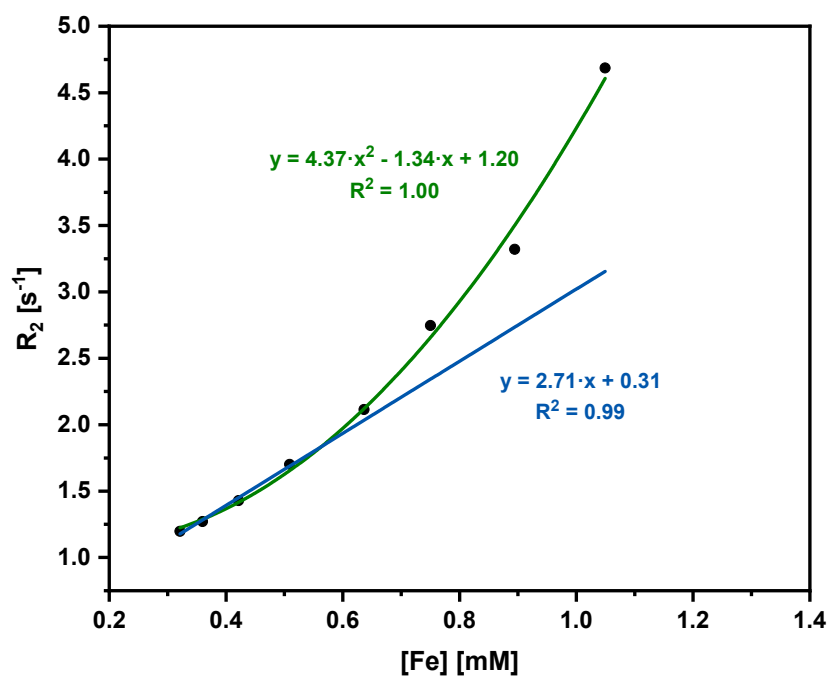Note: Green values were excluded.

Figure S5. Relaxation rates as a function of iron concentration in AuBSA-Fe samples (100% concentration, any dilution is omitted). Comparison of linear and nonlinear (quadratic) fits.

Note: Quadratic fit is best suited for highly concentrated samples where the aggregation of protein occurs. Simultaneously, superparamagnetic iron oxide particles (SPIONs) attached to the protein are aggregated which may lead to the non-linear character of relaxation rate values with increasing sample concentrations.

5. Ageing and storage conditions of AuBSA-Fe samples

XPS spectra of AuBSA-Fe samples were measured shortly after their preparation (M6 in Figures SI-5) and after 1 year of ageing (M3 in Figures SI-5) at room temperature. Interestingly, in both samples only Au (0) was detected by XPS – see Figures SI-5**A** and SI-5**B**, which means that the inorganic part of the samples is not destroyed/changed. On the contrary, the relative contents of various types of organic species derived from N1s, O1s, C1s signals, varied significantly in fresh vs. aged samples – see Figures SI-5**C** – SI-5**J**. This points to a degradation of the organic part of AuBSA-Fe nanocomposites, namely a sort of oxidation takes place (based on occurrence of ammonium signal). It is highly recommended to store the samples in a fridge.
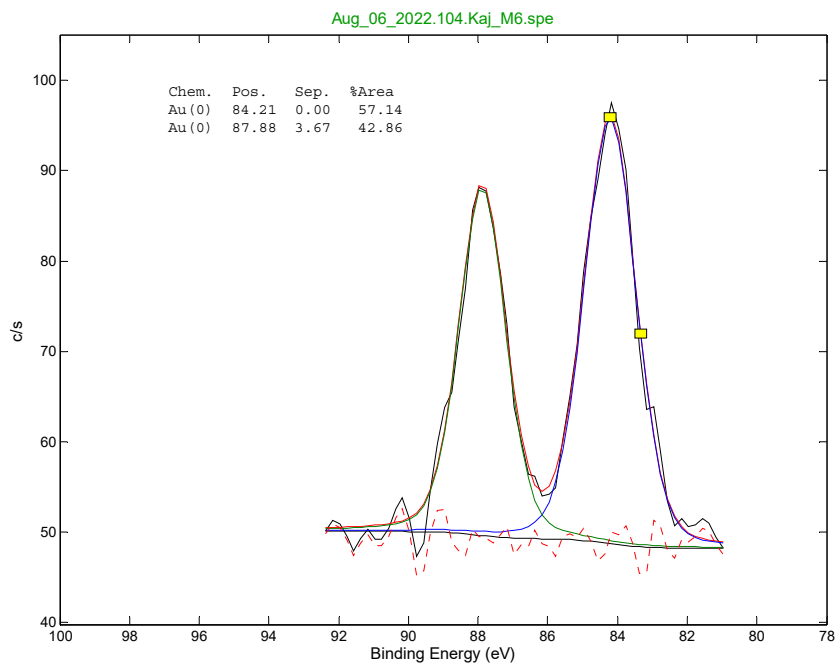
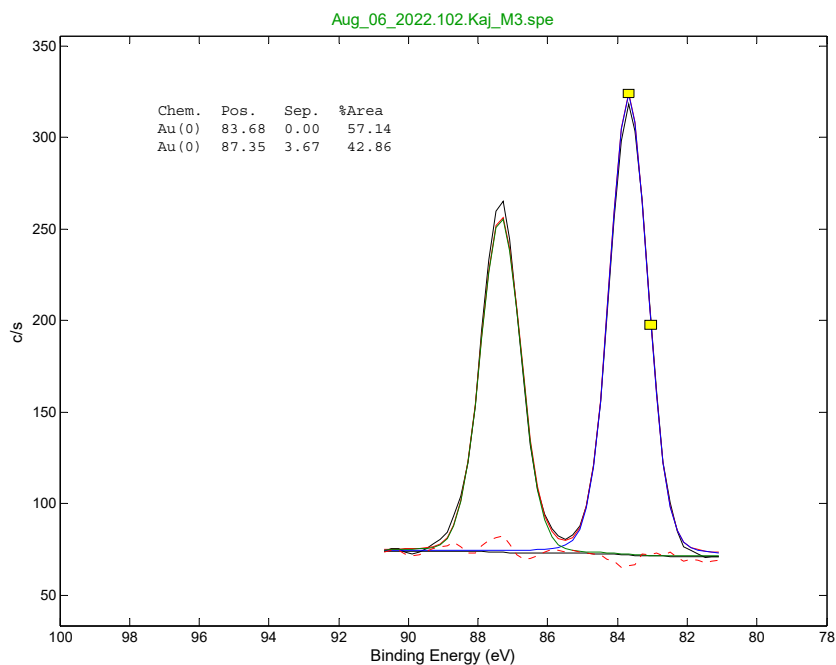**Figure S6A.** XPS signal of fresh AuBSA-Fe sample, Au4f region.

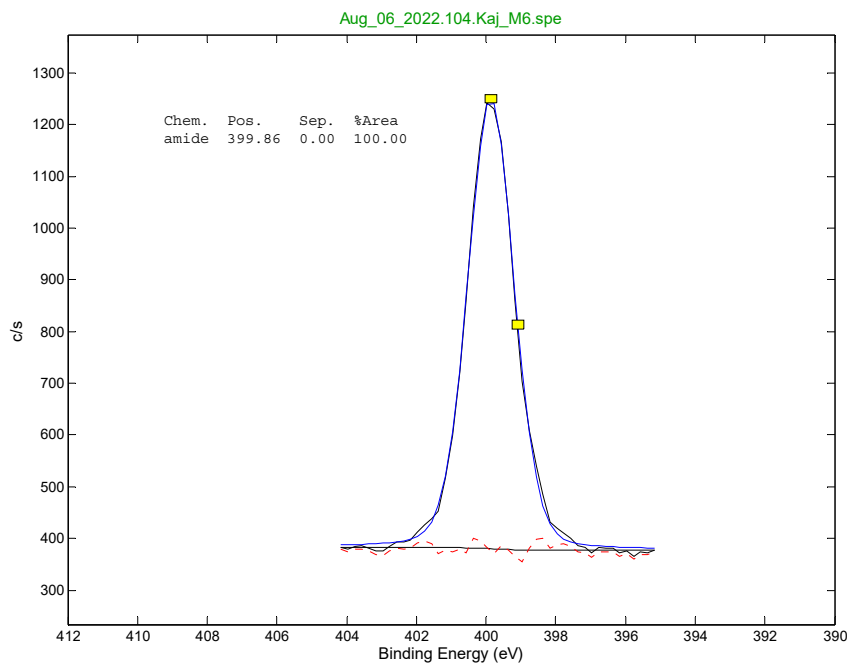**Figure S6B.** XPS signal of one-year aged AuBSA-Fe sample, Au4f region.

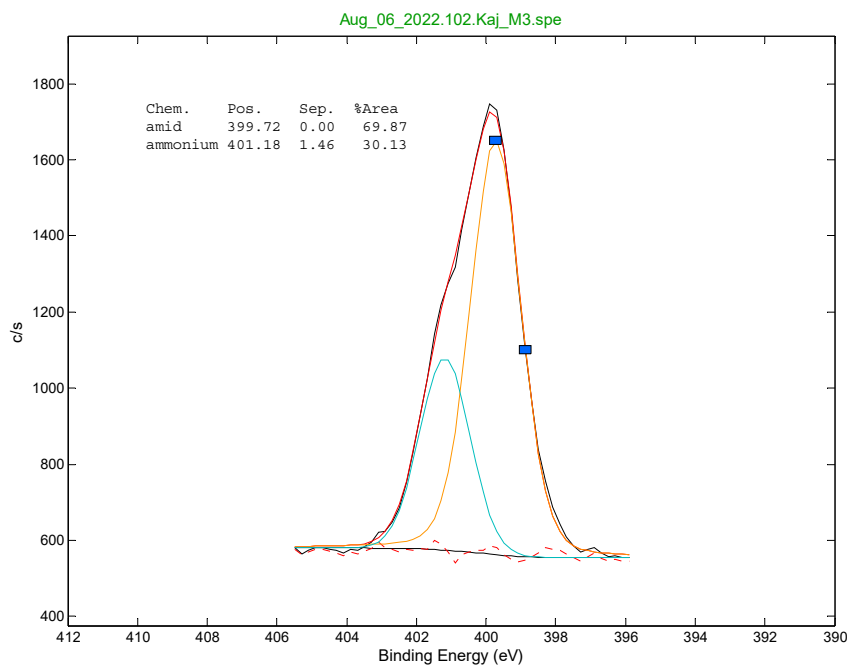**Figure S6C.** XPS signal of fresh AuBSA-Fe sample, N1s region.

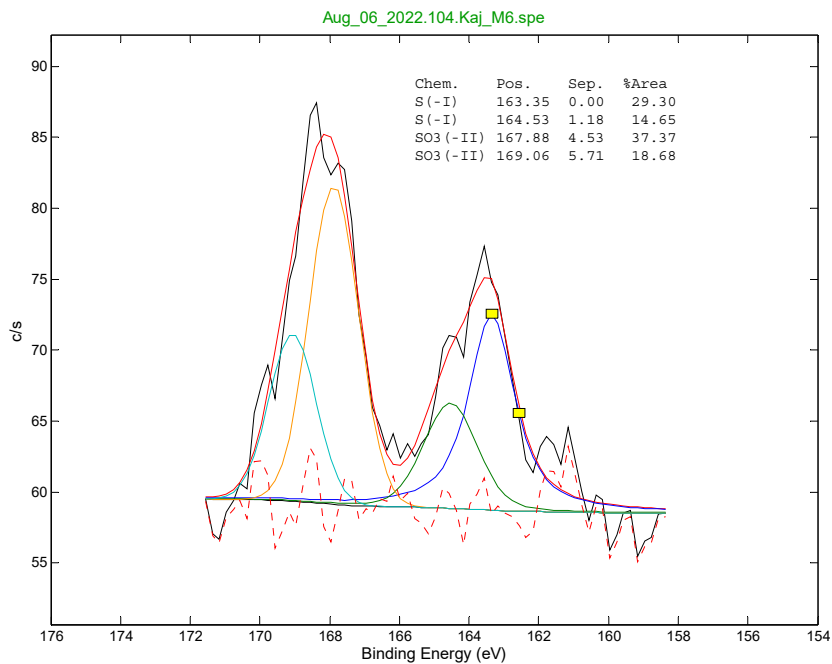**Figure S6D.** XPS signal of one-year aged AuBSA-Fe sample, N1s region**.**

Figure S6E. XPS signal of fresh AuBSA-Fe sample, S2p region.
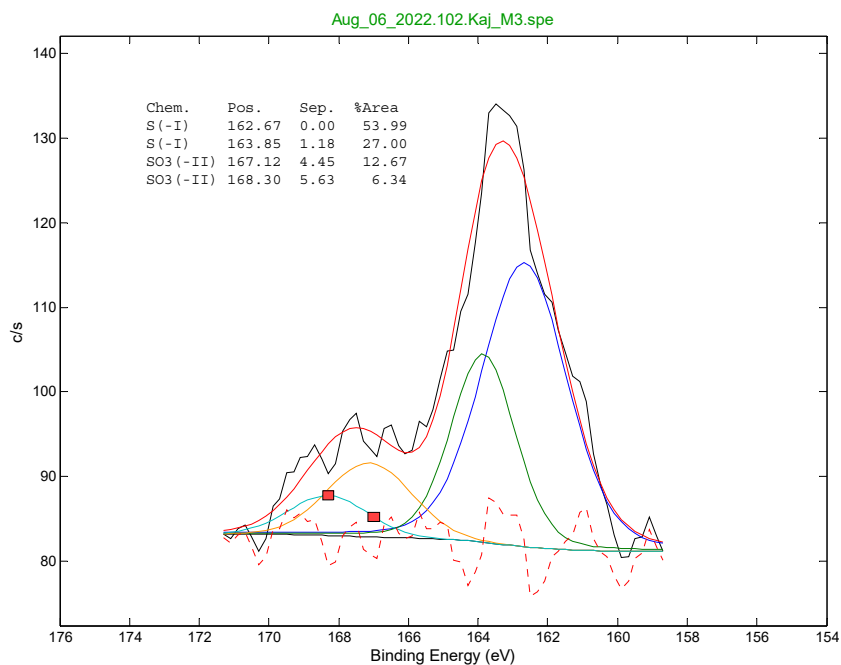

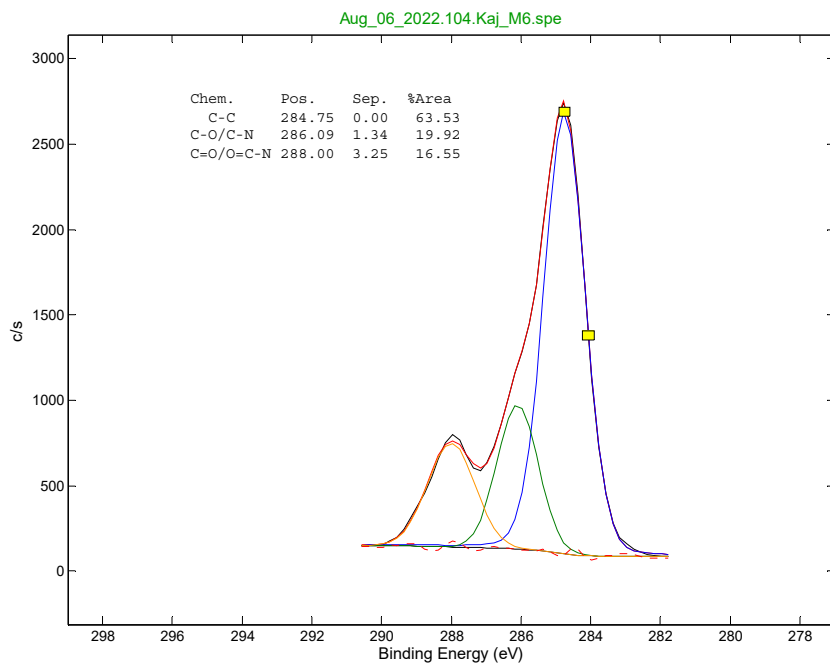**Figure S6F.** XPS signal of one-year aged AuBSA-Fe sample, S2p region.

Figure S6G. XPS signal of fresh AuBSA-Fe sample, C1s region**.**
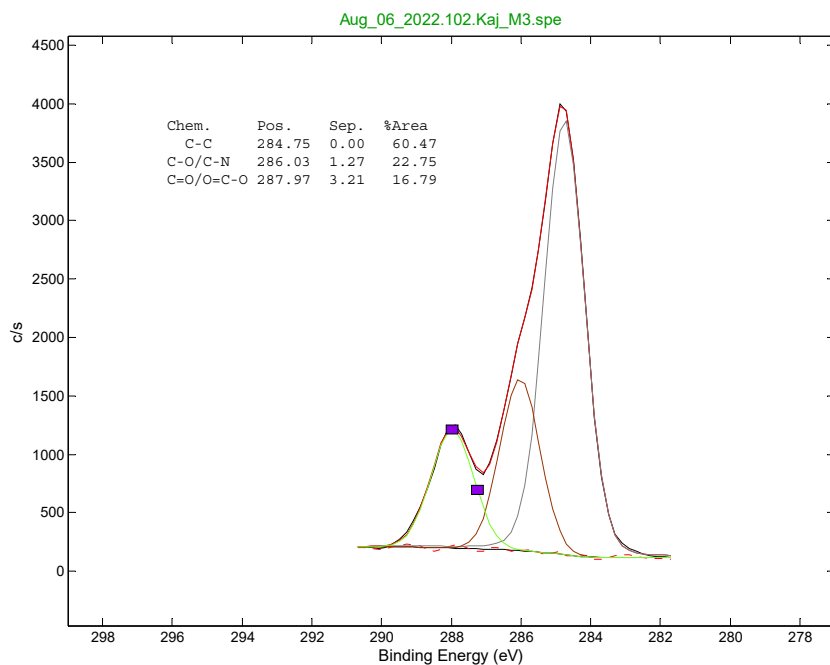

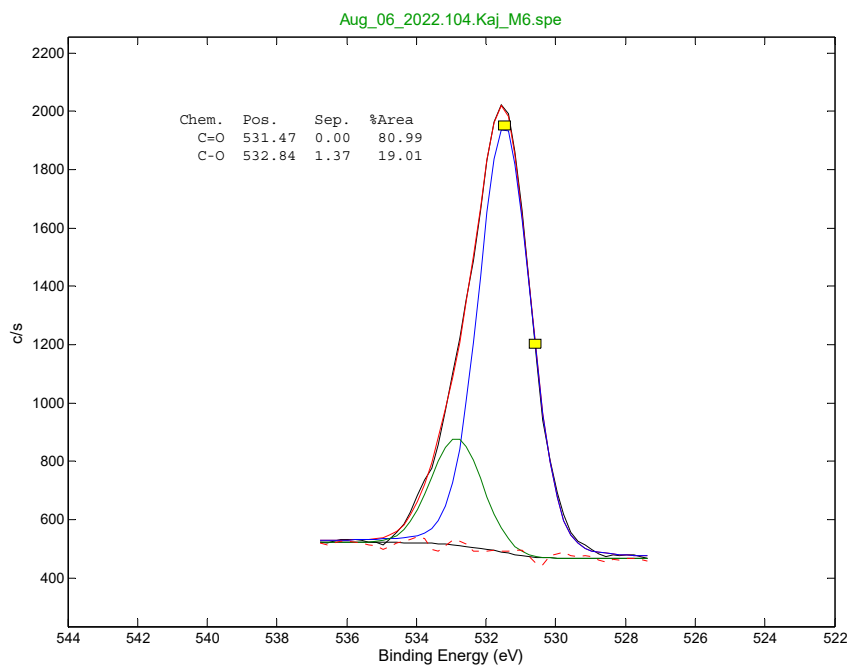**Figure S6H.** XPS signal of one-year aged AuBSA-Fe sample, C1s region.

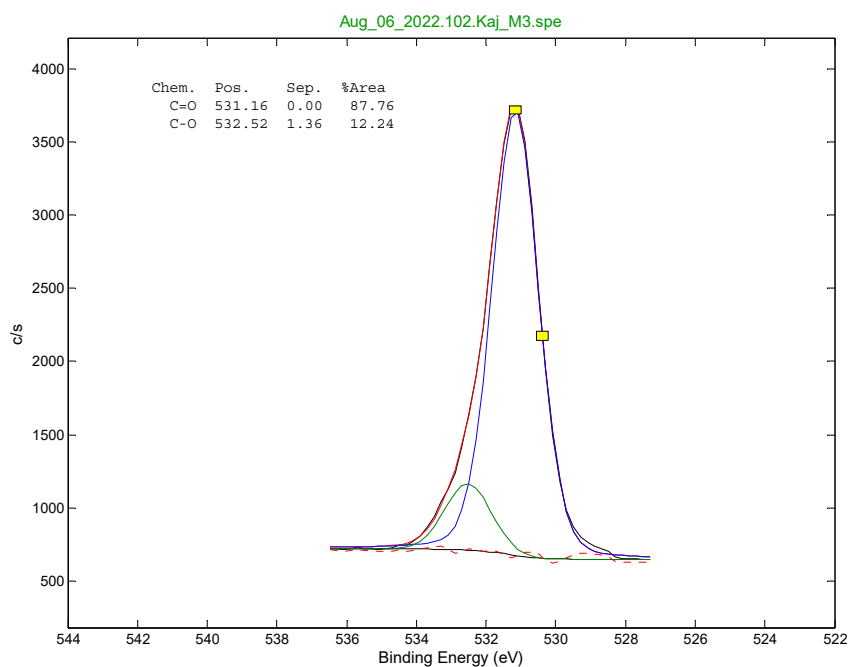**Figure S6I.** XPS signal of fresh AuBSA-Fe sample, O1s region.

Figure S6J. XPS signal of one-year aged AuBSA-Fe sample, O1s region.

6. Cell viability tests of AuBSA-Fe nanocomposites – Alamar blue assay

Table S8: Table showing values of fluorescence in each well of the titration plate when cell viability tests of AuBSA-Fe nanocomposites and their precursors (HAuCl$_4$, mixture of FeCl$_2$ and FeCl$_3$) were performed in two representative iron concentrations (below and above 0.52 mM).

	1	2	3	4	5	6	7	8	9	10	11	12
A												
B		867	29735	2200	29289	24847	24735	1944	22831	24020	21247	
C		835	30876	2210	27409	23349	23919	1955	23864	24412	23791	
D		836	30373	2255	27282	23384	25086	1961	22664	24639	23549	
E		861	31141	2407	20874	23155	25072	2278	794	25358	24243	
F		856	30711	2354	20757	24421	24207	2288	801	25066	24370	
G		880	32978	2283	16906	24822	24941	2318	791	24956	24286	
H												

	1	2	3	4	5	6	7	8	9	10	11	12
A												
B		cultivation medium	RPE-1 cells	HAuCl$_4$	FeCl$_2$ + FeCl$_3$	AuBSA-Fe (c(Fe) < 0.52 mM)	AuBSA-Fe (c(Fe) ≥ 0.52 mM)			The other samples and precursors		
C												
D												
E				HAuCl$_4$	FeCl$_2$ + FeCl$_3$							
F												
G												
H												

Note: For the detection of outliers (green values), Grubbs' or Dixon's test was used.

III

Engineered protein-iron and/or gold-protein-iron nanocomposites in aqueous solutions upon UVA light: Photo-induced electron transfer possibilities and limitations.

Zoppellaro G., Ostruszka R., Šišková K.

Advanced protein-embedded bimetallic nanocomposite optimized for *in vivo* fluorescence and magnetic resonance bimodal imaging

Ostruszka R., Halili A., Pluháček T., Rárová L., Jirák D., Šišková K.

Check for updates
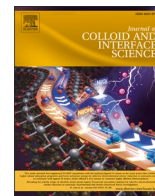
Advanced protein-embedded bimetallic nanocomposite optimized for *in vivo* fluorescence and magnetic resonance bimodal imaging

Radek Ostruszka [a], Aminadav Halili [b], Tomáš Pluháček [c], Lucie Rárová [d], Daniel Jirák [b,e], Karolína Šišková [a,*]

[a] Department of Experimental Physics, Faculty of Science, Palacký University Olomouc, tř. 17. listopadu 12, 77900 Olomouc, Czech Republic
[b] Institute for Clinical and Experimental Medicine, Vídeňská 9, 140 21 Prague, Czech Republic
[c] Department of Analytical Chemistry, Faculty of Science, Palacký University Olomouc, tř. 17. listopadu 12, 77900 Olomouc, Czech Republic
[d] Department of Experimental Biology, Faculty of Science, Palacký University Olomouc, Šlechtitelů 27, 77900 Olomouc, Czech Republic
[e] Faculty of Health Studies, Technical University of Liberec, Studentská 1402/2, 46117 Liberec, Czech Republic

GRAPHICAL ABSTRACT
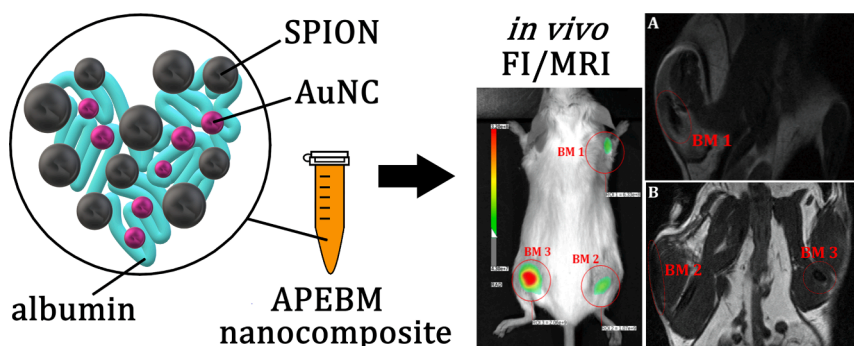
ARTICLE INFO

ABSTRACT

Hypothesis: The development of bimodal imaging probes represents a hot topic of current research. Herein, we deal with developing an innovative bimodal contrast agent enabling fluorescence imaging (FI)/magnetic resonance imaging (MRI) and, simultaneously, consisting of biocompatible nanostructures. Optimized synthesis of advanced protein-embedded bimetallic (APEBM) nanocomposite containing luminescent gold nanoclusters (AuNC) and superparamagnetic iron oxide nanoparticles (SPION), suitable for *in vivo* dual-modal FI/MR imaging is reported.

Experiments: The APEBM nanocomposite was prepared by a specific sequential one-pot green synthetic approach that is optimized to increase metals (Au, Fe) content and, consequently, the imaging ability of the resulting nanostructures. The protein matrix, represented by serum albumin, was intentionally chosen, and used since it creates an efficient protein corona for both types of optically/magnetically-susceptible nanostructures (AuNC, SPION) and ensures biocompatibility of the resulting APEBM nanocomposite although it contains elevated metal concentrations (approx. 1 mg·mL^{-1} of Au, around 0.3 mg·mL^{-1} of Fe). In vitro and *in vivo* imaging was performed.

* Corresponding author.
 E-mail address: karolina.siskova@upol.cz (K. Šišková).

Findings: Successful *in vivo* FI and MRI recorded in healthy mice corroborated the applicability of the APEBM nanocomposite and, simultaneously, served as a proof of concept concerning the potential future exploitation of this new FI/MRI bimodal contrast agent in preclinical and clinical practice.

1. Introduction

Bimodal and/or multimodal contrast agents are frequently asked in preclinical and clinical practice [1] since they can lead to improved localization and sensitivity of a chosen target while using a single injection, mitigating the effects of invasive monitoring. Bimodal imaging probes composed of fluorescent (especially that emitting in the near-infrared region, NIR) and magnetically susceptible parts fulfil both requirements at once, i.e., high sensitivity and unlimited spatial resolution, respectively, overcoming thus the limitations associated with the stand-alone systems [2,3]. Moreover, owing to the unique conjunction of two physical phenomena, luminescence and superparamagnetism, within one contrast agent (i.e., one probe for dual-modal monitoring), *in vivo* imaging is going to become less time-consuming and cost-effective, meeting thus current social and economic requirements. Over the past two years, there have been published more than one hundred scientific reviews (according to Web of Science) dealing with multimodal and *in vivo* imaging. Similarly, the topic of multimodal *in vivo* imaging exploiting nanoarchitectures, nanostructures, and/or nanocomposites of different kinds and compositions is very popular among scientists; almost three hundred papers have been published in recent two years (based on literature investigation using Web of Science). Thus, this research field is undoubtedly fancy and quickly developing.

Nanocomposites are frequently designed in core-shell and/or core-shell-shell architectures, comprising an inorganic core with organic layer/s around [4,5]. Another strategy embodies entrapping functional components into some matrices/scaffolds, such as metal-organic frameworks [6,7], various graphene oxides [8,9], mesoporous silica [10], silica/organosilica cross-linked block copolymer micelles [11,12], and/or proteins [13,14]. Inspired by our latest research [15] as well as by other researchers, serum albumin was chosen as a protein matrix/template for the incorporation of luminescent gold nanoclusters (AuNC) and superparamagnetic iron oxide nanoparticles (SPION) in the present work. Serum albumin, a well-known efficient transportation protein found in vertebrate blood, helps achieve better biocompatibility and prolongs the blood circulation lifetime of functional nanostructures (e. g., [16–19]). The step of biomimetic coating, ensuring biocompatibility of functional nanostructures in living organisms (e.g., [7,20–23]), can be thus avoided, consequently, the synthesis becomes simpler and faster.

Nanocomposites consisting of albumin conjugated with nanostructures composed of gold and gadolinium for *in vivo* FI/MR imaging were prepared and published [24,25]. Both of these bimetallic nanocomposites [24,25] possess magneto-luminescent properties; however, they are based on gadolinium ions that are generally considered toxic and represent potential risks to the environment and human health [26]. Therefore, one should rather avoid the usage of Gd(III) ions and concentrate on benign iron ions instead [27–29]. Beneficial for iron oxide usage in bimetallic nanocomposites intended to be exploited in *in vivo* FI/MR imaging is also a significant number of clinically approved imaging iron-oxide-bearing nanoparticles [30].

Herein, we developed the APEBM (advanced protein-embedded bimetallic) nanocomposite, which was tested as FI/MRI contrast agent *in vivo*. The APEBM nanocomposite is inspired by our previous work [15]; however, there are substantial changes in the preparation procedure developed and described by us in the current work. In fact, we wanted to develop a versatile and robust green synthesis of bimodal (and potentially multimodal) contrast agents, meaning that any other desired metal and/or functionality can be easily added/introduced while the stability of the final functional nanocomposite is maintained and, simultaneously, its applicability improved. To the best of our knowledge,

another system containing luminescent AuNC-SPION and simultaneously demonstrating *in vivo* bimodal imaging capability has not been published yet.

Prior to the subcutaneous injection (aimed to assess the suitability of the nanocomposite for optical imaging, similarly as in [31] into healthy mice and FI/MRI measurements, the APEBM nanocomposite was characterized by appropriate experimental techniques including UV–Vis absorption spectroscopy, steady-state fluorescence, high-resolution transmission electron microscopy (HR-TEM), scanning transmission electron microscopy (STEM), energy dispersive X-ray spectroscopy (EDS), inductively coupled plasma mass spectrometry (ICP-MS), dynamic light scattering (DLS), zeta potential measurements, MR imaging, and relaxometry. Healthy cell (RPE-1) viability in the presence of the APEBM nanocomposite was assessed employing calcein assay. The results of cytotoxicity corroborated the expected biocompatibility that is most probably inherited from the components of the APEBM nanocomposite. Tests of fluorescence signal stability of APEBM nanocomposites in different media (e.g., PBS and cultivation medium) at various temperatures were investigated and revealed relatively stable integrated fluorescence emission that was superior to the average integrated fluorescence emission intensity obtained in deionized water. Moreover, fluorescence emission intensity of APEBM nanocomposites in the presence of HeLa cancer cells was checked after 1, 2, and 24 h of cells incubation (within the cultivation medium). The results confirmed fluorescence signal stability even in the presence of HeLa cells.

2. Materials and methods

2.1. Used chemicals

2.1.1. Chemicals for the APEBM nanocomposite synthesis

Bovine serum albumin (BSA; greater than 98%), gold(III) chloride trihydrate (HAuCl$_4$·3H$_2$O, ≥99.9%), iron(III) chloride hexahydrate (FeCl$_3$·6H$_2$O; ≥99%), and sodium hydroxide (NaOH; ≥98.0%) were purchased from Sigma-Aldrich (Saint Louis, MO, USA) and used as received (without any further purification) for all experiments. Deionized water was prepared by purging Milli-Q purified water (Millipore Corporation, Bedford, MA, USA) and used for fluorescence spectroscopy and DLS measurements.

2.1.2. Chemicals for ICP-MS

Nitric acid (69%, Analpure) and hydrochloric acid (36%, Analpure) certified reference materials of calibration standard solution ASTASOL® of Au, Fe (1 000 ± 2 mg·L^{-1}) and INT-MIX 1 (10.0 ± 0.1 mg·L^{-1}) were purchased from Analytika, Ltd., Czech Republic. Ultrapure 18.2 MΩ cm water was prepared using a Milli-Q reference water purification system (Millipore Corp. Molsheim, France) and used only for ICP-MS analyses.

2.1.3. Chemicals for Calcein-AM assay and fluorescence signal stability experiments

Fetal bovine serum (FBS), L-glutamine, Penicillin-Streptomycin, and trypsin (from the porcine pancreas) were purchased from Sigma-Aldrich (Saint Louis, MO, USA). Dulbecco's Modified Eagle Medium (DMEM, 11054) and Calcein-AM salt were purchased from Thermo Fisher Scientific (Waltham, MA, USA). Sodium chloride (NaCl; p.a.), potassium chloride (KCl; p.a.), potassium dihydrogen phosphate (KH$_2$PO$_4$; p.a.), and disodium hydrogen phosphate (Na$_2$HPO$_4$; p.a.) were purchased from Penta chemicals (Prague, Czech Republic). Healthy RPE-1 cell line was obtained from M. Mistrík (Institute of Molecular and Translational Medicine, Olomouc, Czech Republic).

2.1.4. Chemicals for in vivo imaging experiments

Isoflurane (5% for induction and 1.5–2% for maintenance) was purchased from Baxter (Deerfield, IL, USA), and an eye cream Ophtalmo-Septonex was purchased from Zentiva (Prague, Czech Republic).

2.2. Synthesis of the APEBM nanocomposite, purification, concentrate formation, and storage conditions

The synthetic procedure of the APEBM nanocomposite system is an optimized, specifically modified version of the one-pot synthesis we applied in our previous work devoted to the preparation of bimetallic nanocomposites by green chemical approach [15]. Briefly, $FeCl_3 \cdot 6H_2O$ (200 μL, 0.1 M) was introduced into a microcentrifuge tube. Subsequently, BSA solution (500 μL, 66.43 mg·mL^{-1}) was slowly added while constantly mixed with a pipette (see video in SI). Instantly after that, the same amount of BSA (500 μL, 66.43 mg·mL^{-1}) was analogously pipetted, and the reaction mixture was then swirled in a vortex at 3000 rpm (kept for all further steps when the same vortex was used). Importantly, visible agglomerates were formed during both steps of protein solution addition but gradually dissolved due to the constant mixing with a pipette. NaOH (57.5 μL, 1 M) was rapidly introduced and placed into the tube five minutes later. Then, the tube content was immediately swirled in the vortex. The reaction solution became cloudy, but after several minutes, it started to clear up. Ten minutes later, $HAuCl_4$ (800 μL, 25 mM) was slowly added while constantly mixed. The gradual formation of a cloudy solution was observed again. The tube content was swirled in the vortex, and five minutes later, NaOH (142.5 μL, 1 M) was quickly introduced into the solution. Then, the tube was swirled in the vortex for the last time, immediately accompanied by the solution clearing up. Subsequently, the microcentrifuge tube was put into a dry bath incubator for 22.5 h, where the temperature was set to 50 °C. The as-prepared sample is of orange-brown colour without any aggregate or agglomerate visible to the naked eye. It must be noted that before putting the tube into the dry bath incubator, the solution could sometimes appear mildly cloudy, but this should eventually disappear after several tens of minutes during the incubation at around 50 °C.

After maturing inside a dry bath incubator, the sample was dialyzed with a 14 kDa cut-off dialysis membrane (regenerated cellulose, Membra-Cel^{TM}) against deionized water. Dialysis was performed at room temperature (22 °C) for 5 h, with deionized water being changed four times: after 30 min, 45 min, 60 min, and 75 min. For the cell viability experiments, a concentrated form of the sample was prepared using a centrifugal concentrator (30 kDa). The rotational centrifugal force (RCF) was set to 3000 g, and the centrifugation lasted for 5 min. This process was done repeatedly until the chosen concentration was reached. Dialyzed and concentrated samples were then stored in the dark at 4 °C.

2.3. Characterization techniques

2.3.1. High-resolution transmission electron microscopy (HR-TEM) and energy dispersive X-ray spectroscopy (EDS) analysis

A representative APEBM sample was drop-casted (2–4 μL) on glow discharged TEM copper grid covered with holey carbon and allowed to dry spontaneously at room temperature. Then, the sample was measured by HR-TEM Titan G2 60–300 (FEI, Hillsboro, OR, USA) with an image corrector with an accelerating voltage of 300 kV. Images were taken with a BM UltraScan CCD camera (Gatan, Pleasanton, CA, USA). Energy Dispersive Spectrometry (EDS) was performed in STEM mode by a Super-X system with four silicon drift detectors (Bruker, Billerica, MA, USA). STEM images were taken with an HAADF detector 3000 (Fishione, Export, PA, USA). HAADF mode of STEM is intentionally used to better visualize NCs because heavier elements appear bright, while lighter elements appear dark.

2.3.2. Inductively coupled plasma mass spectrometry (ICP-MS)

The total Au and Fe concentrations were determined by a validated ICP-MS method employing a microwave-assisted digestion of the APEBM nanocomposite matrix [14]. Briefly, each sample was completely dried using a vacuum rotary evaporator Concentrator plus (Eppendorf, Hamburg, Germany) prior to the ICP-MS analysis. The dried samples were digested using a mixture of 2 mL of concentrated nitric acid and 2 mL of concentrated hydrochloric acid in the MLS 1200 mega closed vessel microwave digestion unit (Milestone, Italy) according to the even steps power-controlled digestion program. The cooled digests were quantitatively transferred into 25 volumetric flasks, filled up to the volume with ultrapure water, and mixed properly. The total Au and Fe levels were accessed using an Agilent 7700x ICP-MS (Agilent Technologies Ltd., Japan) using 8-point external calibration and the reliability of ICP-MS results was controlled by a regular measurement of an independently prepared quality control sample. All ICP-MS measurements were performed in six replicates, and the results are expressed as an average ± standard deviation (SD).

2.3.3. MR relaxometry

The MR relaxometry was utilized to determine the relaxivities r_1 and r_2 of the APEBM nanocomposite. The relaxation times T_1 and T_2 were measured on a relaxometer Bruker Minispec mq60 (Bruker Biospin, Ettlingen, Germany) at 1.5 T and stabilized temperatures of 20 °C and 37 °C during the whole experiment. Before imaging, a concentration series (denoted as 100%, 75%, 50%, and 25%) of the dialyzed APPBM nanocomposite was prepared, and distilled water served as a reference (labelled as H_2O). T_1 relaxation times were measured employing the inversion recovery (IR) sequence: repetition time (TR) = 0.01–10000 ms, recycle delay = 4 s, scans = 4, monoexponential fitting, 10 data points for fitting. T_2 relaxation times were measured using the Carr-Purcell-Meiboom-Gill (CPMG) pulse sequence: echo time (TE) = 0.05 ms, recycle delay = 2 s, scans = 8, monoexponential fitting, 20,000 data points per fitting. The relaxivities r_1 and r_2 were then calculated via the least-squares curve fitting of R_1 and R_2 relaxation rates [s^{-1}] versus real iron concentration [mM], which was determined by ICP-MS. The experimentally determined solvent (distilled water) relaxation rate R_0 was subtracted as a starting value from the nanocomposite relaxation rates prior to the linear regression analysis. Each sample was subjected to three measurements under identical conditions.

2.3.4. In vitro MR imaging

In vitro MR imaging was performed on a Bruker Biospec 47/20 (Bruker, Ettlingen, Germany) scanner at 4.7 T. Both T_1-and T_2-weighted MR images of the APEBM nanocomposite samples and distilled water (serving as a reference) were acquired using the Rapid Acquisition with Relaxation Enhancement (RARE) sequence. T_1-weighted sequence: TR = 400 ms, TE = 12 ms, number of acquisitions (NA) = 8, rare factor (RF) = 1, ST = 10 min 14 s, spatial resolution = 0.021 × 0.021 mm^2, slice thickness = 0.6 mm; T_2-weighted sequence: TR = 3300 ms, TE = 36 ms, NA = 1 and 5, RF = 1 and 5, ST = 10 min 33 s and 10 min 27 s, spatial resolution = 0.021 × 0.021 mm^2, slice thickness = 0.6 mm. MR image processing and quantification were performed using ImageJ software developed by the National Institutes of Health (Stapleton, NY, USA). Signal-to-noise ratio (SNR) was calculated from images as 0.655 × $S_{sample}/\sigma_{noise}$ and contrast-to-noise ratio (CNR) was calculated from images as $0.655 \times |S_{sample} - S_{water}|/\sigma_{noise}$, where S is signal intensity in the region of interest, σ is the standard deviation of background noise, and constant 0.655 reflects the Rician distribution of background noise in a magnitude MR image.

2.3.5. In vitro optical imaging

The *in vitro* optical imaging was performed using the SPECTRAL Ami HT imager with the subsequent image processing and quantification utilizing the Aura imaging software developed by the Spectral instruments imaging (Tucson, AZ, USA). The experiment involved

phantoms containing four different APEBM nanocomposite concentrations (100%, 75%, 50%, 25%) and distilled water, serving as a reference (labelled as H_2O). The imaging procedure included various excitation and emission ranges to identify the optimal filter settings. Specifically, the excitation at 430/500 nm and emission at 730/670 nm were used, respectively. Other parameters were set as follows: excitation power = 4, exposure time = 2 s, FOV = 15, F-stop = 2, binning = 2.

2.3.6. Fluorescence spectroscopy and dynamic light scattering (DLS)

Fluorescence measurements of the APEBM nanocomposite were performed on a JASCO F8500 (Jasco, Tokyo, Japan) spectrofluorometer using a 1 cm quartz cuvette. Emission spectra were measured in the 505–850 nm range with the data interval of 1 nm and scan speed of 100 nm·min^{-1}. The excitation wavelength was set to 430 nm and 500 nm. All spectra were corrected to avoid any deviations induced by instrumental components.

The hydrodynamic diameter and zeta potential of both systems were determined by dynamic light scattering using Zetasizer Nano ZS (Malvern Instruments Ltd, Malvern, UK) equipped with a He-Ne laser (λ = 633 nm) at 22 ± 1 °C. For both fluorescence and DLS measurements, the ratio of sample dilution with deionized water was the same (specifically, dialysed samples were diluted 26.66 times).

2.3.7. Calcein-AM assay

In a typical viability assessment, 80 μL of cultivation medium and cell suspension (RPE-1 cell line) was introduced into a 96-well plate (5000 cells per well), which was afterward put inside the incubator (37 °C, 5% CO_2) for 24 h. Subsequently, 20 μL of deionized water was pipetted to the second and third column, and eight different concentrations of the APEBM nanocomposite were pipetted in the form of hexaplicates. 24 h later, each well was washed with 95 μL of PBS two times. Then, 100 μL of calcein-AM was added into each well. After 1 h of incubation, fluorescence intensity was measured on a microplate fluorometer Fluoroskan Ascent (Finland). The excitation and emission wavelengths were set to 485 nm and 538 nm, respectively. Cell viability (CV) was then calculated according to equation (1):

$$CV = 100 \times \frac{F_{\text{sample}} - F_{\text{medium}}}{F_{\text{cells}} - F_{\text{medium}}}, \tag{1}$$

where F is the averaged fluorescence intensity and subscripts sample, cells, and medium indicate the measurement of fluorescence in the suspensions of sample-treated cells, non-treated cells, and the solution of cultivation medium alone, respectively.

2.3.8. Assessment of fluorescence signal stability in different media under varying temperatures and in the presence of HeLa cells

For the investigation of the fluorescence signal stability in different media, dialyzed APEBM nanocomposite was diluted with PBS and/or cultivation medium. The factor of dilution was kept the same as for the cell viability experiment (i.e., 5 times). For the first 24 h, diluted samples were stored at 4 °C and the emission spectra were measured after 1, 2, and 24 h. Subsequently, diluted samples were kept at room temperature (20 °C) and the emission spectra were measured after 48, 72, and 96 h. Finally, diluted samples were incubated in a dry bath incubator (the temperature was set to 37 °C to simulate the body temperature) and the emission spectra were measured after 168, 192, 216, 240, and 267 h. All spectra were measured on a JASCO F8500 (Jasco, Tokyo, Japan) for the excitation wavelength of 500 nm and were corrected to avoid any deviations induced by instrumental components. Other parameters were set the same as described in chapter 2.3.6. Fluorescence spectroscopy and dynamic light scattering (DLS).

Regarding the fluorescence signal stability in the presence of cells, 80 μL of cultivation medium and cell suspension (HeLa cell line) was introduced into a 96-well plate (5000 cells per well), which was afterwards put inside the incubator (37 °C, 5% CO_2) for 24 h. Subsequently,

20 μL of deionized water or dialyzed APEBM nanocomposite were pipetted to the medium and cell suspension in the form of hexaplicates. Then, 1, 2, and 24 h later, fluorescence intensity was measured on a microplate fluorometer Fluoroskan Ascent (Finland). The excitation and emission wavelengths were set to 500 nm and 670 nm, respectively. Fluorescence intensity was further monitored by inverted fluorescent microscope (Olympus Microscope IX51 with Fluorescence and Phase Contrasts, Japan) in the cultivation medium in the presence vs. absence of HeLa cells as a function of time.

2.3.9. In vivo experiments – optical imaging and MRI

A healthy female BALB/c mouse was housed in a temperature-controlled room with a 12-hour light–dark cycle and free access to food pellets and water. The animal preparation procedure was carried out under complete anaesthesia using isoflurane (5% for induction and 1.5–2% for maintenance), which was purchased from Baxter (Deerfield, IL, USA). To avoid eye dryness and its potential damage, an eye cream Ophtalmo-Septonex purchased from Zentiva (Prague, Czech Republic) was thoroughly applied. Additionally, all four limbs were carefully shaved to minimize the optical signal attenuation, leaving a sufficient area around the injection site.

Before *in vivo* optical imaging, the right upper limb and both lower limbs were subcutaneously injected, each with a different replicate of the dialyzed APEBM nanocomposite. Every injection contained 100 μL of the replicate, which was previously diluted 1.33 times (denoted as 75% concentration). The left upper limb was injected with distilled water serving as a reference. Immediately after the injections, optical images were acquired using the identical spectral parameters as those applied during the *in vitro* experiments.

Right before the *in vivo* MR imaging, all four limbs were additionally injected with 100 μL of the corresponding APEBM nanocomposite with the intention of enhancing the visualization and signal quality due to potential animal movement and the elapsed time between optical and MR imaging, which could result in a partial absorption of the contrast agent. For the *in vivo* MRI experiment, the homemade birdcage coil was used. Furthermore, the respiratory rate of the mouse was monitored throughout the whole experiment using a trigger unit purchased from Rapid Biomedical (Berlin, Germany). We acquired both T_1- and T_2-weighted MR images using the Rapid Acquisition with Relaxation Enhancement (RARE) sequence, employing the *in vitro* imaging protocol. To speed up the scan time, we just modified these parameters: NA = 4, RF = 8, ST = 5 min 16 s, and spatial resolution = 0.03 × 0.03 mm^2. Then, MRI data were processed and analysed using ImageJ.

All animal protocols were approved by the Ethics Committee of the Institute for Clinical and Experimental Medicine and the Ministry of Health of the Czech Republic (no. 58/2014) in accordance with the European Communities Council Directive (2010/63/EU).

3. Results and discussion

3.1. Optimized green synthesis of the APEBM nanocomposite and visualization via HR-TEM

In our previous work [15], we successfully developed a facile one-pot green synthesis of functional magneto-luminescent bimetallic nanocomposites, combining luminescent AuNC together with SPION via BSA. However, to achieve a sufficient MRI contrast, these nanocomposites had to be concentrated [15]. Simultaneously, the viscosity of the nanocomposite solutions increased. Since the increased viscosity would be a problem in any *in vivo* application, we decided to further modify and substantially optimize our synthetic approach (details are carefully discussed in Supporting Information and clearly presented in Table SI-1) and, thus, the APEBM nanocomposite was developed. Indeed, numerous preparation trials (including multiple combinations of molar ratios between protein and both metals, different order and timings of reactants addition, various pH changes amongst certain steps of the synthesis, and

several temperatures during the sample maturing in a dry bath incubator) were attempted to increase metals concentration in the final bimetallic nanocomposites with the aim of contrast signals improvement. The stability of the bimetallic nanocomposite was quite challenging because the aggregation either of iron oxide nanoparticles, or of the protein itself often occurred (Table SI-1). Finally, we succeeded in overcoming any aggregation and the specifically optimized synthetic approach respecting green chemistry principles (i.e., usage of aqueous environment, non-toxic species, and omission of abundant chemicals) was developed, i.e., the APEBM nanocomposite created. The optimized synthesis of the APEBM nanocomposite is schematically depicted in Fig. 1.

By direct comparison of the schematic depiction of the APEBM nanocomposite synthesis presented here (Fig. 1) with that used in our previous work [15], one can clearly see the substantial changes in the synthetic approach. There are several, as specified step by step below: (i) type of iron precursor/s employed; (ii) order of reactants addition; (iii) fine pH adjustment prior to auric acid addition (the newly introduced step); (iv) prolonged time among individual steps of the synthesis; (v) type of heating for the acceleration of both chemical processes, Au (III) reduction and SPION formation, under alkaline pH; (vi) increased reaction time and elevated temperature of sample maturation. Importantly, the final APEBM nanocomposite is very stable against aggregation even at elevated metal concentrations; the theoretical molar ratios of BSA: Au: Fe are 1: 20: 20 in the present work, as compared to the ratios of 1: 10: 0.75 reported in our previous article [15]. This could be achieved most probably by the newly involved step among others, i.e., increasing the pH to slightly alkaline (pH = 7.4) before adding a gold precursor. Around this pH value, ferric ions predominantly form neutral aqua complexes [32]. The neutrality may probably lead to a better interaction between the iron complex and the protein molecule (being in its close to natural conformation at the adjusted slightly alkaline pH value). Moreover, it should be pinpointed that a video of the whole synthesis was recorded, showing how BSA and other reactants are slowly pipetted into a tube and mixed together – see Supporting Information.

The final optimized APEBM nanocomposite is visualized using HR-TEM (bright field) and STEM (dark field) as shown in Fig. 2A and Fig. 2B, respectively. It is evident that objects of sizes around 1.6 nm are frequently encountered by both imaging modes. Elemental composition is verified via energy-dispersive X-ray spectroscopy and the characteristic spectrum is shown in Fig. 2C. It clearly evidenced the simultaneous presence of gold (coming from luminescent AuNC), iron (stemming from SPION), and sulphur (representative element evidencing the protein presence directly since any other reactants within the reaction mixture do not contain S). The signal of the other elements detected in the EDS spectrum comes either from the microscopic grid (e.g., Cu, C) and/or from the species being present in the reaction mixture (e.g., O, C, N, Na). Randomly chosen place of APEBM nanocomposite deposited on TEM holey carbon-covered Cu-grid was mapped (area framed by green square in Fig. 2D) as for selected elements (Au, Fe, S) distribution (Fig. 2E).
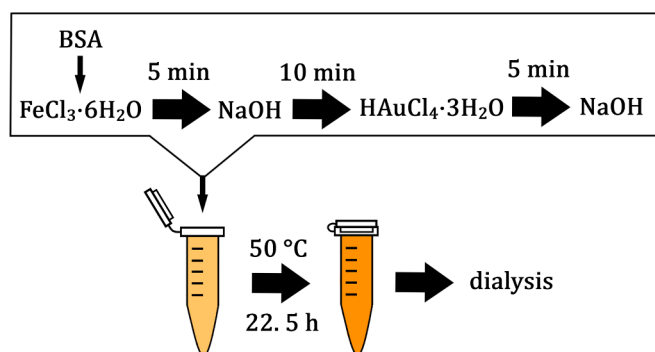
Obviously, protein (detected via S) is spread in the selected area almost homogeneously (blue spots in Fig. 2E). On the other hand, AuNC (green spots) and SPION (red spots) are either co-localized and/or arranged into specific agglomerates as can be clearly seen in Fig. 2E. Regarding the brightness of spots in Fig. 2D (dark field mode), it well corresponds to the elemental composition determined by EDS mapping in Fig. 2E: the brighter and well-separated nanoobjects are AuNC; while somewhat less bright, tiny nanostructures agglomerated into chains can be attributed to SPION. It should be, however, reminded that samples for HR-TEM/STEM/EDS mapping are drop-casted on the microscopic grid and allowed to dry which means that the effect of drying can influence the observed structural arrangement of APEBM nanocomposite. Moreover, it was corroborated in our recent work [33] that the focused electron beam during HR-TEM and EDS mapping can greatly modify the oxidation states of metallic parts as well as their mobility within our nanocomposites, leading thus to structural rearrangement *in situ*, under the electron beam. Consequently, a modified sample is measured and not the as-synthetized one.

3.2. In vitro MR imaging and relaxometry using the APEBM nanocomposite

SPION are considered as efficient T_2 MRI contrast agents since they can influence the transverse (or spin-spin) relaxation time of protons [34]. The T_2-weighted MR images representing the observed MR signal from four different concentrations of the dialyzed APEBM nanocomposite samples (denoted as 100%, 75%, 50%, and 25%) are shown in Table 1, along with distilled water (serving as reference).

By their direct comparison, it is evident that the contrast is sufficiently visible even in the case of the lowest concentration (25%) of the APEBM nanocomposite. Thus, the APEBM nanocomposite is affecting the relaxation time of surrounding water protons. This observation can also be supported numerically with the quantitative imaging parameters: signal-to-noise ratio (SNR) and contrast-to-noise ratio (CNR), which are summarized in the table included as an inset in Table 1. Specifically, the higher the concentration of the sample (iron concentration), the shorter the relaxation time of water protons and, consequently, the higher the change of contrast in MR images was found. These changes reflect the increasing differences in the SNR and CNR values between the APEBM nanocomposite samples and the reference (distilled water). Additionally, T_1-weighted imaging was carried out as well; however, the MR signal from the APEBM nanocomposite was only slightly different than the signal from the reference (Table SI-2), which is in accordance with the majority of scientific literature (e.g., [15,18]). It can be noted that only under favourable preparation conditions, it is feasible to obtain SPION with a relatively high T_1 contrast and low r_2/r_1 ratio [35,36].

Besides the MR imaging in phantoms, relaxometry measurements were conducted to obtain the relaxivity values. Experimentally determined relaxation times T_1 and T_2 were used to calculate the relaxation rates R_1 and R_2 as reciprocal values, respectively. Then, the dependence of the relaxation rate on the real iron concentration was plotted. The real iron concentration in the dialyzed APEBM nanocomposite samples was determined by ICP-MS and is listed in Table SI-3. Subsequently, the experimental R_1 and R_2 values were fitted with a linear function according to equation (1), as shown in Figures SI-1A, SI-1B, and SI-1C. The slope of this function represents the corresponding relaxivity r. Both r_1 and r_2 values are listed in Table SI-4, together with the r_2/r_1 ratio. Indeed, the r_2/r_1 ratio is an important factor correlating with the imaging contrast efficiency. For T_2-weighted contrast agents, it is commonly higher than 2 [37]. According to the results, the r_2/r_1 ratio of the APEBM nanocomposite is slightly higher than 10 (Table SI-4), which is fully comparable with the r_2/r_1 ratios of the commercially available iron oxide nanoparticle-based contrast agents, such as ferucarbotran (Resovist®), ferumoxides (Feridex®), and ferumoxtran-10 (Combinex®), measured in water at 1.5 T [38–40]. It is important to stress that our relaxometry measurement was conducted at 1.5 T, a magnetic field
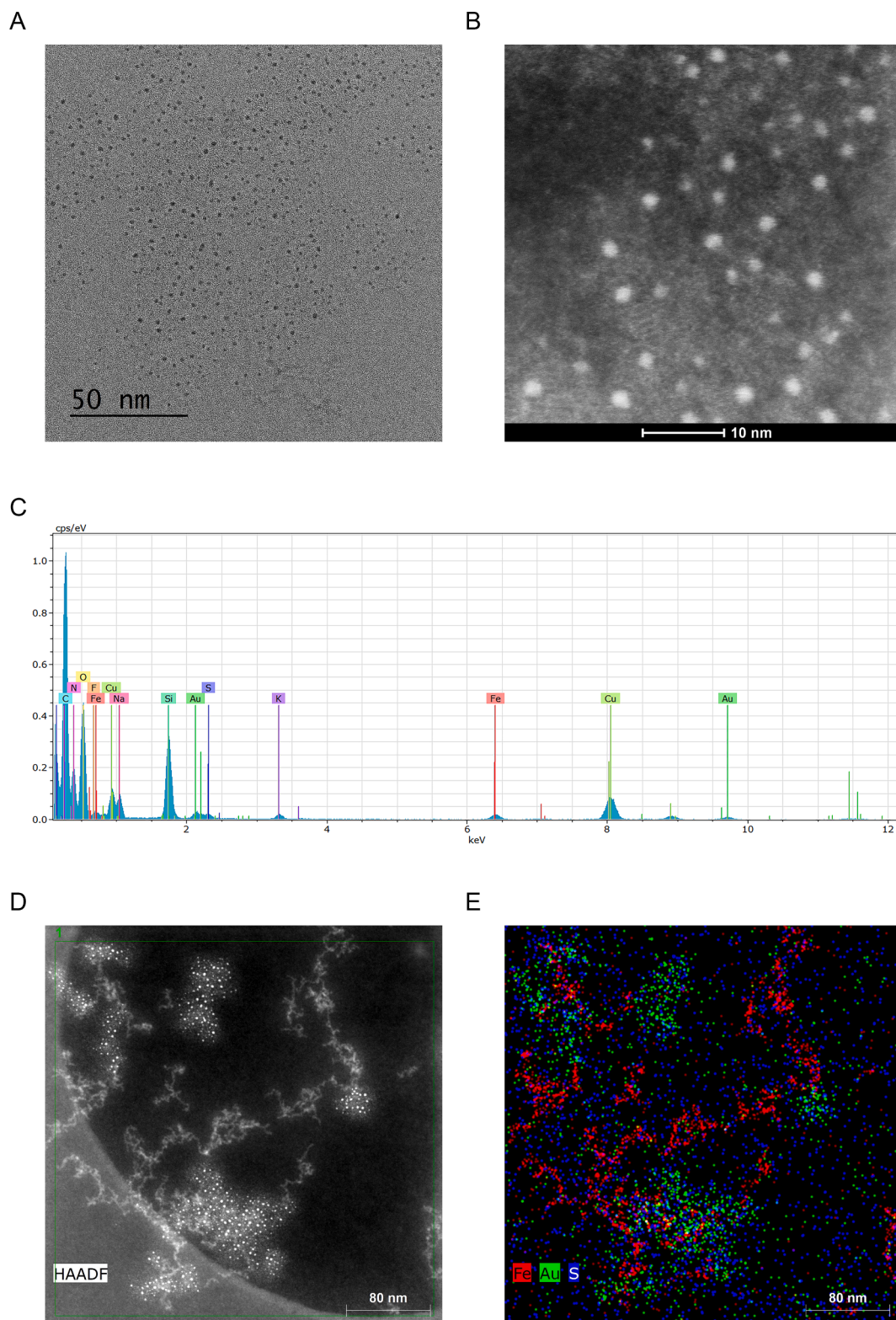
Fig. 1. Schematic depiction of the APEBM nanocomposite synthesis.

Fig. 2. (A) HR-TEM (bright field) and (B) STEM (dark field) images of APEBM nanocomposite. (C) Its EDS spectrum. (D) Randomly chosen place of deposited APEBM nanocomposite to map the elemental composition within a framed area (green square). (E) Selected elements distribution within the map shown in (D). (For interpretation of the references to colour in this figure legend, the reader is referred to the web version of this article.)

strength commonly employed in clinical practice. Furthermore, it should be remembered that the relaxivity and the r_2/r_1 ratio could depend on many parameters, including the field strength, used medium (water, plasma, or blood), and protein corona [37,38]. To sum up, the experimentally determined r_2/r_1 ratio of the APEBM nanocomposite

renders it the capability of a potential MR contrast agent with a beneficial luminescent property (as will be evidenced in the next section).

Table 1

T_2-weighted MR images of phantoms representing four different concentrations (labelled as 100%, 75%, 50%, and 25%) of a representative APEBM nanocomposite sample and distilled water serving as a reference (labelled as H_2O), with corresponding signal-to-noise-ratio (SNR) and contrast-to-noise-ratio (CNR) values.

Sample concentration	100%	75%	50%	25%	H_2O
T_2-weighted MR signal					
SNR	8.34	11.22	13.37	13.70	17.59
CNR	9.24	6.36	4.22	3.89	

3.3. In vitro optical imaging employing the APEBM nanocomposite

Embedded in BSA, AuNC can exhibit bright luminescence in the visible and near-infrared regions with relatively high quantum yield [41–44]. Therefore, we tested optical imaging using our optimized APEBM nanocomposites *in vitro*. The images depicting the observed luminescence signal from four different concentrations of the dialyzed APEBM nanocomposite samples (the same concentration series as used in the MRI and relaxometry measurements) are shown in Fig. 3, together with distilled water (serving as reference).

The luminescence signal for each concentration of the APEBM nanocomposite is strong, i.e., even for the lowest concentration (25%), the emission signal is more than 40 times stronger than the reference signal (excitation and emission wavelengths were 500 nm and 670 nm, respectively). A similar pattern can be observed in Figure SI-2, where a different set of excitation and emission wavelengths (excitation and emission wavelengths were 430 nm and 730 nm, respectively) was used. However, the latter set of wavelengths is out of the optimal range, thus the emission intensities presented in Figure SI-2 are lower than those shown in Fig. 3. Moreover, the results for both excitation/emission sets correspond with the fluorescence measurements of the APEBM nanocomposite in a diluted state (thus avoiding the inner filter effect), as can be seen in Figure SI-3.

In all four concentrations of the APEBM nanocomposite (Fig. 3 and Figure SI-2), the inner filter effect is reflected to a certain extent in the resulting emission intensity: the higher the concentration, the more pronounced the effect is. Alternatively, the dependence of the emission intensity on the sample concentration within this concentration range is non-linear. Consequently, the emission intensity for the 75% concentration of the APEBM nanocomposite sample is higher than that for the 100% concentration within both wavelength sets (Table SI-5 and SI-6). It can be summarized that the APEBM nanocomposite is an efficient fluorescent imaging probe when using appropriate concentration and excitation/emission wavelengths and, thus, could be applied for *in vivo* experiments.

3.4. Biocompatibility and other important characteristics of the APEBM nanocomposite

Prior to performing the *in vivo* imaging experiments, some other characteristics of the APEBM nanocomposite, which can influence its interaction within a living organism, were determined. Specifically, *in vitro* cell viability, particle size distribution, zeta potential of the APEBM nanocomposite and fluorescence signal stability in different media (e.g., PBS, cultivation medium) under varying temperatures and with/without cells presence were measured and assessed.

As for the cell viability assessment, a fluorometric calcein-AM assay was established. Widely used colorimetric MTT, XTT assays, and a fluorometric Alamar blue (resazurin) assay were not employed because of the possible interaction between the protein matrix (BSA) and the corresponding dye, which could lead to false positive or negative results, as discussed in [45–47]. Cell viability was determined for eight different concentrations of the APEBM nanocomposite, as shown in Table SI-7. Even for the highest concentration (labelled as 99%), the viability is higher than 90% (specifically, $93.5 \pm 1.1\%$). The closest value to the one used for both *in vitro* and *in vivo* imaging is the concentration of 70%, with its corresponding viability of $103.5 \pm 0.5\%$. These values fulfil the condition for APEBM nanocomposite to be considered a non-toxic species according to ISO 10993.

Dynamic light scattering was employed for particle size distribution and zeta potential determination of the APEBM nanocomposite in aqueous solution to provide relevant information about the particle size distribution of the entire APEBM nanocomposite in solution, i.e., the hydrodynamic diameter (usually much bigger than sizes determined by TEM measurements for the same sample). DLS has been recommended in a very recent review [44] to tackle this and, therefore, used by us. The
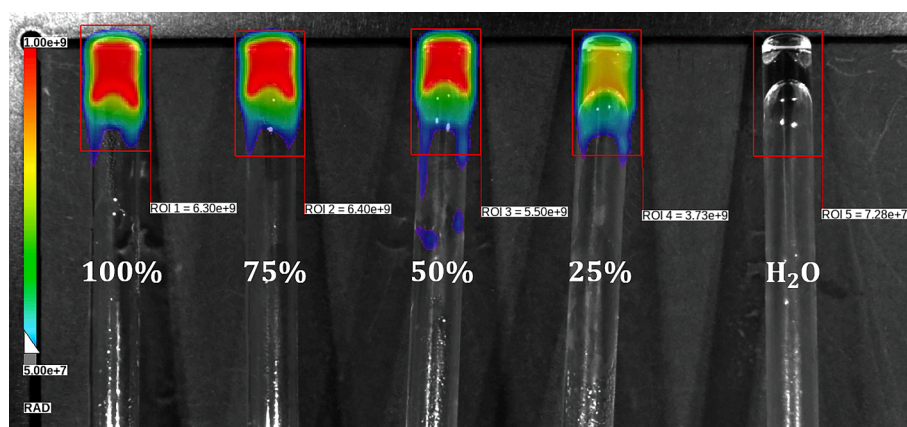

Fig. 3. *In vitro* fluorescence image of phantoms representing four different concentrations (labelled as 100%, 75%, 50%, and 25%) of a representative APEBM nanocomposite sample and distilled water serving as a reference (labelled as H_2O). Excitation and emission wavelengths were 500 nm and 670 nm, respectively.

average values of the polydispersity index (PDI), Z-average, hydrodynamic diameter (based on the changes of scattered light intensity), and zeta potential are listed in Table 2, together with their standard deviations. The measured particle size distribution derived from the changes in scattered light intensity is shown in Figure SI-4.

Obviously, the APEBM nanocomposite possesses a somewhat broad monomodal size distribution and negative zeta potential value. The higher negative value of zeta potential indicates that the APEBM nanocomposite should be stable. However, their stability and particularly the stability of fluorescence signal have to be further checked within the cell cultivation medium used. Thus, we evaluated the integrated fluorescence intensity of APEBM samples within selected media (PBS and/or cultivation medium) under varying temperatures and related it to the averaged integrated fluorescence intensity of APEBM samples in deionized water. The results (graphically depicted in Figure SI-5A) show that integrated fluorescence intensities of APEBM sample in PBS and/or cultivation medium are well above that of APEBM sample in deionized water. The position of emission maximum (Figure SI-5B) slightly shifts in the cultivation medium under varying temperatures in the course of time. Fluorescence intensity was further monitored by inverted fluorescent microscope in the cultivation medium in the presence vs. absence of HeLa cells as a function of time. HeLa cancer cells were intentionally chosen for this type of experiment as inspired by [28]. It corroborated the stability of fluorescence signal after 1, 2, and 24 h of cells incubation (Figure SI-6).

Although both the hydrodynamic diameter and surface charge (which is generally represented as zeta potential), play a certain role within the nanomaterial-cell interactions [48–54], many other factors can also affect the cellular internalization and/or the cytotoxicity of the investigated nanomaterial, including, for instance, the shape [55,56], composition of metal core/surface [56,57], elasticity [58,59], hydrophobicity [57,60], and last but not least, protein corona presence and composition [56,61–63]. The last issue can be modulated by the physicochemical properties of the nanomaterial, surrounding biological environment (e.g., pH, ionic strength, temperature, and plasma concentration) or even the cholesterol levels as known from the literature [61,64–67]. Evidently, the cell internalization of the nanomaterial inside a biological system is very complex since it depends on numerous interconnected parameters. Therefore, besides the *in vitro* imaging, *in vivo* imaging should be performed to verify both the MR and optical contrasts inside a living organism (animal).

3.5. In vivo imaging exploiting the APEBM nanocomposite

Since both *in vitro* MR and optical imaging techniques provided significant change of contrasts from the reference (distilled water), *in vitro* viability experiments proved the biocompatibility of the APEBM nanocomposite even for the highest concentration, *in vivo* imaging experiments were performed. Three replicates of the dialyzed APEBM nanocomposite sample were subcutaneously injected, each into a different limb of a healthy female BALB/c mouse. Based on the results of *in vitro* experiments and considering the potential inner filter effect, the three *in vivo* injections contained a 75% concentration of the APEBM nanocomposite sample. In the fourth limb of the healthy mouse, distilled water (reference) was injected. Immediately after the injections, both optical and MR imaging were conducted, and the images representing

Table 2
Average values of hydrodynamic diameter (based on the changes of scattered light intensity), Z-Average, PDI and zeta potential acquired by DLS measurements of a representative APEBM nanocomposite sample, listed with their standard deviations.

Hydrodynamic diameter [nm]	Z-Average [nm]	PDI	Zeta potential [mV]
296 ± 14	220 ± 3	0.295 ± 0.011	−44 ± 2

the observed luminescence and MR signals are shown in Figs. 4 and 5, respectively.

Evidently, each of the three injection sites, where the APEBM nanocomposite was introduced, exhibits both luminescence and MR signals; while the reference (in the fourth limb) did not provide a detectable impact on the signal given by the local tissue. The luminescence signal from the APEBM nanocomposite is at least 20 times stronger than the signal from the reference (Fig. 4). Similarly, the MR contrast induced by the APEBM nanocomposite can be easily distinguished from the surrounding muscle tissue (Fig. 5A and Fig. 5B).

There are some differences among the intensities of individual replicates, but they may stem from anatomical dissimilarities under the skin within the injection site, subsequently leading to variabilities in the distribution of the APEBM nanocomposite. Furthermore, absorption and scattering of the excitation (namely) and emission wavelengths when they pass through the different thicknesses of skin tissue during optical imaging could alter the resulting intensities. Moreover, the varying position of each limb with respect to the emitter and detector during the imaging procedures could also have an impact on the signal.

Additionally, it has to be stated that MR imaging was performed at 4.7 T. This magnetic field strength closely approaches the clinically used one (3 T). Consequently, the results of MR imaging exploiting the APEBM nanocomposite are tremendously important for clinical research and, hence, the potential translation of the APEBM nanocomposite into

Fig. 4. *In vivo* fluorescence image of a healthy female BALB/c mouse under anaesthesia. Three replicates (denoted as BM1, BM2, and BM3) of the APEBM nanocomposite were subcutaneously injected, each into a different limb. Each injection contained a 75% concentration of the replicate, whereas distilled water was injected into the upper left limb serving as a reference. Excitation and emission wavelengths were 500 nm and 670 nm, respectively.

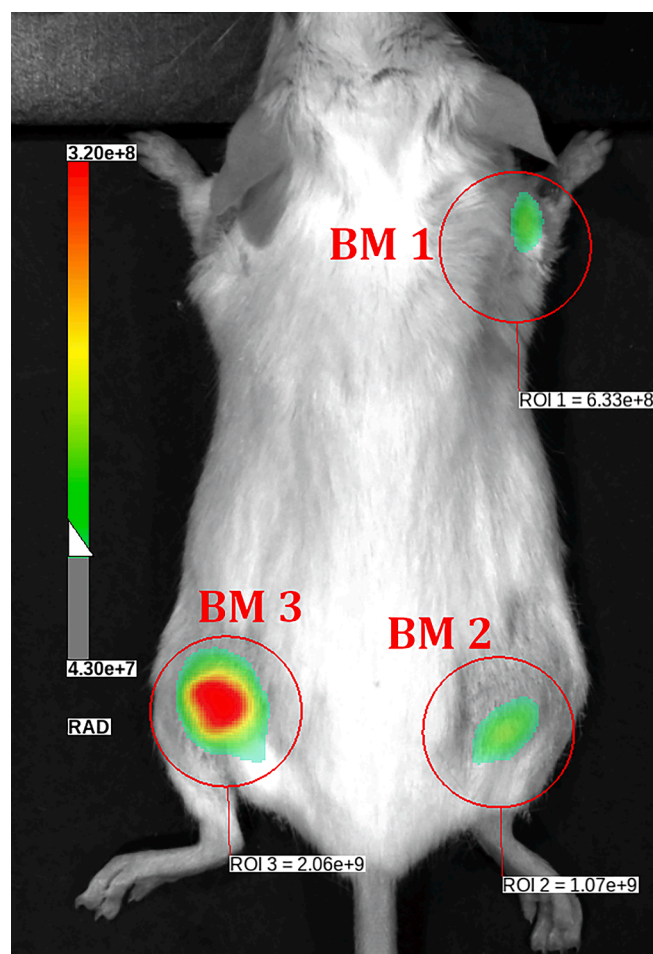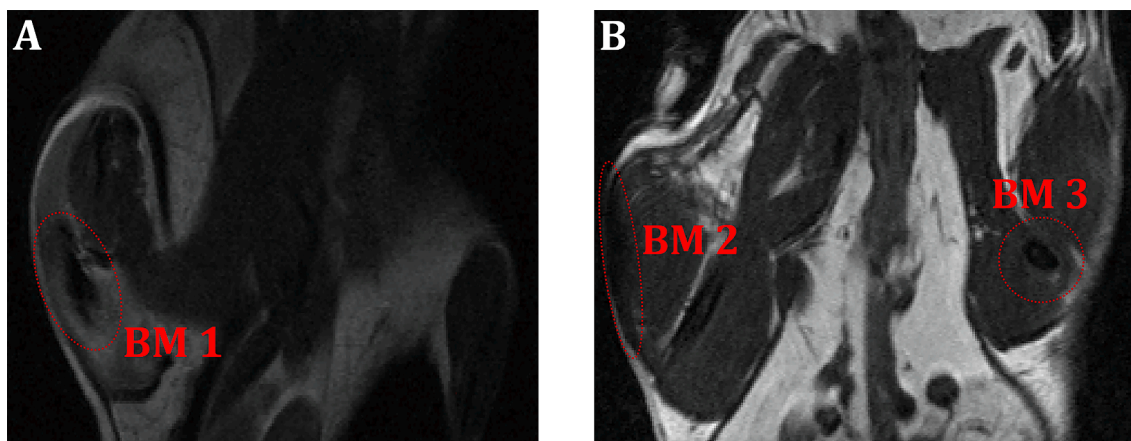**Fig. 5.** (A, B) *In vivo* MR images of a healthy female BALB/c mouse under anaesthesia. Three replicates (denoted as BM1, BM2, and BM3) of the APEBM nanocomposite were subcutaneously injected, each into a different limb. Each injection contained 75% concentration of the replicate, whereas distilled water was injected into the upper left limb serving as a reference.

clinical practice can be envisaged.

Importantly, three months after the imaging experiments, the weight of the animal increased (by 10 % in the first month). The treated areas on the animal's body were also inspected visually and did not show any signs of inflammation, or other pathologies. This supports the conclusion from cytotoxicity testing that the APEBM nanocomposite has no harmful effects and can be considered biocompatible.

To sum up, the APEBM nanocomposite can be successfully exploited as a bimodal FI/MRI contrast agent in a living organism. To the best of our knowledge, the APEBM nanocomposite is the very first bimodal FI/MRI biocompatible probe based solely on nanostructured entities entrapped within a protein matrix and successfully applied *in vivo*. While the existence of T_2-weighted magnetic contrast is caused by the presence of SPION, similarly as in [34], the luminescence is exhibited by AuNC, as in e.g. [68]. Therefore, both signals are provided by two different inorganic nanostructured entities that are embedded in the same transportation protein. It can be remembered here that using a bimodal contrast probe can overcome the limitations of the monomodal probes [69]. In the case of MRI/FI, where the MR and fluorescence signals could be detected simultaneously, the advantage lies in the combination of high spatial resolution and penetration depth of MRI, and high fluorescence sensitivity [69]. Moreover, SPION are widely recognized as inert imaging agents devoid of intended pharmacological functions [70]. These nanoparticles are commonly classified as biocompatible, demonstrating negligible *in vivo* toxicity [71,72]. Our investigations of newly developed APEBM nanocomposites reveal similar inert characteristics. Due to their non-specificity and lack of functional surface modifications, we propose that APEBM nanocomposites could potentially serve as efficient liver contrast agents for future applications. In this respect, we were inspired also by the results of Zhang and co-workers [73] who observed high Au content for the BSA-protected Au$_{25}$ NCs in liver and suggested to use it in targeting therapy for liver cancer. It could be a direction for ongoing research, however, it is beyond the scope of this work. Last but not least, obtaining a biocompatible dual contrast agent utilizing SPION in conjunction with a fluorescent probe is relatively difficult because of the possible aggregation of iron oxide nanoparticles and their strong absorption [74], which could cause the luminescence quenching to a certain extent. In the case of the APEBM nanocomposite, the absorption of SPION together with the emission of AuNC are ideally shifted (Figure SI-7): SPION absorb mainly in the UV region and, in a decreasing manner, in the visible region [74]; whereas the AuNC emit more towards the NIR region (Figure SI-7). It should also be pinpointed that *in vivo* fluorescence visualization is quite challenging [75]. The APEBM nanocomposite is highly stable (based on the zeta potential value listed in Table 2, spectroscopic monitoring over

a year of shelf-life when stored in a fridge, and assessment of fluorescence signal stability in different media under varying temperatures and in the presence of HeLa cells), which can be related to the specifically optimized green synthetic approach developed and adopted in the present work. It can be even envisaged that other metal cations suitable for achieving additional functionality of a resulting nanocomposite (e.g., theranostic purposes and/or multimodal imaging), will be easily incorporated due to the robustness of the developed synthesis. Ongoing research is conducted by us in this direction.

4. Conclusions

Highly optimized one-pot sequential green synthesis of the APEBM nanocomposite resulted in a very stable, reproducible product that was proved capable of serving as an efficient FI/MRI biocompatible bimodal contrast agent *in vitro* as well as *in vivo*. To the best of our knowledge, it is the first bimodal imaging probe of its kind in the world since it combines totally nontoxic components (AuNC, SPION, serum albumin), hence ensuring biocompatibility of the entire nanocomposite; and effectively exploits functionalities of each part, avoiding thus any redundancy. It can be noticed here that the usage of a bimodal contrast probe can overcome the limitations of the monomodal ones [69]. It should also be pinpointed that *in vivo* fluorescence visualization is quite challenging [75]. Since the APEBM nanocomposite is based solely on nanostructured entities entrapped within a protein matrix, it renders the system flexible which can be further developed and exploited.

CRediT authorship contribution statement

Radek Ostruszka: Formal analysis, Investigation (DLS, fluorescence), Methodology (optimized synthesis of the APEBM nanocomposite), Original draft writing. **Aminadav Halili:** Formal analysis, Investigation (FI and MRI in phantoms and in vivo). **Tomáš Pluháček:** Formal analysis, Investigation (ICP-MS analyses), Original draft editing. **Lucie Rárová:** Formal analysis, Investigation (biocompatibility), Methodology. **Daniel Jirák:** Formal analysis, Funding acquisition, Investigation (FI and MRI in vivo), Methodology, Original draft editing. **Karolína Šišková:** Conceptualization, Funding acquisition, Methodology, Resources, Supervision, Writing and editing original draft, original draft - review & editing.

Declaration of competing interest

The authors declare that they have no known competing financial interests or personal relationships that could have appeared to influence

the work reported in this paper.

Appendix A. Supplementary data

Supplementary data to this article can be found online at https://doi.org/10.1016/j.jcis.2024.02.116.

References

[1] O. Betzer, M. Motiei, T. Dreifuss, T. Sadan, N. Omer, T. Blumenfeld-Katzir, Z. Liu, N. Ben-Eliezer, R. Popovtzer, Core/Shell Iron Oxide@Gold Nanoparticles for Dual-Modal CT/MRI Imaging, in: D. Fixler, S. Wachsmann-Hogiu, E.M. Goldys (Eds.), Proceedings of the Nanoscale Imaging, Sensing, and Actuation for Biomedical Applications XVII, SPIE, San Francisco, United States, 2020, p. 51, https://doi.org/10.1117/12.2548430.
[2] A.S. Wadajkar, T. Kadapure, Y. Zhang, W. Cui, K.T. Nguyen, J. Yang, Dual-Imaging Enabled Cancer-Targeting Nanoparticles, Adv. Healthc. Mater. 1 (2012) 450–456, https://doi.org/10.1002/adhm.201100055.
[3] M. Luo, Y. Lv, X. Luo, Q. Ren, Z. Sun, T. Li, A. Wang, Y. Liu, C. Yang, X. Li, Developing Smart Nanoparticles Responsive to the Tumor Micro-Environment for Enhanced Synergism of Thermo-Chemotherapy With PA/MR Bimodal Imaging, Front. Bioeng. Biotechnol. 10 (2022) 799610, https://doi.org/10.3389/fbioe.2022.799610.
[4] M.F. Matus, H. Häkkinen, Understanding Ligand-Protected Noble Metal Nanoclusters at Work, Nat. Rev. Mater. 8 (2023) 372–389, https://doi.org/10.1038/s41578-023-00537-1.
[5] M. Hasan, H. Gulzar, A. Zafar, A. Ul Haq, G. Mustafa, T. Tariq, A. Khalid, A. Mahmmod, X. Shu, N. Mahmood, Multiplexing Surface Anchored Functionalized Iron Carbide Nanoparticle: A Low Molecular Weight Proteome Responsive Nano-Tracer, Colloids Surf. B Biointerfaces 203 (2021) 111746, https://doi.org/10.1016/j.colsurfb.2021.111746.
[6] F. Demir Duman, R.S. Forgan, Applications of Nanoscale Metal-Organic Frameworks as Imaging Agents in Biology and Medicine, J. Mater. Chem. B 9 (2021) 3423–3449, https://doi.org/10.1039/D1TB00358E.
[7] D. Wang, H. Wu, J. Zhou, P. Xu, C. Wang, R. Shi, H. Wang, H. Wang, Z. Guo, Q. Chen, In Situ One-Pot Synthesis of MOF–Polydopamine Hybrid Nanogels with Enhanced Photothermal Effect for Targeted Cancer Therapy, Adv. Sci. 5 (2018) 1800287, https://doi.org/10.1002/advs.201800287.
[8] V. Karthika, M.S. AlSalhi, S. Devanesan, K. Gopinath, A. Arumugam, M. Govindarajan, Chitosan Overlaid Fe3O4/rGO Nanocomposite for Targeted Drug Delivery, Imaging, and Biomedical Applications, Sci. Rep. 10 (2020) 18912, https://doi.org/10.1038/s41598-020-76015-3.
[9] X. Chang, Y. Zhang, P. Xu, M. Zhang, H. Wu, S. Yang, Graphene Oxide / MnWO4 Nanocomposite for Magnetic Resonance / Photoacoustic Dual-Model Imaging and Tumor Photothermo-Chemotherapy, Carbon 138 (2018) 397–409, https://doi.org/10.1016/j.carbon.2018.07.058.
[10] J.E. Lee, N. Lee, T. Kim, J. Kim, T. Hyeon, Multifunctional Mesoporous Silica Nanocomposite Nanoparticles for Theranostic Applications, Acc. Chem. Res. 44 (2011) 893–902, https://doi.org/10.1021/ar2000259.
[11] D. Niu, Y. Li, J. Shi, Silica/Organosilica Cross-Linked Block Copolymer Micelles: A Versatile Theranostic Platform, Chem. Soc. Rev. 46 (2017) 569–585, https://doi.org/10.1039/C6CS00495D.
[12] S. Yang, Y. Li, Fluorescent Hybrid Silica Nanoparticles and Their Biomedical Applications, WIREs Nanomed. Nanobiotechnol. 12 (2020) e1603, https://doi.org/10.1002/wnan.1603.

[13] M. Luo, H. Yukawa, K. Sato, M. Tozawa, M. Tokunaga, T. Kameyama, T. Torimoto, Y. Baba, Multifunctional Magnetic CuS/Gd2O3 Nanoparticles for Fluorescence/Magnetic Resonance Bimodal Imaging-Guided Photothermal-Intensified Chemodynamic Synergetic Therapy of Targeted Tumors, ACS Appl. Mater. Interfaces 14 (2022) 34365–34376, https://doi.org/10.1021/acsami.2c06503.
[14] Y. An, W. Chen, Y. Li, H. Zhao, D. Ye, H. Liu, K. Wu, H. Ju, Crosslinked Albumin-Manganese Nanoaggregates with Sensitized T1 Relaxivity and Indocyanine Green Loading for Multimodal Imaging and Cancer Phototherapy, J. Mater. Chem. B 11 (2023) 2157–2165, https://doi.org/10.1039/D2TB02529A.
[15] R. Ostruszka, D. Půlpánová, T. Pluháček, O. Tomanec, P. Novák, D. Jirák, K. Šišková, Facile One-Pot Green Synthesis of Magneto-Luminescent Bimetallic Nanocomposites with Potential as Dual Imaging Agent, Nanomaterials 13 (2023) 1027, https://doi.org/10.3390/nano13061027.
[16] H. Li, K. Yan, Y. Shang, L. Shrestha, R. Liao, F. Liu, P. Li, H. Xu, Z. Xu, P.K. Chu, Folate-Bovine Serum Albumin Functionalized Polymeric Micelles Loaded with Superparamagnetic Iron Oxide Nanoparticles for Tumor Targeting and Magnetic Resonance Imaging, Acta Biomater. 15 (2015) 117–126, https://doi.org/10.1016/j.actbio.2015.01.006.
[17] D. Li, M. Hua, K. Fang, R. Liang, BSA Directed-Synthesis of Biocompatible Fe3O4 Nanoparticles for Dual-Modal T1 and T2 MR Imaging in Vivo, Anal. Methods 9 (2017) 3099–3104, https://doi.org/10.1039/C7AY00270J.
[18] Y. Wang, C. Xu, Y. Chang, L. Zhao, K. Zhang, Y. Zhao, F. Gao, X. Gao, Ultrasmall Superparamagnetic Iron Oxide Nanoparticle for T2-Weighted Magnetic Resonance Imaging, ACS Appl. Mater. Interfaces 9 (2017) 28959–28966, https://doi.org/10.1021/acsami.7b10030.
[19] S. Xu, J. Wang, Y. Wei, H. Zhao, T. Tao, H. Wang, Z. Wang, J. Du, H. Wang, J. Qian, et al., In Situ One-Pot Synthesis of Fe2O3 @BSA Core-Shell Nanoparticles as Enhanced T1-Weighted Magnetic Resonance Imagine Contrast Agents, ACS Appl. Mater. Interfaces 12 (2020) 56701–56711, https://doi.org/10.1021/acsami.0c13825.
[20] S. Wang, Y. Yin, W. Song, Q. Zhang, Z. Yang, Z. Dong, Y. Xu, S. Cai, K. Wang, W. Yang, et al., Red-Blood-Cell-Membrane-Enveloped Magnetic Nanoclusters as a Biomimetic Theranostic Nanoplatform for Bimodal Imaging-Guided Cancer Photothermal Therapy, J. Mater. Chem. B 8 (2020) 803–812, https://doi.org/10.1039/C9TB01829H.
[21] D. Stanicki, L. Larbanoix, S. Boutry, T. Vangijzegem, I. Ternad, S. Garifo, R. N. Muller, S. Laurent, Impact of the Chain Length on the Biodistribution Profiles of PEGylated Iron Oxide Nanoparticles: A Multimodal Imaging Study, J. Mater. Chem. B 9 (2021) 5055–5068, https://doi.org/10.1039/D1TB00573A.
[22] H. Yan, Q. Wang, J. Wang, W. Shang, Z. Xiong, L. Zhao, X. Sun, J. Tian, F. Kang, S. Yun, Planted Graphene Quantum Dots for Targeted, Enhanced Tumor Imaging and Long-Term Visualization of Local Pharmacokinetics, Adv. Mater. 35 (2023) 2210809, https://doi.org/10.1002/adma.202210809.
[23] Y. Yin, Y. Li, S. Wang, Z. Dong, C. Liang, J. Sun, C. Wang, R. Chai, W. Fei, J. Zhang, et al., MSCs-Engineered Biomimetic PMAA Nanomedicines for Multiple Bioimaging-Guided and Photothermal-Enhanced Radiotherapy of NSCLC, J. Nanobiotechnol. 19 (2021) 80, https://doi.org/10.1186/s12951-021-00823-6.
[24] S.-K. Sun, L.-X. Dong, Y. Cao, H.-R. Sun, X.-P. Yan, Fabrication of Multifunctional Gd2O3 /Au Hybrid Nanoprobe via a One-Step Approach for Near-Infrared Fluorescence and Magnetic Resonance Multimodal Imaging in Vivo, Anal. Chem. 85 (2013) 8436–8441, https://doi.org/10.1021/ac401879y.
[25] D.-H. Hu, Z.-H. Sheng, P.-F. Zhang, D.-Z. Yang, S.-H. Liu, P. Gong, D.-Y. Gao, S.-T. Fang, Y.-F. Ma, L.-T. Cai, Hybrid Gold-Gadolinium Nanoclusters for Tumor-Targeted NIRF/CT/MRI Triple-Modal Imaging in Vivo, Nanoscale 5 (2013) 1624, https://doi.org/10.1039/c2nr33543c.
[26] G. Harini, S. Balasurya, S.S. Khan, Recent Advances on Gadolinium-Based Nano-Photocatalysts for Environmental Remediation and Clean Energy Production: Properties, Fabrication, Defect Engineering and Toxicity, J. Clean. Prod. 345 (2022) 131139, https://doi.org/10.1016/j.jclepro.2022.131139.
[27] N. Lee, D. Yoo, D. Ling, M.H. Cho, T. Hyeon, J. Cheon, Iron Oxide Based Nanoparticles for Multimodal Imaging and Magnetoresponsive Therapy, Chem. Rev. 115 (2015) 10637–10689, https://doi.org/10.1021/acs.chemrev.5b00112.
[28] M. Hasan, W. Yang, Y. Ju, X. Chu, Y. Wang, Y. Deng, N. Mahmood, Y. Hou, Biocompatibility of Iron Carbide and Detection of Metals Ions Signaling Proteomic Analysis via HPLC/ESI-Orbitrap, Nano Res. 10 (2017) 1912–1923, https://doi.org/10.1007/s12274-016-1375-4.
[29] M. Hasan, H. Xue, A. Zafar, A. Ul Haq, T. Tariq, M.M. Ahmad, S.G. Hassan, H. U. Javed, X. Chen, X. Shu, Biochemical Surface Functionalization of Iron Oxide for Efficient Biomarker Detector: A New Visions of Nano-Bio Interactions, Applied Surface Science Advances 18 (2023) 100486, https://doi.org/10.1016/j.apsadv.2023.100486.
[30] https://clinicaltrials.gov/search?term=%22imaging%22%20AND%20%22nano*%22%20AND%20%22Au%22 – Accessed 20 October 2023.
[31] F. Chen, P. Huang, Y.-J. Zhu, J. Wu, C.-L. Zhang, D.-X. Cui, The Photoluminescence, Drug Delivery and Imaging Properties of Multifunctional Eu3+/Gd3+ Dual-Doped Hydroxyapatite Nanorods, Biomaterials 32 (2011) 9031–9039, https://doi.org/10.1016/j.biomaterials.2011.08.032.
[32] J.-P. Jolivet, C. Chanéac, E. Tronc, Iron Oxide Chemistry. From Molecular Clusters to Extended Solid Networks, Chem. Commun. 477–483 (2004), https://doi.org/10.1039/B304532N.
[33] R. Ostruszka, G. Zoppellaro, O. Tomanec, D. Pinkas, V. Filimonenko, K. Šišková, Evidence of Au(II) and Au(0) States in Bovine Serum Albumin-Au Nanoclusters Revealed by CW-EPR/LEPR and Peculiarities in HR-TEM/STEM Imaging, Nanomaterials 12 (2022) 1425, https://doi.org/10.3390/nano12091425.
[34] C. Chen, J. Ge, J. Gao, L. Chen, J. Cui, J. Zeng, M. Gao, Ultrasmall Superparamagnetic Iron Oxide Nanoparticles: A next Generation Contrast Agent

for Magnetic Resonance Imaging, WIREs Nanomed. Nanobiotechnol. 14 (2022) e1740, https://doi.org/10.1002/wnan.1740.

[35] C. Du, X. Liu, H. Hu, H. Li, L. Yu, D. Geng, Y. Chen, J. Zhang, Dual-Targeting and Excretable Ultrasmall SPIONs for T_1-Weighted Positive MR Imaging of Intracranial Glioblastoma Cells by Targeting the Lipoprotein Receptor-Related Protein, J. Mater. Chem. B 8 (2020) 2296–2306, https://doi.org/10.1039/C9TB02391G.

[36] Y.-P. Rui, B. Liang, F. Hu, J. Xu, Y.-F. Peng, P.-H. Yin, Y. Duan, C. Zhang, H. Gu, Ultra-Large-Scale Production of Ultrasmall Superparamagnetic Iron Oxide Nanoparticles for T_1-Weighted MRI, RSC Adv. 6 (2016) 22575–22585, https://doi.org/10.1039/C6RA00347H.

[37] H. Amiri, L. Bordonali, A. Lascialfari, S. Wan, M.P. Monopoli, I. Lynch, S. Laurent, M. Mahmoudi, Protein Corona Affects the Relaxivity and MRI Contrast Efficiency of Magnetic Nanoparticles, Nanoscale 5 (2013) 8656, https://doi.org/10.1039/c3nr00345k.

[38] M. Rohrer, H. Bauer, J. Mintorovitch, M. Requardt, H.-J. Weinmann, Comparison of Magnetic Properties of MRI Contrast Media Solutions at Different Magnetic Field Strengths, Invest. Radiol. 40 (2005) 715–724, https://doi.org/10.1097/01.rli.0000184756.66360.d3.

[39] G.H. Simon, J. Bauer, O. Saborovski, Y. Fu, C. Corot, M.F. Wendland, H.E. Daldrup-Link, T1 and T2 Relaxivity of Intracellular and Extracellular USPIO at 1.5T and 3T Clinical MR Scanning, Eur. Radiol. 16 (2006) 738–745, https://doi.org/10.1007/s00330-005-0031-2.

[40] M. Uchida, M. Terashima, C.H. Cunningham, Y. Suzuki, D.A. Willits, A.F. Willis, P. C. Yang, P.S. Tsao, M.V. McConnell, M.J. Young, et al., A Human Ferritin Iron Oxide Nano-Composite Magnetic Resonance Contrast Agent, Magn. Reson. Med. 60 (2008) 1073–1081, https://doi.org/10.1002/mrm.21761.

[41] J. Xie, Y. Zheng, J.Y. Ying, Protein-Directed Synthesis of Highly Fluorescent Gold Nanoclusters, J. Am. Chem. Soc. 131 (2009) 888–889, https://doi.org/10.1021/ja806804u.

[42] X. Wu, X. He, K. Wang, C. Xie, B. Zhou, Z. Qing, Ultrasmall Near-Infrared Gold Nanoclusters for Tumor Fluorescence Imaging in Vivo, Nanoscale 2 (2010) 2244, https://doi.org/10.1039/c0nr00359j.

[43] J. Wu, K. Jiang, X. Wang, C. Wang, C. Zhang, On−off−on Gold Nanocluster-Based near Infrared Fluorescent Probe for Recognition of Cu(II) and Vitamin C, Microchim. Acta 184 (2017) 1315–1324, https://doi.org/10.1007/s00604-017-2111-9.

[44] R. Yan, Z. Shou, J. Chen, H. Wu, Y. Zhao, L. Qiu, P. Jiang, X.-Z. Mou, J. Wang, Y.-Q. Li, On–Off–On Gold Nanocluster-Based Fluorescent Probe for Rapid *Escherichia Coli* Differentiation, Detection and Bactericide Screening, ACS Sustain. Chem. Eng. 6 (2018) 4504–4509, https://doi.org/10.1021/acssuschemeng.8b00112.

[45] P. Goegan, G. Johnson, R. Vincent, Effects of Serum Protein and Colloid on the alamarBlue Assay in Cell Cultures, Toxicol. In Vitro 9 (1995) 257–266, https://doi.org/10.1016/0887-2333(95)00004-R.

[46] D. Funk, H.-H. Schrenk, E. Frei, Serum Albumin Leads to False-Positive Results in the XTT and the MTT Assay, Biotechniques 43 (2007) 178–186, https://doi.org/10.2144/000112528.

[47] B.H. Neufeld, J.B. Tapia, A. Lutzke, M.M. Reynolds, Small Molecule Interferences in Resazurin and MTT-Based Metabolic Assays in the Absence of Cells, Anal. Chem. 90 (2018) 6867–6876, https://doi.org/10.1021/acs.analchem.8b01043.

[48] N.D. Donahue, H. Acar, S. Wilhelm, Concepts of Nanoparticle Cellular Uptake, Intracellular Trafficking, and Kinetics in Nanomedicine, Adv. Drug Deliv. Rev. 143 (2019) 68–96, https://doi.org/10.1016/j.addr.2019.04.008.

[49] V. Ayala, A.P. Herrera, M. Latorre-Esteves, M. Torres-Lugo, C. Rinaldi, Effect of Surface Charge on the Colloidal Stability and in Vitro Uptake of Carboxymethyl Dextran-Coated Iron Oxide Nanoparticles, J. Nanopart. Res. 2013 (1874) 15, https://doi.org/10.1007/s11051-013-1874-0.

[50] X. Liu, N. Huang, H. Li, Q. Jin, J. Ji, Surface and Size Effects on Cell Interaction of Gold Nanoparticles with Both Phagocytic and Nonphagocytic Cells, Langmuir 29 (2013) 9138–9148, https://doi.org/10.1021/la401556k.

[51] C. He, Y. Hu, L. Yin, C. Tang, C. Yin, Effects of Particle Size and Surface Charge on Cellular Uptake and Biodistribution of Polymeric Nanoparticles, Biomaterials 31 (2010) 3657–3666, https://doi.org/10.1016/j.biomaterials.2010.01.065.

[52] J.-S. Choi, J. Cao, M. Naeem, J. Noh, N. Hasan, H.-K. Choi, J.-W. Yoo, Size-Controlled Biodegradable Nanoparticles: Preparation and Size-Dependent Cellular Uptake and Tumor Cell Growth Inhibition, Colloids Surf. B Biointerfaces 122 (2014) 545–551, https://doi.org/10.1016/j.colsurfb.2014.07.030.

[53] D. Hühn, K. Kantner, C. Geidel, S. Brandholt, I. De Cock, S.J.H. Soenen, P. Rivera Gil, J.-M. Montenegro, K. Braeckmans, K. Müllen, et al., Polymer-Coated Nanoparticles Interacting with Proteins and Cells: Focusing on the Sign of the Net Charge, ACS Nano 7 (2013) 3253–3263, https://doi.org/10.1021/nn3059295.

[54] Y. Jiang, S. Huo, T. Mizuhara, R. Das, Y.-W. Lee, S. Hou, D.F. Moyano, B. Duncan, X.-J. Liang, V.M. Rotello, The Interplay of Size and Surface Functionality on the Cellular Uptake of Sub-10 Nm Gold Nanoparticles, ACS Nano 9 (2015) 9986–9993, https://doi.org/10.1021/acsnano.5b03521.

[55] Y.J. Lee, E.-Y. Ahn, Y. Park, Shape-Dependent Cytotoxicity and Cellular Uptake of Gold Nanoparticles Synthesized Using Green Tea Extract, Nanoscale Res. Lett. 14 (2019) 129, https://doi.org/10.1186/s11671-019-2967-1.

[56] C. Carnovale, G. Bryant, R. Shukla, V. Bansal, Identifying Trends in Gold Nanoparticle Toxicity and Uptake: Size, Shape, Capping Ligand, and Biological Corona, ACS Omega 4 (2019) 242–256, https://doi.org/10.1021/acsomega.8b03227.

[57] X. Bai, X. Wang, X. Yan, H. Zhou, J. Zhan, S. Liu, V.K. Sharma, G. Jiang, H. Zhu, B. Yan, Regulation of Cell Uptake and Cytotoxicity by Nanoparticle Core under the Controlled Shape, Size, and Surface Chemistries, ACS Nano 14 (2020) 289–302, https://doi.org/10.1021/acsnano.9b04407.

[58] P. Guo, D. Liu, K. Subramanyam, B. Wang, J. Yang, J. Huang, D.T. Auguste, M. A. Moses, Nanoparticle Elasticity Directs Tumor Uptake, Nat. Commun. 9 (2018) 130, https://doi.org/10.1038/s41467-017-02588-9.

[59] A.C. Anselmo, M. Zhang, S. Kumar, D.R. Vogus, S. Menegatti, M.E. Helgeson, S. Mitragotri, Elasticity of Nanoparticles Influences Their Blood Circulation, Phagocytosis, Endocytosis, and Targeting, ACS Nano 9 (2015) 3169–3177, https://doi.org/10.1021/acsnano.5b00147.

[60] M. Samadi Moghaddam, M. Heiny, V.P. Shastri, Enhanced Cellular Uptake of Nanoparticles by Increasing the Hydrophobicity of Poly(Lactic Acid) through Copolymerization with Cell-Membrane-Lipid Components, Chem. Commun. 51 (2015) 14605–14608, https://doi.org/10.1039/C5CC06397C.

[61] M. Mahmoudi, M.P. Landry, A. Moore, R. Coreas, The Protein Corona from Nanomedicine to Environmental Science, Nat. Rev. Mater. 8 (2023) 422–438, https://doi.org/10.1038/s41578-023-00552-2.

[62] A. Aliyandi, C. Reker-Smit, R. Bron, I.S. Zuhorn, A. Salvati, Correlating Corona Composition and Cell Uptake to Identify Proteins Affecting Nanoparticle Entry into Endothelial Cells, ACS Biomater Sci. Eng. 7 (2021) 5573–5584, https://doi.org/10.1021/acsbiomaterials.1c00804.

[63] V. Francia, K. Yang, S. Deville, C. Reker-Smit, I. Nelissen, A. Salvati, Corona Composition Can Affect the Mechanisms Cells Use to Internalize Nanoparticles, ACS Nano 13 (2019) 11107–11121, https://doi.org/10.1021/acsnano.9b03824.

[64] N. Liu, M. Tang, J. Ding, The Interaction between Nanoparticles-Protein Corona Complex and Cells and Its Toxic Effect on Cells, Chemosphere 245 (2020) 125624, https://doi.org/10.1016/j.chemosphere.2019.125624.

[65] J. Oberländer, C. Champanhac, R. Da Costa Marques, K. Landfester, V. Mailänder, Temperature, Concentration, and Surface Modification Influence the Cellular Uptake and the Protein Corona of Polystyrene Nanoparticles, Acta Biomater. 148 (2022) 271–278, https://doi.org/10.1016/j.actbio.2022.06.028.

[66] C.D. Walkey, J.B. Olsen, F. Song, R. Liu, H. Guo, D.W.H. Olsen, Y. Cohen, A. Emili, W.C.W. Chan, Protein Corona Fingerprinting Predicts the Cellular Interaction of Gold and Silver Nanoparticles, ACS Nano 8 (2014) 2439–2455, https://doi.org/10.1021/nn406018q.

[67] H. Tang, Y. Zhang, T. Yang, C. Wang, Y. Zhu, L. Qiu, J. Liu, Y. Song, L. Zhou, J. Zhang, et al., Cholesterol Modulates the Physiological Response to Nanoparticles by Changing the Composition of Protein Corona, Nat. Nanotechnol. 18 (2023) 1067–1077, https://doi.org/10.1038/s41565-023-01455-7.

[68] A.-M. Hada, A.-M. Craciun, M. Focsan, R. Borlan, O. Soritau, M. Todea, S. Astilean, Folic Acid Functionalized Gold Nanoclusters for Enabling Targeted Fluorescence Imaging of Human Ovarian Cancer Cells, Talanta 225 (2021) 121960, https://doi.org/10.1016/j.talanta.2020.121960.

[69] H. Chen, Y. Wang, T. Wang, D. Shi, Z. Sun, C. Xia, B. Wang, Application Prospective of Nanoprobes with MRI and FI Dual-Modality Imaging on Breast Cancer Stem Cells in Tumor, J. Nanobiotechnol. 14 (2016) 52, https://doi.org/10.1186/s12951-016-0195-8.

[70] M. Mahmoudi, S. Sant, B. Wang, S. Laurent, T. Sen, Superparamagnetic Iron Oxide Nanoparticles (SPIONs): Development, Surface Modification and Applications in Chemotherapy, Adv. Drug Deliv. Rev. 63 (2011) 24–46, https://doi.org/10.1016/j.addr.2010.05.006.

[71] M. Mahmoudi, I. Lynch, M.R. Ejtehadi, M.P. Monopoli, F.B. Bombelli, S. Laurent, Protein−Nanoparticle Interactions: Opportunities and Challenges, Chem. Rev. 111 (2011) 5610–5637, https://doi.org/10.1021/cr100440g.

[72] N. Singh, G.J.S. Jenkins, R. Asadi, S.H. Doak, Potential Toxicity of Superparamagnetic Iron Oxide Nanoparticles (SPION), Nano Rev. 1 (2010) 5358, https://doi.org/10.3402/nano.v1i0.5358.

[73] X.-D. Zhang, D. Wu, X. Shen, P.-X. Liu, F.-Y. Fan, S.-J. Fan, In Vivo Renal Clearance, Biodistribution, Toxicity of Gold Nanoclusters, Biomaterials 33 (2012) 4628–4638, https://doi.org/10.1016/j.biomaterials.2012.03.020.

[74] E.V. Dukhopelnykov, Y.N. Blyzniuk, A.A. Skuratovska, E.G. Bereznyak, N. A. Gladkovskaya, Interaction of Doxorubicin Delivered by Superparamagnetic Iron Oxide Nanoparticles with DNA, Colloids Surf. B Biointerfaces 219 (2022) 112815, https://doi.org/10.1016/j.colsurfb.2022.112815.

[75] G. Fei, S. Ma, C. Wang, T. Chen, Y. Li, Y. Liu, B. Tang, T.D. James, G. Chen, Imaging Strategies Using Cyanine Probes and Materials for Biomedical Visualization of Live Animals, Coord. Chem. Rev. 447 (2021) 214134, https://doi.org/10.1016/j.ccr.2021.214134.

Advanced Protein-Embedded Bimetallic Nanocomposite Optimized for *In Vivo* Fluorescence and Magnetic Resonance Bimodal Imaging

Authors: Radek Ostruszka[1], Aminadav Halili[2], Tomáš Pluháček[3], Lucie Rárová[4], Daniel Jirák[2,5], Karolína Šišková[1,*]

[1]Department of Experimental Physics, Faculty of Science, Palacký University Olomouc, tř. 17. listopadu 12, 77900 Olomouc, Czech Republic

[2]Institute for Clinical and Experimental Medicine, Vídeňská 9, 14021 Prague, Czech Republic

[3]Department of Analytical Chemistry, Faculty of Science, Palacký University Olomouc, tř. 17. listopadu 12, 77900 Olomouc, Czech Republic

[4]Department of Experimental Biology, Faculty of Science, Palacký University Olomouc, Šlechtitelů 27, 77900 Olomouc, Czech Republic

[5]Faculty of Health Studies, Technical University of Liberec, Studentská 1402/2, 46117 Liberec, Czech Republic

*Corresponding author (K.Š.) email and phone no.: karolina.siskova@upol.cz; tel.: +420-585-634-175

Keywords: magnetic resonance imaging; fluorescent imaging; bioimaging; contrast agent; inorganic-organic nanocomposite; magneto-luminescent nanocomposite.

*Table of contents***:**

1. Optimization of synthesis

Samples containing various molar ratios of BSA : Au : Fe were synthesized under the same conditions as the final optimized APEBM nanocomposite (see chapter *1.2 Synthesis of the APEBM nanocomposite, purification, concentrate formation, and storage conditions*). There was only a minor exception: the step of microwave irradiation was used between the second addition of NaOH and the sample incubation inside a dry bath incubator. This was done due to the fact that the optimizing experiments were influenced by the synthesis described in one of our previous publications (Ostruszka et al.2022). The power of the microwave oven was set to 150 W, and the irradiation lasted 10 seconds. Additionally, the samples were not dialyzed to be able to investigate the fluorescence intensity changes in time.

To prepare different variations of the Au : Fe molar ratio, the concentrations of both metal precursors were adjusted accordingly. Therefore, the volume of NaOH added during the first NaOH addition (V_1) was also modified based on the concentration of ferric chloride used. A higher ferric chloride concentration required a higher V_1 to obtain the pH of 7.4. However, the total volume of added NaOH was kept the same (200 µL), thus the volume of NaOH during the second NaOH addition was equal to $200 - V_1$ [µL].

To obtain the integrated fluorescence intensities, the emission spectra at numerous incubation times were measured. For this purpose, JASCO F8500 (Jasco, Tokyo, Japan) spectrofluorimeter was used. The excitation wavelength was set to 480 nm and all spectra were corrected to avoid any deviations induced by instrumental components. Other parameters were the same as described in chapter *1.3.6 Fluorescence spectroscopy and dynamic light scattering (DLS)*. It should be noticed that fluorescence quantum yield (FQY) values were not used because the concentration-dependent iron absorption at the excitation wavelength distorts FQY to different extents. Therefore, the concentration of gold was considered when the comparison of fluorescence intensities was performed. When deciding on the most suitable molar ratio, the following important requirements were taken into consideration: (i) the highest fluorescence intensity reached within 20-24 hours, (ii) the concentration of iron as high as possible (to increase magnetic resonance contrast), and, concomitantly, (iii) no visible precipitation of iron oxides, nor protein gelation. The specific range of maturing time was set based on our previous experiences with the protein-embedded nanocomposite syntheses (Andrýsková et al. 2020; Ostruszka et al. 2023).

The resulting integrated fluorescence intensities for many types of APEBM nanocomposites are shown in Table SI-1. For clarity of presentation, only two incubation times are shown for each molar ratio. The molar ratio that best fulfils the requirements mentioned in the previous paragraph is the 1:20:20 ratio with its emission maximum reached after approximately 20 hours of incubation. Apparently, irreversible protein and/or iron aggregation occurred during or after the synthesis in several molar ratios (Table SI-1). With the protein to total metal ratio being 1:55 or 1:60, samples started to form very viscose liquid or even insoluble gel. Moreover, with the increasing iron and/or gold concentration, either the maturing time is prolonged, and/or the intensity does not increase as much as in the case of the 1:20:20 ratio. For instance, if we compare the ratios of 1:20:20, 1:20:25, and 1:20:30, one can see that in the first case, the sample is at its maximum after 20 hours, and after 39 hours, the intensity is already lower. On the contrary, the intensity is still increasing from 20 to 39 hours in the samples containing molar ratios of 1:20:25 and 1:20:30 (the intensity increase is even more pronounced in the latter). Very similar trend applies for gold content increase as well.
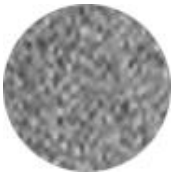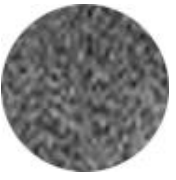
Table SI-1: *Integrated fluorescence intensities at different incubation times for samples containing various molar ratios of BSA:Au:Fe. Excitation wavelength was set to 480 nm.*

Molar ratio of BSA:Au:Fe	Integrated fluorescence intensity [a.u.]		
	Time [hours]		
	6	17 or 20	39
1:10:10	aggregation		
1:15:25	73198	73819	-
1:15:30	62291	85716	-
1:20:20	-	144465	122818
1:20:25	-	103746	125923
1:20:30	-	23963	75829
1:25:20	-	37766	78970
1:25:25	-	7885	15952
1:25:30	aggregation, high viscosity		
1:30:20	-	6561	8581
1:30:25	aggregation, high viscosity		
1:30:30	aggregation, mostly insoluble solid gel		

Note: increasing integrated fluorescence intensity is colour coded: going from yellow to dark green (the highest).

2. *In vitro MR imaging, metal concentrations, and relaxometry measurements*

Table SI-2: *T_1- weighted MR images of phantoms representing four different concentrations (labelled as 100%, 75%, 50%, and 25%) of a representative APEBM nanocomposite sample and distilled water serving as a reference (labelled as H_2O), with corresponding signal-to-noise-ratio (SNR) and contrast-to-noise-ratio (CNR) values.*

Sample concentration	100%	75%	50%	25%	H_2O
T_1-weighted MR signal					
SNR	6.70	6.69	5.97	4.31	3.11
CNR	3.59	3.58	2.85	1.21	

3. Determination of total gold and iron concentrations by ICP-MS

Table SI-3: *Experimentally accessed total gold and iron concentrations for three replicates (denoted as BM 1, BM 2, and BM 3) of the APEBM nanocomposite determined by ICP-MS and corresponding theoretical BSA concentration.*

Sample	$[BSA]_T$ [mM]	$[BSA]_T$ [mg·mL^{-1}]	$[Fe]_E$ [mM]	$[Fe]_E$ [mg·mL^{-1}]	$[Au]_E$ [mM]	$[Au]_E$ [mg·mL^{-1}]
BM 1			5.47	0.31	4.91	0.97
BM 2	0.30	20.13	5.45	0.30	4.87	0.96
BM 3			5.39	0.30	4.74	0.93

4. Relaxometry measurements

$R_2 = 2.1890 \cdot [\text{Fe}] - 0.1578$

$R_1 = 0.2118 \cdot [\text{Fe}] + 0.2126$
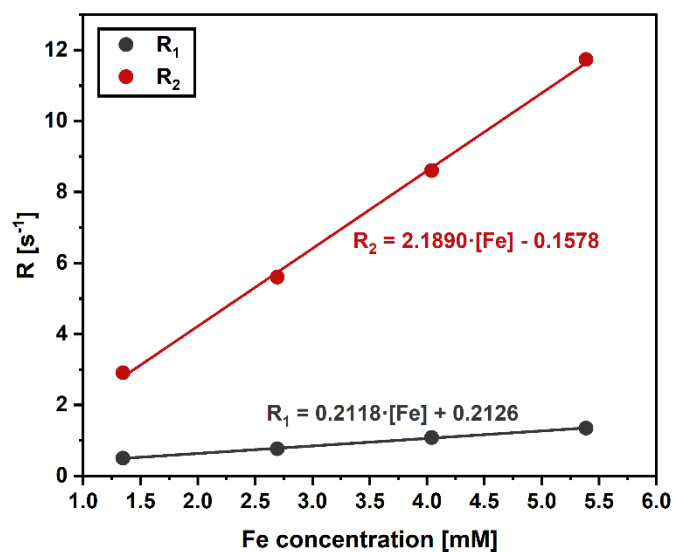
Figure SI-1A: *Relaxation rate R versus Fe concentration for the BM 1 sample. R_1 and R_2 values were fitted with a linear function according to equation (1).*

$R_2 = 2.1048 \cdot [\text{Fe}] + 0.0098$

$R_1 = 0.2059 \cdot [\text{Fe}] + 0.2176$
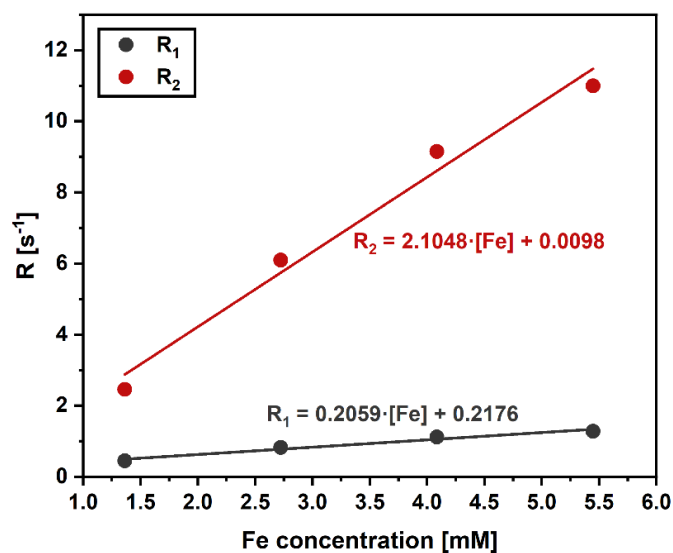
Figure SI-1B: *Relaxation rate R versus Fe concentration for the BM 2 sample. R_1 and R_2 values were fitted with a linear function according to equation (1).*
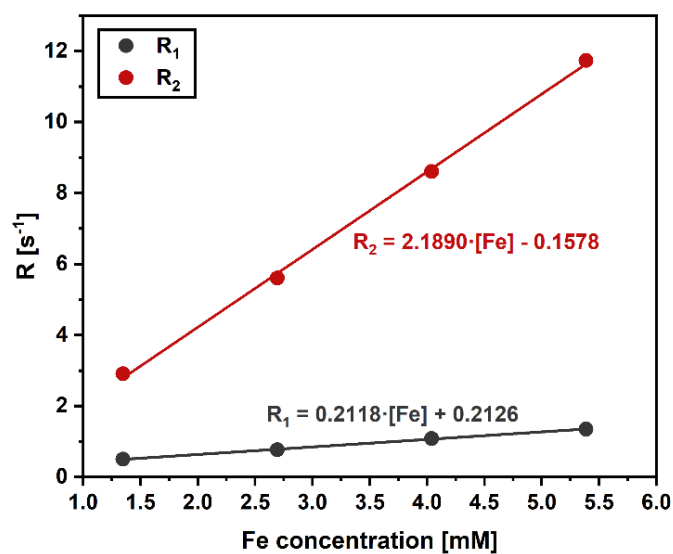
Figure SI-1C: *Relaxation rate R versus Fe concentration for the BM 3 sample. R_1 and R_2 values were fitted with a linear function according to equation (1).*

Table SI-4: *Relaxivity values and the corresponding r_2/r_1 ratio for three replicates (denoted as BM 1, BM 2, and BM 3) of the APEBM nanocomposite.*

Sample	r_1 [L·mmol⁻¹·s⁻¹]	r_2 [L·mmol⁻¹·s⁻¹]	r_2/r_1
BM 1	0.207	2.129	10.3
BM 2	0.206	2.105	10.2
BM 3	0.212	2.189	10.3

5. In vitro fluorescence imaging and emission spectra
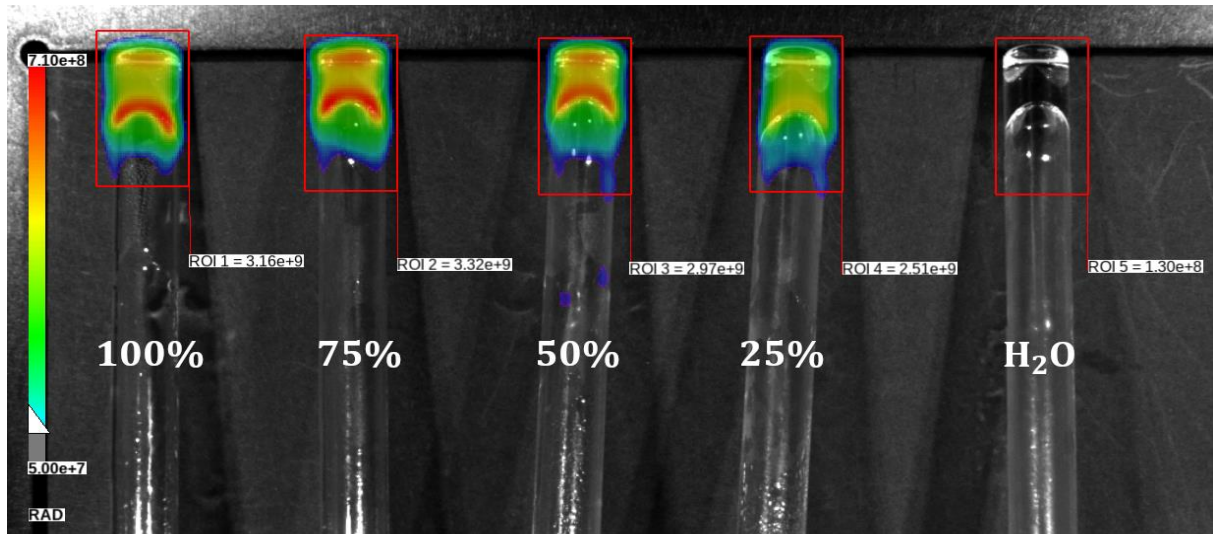
Figure SI-2: *In vitro fluorescence image of phantoms representing four different concentrations (labelled as 100%, 75%, 50%, and 25%) of a representative APEBM nanocomposite sample and distilled water serving as a reference (labelled as H2O). Excitation and emission wavelengths were 430 nm and 730 nm, respectively.*
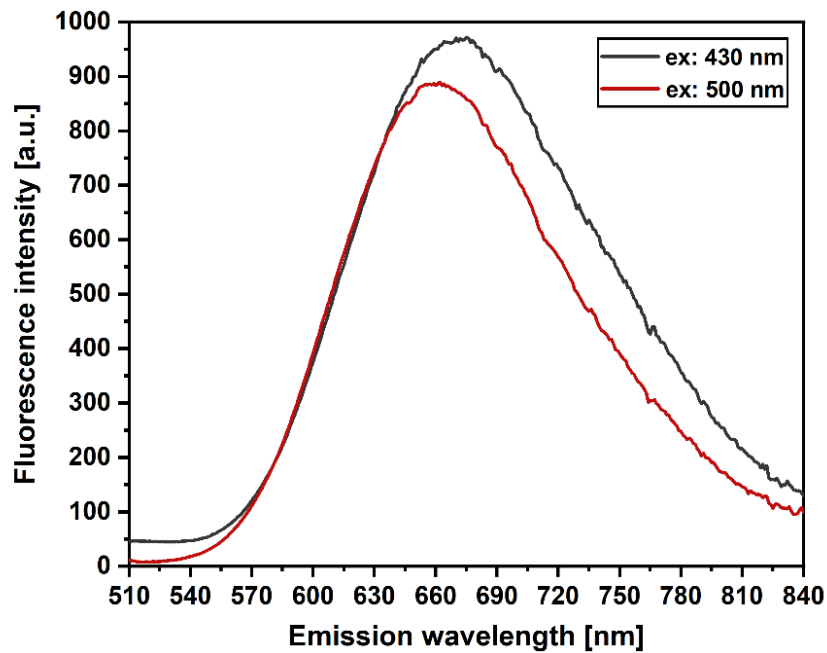
Figure SI-3: *Emission spectra of the representative APEBM nanocomposite sample for two different excitation wavelengths: 430 nm (grey line) with the emission maximum at 675 nm and 500 nm (red line) with the emission maximum at 662 nm.*

8

Table SI-5: *Values of the total emission E acquired by in vitro fluorescence imaging (FI) of phantoms using four different concentrations (labelled as 100%, 75%, 50%, and 25%) of three replicates (denoted as BM 1, BM 2, and BM 3) of the APEBM nanocomposite; distilled water served as a reference. <u>Excitation and emission wavelengths were 500 nm and 670 nm</u>, respectively. Note: total emissions for the selected APEBM concentrations, after subtraction of distilled water signal, are listed.*

| Sample	$E \cdot 10^8$ [photons·s^{-1}]				
	100%	**75%**	**50%**	**25%**	**H$_2$O**
BM 1	61.5	57.3	49.5	33.0	0.8
BM 2	62.3	63.3	54.3	36.6	0.7
BM 3	56.5	59.3	52.7	32.3	0.7

Table SI-6: *Values of the total emission E acquired by in vitro fluorescence imaging (FI) of phantoms using four different concentrations (labelled as 100%, 75%, 50%, and 25%) of three replicates (denoted as BM 1, BM 2, and BM 3) of the APEBM nanocomposite; distilled water served as a reference. <u>Excitation and emission wavelengths were 430 nm and 730 nm</u>, respectively. Note: total emissions for the selected APEBM concentrations, after subtraction of distilled water signal, are listed.*

Sample	$E \cdot 10^8$ [photons·s^{-1}]				
	100%	**75%**	**50%**	**25%**	**H$_2$O**
BM 1	29.7	29.2	26.8	19.7	1.4
BM 2	30.3	31.9	28.4	23.8	1.3
BM 3	27.3	30.5	26.9	17.9	1.2

6. Biocompatibility and DLS characterization

Gold and iron concentrations for the concentrated representative APEBM sample (that was used for the cell viability assessment) were determined by ICP-MS and the average values are listed in the second row of the Table SI-7.

Table SI-7: *Average cell viability ($\overline{CV}$) values with corresponding standard deviations (SD) and average gold and iron concentrations for eight different concentrations of a representative APEBM nanocomposite (labelled as 99%, 70%, 50%, 36%, 26%, 18%, 13%, and 9%).*

Sample concentration	[Au] [mM]	[Fe] [mM]	$\overline{CV} \pm$ SD [%]
concentrated sample	28.04	26.81	-
99%	5.61	5.36	93.5 ± 1.1
70%	4.01	3.83	103.5 ± 0.5
50%	2.86	2.74	106.7 ± 2.3
36%	2.04	1.95	100.5 ± 0.5
26%	1.46	1.40	108.9 ± 3.6
18%	1.04	1.00	107.3 ± 2.3
13%	0.74	0.71	115.3 ± 0.8
9%	0.53	0.51	122.1 ± 13.0

Note 1: Considering the cell viability assay methodology, the concentrated samples are diluted 5 times with the cell suspension when viability tests are performed. The listed concentration series is given by further dilution of APEBM sample. This dilution was considered when the sample concentration and the concentrations of both metals in the tested samples were calculated.

Note 2: Sometimes cell viability exceeds 100% which is a generally observed phenomenon (reported by many researchers) and can be considered as normal.
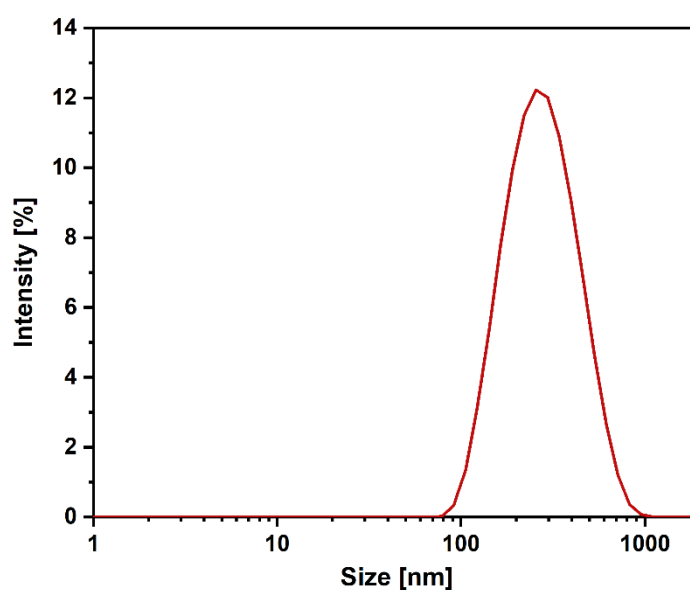
Figure SI-4: *Averaged particle size distribution derived from the changes of scattered light intensity of a representative APEBM nanocomposite sample. The resulting hydrodynamic diameter (size) is 296 ± 14 nm.*

7. Assessment of fluorescence signal stability under different conditions
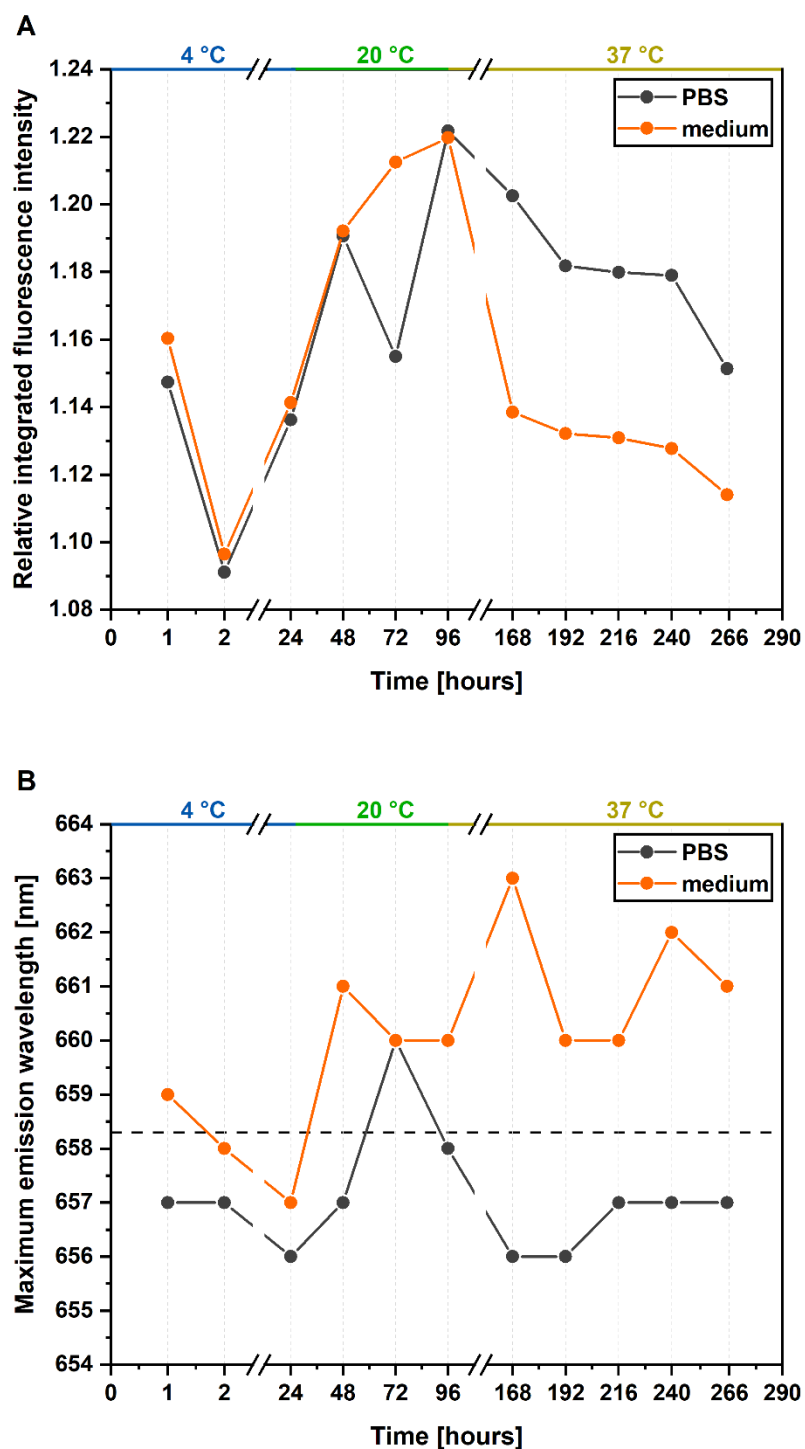
Figure SI-5: *(A) Integrated fluorescence intensity of APEBM sample in selected media (PBS, cultivation medium) under varying temperatures as a function of time relative to averaged integrated fluorescence intensity of APEBM sample in deionized water. Excitation wavelength was set to 500 nm. (B) Position of emission maximum of APEBM samples under varying conditions as a function of time. Horizontal dash line represents the averaged position of emission maximum of dialysed APEBM nanocomposite in deionized water.*
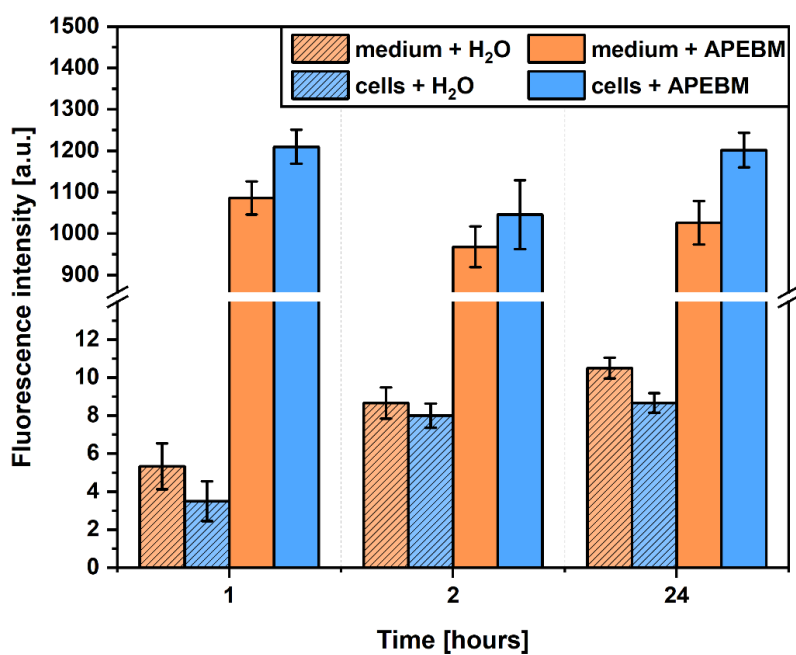
Figure SI-6: *Fluorescence intensity changes in selected periods elapsed from APEBM samples introduction to the cultivation medium, with/without HeLa cells presence. Excitation and emission wavelengths were set to 500 nm and 670 nm, respectively.*

8. Normalized absorption and emission spectra
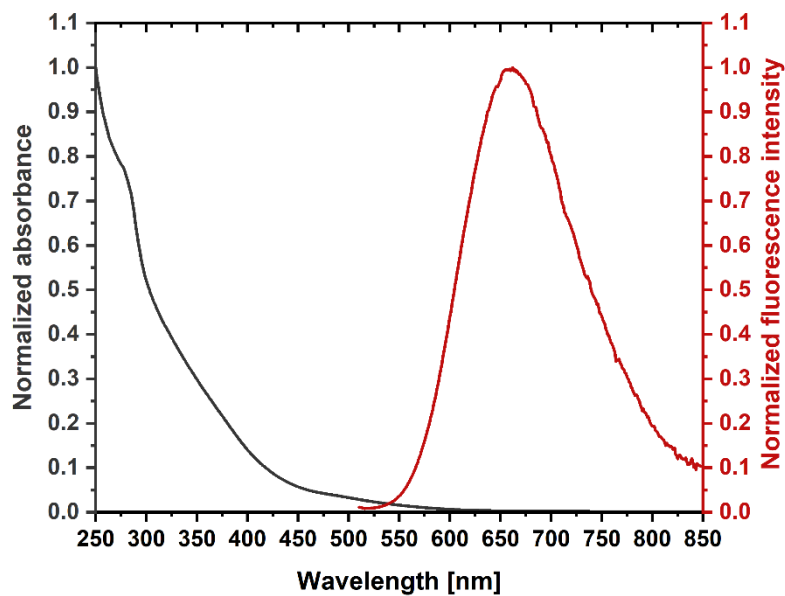
Figure SI-7: *Normalized absorption (grey line) and emission (red line) spectra of the representative APEBM nanocomposite sample. The excitation wavelength was set to 500 nm.*

9. References for Supporting Information

Andrýsková, P.; Šišková, K.M.; Michetschlägerová, Š.; Jiráková, K.; Kubala, M.; Jirák, D. The Effect of Fatty Acids and Bsa Purity on Synthesis and Properties of Fluorescent Gold Nanoclusters. *Nanomaterials* **2020**, *10*, 1–20, doi:10.3390/nano10020343.

Ostruszka, R.; Zoppellaro, G.; Tomanec, O.; Pinkas, D.; Filimonenko, V.; Šišková, K. Evidence of Au(II) and Au(0) States in Bovine Serum Albumin-Au Nanoclusters Revealed by CW-EPR/LEPR and Peculiarities in HR-TEM/STEM Imaging. *Nanomaterials* **2022**, *12*, 1425, doi:10.3390/nano12091425.

Ostruszka, R.; Půlpánová, D.; Pluháček, T.; Tomanec, O.; Novák, P.; Jirák, D.; Šišková, K. Facile One-Pot Green Synthesis of Magneto-Luminescent Bimetallic Nanocomposites with Potential as Dual Imaging Agent. *Nanomaterials* **2023**, *13*, 1027, doi:10.3390/nano13061027.

UNIVERZITA PALACKÉHO V OLOMOUCI

PŘÍRODOVĚDECKÁ FAKULTA

KATEDRA EXPERIMENTÁLNÍ FYZIKY

AUTOREFERÁT DISERTAČNÍ PRÁCE

Funkční nanokompozity pro duální zobrazování fluorescencí a magnetickou rezonancí

Autor práce:	Mgr. Radek Ostruszka
Studijní program:	Nanotechnologie
Vedoucí práce:	doc. RNDr. Karolína Šišková, Ph.D.

Olomouc 2024

Uchazeč	*Školitel*
Mgr. Radek Ostruszka	**doc. RNDr. Karolína Šišková, Ph.D.**
Katedra experimentální fyziky	Katedra experimentální fyziky
Přírodovědecká fakulta	Přírodovědecká fakulta
Univerzita Palackého v Olomouci	Univerzita Palackého v Olomouci

<div align="center">Oponenti</div>

RNDr. Eva Kočišová, Ph.D.	**prof. Pavel Matějíček, Ph.D.**
Fyzikální ústav	Katedra fyzikální a makromolekulární chemie
Matematicko-fyzikální fakulta	Přírodovědecká fakulta
Univerzita Karlova v Praze	Univerzita Karlova v Praze

<div align="center">Místo a termín obhajoby</div>

…………………………………………………………………………………..

S plným textem této disertační práce je možné se seznámit na studijním oddělení Přírodovědecké fakulty Univerzity Palackého v Olomouci.

Prohlašuji, že jsem tento autoreferát disertační práce vypracoval samostatně, pod vedením doc. RNDr. Karolíny Šiškové, Ph.D. a za použití literatury uvedené v kapitole 4. Reference.

V Olomouci dne……………..………   …………………………………..…

Abstrakt

Předložená dizertační práce se především zaměřuje na poskytnutí širšího vhledu do problematiky kovových nanostruktur (NSs) a nanokompozitů (NCPs). Na počátku je práce věnována velikostním přechodům kovového materiálu z makroskopických rozměrů do velikostního režimu nanočástic (NPs) a dále nanoklastrů (NCs), přičemž přechod mezi posledně zmíněnými NSs je pro případ Au detailněji rozebrán. Posléze je text zaměřen na kovové NSs, se kterými jsem se v rámci studia setkal. Jedná se o zlaté nanoklastry (AuNCs) a superparamagnetické nanočástice oxidů železa (SPIONs). V případě AuNCs jsou popisovány vlastnosti optické, zejména tedy absorpční a luminiscenční, a v případě SPIONs pak vlastnosti magnetické. V obou případech jsou rovněž uvedeny jednotlivé strategie syntéz a také praktické využití těchto NSs. Následně práce pojednává o bimetalických NCPs tvořených jak z AuNCs, tak SPIONs, jejich syntéze a praktickém využití. Posléze je popsána matrice užívaná pro syntézu zmíněných NSs, kterou je protein, albumin hovězího séra (BSA). Závěrečná část dizertační práce se věnuje shrnutí vědecké činnosti jejího autora spolu s poznatky z přiložených publikací, které svou náplní postupně směřují od systému referenčního (tj. monometalický nanokompozit sestávající z proteinové matrice a AuNCs, nebo proteinové matrice a SPIONs) až k systému bimetalickému, který kombinuje jak vlastnosti AuNCs, tak i SPIONs. Optimalizované optické a superparamagnetické vlastnosti byly využity při *in vivo* fluorescenčním zobrazování (FI) a zobrazování magnetickou rezonancí (MRI), přičemž prezentovaný optimalizovaný bimetalický systém má potenciál sloužit jakožto efektivní inertní kontrastní látka pro duální FI/MRI.

Abstract

The presented dissertation thesis mainly focuses on providing a broader insight into the issue of metal nanostructures (NSs) and nanocomposites (NCPs). Initially, the thesis is devoted to the size transitions of the metallic material from the macroscopic dimensions to the size regime of nanoparticles (NPs) and then to nanoclusters (NCs). In the case of Au, the transition between the last mentioned NSs is analysed in more detail. Afterwards, the thesis is focused on the metallic NSs, which I encountered during my studies; namely, gold nanoclusters (AuNCs) and superparamagnetic iron oxide nanoparticles (SPIONs). In the case of AuNCs, optical properties are described, specifically absorption and luminescence. Regarding SPIONs, a description of the magnetic properties is given. In both cases, individual synthetic strategies and the practical use of these NSs are also presented. Subsequently, the thesis discusses bimetallic NCPs formed of both the AuNCs and SPIONs, their synthesis and practical usage. Then, the protein matrix (namely, bovine serum albumin, BSA) employed for the synthesis of the mentioned NSs is introduced. The final part of the dissertation thesis is dedicated to a summary of the scientific activity of its author together with findings described in the attached publications. The content of these publications gradually goes from a reference system (i.e., monometallic nanocomposite consisting of a protein matrix and AuNCs, or a protein matrix and SPIONs) towards a bimetallic system, which combines the properties of both the AuNCs and SPIONs. The optimized optical and superparamagnetic properties have been exploited in *in vivo* fluorescence imaging (FI) and magnetic resonance imaging (MRI). The presented optimized bimetallic system has the potential to serve as an effective inert contrast agent for dual FI/MRI.

SEZNAM ZKRATEK uvedených v textu

Zkratka	Český název/*Anglický název*
AuNCs	zlaté nanoklastry/*gold nanoclusters*
AuNPs	zlaté nanočástice/*gold nanoparticles*
AuNSs	zlaté nanostruktury/*gold nanostructures*
BSA	hovězí sérový albumin/*bovine serum albumin*
DOS	hustota energetických stavů/*density of states*
EPR	elektronová paramagnetická rezonance/*electron paramagnetic resonance*
FI	fluorescenční zobrazování/*fluorescence imaging*
GSH	glutathion/*glutathione*
HOMO	nejvyšší obsazený molekulový orbital/*highest occupied molecular orbital*
LUMO	nejnižší neobsazený molekulový orbital/*lowest unoccupied molecular orbital*
MRI	zobrazování magnetickou rezonancí/*magnetic resonance imaging*
NCs	nanoklastry/*nanoclusters*
NCP	nanokompozit/*nanocomposite*
NCPs	nanokompozity/*nanocomposites*
NPs	nanočástice/*nanoparticles*
NSs	nanostruktury/*nanostructures*
PL	fotoluminiscence/*photoluminescence*
QY	kvantový výtěžek/*quantum yield*
SPIONs	superparamagnetické nanočástice oxidů železa/*superparamagnetic iron oxide nanoparticles*
SPR	povrchová plazmonová rezonance/*surface plasmon resonance*
SR	thiolát/*thiolate*
UVA oblast	ultrafialová oblast A/*ultraviolet region A*

OBSAH

1. Rozšířený přehled problematiky

1.1. Od objemového kovu k NCs

Kovy makroskopických rozměrů jsou tvořeny tak obrovským množstvím atomů, že jejich hustota energetických stavů (DOS) je natolik vysoká, že se projevuje existencí spojitých energetických pásů, které jsou výsledkem lineárních kombinací nezměrného počtu energeticky velice podobných atomových orbitalů. Pásovou strukturu kovů lze charakterizovat pomocí valenčního a vodivostního pásu, zatímco zakázaný pás v případě kovů neexistuje, jelikož se oba zmíněné pásy částečně překrývají [1,2]. Vlivem této skutečnosti se elektrony mohou za normálních podmínek vyskytovat volně také v pásu vodivostním, díky čemuž jsou kovy výbornými elektrickými vodiči [3]. Emise záření při excitaci objemového Au, Cu a jejich slitiny byla poprvé demonstrována v roce 1969 autorem Mooradian (1969) [4] jako neefektivní proces s QY v řádu 10^{-10}.

Zmenšíme-li velikost kovové částice na hodnotu srovnatelnou či menší, než je střední volná dráha vodivostních elektronů, dostaneme se do oblasti kovových NPs, kdy pohyb elektronů začíná být omezován rozměrem kovu, a k interakcím se zářením tak dochází primárně v rámci povrchu částice [1]. Tato skutečnost je příčinou optického jevu nazývaného jako povrchová plazmonová rezonance (SPR), jejíž podstatou jsou kolektivní oscilace vodivostních elektronů během interakce se zářením [1,2]. Díky tomuto NPs vykazují silnou absorpci světla, nicméně intenzita fluorescence je relativně slabá, kdy QY se pohybuje řádově od 10^{-7} do 10^{-2}, přičemž velikost, tvar a metoda přípravy NPs mají vliv na hodnotu QY [5]. DOS je charakterizována existencí kvazi-spojité pásové struktury [6,7].

Zmenšujeme-li velikost kovové částice nadále, až na hodnotu srovnatelnou s Fermiho vlnovou délkou elektronu (tj. de Broglieho vlnová délka elektronu na Fermiho hladině, přičemž pro případ Au je ≈ 0,5 nm [8]), dochází postupně k dalšímu řídnutí energetických hladin, a tím k rozpadu kvazi-spojité pásové struktury NPs, kdy DOS začíná být tvořena víceméně diskrétními energetickými hladinami, mezi kterými může docházet k elektronovým přechodům vlivem interakce se zářením [1,9,10]. Dostáváme se do oblasti NCs, jejichž chování je podobné molekulám a jejich chemické, optické a elektrické vlastnosti se výrazně odlišují jak od NPs, tak rovněž i od objemového kovu [1,6,9]. Průměr kovového jádra takovýchto NSs bývá zpravidla menší než 2 nm [11–13].

NCs již nevykazují SPR [1,2], naproti tomu však vykazují silnou luminiscenci s QY v řádu jednotek, a dokonce i desítek procent [11,13,14].

1.2. AuNCs a jejich optické vlastnosti

AuNCs značené jako $Au_n(SR)_m$, kde *n* označuje počet atomů Au a *m* počet thiolátových (SR) ligandů, představují modelový systém, jehož **struktura** se obecně skládá z kovového jádra a vnějšího obalu tvořeného jak povrchovými atomy Au, tak samotnými SR ligandy. Přítomnost tohoto obalu komplikuje studium optických vlastností AuNCs vzhledem k tomu, že nejen kovové jádro, ale i obal přispívá svými energetickými hladinami k hraničním molekulovým orbitalům [15], tj. HOMO a LUMO. Výzkumný tým Jin a spol. [16] poprvé uvedli do souvislosti krystalovou strukturu a optické vlastnosti aniontu modelové sloučeniny $Au_{25}(SR)_{18}^-$ (kde R = CH_2CH_2Ph představuje fenylethylový zbytek) provedením výpočtů s užitím časově závislé teorie funkcionálu hustoty týkajících se elektronové struktury (viz Obrázek 1A) a optického absorpčního spektra (viz Obrázek 1B) [16].
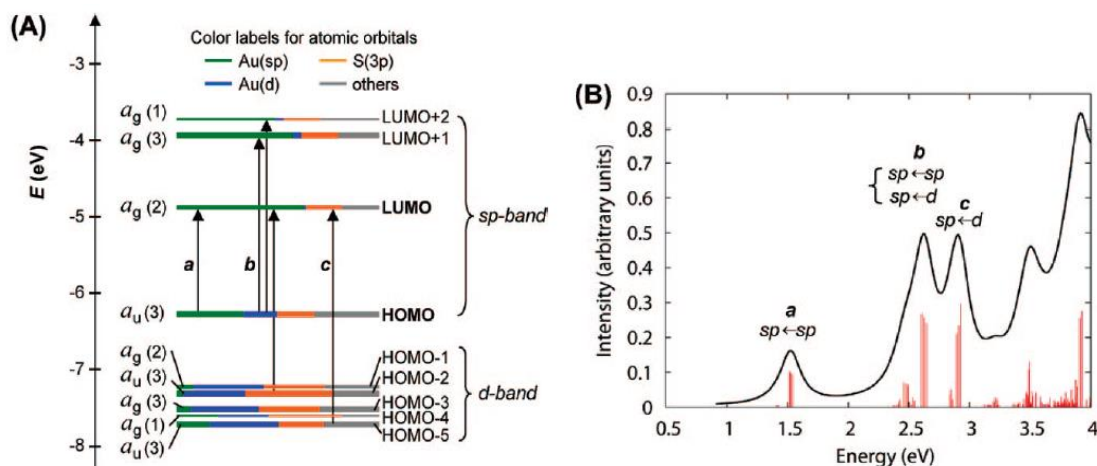
Obrázek 1: *(A) Kohn-Shamův diagram energetických hladin molekulových orbitalů aniontu modelové sloučeniny $Au_{25}(SR)_{18}^-$, kde R představuje fenylethylový zbytek. Barevné označení každého molekulového orbitalu naznačuje relativní příspěvek atomových orbitalů Au (6sp) (zeleně), Au (5d) (modře), S (3p) (oranžově) a ostatních komponent (šedě). Nalevo je uvedena symetrie (a_g, a_u) a stupeň degenerace (číslo v závorce) daného molekulového orbitalu. HOMO = nejvyšší obsazený molekulový orbital, LUMO = nejnižší neobsazený molekulový orbital. (B) Teoretické absorpční spektrum $Au_{25}(SR)_{18}^-$. Převzato z [16].*

Na základě Kohn-Shamova diagramu energetických hladin molekulových orbitalů Jin a spol. [16] přisoudili jednotlivé píky v teoretickém absorpčním spektru (viz Obrázek 1B) aniontu modelové sloučeniny elektronovým přechodům mezi jejími energetickými hladinami (viz Obrázek 1A). Pík při 1,52 eV (≈ 816 nm) přiřadili přechodu mezi hladinami HOMO a LUMO, jenž je v obou obrázcích označen písmenem a. Jde tedy v podstatě o vnitropásový (sp ← sp) přechod. Pík při 2,63 eV (≈ 471 nm) přiřadili jak vnitropásovému, tak mezipásovému (sp ← d) přechodu (oba označeny písmenem b) a pík při 2,91 eV (≈ 426 nm) přiřadili mezipásovému přechodu, který je označen písmenem c. Jelikož jsou HOMO a LUMO (a také HOMO-1 a LUMO+1) složeny převážně z atomových orbitalů Au v kovovém jádru, na pík při 1,52 eV lze pohlížet jako na přechod, jenž je zcela definován elektronovou a geometrickou strukturou kovového jádra [16]. K odlišnému výsledku dospěli Nobusada a Iwasa (2007) [17], kteří přisoudili absorpční pík při 1,77 eV (≈ 702 nm) přechodu mezi hladinami HOMO a LUMO, kdy LUMO je primárně tvořen orbitaly nacházejícími se okolo atomu Au sdíleného dvěma ikosaedrálními Au_{13} jádry. Rozdílnost výsledků obou skupin autorů poukazuje na vliv struktury nanoklastru na jeho absorpční vlastnosti. Kromě struktury nanoklastru má na optické vlastnosti vliv např. i jeho **velikost** [15], **oxidační stav** , [6,18] a t**eplota** [19].

Velmi studovanou optickou vlastností AuNCs je jejich schopnost vykazovat **luminiscenci**. Jsou přijímány dva primární **mechanismy** fotoluminiscence (PL) AuNCs: (i) efekt kvantového omezení a (ii) přenos náboje, jenž zahrnuje přenos náboje z ligandu na kov (LMCT) a z ligandu na systém kov-kov (LMMCT) [20]. Link a kol. (2002) [21] připravili AuNCs s využitím glutathionu (GSH) jakožto thiolového ligandu, které po předchozí excitaci vlnovou délkou 514 nm vykazují emisi jak ve viditelné (při 1,55 eV ≈ 800 nm), tak i v infračervené (při 1,13 eV ≈ 1097 nm) oblasti. Strukturu energetických hladin a původ PL píků poté prezentují na základě dvou modelů: pevnolátkového a molekulárního. Na základě pevnolátkového modelu přiřadili PL ve viditelné oblasti mezipásovému přechodu (6sp → 5d), kdežto PL v oblasti infračervené přechodu vnitropásovému (sp → sp) mezi hladinami HOMO a LUMO. Na základě molekulárního modelu pak přisoudili pík ve viditelné oblasti fluorescenci a pík v infračervené oblasti fosforescenci. K opačnému závěru však došli autoři Devadas a kol. (2010) [22], kteří připravili AuNCs odlišující se svými thiolovými ligandy, kdy využili 1-hexanthiol a GSH. Oba systémy vykazovaly PL jak ve viditelné, tak infračervené oblasti. Fotoluminiscenci ve viditelné oblasti přiřadili přechodu mezi hladinami HOMO a LUMO

kovového jádra, kdežto PL v oblasti infračervené přiřadili přechodu mezi hladinami kovového jádra a hladinami vnějšího obalu. Závěr autorů Link a kol. (2002) [21] podporují výsledky autorů Li a kol. (2019) [23] a Zhou a Song (2021) [24], kteří uvádějí, že původcem PL v infračervené oblasti je kovové jádro. Zhou a Song (2021) [24] také dále uvádějí, že zdrojem PL ve viditelné oblasti je přenos náboje mezi kovovým jádrem a vnějším obalem (viz Obrázek 2).
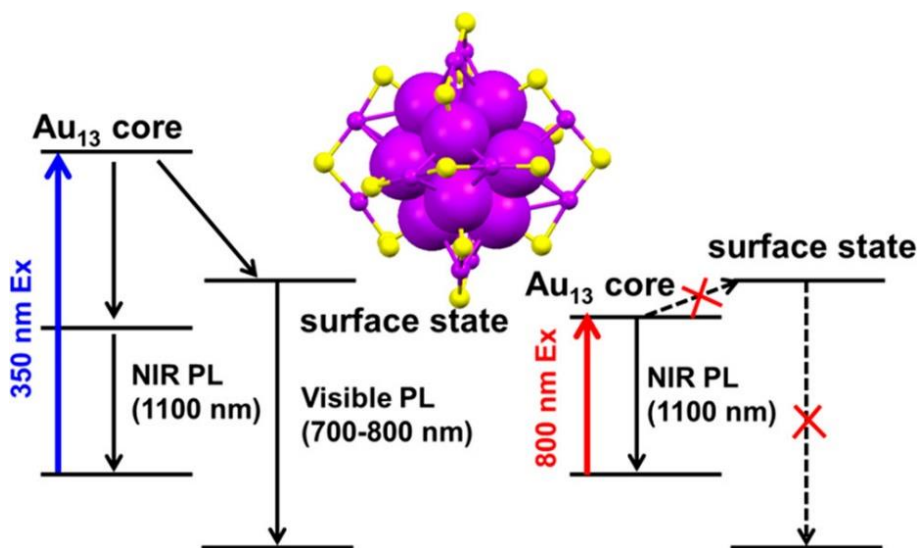
Obrázek 2: *Mechanismus fotoluminiscence (PL) $Au_{25}(SR)_{18}^-$. Převzato z [24].*

V nedávné práci naší výzkumné skupiny Šišková a spol. [25] bylo pomocí elektronové paramagnetické rezonance (EPR) prokázáno, že luminiscence AuNCs zanořených v BSA, vykazujících emisi u 655 nm (při excitaci u nižších vlnových délek), je jejich vnitřní vlastností a nejedná se v tomto případě o přenos náboje. Současně bylo v této práci zjištěno, že kromě oxidačního stavu Au^0 je přítomen též oxidační stav Au^{2+}.

V porovnání s např. anorganickými kvantovými tečkami (II. B – VI. A skupin) je **intenzita PL** AuNCs poměrně slabá. Jednou z možností, jak navýšit intenzitu PL, je **výměna ligandů** [26–28]. Kromě intenzity PL může mít výměna ligandů vliv i na **pozici maxima emise** [29,30]. Další možností navýšení intenzity luminiscence je **změna oxidačního stavu** Au [31–33], využití fotofyzikálního jevu nazývaného jakožto **agregací indukovaná emise** nebo **nahrazování jednoho či více atomů Au heteroatomem/y**, jakými mohou například být Ag, Cu, Cd, Er, Pt a Zn [34–36].

1.3. Metody syntézy a praktické využití AuNCs

K provedení syntézy AuNCs lze užít jednu ze dvou strategií: shora dolů, tedy z objemového materiálu směrem k NSs (anglicky top-down), nebo zdola nahoru, tudíž poskládáním jednotlivých atomů do NSs (anglicky bottom-up). **Top-down** metoda zahrnuje především chemické leptání, kdy jsou materiály větších rozměrů, jakými mohou být například Au nanokrystaly [37], AuNPs [38] či větší AuNCs [39], leptány prostřednictvím nadbytku ligandů [40], nebo rovněž s využitím samotného prekurzoru Au [41] za vzniku AuNCs. Mezi ligandy užívané k leptání patří různé thiolové sloučeniny [39,42], merkaptanové kyseliny [29], polyethylenimin [37] či GSH [38,43].

Princip **bottom-up** metody spočívá v redukci iontů Au (převážně Au^{3+}) na atomy Au^0 a následné nukleaci těchto atomů za vzniku AuNCs [44]. Mezi užívané formy redukce patří **redukce chemická** [13,45,46] a elektrochemická [47], fotoredukce [14,48,49] a redukce uvnitř biologického systému [50,51]. Je známo, že zvýšená teplota může usnadnit redukční reakce poskytnutím potřebné aktivační energie pro přeměnu prekurzorů obsahujících Au ionty na Au atomy či AuNCs [20]. Yan a kol. (2012) [52] byli první, kdo k syntéze AuNCs chráněných BSA využili mikrovlnné záření, čímž podstatně zkrátili reakční dobu z desítek hodin na několik minut. Kromě výše uvedených forem redukce byly provedeny syntézy pomocí **sonochemické metody** [11,53,54] a **mikroemulzního procesu** [55].

V rámci syntézy AuNCs se kromě samotných prekurzorů a redukčních činidel užívá téměř vždy nějaká templátová molekula či ligand. V případě syntézy bez této komponenty by mohlo dojít k interakcím mezi jednotlivými NCs, které by vedly k nevratné agregaci z důvodu snížení jejich povrchové energie [56]. Rovněž by mohlo postupně docházet k přerůstání AuNCs v AuNPs, jak bylo v naší skupině dříve pozorováno [57]. Ke stabilizaci AuNCs je možno užít širokou škálu ligandů, jakými jsou například: různé thiolové sloučeniny [58]; dendrimery [59,60], což jsou polymery s pravidelnou rozvětvenou strukturou, velmi dobře definovaným chemickým složením a molekulovou hmotností [61]; dále polymery [62,63]; proteiny [53,64]; peptidy [65,66]; různé sekvence DNA [67] a jednotlivé nukleotidy [68,69].

Praktické **využití AuNCs** je poměrně rozmanité, počínaje **detekcí** iontů kovů [70–72], různých aniontů jako S^{2-}, CN^-, NO_2^- [73–75] a malých molekul jako například bilirubin, cystein, dopamin, H_2O_2, H_2S a cholesterol [76–82]. AuNCs lze také úspěchem

využít k detekci enzymů [83–85], měření pH [86,87] a teploty [88,89], detekci patogenních bakterií [90,91] a metastází rakoviny [92]. Detekce bývá z převážné části založena na zhášení signálu PL (kupříkladu [73,79,93]) vlivem interakce AuNCs s ionty kovů či malými molekulami. Existují však některé systémy, jejichž intenzita PL je vlivem interakce naopak navýšena (například [72,94,95]). V leckterých případech jsou AuNCs konjugovány s jinými entitami vykazujícími také luminiscenci [94,96], ale v jiné oblasti spektra. Tyto pak slouží jako reference, neboť jejich luminiscenční signál je oproti AuNCs konstantní. Mezi další principy detekce patří například agregací indukované zhášení [97], agregací indukovaná emise [71], změna signálu elektrochemiluminiscence [98] či změna v poloze maxima absorpce [85].

Mimo detekci lze AuNCs využít také ke **katalýze** chemických reakcí [99–102], regulace hladiny glukózy v krvi [103,104], *in vitro* nebo *in vivo* **zobrazování** s užitím výpočetní tomografie a/nebo PL [105–107], fototermální [108–110] a fotodynamické [109,111,112] **terapii**, **transportu léčiv** do nádorových buněk [106,113,114] a v neposlední řadě jako teranostický systém [105,114], tj. kombinace diagnostiky a terapie [115].

1.4. SPIONs a jejich magnetické vlastnosti

NPs tvořené z feromagnetického či ferimagnetického materiálu mající velikost zhruba do 20 nm mohou vykazovat unikátní formu magnetismu nazývanou jako **superparamagnetismus** [116–118]. V případě SPIONs se nejčastěji jedná o magnetit (Fe_3O_4), maghemit (γ-Fe_2O_3) či ferity (oxid železa s příměsí jednoho či více přechodných kovů, například Ba, Co, Cu, Mn, Ni) [119,120].

Pro vysvětlení podstaty superparamagnetismu je potřeba začít s magnetickými materiály větších, okem viditelných, rozměrů. Magnetické materiály makroskopických velikostí jsou složeny z magnetických domén, což jsou oblasti uniformní magnetizace, které jsou od sebe odděleny doménovými stěnami, uvnitř kterých se směr magnetizace mění plynule od jedné domény ke druhé [121]. Když se velikost materiálu zmenšuje, počet magnetických domén klesá, přičemž jakmile je velikost částice srovnatelná se šířkou doménové stěny, vznik vícera domén není možný, a částice je tedy tvořena pouze jednou doménou [121,122]. Přesněji řečeno, materiál je tvořen pouze jednou magnetickou doménou, pokud energie nutná k tvorbě další domény je větší než pokles

energie, ke kterému by došlo v důsledku snížení výsledného magnetického toku [116]. Se změnou velikosti materiálu se obecně mění také magnetická koercivita, která představuje intenzitu vnějšího magnetického pole potřebnou k odstranění zbytkové magnetizace (tzv. magnetické remanence) [118,123,124]. Její průběh v závislosti na velikosti pro NPs magnetitu (Fe_3O_4) mající krychlový tvar lze pozorovat na obrázku níže (viz Obrázek 3), kdy během přechodu z multidoménového charakteru částice na jednodoménový je koercivita maximální a s dalším snižováním velikosti částice klesá k nule.
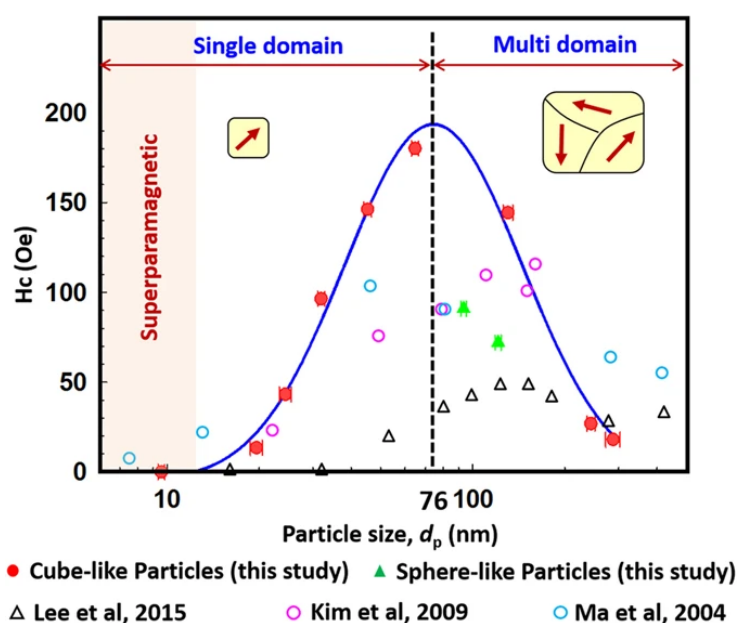
Obrázek 3: *Závislost magnetické koercivity nanočástic Fe_3O_4 na jejich velikosti při teplotě 300 K. Červené kruhové značky představují nanočástice s kubickou strukturou, zelené trojúhelníkové značky představují nanočástice se sférickou strukturou a černé trojúhelníkové, fialové kruhové a modré kruhové značky jsou postupně výsledky autorů Ma a kol. (2004) [125], Kim a kol. (2009) [126] a Lee a kol. (2015) [124]. Převzato z [118].*

Při dosažení určité hraniční velikosti částice, kdy je tepelná energie srovnatelná s energií potřebnou k reorientaci spinů (magnetická anizotropní energie), je koercivita nulová, a materiál se tedy nachází v superparamagnetickém režimu [123,124]. Tepelná energie tak umožňuje po odstranění působení vnějšího magnetického pole uskutečnit spontánní reorientaci spinů, která vede ke znáhodnění magnetických dipólů v určitém časovém intervalu, a tudíž k demagnetizaci materiálu není potřeba žádná dodatečná vnější energie [116,123]. Z důvodu potřeby dostatečné tepelné energie je poněkud zřejmé, že

kromě velikosti částice je superparamagnetismus svázán také s její teplotou. Teplota, při které je tepelná energie k_BT rovna magnetické anizotropní energii, se nazývá blokační teplota T_B [123]. V případě, kdy $T < T_B$, není tepelná energie potřebná ke spontánní reorientaci spinů dostatečná, a koercivita tak začíná být opět nenulová [116].

V superparamagnetickém režimu tedy materiál nevykazuje hysterezní chování, jinými slovy, vykazuje nulovou magnetickou remanenci a koercivitu [116,123,127,128]. Jak název tohoto jevu napovídá, hodnota saturační magnetizace superparamagnetických NPs je větší než v případě částic paramagnetických, nicméně je srovnatelná se saturační magnetizací feromagnetických a ferimagnetických částic [116]. Saturační magnetizace SPIONs závisí jak na velikosti částic [118], tak na krystalové struktuře a typu obalujícího materiálu [129], dále také na tloušťce obalu [130], molárním poměru Fe^{2+}/Fe^{3+}, iontové síle, pH a na tom, zda byla při syntéze použita inertní (N_2) atmosféra [131].

1.5. Metody syntézy a praktické využití SPIONs

Obdobně jako v případě AuNCs mohou být k **přípravě SPIONs** použity oba popisované přístupy: shora dolů či zdola nahoru [132]. Celkově lze využít mnoha různých strategií, které lze rozdělit na chemické, fyzikální a biologické, přičemž volbou syntézy lze dosáhnout různých tvarů, velikostí, struktury, koloidní stability a magnetických vlastností, čímž lze zajistit různé oblasti využití [133]. Mezi chemické metody lze zařadit tepelný rozklad, hydrotermální či solvotermální syntézu, syntézu s využitím polyolů, mikroemulzní a sol-gelovou syntézu a spolusrážení (koprecipitaci) [127]. K fyzikálním metodám patří kulové mletí, laserová ablace, pyrolýza či spalování [132]. V případě biologických metod lze k syntéze využít rostliny [134], zdravé či rakovinné buňky [135], plísně [136], řasy [137,138], bakterie [139] či kvasinky [140].

Povrch SPIONs je velice reaktivní z důvodu zvýšené plochy povrchu vůči objemu, tudíž se povrch SPIONs obvykle **obaluje** k zamezení aglomerace či agregace a modulace velikosti a tvaru [127]. Nicméně, tyto povrchové úpravy mohou **ovlivnit** jednak magnetické **vlastnosti** SPIONs v závislosti na množství, složení či šířce povrchové vrstvy [127], jednak například vstup NPs do buněk [141]. Mezi ligandy užívané k obalování SPIONs patří např. dextran [142], chitosan [143], polyethylenglykol [144] a polyvinylpyrrolidon [145].

Jedním ze směrů aplikovatelnosti **SPIONs** je jejich **uplatnění** jakožto kontrastní látky v rámci **zobrazování** magnetickou rezonancí (MRI) (například [146,147]). SPIONs jsou považovány za účinné T_2 kontrastní látky, jelikož dokáží zkrátit dobu transverzálního (neboli spin-spinového) relaxačního času magnetického momentu jednotlivých protonů, díky čemuž se ovlivněná oblast jeví jako tmavší [148,149]. Dalším využitím SPIONs je magnetickým polem indukovaná **hypertermie**. Její fyzikální princip spočívá v generaci tepla NPs vlivem působení nestacionárního vnějšího magnetického pole [135]. Biologický účinek hypertermie je založen na skutečnosti, že zdravé buňky dokáží vydržet působení vyšších teplot, kdežto naopak rakovinné buňky při takovýchto teplotách podstupují apoptózu [150]. SPIONs lze také využít k **cílenému transportu léčiv** do nádorových buněk, jenž může být aktivně zprostředkován jednak působením vnějšího magnetického pole [151–153], jednak konjugací SPIONs s látkou umožňující cílit na nádorové buňky [154–157]. Takovými látkami mohou být protilátky a jejich fragmenty, ligandy receptorů, peptidy či aptamery [150]. Příkladem budiž hojně užívaná kyselina listová [154–156]. Přidanou výhodou k cílenému transportu může být rovněž možnost kontrolovaného uvolňování transportovaného léčiva v reakci na určitý stimul, a to například působením blízkého infračerveného záření [158] či ultrazvuku [156] nebo změnou pH [159]. Cílený transport léčiv lze kombinovat s hypertermií [160,161]. Mirzaghavami a kol. (2021) [162] dokonce připravili systém kombinující cílený transport léčiv, hypertermii a také možnost radioterapie, přičemž jejich spojením dosáhli signifikantně lepších terapeutických účinků. Posledním příkladem využití SPIONs je **odstraňování iontů těžkých kovů** jako například Cd^{2+}, Co^{2+}, Cr^{6+}, Cu^{2+}, Pb^{2+} a Hg^{2+} [163–166].

1.6. Bimetalické NCPs složené z AuNCs a SPIONs nebo magnetických nanočástic oxidů železa, jejich syntéza a využití

Nanokompozit (NCP) je soustava složená ze dvou či více materiálů, přičemž minimálně jeden z jeho rozměrů je řádově v nanometrech [167]. **Bimetalický NCP** je pak NCP obsahující dva kovové materiály [168]. Existují dva různé přístupy přípravy NCPs, jejichž jednou ze součástí jsou kovové NCs: postsyntetická funkcionalizace a *in situ* syntéza [10]. Prvně zmiňovaný přístup spočívá v přípravě jednotlivých součástí NCP, jejich následné funkcionalizaci a propojení ve výsledný NCP. K metodám

využívajícím tento přístup patří například **chemická konjugace** [169,170], metoda **povrchové redukce** [171], **nekovalentní interakce** [172,173] a **samouspořádání** [174]. V případě *in situ* syntézy je NCP připraven postupným smísením všech prekurzorů v jednu reakční směs [175]. Zmíněné příklady syntéz byly uvedeny pro případ, kdy byl NCP tvořen jak AuNCs, tak SPIONs nebo magnetickými nanočásticemi oxidů železa. Obecně lze však bimetalické NCPs syntetizovat také **pomocí dalších metod**, ke kterým patří kupříkladu solvotermální a hydrotermální metoda, pyrolýza nebo elektrodepozice [10].

Přidáním další kovové NSs lze vylepšit stávající vlastnosti monometalického NCP [169,176] a/nebo rozšířit jeho aplikovatelnost o další zobrazovací modalitu či jiné **využití** (například [170,173,174]). Zobrazování s využitím několika modalit současně může být velmi přínosné, neboť jejich užitečnou kombinací lze překonat omezení související s jejich samostatným používáním. Kupříkladu, vysoká citlivost optického zobrazování umožňuje sledování biologických dějů na molekulární úrovni v reálném čase, nicméně kvůli omezené propustnosti záření skrz tkáně neumožňuje získat její detailní 3D obraz. Na rozdíl od toho MRI poskytuje 3D obraz měkkých tkání s vysokým prostorovým rozlišením, ale bohužel citlivost této metody je nízká [173,177].

1.7. Proteinová matrice BSA

Sérové albuminy jsou hojně zastoupené v tělech všech obratlovců, podílejí se na udržování osmotického tlaku krve a hrají důležitou roli v distribuci mnoha metabolitů, hormonů, léčiv a přechodných kovů [178,179]. Většina albuminů savců (i BSA) obsahuje 4 vazebná místa pro kovy, které se však značně liší svou strukturou a specifitou [178]. Jmenovitě jde o N-koncové místo (známé jako NTS), Cys34 a jeho okolí, vazebné místo A, které bylo později ztotožněno s vícekovovým vazebným místem, a vazebné místo B [178].

Primární struktura BSA je dána sekvencí 583 aminokyselin, přičemž její podobnost se sekvencí lidského sérového albuminu je 75,6 % [180,181]. Je tvořen celkem 2 tryptofanovými rezidui, 20 tyrozinovými rezidui a 35 cysteinovými rezidui, z nichž 34 vytváří disulfidické můstky [180–182]. Sekundární struktura BSA je převážně α-helikální [183,184]. Terciární struktura se skládá ze tří homologních domén (I, II a III), přičemž každá doména se skládá ze dvou subdomén (A a B) (viz Obrázek 4) [181].
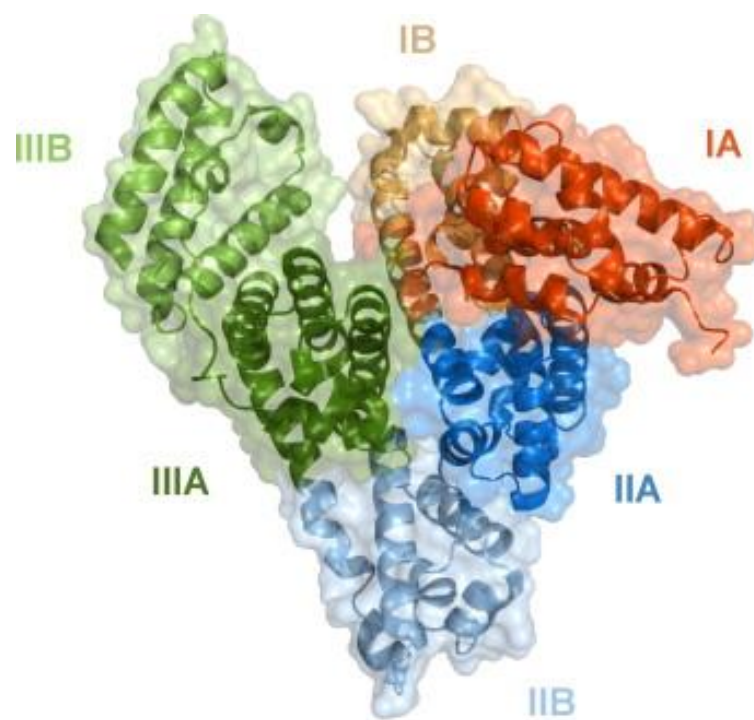
Obrázek 4: *Terciární struktura hovězího sérového albuminu sestává ze tří domén (I, II a III), přičemž každá doména se skládá ze dvou subdomén (A a B). Převzato z [181].*

2. Stručné shrnutí vědecké činnosti

Práci na bimetalických NCPs obsahujících jak AuNCs, tak SPIONs předcházela příprava a charakterizace monometalických NCPs sestávajících pouze z AuNCs. Tento systém je logicky jednodušší, jeho příprava je tvořena menším množstvím kroků a hlavně parametrů, což bylo pro následně uskutečněné optimalizace výhodnější. Monometalický systém sloužil také jako reference ke zmíněnému bimetalickému NCP. Příprava tohoto monometalického systému byla inspirována syntézou publikovanou autory Xie a kol. (2009) [64], přičemž místo konvenčního ohřevu byl pro urychlení vývoje AuNCs použit ohřev mikrovlnný dle autorů Yan a kol. (2012) [52]. Matricí obou výše zmíněných skupin autorů byl protein hovězí sérový albumin (BSA). Jeho význam spočívá v redukci iontů Au^{3+} a následné stabilizaci tvorby a růstu AuNCs [25]. Některé parametry syntézy (koncentrace, molární poměry a doba mezi přidáním jednotlivých vstupních látek, doba mikrovlnného ohřevu, výkon mikrovlnného záření a doba vývoje systému) však byly upraveny s přihlédnutím k výsledkům optimalizačních experimentů, jež byly provedeny z důvodu dosažení co největší hodnoty QY v rozumném čase vývoje systému. Část těchto výsledků, konkrétně vliv molárního poměru $HAuCl_4$ a NaOH (ovlivňující pH reakční směsi) na hodnotu QY a vlnovou délku maxima emise, je uvedena v konferenčním příspěvku autorů Ostruszka a Šišková (2022) [185].

Připravený monometalický NCP, značený jako AuBSA, vykazuje emisi v červené oblasti spektra s výskytem jednoho maxima při vlnové délce 655 ± 1 nm a hodnotou QY stanovenou jako $6,7 \pm 0,1$ % [25]. Průměrná velikost AuNCs určená pomocí transmisní elektronové mikroskopie je $1,01 \pm 0,24$ nm, kdežto v případě užití transmisní elektronové mikroskopie s vysokým rozlišením byla průměrná velikost větší než 2 nm, což bylo vysvětleno pozorováním *in situ* tvorby AuNPs pod fokusovaným svazkem elektronů při užití většího zvětšení a/nebo během mapování s využitím energiově disperzní spektroskopie. Pomocí EPR bylo jednak zjištěno, že okamžitě po zahájení ozařování systému AuBSA UVA zářením o vlnové délce 325 nm dochází k tvorbě thiylových (RS$^{\bullet}$), tryptofanových (Trp$^{\bullet}$) a C-centrovaných (C$^{\bullet}$) radikálů, které s AuNCs magneticky neinteragují, ale při prodlouženém ozařování (nad 10 minut) vedou k nevratnému poškození proteinové matrice; jednak byla poprvé v rámci NCP tvořeného BSA a AuNCs prokázána přítomnost Au^{2+}, přičemž autoři většinou uvádějí výskyt oxidačních stavů Au^0 a Au^+, jež nejčastěji detekují pomocí rentgenové fotoelektronové spektroskopie (například [45,64,186,187]). Rovněž byla porovnáním EPR spekter systému AuBSA

a prekurzoru Au, kterým byla kyselina tetrachlorozlatitá (HAuCl₄), potvrzena schopnost BSA redukovat Au^{3+} na nižší oxidační stavy, přičemž s využitím absorpční spektroskopie byla pozorována redukce Au^{3+} na Au^0 za vzniku AuNPs (jejichž projevem je pík SPR) v případě, kdy byla HAuCl₄ inkubována s tyrosinem (aminokyselina, která je součástí BSA).

V návaznosti na monometalický systém AuBSA byl současně připraven jednak NCP bimetalický, značený jako AuBSA-Fe, jehož syntéza byla obohacena o prekurzory železa (FeCl₂·4H₂O a FeCl₃·6H₂O), nicméně původní molární poměry pro ostatní reaktanty (tj. BSA: HAuCl₄ a HAuCl₄: NaOH) byly zachovány; jednak byl připraven další referenční NCP, označený jako BSA-Fe, jenž se od AuBSA liší tím, že neobsahuje AuNCs, ale naopak je tvořený SPIONs generovanými v přítomnosti BSA. Syntéza tohoto NCP je obdobou syntézy AuBSA-Fe s tím rozdílem, že HAuCl₄ byla nahrazena HCl tak, že bylo ponecháno stejné látkové množství Cl^-. Jak systém BSA-Fe, tak AuBSA-Fe byly opět zkoumány pomocí EPR spektroskopie a bylo experimentálně prokázáno, že v rámci obou systémů je Fe přítomno jednak ve formě jednojaderných komplexů, jednak ve formě SPIONs (jak bylo dříve prokázáno pomocí Mössbauerovy spektroskopie v [25], přičemž v případě bimetalického NCP dochází k tvorbě SPIONs menších velikostí než v rámci systému monometalického BSA-Fe [188]. Také byla pozorována komunikace v podobě přenosu náboje mezi SPIONs (donor) a komplexy Fe (akceptor) po ozáření UVA zářením o vlnové délce 325 nm, avšak pouze v případě BSA-Fe (v rámci AuBSA-Fe nebyl tento přenos náboje pozorován). V neposlední řadě byl proveden experiment s užitím spinové pasti (anglicky spin trap), který odhalil přítomnost hydroxylových radikálů (˙OH) generovaných ve vodném roztoku po ozáření obou studovaných NCPs (BSA-Fe a AuBSA-Fe) UVA zářením po dobu 5 minut při pokojové teplotě.

AuNCs v systému AuBSA-Fe opět emitují v červené oblasti spektra s obdobnými hodnotami vlnové délky maxima emise a QY, jaké měly AuNCs v systému AuBSA [189]. Z průběhu mössbauerovských spekter při teplotách 300 a 5 K (u druhého též v externím magnetickém poli) bylo prokázáno, že nanočásticová forma Fe v systému AuBSA-Fe je superparamagnetický oxid železa v oxidačním stavu III. Výsledky z energiově disperzní spektroskopie poukazují na dominantní výskyt O v blízkosti Fe v nanočásticové formě a přítomnost S poblíž Au. Je známo, že AuNCs je k BSA vázáno přes S (například [190,191]) a SPIONs (a oxidy železa obecně) interagují snadno s COOH a/nebo OH skupinami [192,193]. Důsledkem této odlišné afinity je fakt, že jak AuNCs, tak SPIONs

mohou být v rámci BSA lokalizovány poblíž odlišných aminokyselinových reziduí [188]. Také bylo provedeno *in vitro* MRI s viditelným T_2 kontrastem a relaxometrie, kdy hodnoty relaxivity byly získány fitováním závislosti reciproké hodnoty relaxačního času na koncentraci Fe, přičemž ve zkoumaném rozsahu koncentrací byly identifikovány dvě lineární závislosti, a byly tedy získány dvě hodnoty relaxivity. V neposlední řadě byla stanovena viabilita nerakovinných RPE-1 buněk při jejich inkubaci s AuBSA-Fe, která dosahovala hodnot okolo 80 % pro obě koncentrační oblasti, což dle ISO 10993 řadí tento NCP stále mezi netoxické látky [189].

V mezičase probíhaly četné optimalizace diskutovaného bimetalického systému, jednak na základě znalostí získaných z optimalizačních experimentů monometalického systému AuBSA, jednak byly některé experimenty inspirovány kupříkladu autory Babes a kol. (1999) [194], Andrade a kol. (2010) [195] a Ueno a kol. (2014) [196]. Optimalizace byly převážně zaměřeny na vylepšení magnetického kontrastu, jelikož uspokojivého kontrastu v případě systému AuBSA-Fe bylo dosaženo pouze po předchozím zakoncentrování vzorků, což mimo jiné vedlo ke zvýšení viskozity roztoku a snížení viability buněk zhruba na hraničních 80 %. Optimalizace bimetalického systému byla mnohem komplexnější, a to jednak proto, že zpočátku byla nepřekonatelnou překážkou jeho stabilita, jelikož docházelo k častým agregacím proteinové matrice nebo převážně agregacím Fe v mikročástice, jednak bylo potřeba najít takové podmínky, aby obě výsledné NSs (jak AuNCs, tak SPIONs) vykazovaly současně co možná nejlepší vlastnosti za daný čas jejich společného vývoje. Jedny z posledních experimentů byly inspirovány Jolivet a kol. (2004) [197], přičemž byly prováděny s myšlenkou, že zvýšení pH na hodnotu 7,4 před přidáním $HAuCl_4$, kdy se Fe^{3+} vyskytují převážně ve formě neutrálních komplexů [197], by mohlo vést ke zvýšení interakcí mezi komplexy Fe a proteinovou matricí, která by se navíc měla v tomto pH nacházet ve své přirozené konformaci [198,199]. Některé výsledky z těchto optimalizačních experimentů jsou uvedeny v Ostruszka a kol. (2024) [175].

Nakonec se povedlo připravit bimetalický NCP, označený jako APEBM, jehož syntéza respektuje principy „zelené chemie" (tj. práce ve vodném prostředí, použití netoxických látek a vyvarování se nadbytečnému množství chemikálií) [175]. Oproti syntéze AuBSA-Fe byly upraveny a/nebo nově zavedeny následující parametry: typ prekurzoru Fe, pořadí přidání jednotlivých reaktantů, jemná úprava pH před přidáním $HAuCl_4$, prodloužená doba mezi jednotlivými kroky syntézy, typ ohřevu pro urychlení

obou chemických procesů (redukce Au^{3+} iontů a formace SPIONS) a delší doba dozrávání vzorku, a to navíc při vyšší teplotě. Výsledkem je NCP velmi stabilní vůči agregaci jak v deionizované vodě, tak i v pufru PBS a kultivačním médiu, a to při různých teplotách inkubace (4, 20 a 37 °C). Teoretické molární poměry BSA: Au: Fe byly z původních hodnot 1: 10: 0,75 navýšeny na 1: 20: 20, přičemž experimentální poměry po dialýze jsou 1: 16: 18. Koncentrace Fe v optimalizovaném NCP byla tedy celkově navýšena více než dvacetinásobně. Bimetalický APEBM NCP vykazuje monomodální distribuci velikostí s hodnotou hydrodynamického průměru $d_H = 296 \pm 14$ nm a buněčné viability větší než 90 % pro nejvyšší koncentraci vzorku (tj. koncentrace přímo po dialýze, jež vzorek naředí vždy 1,5x deionizovanou vodou). Nejprve bylo provedeno *in vitro* FI a MRI, avšak s přihlédnutím ke komplexnosti buněčné internalizace nanomateriálů, která je závislá na mnoha vzájemně propojených parametrech, bylo rovněž provedeno zobrazování *in vivo*. Z výsledných obrázků pořízených během i*n vivo* MRI (viz Obrázek 5A a 5B) a FI (viz Obrázek 5C) je zřejmé, že prezentovaný NCP má schopnost sloužit jakožto efektivní inertní kontrastní látka pro duální zobrazování. Luminiscenční signál optimalizovaného NCP je nejméně 20x silnější než signál reference (tj. končetina injektovaná destilovanou vodou) a MR kontrast lze relativně dobře odlišit od okolní svalové tkáně.
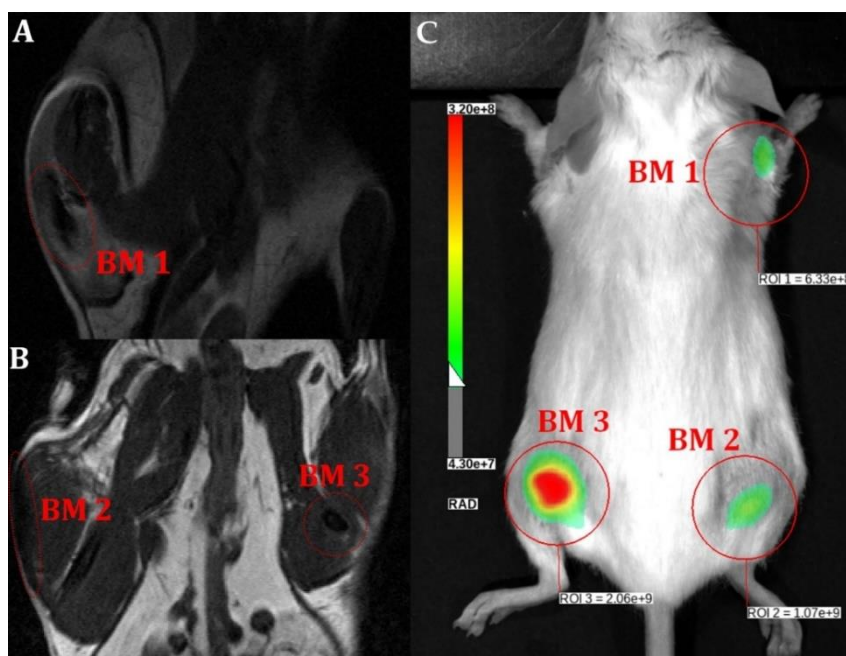
Obrázek 5: *In vivo (A, B) zobrazování magnetickou rezonancí a (C) fluorescenční zobrazování zdravé BALB/c myši pod anestézií. Triplikát bimetalického nanokompozitu APEBM (označené jako BM 1, BM 2 a BM 3) byl aplikován do jednotlivých končetin. Do neoznačené končetiny byla vpíchnuta destilovaná voda sloužící jako reference. Obrázky převzaty z [175] a zkombinovány.*

3. Závěr

Předložená dizertační práce se ze své převážné části soustředí na předání poznatků ohledně dvou zcela odlišných kovových NSs, AuNCs a SPIONS, které rozebírá z hlediska jejich optických (případ AuNCs) či magnetických (případ SPIONs) vlastností, strategií syntézy a rovněž možností praktického využití. Posléze se práce věnuje jednak systémům kombinujícím uvedené NSs, jednak proteinu BSA, jenž byl po celou dobu vědecké činnosti autora používán jako matrice pro syntézu těchto NSs. Druhá část práce se zaměřuje právě na zmíněnou vědeckou činnost autora, ve které jsou rozebírány jak NCPs monometalické (značené jako AuBSA, BSA-Fe) sloužící jako referenční systémy, tak NCPs bimetalické (označené jako AuBSA-Fe a APEBM). Díky relativně velkému množství postupných optimalizací syntézy bylo nakonec dosaženo přípravy systému APEBM, jenž je stabilní vůči agregaci v různých prostředích při různých teplotách, vysoce biokompatibilní a má schopnost sloužit jako inertní kontrastní látka pro *in vivo* **duální zobrazování** (FI a MRI). Důležité je zdůraznit, že APEBM nebylo nutné zakoncentrovat pro to, aby poskytoval dostatečný MRI signál, což je velký pokrok oproti systému AuBSA-Fe, jehož zakoncentrování vedlo k poklesu biokompatibility a nárůstu viskozity. Další potenciální využití systémů obsahujících SPIONs (ať už jde o systém monometalický či bimetalický) souvisí s generováním ˙OH (detekovaných pomocí EPR spektroskopie) ve vodném roztoku po ozáření daného systému UVA zářením po dobu 5 minut, čehož by se v budoucnu mohlo využít v environmentální oblasti k odstraňování polutantů ve vodě či k eliminaci mikroorganismů. V tomto směru je nicméně potřeba provést další experimenty. Mimo to lze samozřejmě pokračovat také v biomedicínské oblasti, kdy lze systém vylepšit například o možnost cílení do nádorových buněk, a tím umožnit jejich zobrazení a/nebo eliminaci. Nakonec je rovněž podstatné neopomenout roli referenčních monometalických systémů, díky kterým byly osvětleny mnohé vlastnosti nejen samotných monometalických, ale také bimetalických NCPs, což mimo jiné vedlo k přesnějším interpretacím získaných dat a k lepšímu pochopení těchto systémů.

4. Reference

[1] Díez I., Ras R.H.A. (2010) Few-Atom Silver Clusters as Fluorescent Reporters. In: *Advanced Fluorescence Reporters in Chemistry and Biology II: Molecular Constructions, Polymers and Nanoparticles.*, pp. 307–332. DOI: 10.1007/978-3-642-04701-5_10.

[2] Zhang L., Wang E. (2014) Metal nanoclusters: New fluorescent probes for sensors and bioimaging. *Nano Today* **9**, 132–157. DOI: 10.1016/j.nantod.2014.02.010.

[3] Sonia, Komal, Kukreti S., Kaushik M. (2021) Gold nanoclusters: An ultrasmall platform for multifaceted applications. *Talanta* **234**, 122623. DOI: 10.1016/j.talanta.2021.122623.

[4] Mooradian A. (1969) Photoluminescence of Metals. *Physical Review Letters* **22**, 185–187. DOI: 10.1103/PhysRevLett.22.185.

[5] Olesiak-Banska J., Waszkielewicz M., Obstarczyk P., Samoc M. (2019) Two-photon absorption and photoluminescence of colloidal gold nanoparticles and nanoclusters. *Chemical Society Reviews* **48**, 4087–4117. DOI: 10.1039/C8CS00849C.

[6] Liu Z., Zhu M., Meng X., Xu G., Jin R. (2011) Electron Transfer between [Au$_{25}$(SC$_2$H$_4$Ph)$_{18}$]$^-$TOA$^+$ and Oxoammonium Cations. *The Journal of Physical Chemistry Letters* **2**, 2104–2109. DOI: 10.1021/jz200925h.

[7] Zhou M., Du X., Wang H., Jin R. (2021) The Critical Number of Gold Atoms for a Metallic State Nanocluster: Resolving a Decades-Long Question. *ACS Nano* **15**, 13980–13992. DOI: 10.1021/acsnano.1c04705.

[8] Xu H., Suslick K.S. (2010) Water-Soluble Fluorescent Silver Nanoclusters. *Advanced Materials* **22**, 1078–1082. DOI: 10.1002/adma.200904199.

[9] Zheng J., Nicovich P.R., Dickson R.M. (2007) Highly Fluorescent Noble-Metal Quantum Dots. *Annual Review of Physical Chemistry* **58**, 409–431. DOI: 10.1146/annurev.physchem.58.032806.104546.

[10] Shang L., Xu J., Nienhaus G.U. (2019) Recent advances in synthesizing metal nanocluster-based nanocomposites for application in sensing, imaging and catalysis. *Nano Today* **28**, 100767. DOI: 10.1016/j.nantod.2019.100767.

[11] Jia Y., Sun T., Jiang Y., Sun W., Zhao Y., Xin J., Hou Y., Yang W. (2018) Green, fast, and large-scale synthesis of highly fluorescent Au nanoclusters for Cu^{2+} detection and temperature sensing. *The Analyst* **143**, 5145–5150. DOI: 10.1039/C8AN01617H.

[12] Sakthivel N.A., Stener M., Sementa L., Fortunelli A., Ramakrishna G., Dass A. (2018) Au$_{279}$(SR)$_{84}$: The Smallest Gold Thiolate Nanocrystal That Is Metallic and the Birth of Plasmon. *The Journal of Physical Chemistry Letters* **9**, 1295–1300. DOI: 10.1021/acs.jpclett.8b00308.

[13] Chuang C.-H., Chen W.-Y., Tseng W.-B., Lin A., Lu C.-Y., Tseng W.-L. (2022) Microwave-Mediated Synthesis of Near-Infrared-Emitting Silver Ion-Modified Gold Nanoclusters for Ratiometric Sensing of Hydrosulfide in Environmental Water and Hydrogen Sulfide in Live Cells. *ACS Sustainable Chemistry & Engineering* **10**, 2461–2472. DOI: 10.1021/acssuschemeng.1c07440.

[14] Zhang H., Huang X., Li L., Zhang G., Hussain I., Li Z., Tan B. (2012) Photoreductive synthesis of water-soluble fluorescent metal nanoclusters. *Chem. Commun.* **48**, 567–569. DOI: 10.1039/C1CC16088E.

[15] Zhou M., Higaki T., Li Y., Zeng C., Li Q., Sfeir M.Y., Jin R. (2019) Three-Stage Evolution from Nonscalable to Scalable Optical Properties of Thiolate-Protected Gold Nanoclusters. *Journal of the American Chemical Society* **141**, 19754–19764. DOI: 10.1021/jacs.9b09066.

[16] Zhu M., Aikens C.M., Hollander F.J., Schatz G.C., Jin R. (2008) Correlating the Crystal Structure of A Thiol-Protected Au$_{25}$ Cluster and Optical Properties. *Journal of the American Chemical Society* **130**, 5883–5885. DOI: 10.1021/ja801173r.

[17] Nobusada K., Iwasa T. (2007) Oligomeric Gold Clusters with Vertex-Sharing Bi- and Triicosahedral Structures. *The Journal of Physical Chemistry C* **111**, 14279–14282. DOI: 10.1021/jp075509w.

[18] Zhu M., Eckenhoff W.T., Pintauer T., Jin R. (2008) Conversion of Anionic [Au$_{25}$(SCH$_2$CH$_2$Ph)$_{18}$]$^-$ Cluster to Charge Neutral Cluster via Air Oxidation. *The Journal of Physical Chemistry C* **112**, 14221–14224. DOI: 10.1021/jp805786p.

[19] Devadas M.S., Bairu S., Qian H., Sinn E., Jin R., Ramakrishna G. (2011) Temperature-Dependent Optical Absorption Properties of Monolayer-Protected Au$_{25}$ and Au$_{38}$ Clusters. *The Journal of Physical Chemistry Letters* **2**, 2752–2758. DOI: 10.1021/jz2012897.

[20] Mussa Farkhani S., Dehghankelishadi P., Refaat A., Veerasikku Gopal D., Cifuentes-Rius A., Voelcker N.H. (2024) Tailoring gold nanocluster properties for biomedical applications: From

sensing to bioimaging and theranostics. *Progress in Materials Science* **142**, 101229. DOI: 10.1016/j.pmatsci.2023.101229.

[21] Link S., Beeby A., FitzGerald S., El-Sayed M.A., Schaaff T.G., Whetten R.L. (2002) Visible to Infrared Luminescence from a 28-Atom Gold Cluster. *The Journal of Physical Chemistry B* **106**, 3410–3415. DOI: 10.1021/jp014259v.

[22] Devadas M.S., Kim J., Sinn E., Lee D., Goodson T., Ramakrishna G. (2010) Unique Ultrafast Visible Luminescence in Monolayer-Protected Au_{25} Clusters. *The Journal of Physical Chemistry C* **114**, 22417–22423. DOI: 10.1021/jp107033n.

[23] Li Q. *et al.* (2019) A Mono-cuboctahedral Series of Gold Nanoclusters: Photoluminescence Origin, Large Enhancement, Wide Tunability, and Structure–Property Correlation. *Journal of the American Chemical Society* **141**, 5314–5325. DOI: 10.1021/jacs.8b13558.

[24] Zhou M., Song Y. (2021) Origins of Visible and Near-Infrared Emissions in $[Au_{25}(SR)_{18}]^-$ Nanoclusters. *The Journal of Physical Chemistry Letters* **12**, 1514–1519. DOI: 10.1021/acs.jpclett.1c00120.

[25] Ostruszka R., Zoppellaro G., Tomanec O., Pinkas D., Filimonenko V., Šišková K. (2022) Evidence of Au(II) and Au(0) States in Bovine Serum Albumin-Au Nanoclusters Revealed by CW-EPR/LEPR and Peculiarities in HR-TEM/STEM Imaging. *Nanomaterials* **12**, 1425. DOI: 10.3390/nano12091425.

[26] Wang G., Guo R., Kalyuzhny G., Choi J.-P., Murray R.W. (2006) NIR Luminescence Intensities Increase Linearly with Proportion of Polar Thiolate Ligands in Protecting Monolayers of Au_{38} and Au_{140} Quantum Dots. *The Journal of Physical Chemistry B* **110**, 20282–20289. DOI: 10.1021/jp0640528.

[27] Wu Z., Jin R. (2010) On the Ligand's Role in the Fluorescence of Gold Nanoclusters. *Nano Letters* **10**, 2568–2573. DOI: 10.1021/nl101225f.

[28] Londoño-Larrea P., Vanegas J.P., Cuaran-Acosta D., Zaballos-García E., Pérez-Prieto J. (2017) Water-Soluble Naked Gold Nanoclusters Are Not Luminescent. *Chemistry – A European Journal* **23**, 8137–8141. DOI: 10.1002/chem.201700913.

[29] Kundu S., Ghosh B., Nandi S., Ghosh M., Pyne A., Chatterjee J., Sarkar N. (2020) Surface Ligand-Controlled Wavelength-Tunable Luminescence of Gold Nanoclusters: Cellular Imaging and Smart Fluorescent Probes for Amyloid Detection. *ACS Applied Bio Materials* **3**, 4282–4293. DOI: 10.1021/acsabm.0c00337.

[30] Zhu L. *et al.* (2021) Surface Engineering of Gold Nanoclusters Protected with 11-Mercaptoundecanoic Acid for Photoluminescence Sensing. *ACS Applied Nano Materials* **4**, 3197–3203. DOI: 10.1021/acsanm.1c00404.

[31] Peng H., Jian M., Deng H., Wang W., Huang Z., Huang K., Liu A., Chen W. (2017) Valence States Effect on Electrogenerated Chemiluminescence of Gold Nanocluster. *ACS Applied Materials & Interfaces* **9**, 14929–14934. DOI: 10.1021/acsami.7b02446.

[32] Kim J.M., Jeong S., Song J.K., Kim J. (2018) Near-infrared electrochemiluminescence from orange fluorescent Au nanoclusters in water. *Chemical Communications* **54**, 2838–2841. DOI: 10.1039/C7CC09394B.

[33] Huang Z., Li Z., Chen Y., Xu L., Xie Q., Deng H., Chen W., Peng H. (2021) Regulating Valence States of Gold Nanocluster as a New Strategy for the Ultrasensitive Electrochemiluminescence Detection of Kanamycin. *Analytical Chemistry* **93**, 4635–4640. DOI: 10.1021/acs.analchem.1c00063.

[34] Negishi Y., Iwai T., Ide M. (2010) Continuous modulation of electronic structure of stable thiolate-protected Au_{25} cluster by Ag doping. *Chemical Communications* **46**, 4713. DOI: 10.1039/c0cc01021a.

[35] Oh E., Delehanty J.B., Field L.D., Mäkinen A.J., Goswami R., Huston A.L., Medintz I.L. (2016) Synthesis and Characterization of PEGylated Luminescent Gold Nanoclusters Doped with Silver and Other Metals. *Chemistry of Materials* **28**, 8676–8688. DOI: 10.1021/acs.chemmater.6b03838.

[36] Liu H. *et al.* (2019) Atomic-Precision Gold Clusters for NIR-II Imaging. *Advanced Materials* **31**. DOI: 10.1002/adma.201901015.

[37] Duan H., Nie S. (2007) Etching Colloidal Gold Nanocrystals with Hyperbranched and Multivalent Polymers: A New Route to Fluorescent and Water-Soluble Atomic Clusters. *Journal of the American Chemical Society* **129**, 2412–2413. DOI: 10.1021/ja067727t.

[38] Bain D., Maity S., Paramanik B., Patra A. (2018) Core-Size Dependent Fluorescent Gold Nanoclusters and Ultrasensitive Detection of Pb^{2+} Ion. *ACS Sustainable Chemistry & Engineering* **6**, 2334–2343. DOI: 10.1021/acssuschemeng.7b03794.

[39] Qian H., Zhu Y., Jin R. (2009) Size-Focusing Synthesis, Optical and Electrochemical Properties of Monodisperse $Au_{38}(SC_2H_4Ph)_{24}$ Nanoclusters. *ACS Nano* **3**, 3795–3803. DOI: 10.1021/nn901137h.

[40]   Cao Y., Liu T., Chen T., Zhang B., Jiang D., Xie J. (2021) Revealing the etching process of water-soluble Au_{25} nanoclusters at the molecular level. *Nature Communications* **12**, 3212. DOI: 10.1038/s41467-021-23568-0.

[41]   Lin C.-A.J. *et al.* (2009) Synthesis, Characterization, and Bioconjugation of Fluorescent Gold Nanoclusters toward Biological Labeling Applications. *ACS Nano* **3**, 395–401. DOI: 10.1021/nn800632j.

[42]   Ke C.-Y., Chen T.-H., Lu L.-C., Tseng W.-L. (2014) Understanding thiol-induced etching of luminescent gold nanoclusters. *RSC Adv.* **4**, 26050–26056. DOI: 10.1039/C4RA02111H.

[43]   Habeeb Muhammed M.A., Ramesh S., Sinha S.S., Pal S.K., Pradeep T. (2008) Two distinct fluorescent quantum clusters of gold starting from metallic nanoparticles by pH-dependent ligand etching. *Nano Research* **1**, 333–340. DOI: 10.1007/s12274-008-8035-2.

[44]   Hao D., Zhang X., Su R., Wang Y., Qi W. (2023) Biomolecule-protected gold nanoclusters: synthesis and biomedical applications. *Journal of Materials Chemistry B* **11**, 5051–5070. DOI: 10.1039/D3TB00651D.

[45]   Hsu N.-Y., Lin Y.-W. (2016) Microwave-assisted synthesis of bovine serum albumin–gold nanoclusters and their fluorescence-quenched sensing of Hg^{2+} ions. *New Journal of Chemistry* **40**, 1155–1161. DOI: 10.1039/C5NJ02263K.

[46]   Lin Y.-C., Wu T., Lin Y.-W. (2018) Fluorescence sensing of mercury(II) and melamine in aqueous solutions through microwave-assisted synthesis of egg-white-protected gold nanoclusters. *Analytical Methods* **10**, 1624–1632. DOI: 10.1039/C8AY00308D.

[47]   Santiago González B., Rodríguez M.J., Blanco C., Rivas J., López-Quintela M.A., Martinho J.M.G. (2010) One Step Synthesis of the Smallest Photoluminescent and Paramagnetic PVP-Protected Gold Atomic Clusters. *Nano Letters* **10**, 4217–4221. DOI: 10.1021/nl1026716.

[48]   Li L., Li Z., Zhang H., Zhang S., Majeed I., Tan B. (2013) Effect of polymer ligand structures on fluorescence of gold clusters prepared by photoreduction. *Nanoscale* **5**, 1986. DOI: 10.1039/c2nr33693f.

[49]   Zhou S., Duan Y., Wang F., Wang C. (2017) Fluorescent Au nanoclusters stabilized by silane: facile synthesis, color-tunability and photocatalytic properties. *Nanoscale* **9**, 4981–4988. DOI: 10.1039/C7NR01052D.

[50]   Lai L., Zhao C., Li X., Liu X., Jiang H., Selke M., Wang X. (2016) Fluorescent gold nanoclusters for *in vivo* target imaging of Alzheimer's disease. *RSC Advances* **6**, 30081–30088. DOI: 10.1039/C6RA01027J.

[51]   Ouyang X., Jia N., Luo J., Li L., Xue J., Bu H., Xie G., Wan Y. (2023) DNA Nanoribbon-Assisted Intracellular Biosynthesis of Fluorescent Gold Nanoclusters for Cancer Cell Imaging. *JACS Au* **3**, 2566–2577. DOI: 10.1021/jacsau.3c00365.

[52]   Yan L., Cai Y., Zheng B., Yuan H., Guo Y., Xiao D., Choi M.M.F. (2012) Microwave-assisted synthesis of BSA-stabilized and HSA-protected gold nanoclusters with red emission. *J. Mater. Chem.* **22**, 1000–1005. DOI: 10.1039/C1JM13457D.

[53]   Liu H., Zhang X., Wu X., Jiang L., Burda C., Zhu J.-J. (2011) Rapid sonochemical synthesis of highly luminescent non-toxic AuNCs and Au@AgNCs and Cu (II) sensing. *Chemical Communications* **47**, 4237. DOI: 10.1039/c1cc00103e.

[54]   Li J.K.-J., Ke C.-J., Lin C.-A., Cai Z.-H., Chen C.-Y., Chang W.H. (2013) Facile Method for Gold Nanocluster Synthesis and Fluorescence Control Using Toluene and Ultrasound. *Journal of Medical and Biological Engineering* **33**, 23–28. DOI: 10.5405/jmbe.874.

[55]   Lemke K., Prietzel C., Koetz J. (2013) Fluorescent gold clusters synthesized in a poly(ethyleneimine) modified reverse microemulsion. *Journal of Colloid and Interface Science* **394**, 141–146. DOI: 10.1016/j.jcis.2012.11.057.

[56]   Yang T.-Q., Peng B., Shan B.-Q., Zong Y.-X., Jiang J.-G., Wu P., Zhang K. (2020) Origin of the Photoluminescence of Metal Nanoclusters: From Metal-Centered Emission to Ligand-Centered Emission. *Nanomaterials* **10**, 261. DOI: 10.3390/nano10020261.

[57]   Andrýsková P., Šišková K.M., Michetschlägerová Š., Jiráková K., Kubala M., Jirák D. (2020) The Effect of Fatty Acids and BSA Purity on Synthesis and Properties of Fluorescent Gold Nanoclusters. *Nanomaterials* **10**, 343. DOI: 10.3390/nano10020343.

[58]   Yu Y., Chen X., Yao Q., Yu Y., Yan N., Xie J. (2013) Scalable and Precise Synthesis of Thiolated $Au_{10–12}$, Au_{15}, Au_{18}, and Au_{25} Nanoclusters via pH Controlled CO Reduction. *Chemistry of Materials* **25**, 946–952. DOI: 10.1021/cm304098x.

[59]   Zheng J., Zhang C., Dickson R.M. (2004) Highly Fluorescent, Water-Soluble, Size-Tunable Gold Quantum Dots. *Physical Review Letters* **93**, 077402. DOI: 10.1103/PhysRevLett.93.077402.

[60]   Bao Y., Zhong C., Vu D.M., Temirov J.P., Dyer R.B., Martinez J.S. (2007) Nanoparticle-Free Synthesis of Fluorescent Gold Nanoclusters at Physiological Temperature. *The Journal of Physical Chemistry C* **111**, 12194–12198. DOI: 10.1021/jp071727d.

[61]   Lee C.C., MacKay J.A., Fréchet J.M.J., Szoka F.C. (2005) Designing dendrimers for biological applications. *Nature Biotechnology* **23**, 1517–1526. DOI: 10.1038/nbt1171.

[62]   Schaeffer N. *et al.* (2008) Fluorescent or not? Size-dependent fluorescence switching for polymer-stabilized gold clusters in the 1.1–1.7 nm size range. *Chemical Communications* , 3986. DOI: 10.1039/b809876j.

[63]   Chen Y., Zheng X., Wang X., Wang C., Ding Y., Jiang X. (2014) Near-Infrared Emitting Gold Cluster–Poly(acrylic acid) Hybrid Nanogels. *ACS Macro Letters* **3**, 74–76. DOI: 10.1021/mz5005748.

[64]   Xie J., Zheng Y., Ying J.Y. (2009) Protein-Directed Synthesis of Highly Fluorescent Gold Nanoclusters. *Journal of the American Chemical Society* **131**, 888–889. DOI: 10.1021/ja806804u.

[65]   Wang Y., Cui Y., Zhao Y., Liu R., Sun Z., Li W., Gao X. (2012) Bifunctional peptides that precisely biomineralize Au clusters and specifically stain cell nuclei. *Chem. Commun.* **48**, 871–873. DOI: 10.1039/C1CC15926G.

[66]   Wen Q., Gu Y., Tang L.-J., Yu R.-Q., Jiang J.-H. (2013) Peptide-Templated Gold Nanocluster Beacon as a Sensitive, Label-Free Sensor for Protein Post-translational Modification Enzymes. *Analytical Chemistry* **85**, 11681–11685. DOI: 10.1021/ac403308b.

[67]   Kennedy T.A.C., MacLean J.L., Liu J. (2012) Blue emitting gold nanoclusters templated by poly-cytosine DNA at low pH and poly-adenine DNA at neutral pH. *Chemical Communications* **48**, 6845. DOI: 10.1039/c2cc32841k.

[68]   Liu G., Shao Y., Wu F., Xu S., Peng J., Liu L. (2013) DNA-hosted fluorescent gold nanoclusters: sequence-dependent formation. *Nanotechnology* **24**, 015503. DOI: 10.1088/0957-4484/24/1/015503.

[69]   Jiang H., Zhang Y., Wang X. (2014) Single cytidine units-templated syntheses of multi-colored water-soluble Au nanoclusters. *Nanoscale* **6**, 10355–10362. DOI: 10.1039/C4NR02180K.

[70]   Roy S., Palui G., Banerjee A. (2012) The as-prepared gold cluster-based fluorescent sensor for the selective detection of As^{III} ions in aqueous solution. *Nanoscale* **4**, 2734. DOI: 10.1039/c2nr11786j.

[71]   Wang H., Da L., Yang L., Chu S., Yang F., Yu S., Jiang C. (2020) Colorimetric fluorescent paper strip with smartphone platform for quantitative detection of cadmium ions in real samples. *Journal of Hazardous Materials* **392**, 122506. DOI: 10.1016/j.jhazmat.2020.122506.

[72]   Jiang X., Zhang H., Yang C., Xia J., Liu G., Luo X. (2022) A novel electrostatic drive strategy to prepare glutathione-capped gold nanoclusters embedded quaternized cellulose membranes fluorescent colorimetric sensor for Pb(II) and Hg(II) ions detection. *Sensors and Actuators B: Chemical* **368**, 132046. DOI: 10.1016/j.snb.2022.132046.

[73]   Zhang G., Qiao Y., Xu T., Zhang C., Zhang Y., Shi L., Shuang S., Dong C. (2015) Highly selective and sensitive nanoprobes for cyanide based on gold nanoclusters with red fluorescence emission. *Nanoscale* **7**, 12666–12672. DOI: 10.1039/C5NR03033A.

[74]   Zhang J., Chen C., Xu X., Wang X., Yang X. (2013) Use of fluorescent gold nanoclusters for the construction of a NAND logic gate for nitrite. *Chemical Communications* **49**, 2691. DOI: 10.1039/c3cc38298b.

[75]   Nejad M.A.F., Bigdeli A., Hormozi-Nezhad M.R. (2020) Wide color-varying visualization of sulfide with a dual emissive ratiometric fluorescence assay using carbon dots and gold nanoclusters. *Microchemical Journal* **157**, 104960. DOI: 10.1016/j.microc.2020.104960.

[76]   Santhosh M., Chinnadayyala S.R., Kakoti A., Goswami P. (2014) Selective and sensitive detection of free bilirubin in blood serum using human serum albumin stabilized gold nanoclusters as fluorometric and colorimetric probe. *Biosensors and Bioelectronics* **59**, 370–376. DOI: 10.1016/j.bios.2014.04.003.

[77]   Hong L.-N., Cao H.-T., Feng Y.-X., Guo L.-Z., Liu M.-Q., Zhang K., Mai X., Li N. (2023) Aggregation-caused dual-signal response of gold nanoclusters for ratiometric optical detection of cysteine. *Analytical Sciences* **39**, 1719–1726. DOI: 10.1007/s44211-023-00385-7.

[78]   Liu Y., Liu Y., Zhang J., Zheng J., Yuan Z., Lu C. (2022) Catechin-inspired gold nanocluster nanoprobe for selective and ratiometric dopamine detection via forming azamonardine. *Spectrochimica Acta Part A: Molecular and Biomolecular Spectroscopy* **274**, 121142. DOI: 10.1016/j.saa.2022.121142.

[79]   Lee M.J., Song J.A., Choi J.H., Shin J.H., Myeong J.W., Lee K.P., Kim T., Park K.E., Oh B.K. (2023) Horseradish Peroxidase-Encapsulated Fluorescent Bio-Nanoparticle for Ultra-Sensitive and Easy Detection of Hydrogen Peroxide. *Biosensors* **13**. DOI: 10.3390/bios13020289.

[80] Gao P., Li M., Zhang Y., Dong C., Zhang G., Shi L., Li G., Yuan M., Shuang S. (2019) Facile, rapid one-pot synthesis of multifunctional gold nanoclusters for cell imaging, hydrogen sulfide detection and pH sensing. *Talanta* **197**, 1–11. DOI: 10.1016/j.talanta.2018.12.078.

[81] Zhang Y., Li M., Niu Q., Gao P., Zhang G., Dong C., Shuang S. (2017) Gold nanoclusters as fluorescent sensors for selective and sensitive hydrogen sulfide detection. *Talanta* **171**, 143–151. DOI: 10.1016/j.talanta.2017.04.077.

[82] Chen X., Baker G.A. (2013) Cholesterol determination using protein-templated fluorescent gold nanocluster probes. *The Analyst* **138**, 7299. DOI: 10.1039/c3an01548c.

[83] Xu S., Feng X., Gao T., Wang R., Mao Y., Lin J., Yu X., Luo X. (2017) A novel dual-functional biosensor for fluorometric detection of inorganic pyrophosphate and pyrophosphatase activity based on globulin stabilized gold nanoclusters. *Analytica Chimica Acta* **958**, 22–29. DOI: 10.1016/j.aca.2016.12.026.

[84] Li H., Yang M., Kong D., Jin R., Zhao X., Liu F., Yan X., Lin Y., Lu G. (2019) Sensitive fluorescence sensor for point-of-care detection of trypsin using glutathione-stabilized gold nanoclusters. *Sensors and Actuators B: Chemical* **282**, 366–372. DOI: 10.1016/j.snb.2018.11.077.

[85] Luo Q., Tian M., Luo F., Zhao M., Lin C., Qiu B., Wang J., Lin Z. (2023) Multicolor Biosensor for Trypsin Detection Based on the Regulation of the Peroxidase Activity of Bovine Serum Albumin-Coated Gold Nanoclusters and Etching of Gold Nanobipyramids. *Analytical Chemistry* **95**, 2390–2397. DOI: 10.1021/acs.analchem.2c04418.

[86] Bonanno A., Pérez-Herráez I., Zaballos-García E., Pérez-Prieto J. (2020) Gold nanoclusters for ratiometric sensing of pH in extremely acidic media. *Chemical Communications* **56**, 587–590. DOI: 10.1039/C9CC08539D.

[87] Shen J., Xiao Q., Sun P., Feng J., Xin X., Yu Y., Qi W. (2021) Self-Assembled Chiral Phosphorescent Microflowers from Au Nanoclusters with Dual-Mode pH Sensing and Information Encryption. *ACS Nano* **15**, 4947–4955. DOI: 10.1021/acsnano.0c09766.

[88] Qiao J., Chen C., Shangguan D., Mu X., Wang S., Jiang L., Qi L. (2018) Simultaneous Monitoring of Mitochondrial Temperature and ATP Fluctuation Using Fluorescent Probes in Living Cells. *Analytical Chemistry* **90**, 12553–12558. DOI: 10.1021/acs.analchem.8b02496.

[89] Zhang H., Han W., Cao X., Gao T., Jia R., Liu M., Zeng W. (2019) Gold nanoclusters as a near-infrared fluorometric nanothermometer for living cells. *Microchimica Acta* **186**, 353. DOI: 10.1007/s00604-019-3460-3.

[90] Ji H., Wu L., Pu F., Ren J., Qu X. (2018) Point-of-Care Identification of Bacteria Using Protein-Encapsulated Gold Nanoclusters. *Advanced Healthcare Materials* **7**. DOI: 10.1002/adhm.201701370.

[91] Yan R. *et al.* (2018) On–Off–On Gold Nanocluster-Based Fluorescent Probe for Rapid *Escherichia coli* Differentiation, Detection and Bactericide Screening. *ACS Sustainable Chemistry & Engineering* **6**, 4504–4509. DOI: 10.1021/acssuschemeng.8b00112.

[92] Tan Y., He K., Tang B., Chen H., Zhao Z., Zhang C., Lin L., Liu J. (2020) Precisely Regulated Luminescent Gold Nanoparticles for Identification of Cancer Metastases. *ACS Nano* **14**, 13975–13985. DOI: 10.1021/acsnano.0c06388.

[93] Wang Y. *et al.* (2023) A fluorescent probe based on aptamer gold nanoclusters for rapid detection of mercury ions. *Analytical Methods* **15**, 3893–3901. DOI: 10.1039/D3AY00967J.

[94] Gao X., Ma Z., Sun M., Liu X., Zhong K., Tang L., Li X., Li J. (2022) A highly sensitive ratiometric fluorescent sensor for copper ions and cadmium ions in scallops based on nitrogen doped graphene quantum dots cooperating with gold nanoclusters. *Food Chemistry* **369**, 130964. DOI: 10.1016/j.foodchem.2021.130964.

[95] Tian D., Qian Z., Xia Y., Zhu C. (2012) Gold Nanocluster-Based Fluorescent Probes for Near-Infrared and Turn-On Sensing of Glutathione in Living Cells. *Langmuir* **28**, 3945–3951. DOI: 10.1021/la204380a.

[96] Liu H., Jia L., Wang Y., Wang M., Gao Z., Ren X. (2019) Ratiometric fluorescent sensor for visual determination of copper ions and alkaline phosphatase based on carbon quantum dots and gold nanoclusters. *Analytical and Bioanalytical Chemistry* **411**, 2531–2543. DOI: 10.1007/s00216-019-01693-6.

[97] Ye C., Wang Y., Wang S., Wang Z. (2019) Fabrication of cefotaxime sodium-functionalized gold nanoclusters for the detection of copper ions in Chinese herbal medicines. *RSC Advances* **9**, 5037–5044. DOI: 10.1039/C8RA09987A.

[98] Jiang P., Luo L., Liu X., Zhao W., Bi X., Luo L., Li L., You T. (2023) A potential-resolved ratiometric electrochemiluminescence aptasensor for Pb^{2+}: Gold nanoclusters and amino-terminated perylene derivative as both emitters and resonance energy transfer donor-acceptor pair. *Sensors and Actuators B: Chemical* **386**, 133758. DOI: 10.1016/j.snb.2023.133758.

[99]   Zhao S., Das A., Zhang H., Jin R., Song Y., Jin R. (2016) Mechanistic insights from atomically precise gold nanocluster-catalyzed reduction of 4-nitrophenol. *Progress in Natural Science: Materials International* **26**, 483–486. DOI: 10.1016/j.pnsc.2016.08.009.

[100]   Feng A.-L., Jiang Q.-Y., Song G.-G., Xu Z., Liu X.-Q. (2022) DNA-templated NIR-emitting gold nanoclusters with peroxidase-like activity as a multi-signal probe for Hg^{2+} detection. *Chinese Journal of Analytical Chemistry* **50**, 100118. DOI: 10.1016/j.cjac.2022.100118.

[101]   Shan H. *et al.* (2023) Modulating Catalytic Activity and Stability of Atomically Precise Gold Nanoclusters as Peroxidase Mimics via Ligand Engineering. *ACS Nano* **17**, 2368–2377. DOI: 10.1021/acsnano.2c09238.

[102]   Huang Y., Yue N., Li Y., Han L., Fan A. (2021) One-step synthesis of cationic gold nanoclusters with high catalytic activity on luminol chemiluminescence reaction. *Luminescence* **36**, 85–93. DOI: 10.1002/bio.3916.

[103]   Liu C. *et al.* (2011) Insulin-Directed Synthesis of Fluorescent Gold Nanoclusters: Preservation of Insulin Bioactivity and Versatility in Cell Imaging. *Angewandte Chemie International Edition* **50**, 7056–7060. DOI: 10.1002/anie.201100299.

[104]   Zhang Y. *et al.* (2019) Gold nanoclusters for controlled insulin release and glucose regulation in diabetes. *Nanoscale* **11**, 6471–6479. DOI: 10.1039/C9NR00668K.

[105]   Yang J. *et al.* (2020) Gold/alpha-lactalbumin nanoprobes for the imaging and treatment of breast cancer. *Nature Biomedical Engineering* **4**, 686–703. DOI: 10.1038/s41551-020-0584-z.

[106]   Yang J., Li X., Tong Y., Yang Y., Zhao L., Zhou Q., Xu J., Dong L., Jiang Y. (2022) Targeting co-delivery of doxorubicin and gefitinib by biotinylated Au NCs for overcoming multidrug resistance in imaging-guided anticancer therapy. *Colloids and Surfaces B: Biointerfaces* **217**, 112608. DOI: 10.1016/j.colsurfb.2022.112608.

[107]   Yu Z. *et al.* (2020) High-Resolution Shortwave Infrared Imaging of Vascular Disorders Using Gold Nanoclusters. *ACS Nano* **14**, 4973–4981. DOI: 10.1021/acsnano.0c01174.

[108]   Kim J. *et al.* (2020) Gold nanoparticle clusters for the investigation of therapeutic efficiency against prostate cancer under near-infrared irradiation. *Nano Convergence* **7**, 5. DOI: 10.1186/s40580-019-0216-z.

[109]   Xie Y., Zheng W., Jiang X. (2020) Near-Infrared Light-Activated Phototherapy by Gold Nanoclusters for Dispersing Biofilms. *ACS Applied Materials & Interfaces* **12**, 9041–9049. DOI: 10.1021/acsami.9b21777.

[110]   Zhu S., Wang X., Liu L., Li L. (2020) Gold nanocluster grafted conjugated polymer nanoparticles for cancer cell imaging and photothermal killing. *Colloids and Surfaces A: Physicochemical and Engineering Aspects* **597**, 124764. DOI: 10.1016/j.colsurfa.2020.124764.

[111]   Han R. *et al.* (2020) Super-efficient *in Vivo* Two-Photon Photodynamic Therapy with a Gold Nanocluster as a Type I Photosensitizer. *ACS Nano* **14**, 9532–9544. DOI: 10.1021/acsnano.9b05169.

[112]   Poderys V., Jarockyte G., Bagdonas S., Karabanovas V., Rotomskis R. (2020) Protein-stabilized gold nanoclusters for PDT: ROS and singlet oxygen generation. *Journal of Photochemistry and Photobiology B: Biology* **204**, 111802. DOI: 10.1016/j.jphotobiol.2020.111802.

[113]   Kong Y. *et al.* (2021) A NIR-II-emitting gold nanocluster-based drug delivery system for smartphone-triggered photodynamic theranostics with rapid body clearance. *Materials Today* **51**, 96–107. DOI: 10.1016/j.mattod.2021.09.022.

[114]   Li W., Zhou T., Sun W., Liu M., Wang X., Wang F., Zhang G., Zhang Z. (2023) A conjugated aptamer and oligonucleotides-stabilized gold nanoclusters nanoplatform for targeted fluorescent imaging and efficient drug delivery. *Colloids and Surfaces A: Physicochemical and Engineering Aspects* **657**, 130521. DOI: 10.1016/j.colsurfa.2022.130521.

[115]   Cifuentes-Rius A., Deepagan V.G., Xie J., Voelcker N.H. (2021) Bright Future of Gold Nanoclusters in Theranostics. *ACS Applied Materials & Interfaces* **13**, 49581–49588. DOI: 10.1021/acsami.1c14275.

[116]   Huber D.L. (2005) Synthesis, Properties, and Applications of Iron Nanoparticles. *Small* **1**, 482–501. DOI: 10.1002/smll.200500006.

[117]   Mahmoudi M., Simchi A., Milani A.S., Stroeve P. (2009) Cell toxicity of superparamagnetic iron oxide nanoparticles. *Journal of Colloid and Interface Science* **336**, 510–518. DOI: 10.1016/j.jcis.2009.04.046.

[118]   Li Q., Kartikowati C.W., Horie S., Ogi T., Iwaki T., Okuyama K. (2017) Correlation between particle size/domain structure and magnetic properties of highly crystalline Fe_3O_4 nanoparticles. *Scientific Reports* **7**, 9894. DOI: 10.1038/s41598-017-09897-5.

[119]   Wahajuddin, Arora. (2012) Superparamagnetic iron oxide nanoparticles: magnetic nanoplatforms as drug carriers. *International Journal of Nanomedicine* **7**, 3445. DOI: 10.2147/IJN.S30320.

[120] Houbi A., Aldashevich Z.A., Atassi Y., Bagasharova Telmanovna Z., Saule M., Kubanych K. (2021) Microwave absorbing properties of ferrites and their composites: A review. *Journal of Magnetism and Magnetic Materials* **529**, 167839. DOI: 10.1016/j.jmmm.2021.167839.

[121] Dickson D.P.E., Frankel R.B. (1992) Magnetic Fine Particles in Biological Systems. In: *Magnetic Properties of Fine Particles*., pp. 393–402. Elsevier. DOI: 10.1016/B978-0-444-89552-3.50047-5.

[122] Teja A.S., Koh P.-Y. (2009) Synthesis, properties, and applications of magnetic iron oxide nanoparticles. *Progress in Crystal Growth and Characterization of Materials* **55**, 22–45. DOI: 10.1016/j.pcrysgrow.2008.08.003.

[123] Jeong U., Teng X., Wang Y., Yang H., Xia Y. (2007) Superparamagnetic Colloids: Controlled Synthesis and Niche Applications. *Advanced Materials* **19**, 33–60. DOI: 10.1002/adma.200600674.

[124] Sung Lee J., Myung Cha J., Young Yoon H., Lee J.-K., Keun Kim Y. (2015) Magnetic multi-granule nanoclusters: A model system that exhibits universal size effect of magnetic coercivity. *Scientific Reports* **5**, 12135. DOI: 10.1038/srep12135.

[125] Ma M., Wu Y., Zhou J., Sun Y., Zhang Y., Gu N. (2004) Size dependence of specific power absorption of Fe_3O_4 particles in AC magnetic field. *Journal of Magnetism and Magnetic Materials* **268**, 33–39. DOI: 10.1016/S0304-8853(03)00426-8.

[126] Kim D., Lee N., Park M., Kim B.H., An K., Hyeon T. (2009) Synthesis of Uniform Ferrimagnetic Magnetite Nanocubes. *Journal of the American Chemical Society* **131**, 454–455. DOI: 10.1021/ja8086906.

[127] Kandasamy G., Maity D. (2015) Recent advances in superparamagnetic iron oxide nanoparticles (SPIONs) for *in vitro* and *in vivo* cancer nanotheranostics. *International Journal of Pharmaceutics* **496**, 191–218. DOI: 10.1016/j.ijpharm.2015.10.058.

[128] Mohammed L., Gomaa H.G., Ragab D., Zhu J. (2017) Magnetic nanoparticles for environmental and biomedical applications: A review. *Particuology* **30**, 1–14. DOI: 10.1016/j.partic.2016.06.001.

[129] Dadfar S.M. *et al.* (2020) Size-isolation of superparamagnetic iron oxide nanoparticles improves MRI, MPI and hyperthermia performance. *Journal of Nanobiotechnology* **18**, 22. DOI: 10.1186/s12951-020-0580-1.

[130] Tadic M., Kralj S., Kopanja L. (2019) Synthesis, particle shape characterization, magnetic properties and surface modification of superparamagnetic iron oxide nanochains. *Materials Characterization* **148**, 123–133. DOI: 10.1016/j.matchar.2018.12.014.

[131] Alp E., Aydogan N. (2016) A comparative study: Synthesis of superparamagnetic iron oxide nanoparticles in air and N_2 atmosphere. *Colloids and Surfaces A: Physicochemical and Engineering Aspects* **510**, 205–212. DOI: 10.1016/j.colsurfa.2016.06.033.

[132] Niculescu A.-G., Chircov C., Grumezescu A.M. (2022) Magnetite nanoparticles: Synthesis methods – A comparative review. *Methods* **199**, 16–27. DOI: 10.1016/j.ymeth.2021.04.018.

[133] Samrot A. V., Sahithya C.S., Selvarani A J., Purayil S.K., Ponnaiah P. (2021) A review on synthesis, characterization and potential biological applications of superparamagnetic iron oxide nanoparticles. *Current Research in Green and Sustainable Chemistry* **4**, 100042. DOI: 10.1016/j.crgsc.2020.100042.

[134] Rahmani R., Gharanfoli M., Gholamin M., Darroudi M., Chamani J., Sadri K., Hashemzadeh A. (2020) Plant-mediated synthesis of superparamagnetic iron oxide nanoparticles (SPIONs) using aloe vera and flaxseed extracts and evaluation of their cellular toxicities. *Ceramics International* **46**, 3051–3058. DOI: 10.1016/j.ceramint.2019.10.005.

[135] Kaushik S., Thomas J., Panwar V., Ali H., Chopra V., Sharma A., Tomar R., Ghosh D. (2020) In Situ Biosynthesized Superparamagnetic Iron Oxide Nanoparticles (SPIONS) Induce Efficient Hyperthermia in Cancer Cells. *ACS Applied Bio Materials* **3**, 779–788. DOI: 10.1021/acsabm.9b00720.

[136] Chatterjee S., Mahanty S., Das P., Chaudhuri P., Das S. (2020) Biofabrication of iron oxide nanoparticles using manglicolous fungus Aspergillus niger BSC-1 and removal of Cr(VI) from aqueous solution. *Chemical Engineering Journal* **385**, 123790. DOI: 10.1016/j.cej.2019.123790.

[137] Khaleelullah M.M.S.I., Murugan M., Radha K. V, Thiyagarajan D., Shimura Y., Hayakawa Y. (2017) Synthesis of super-paramagnetic iron oxide nanoparticles assisted by brown seaweed *Turbinaria decurrens* for removal of reactive navy blue dye. *Materials Research Express* **4**, 105038. DOI: 10.1088/2053-1591/aa9131.

[138] Parandhaman T., Pentela N., Ramalingam B., Samanta D., Das S.K. (2017) Metal Nanoparticle Loaded Magnetic-Chitosan Microsphere: Water Dispersible and Easily Separable Hybrid Metal Nano-biomaterial for Catalytic Applications. *ACS Sustainable Chemistry & Engineering* **5**, 489–501. DOI: 10.1021/acssuschemeng.6b01862.

[139] Abouelkheir S.S., Ibrahim H.A.H., Beltagy E.A. (2023) Functionalized maghemite superparamagnetic iron oxide nanoparticles (γ-Fe$_2$O$_3$-SPIONs)-amylase enzyme hybrid in biofuel production. *Scientific Reports* **13**, 11117. DOI: 10.1038/s41598-023-37826-2.

[140] Rajesh Kumar S., Jayavignesh V., Selvakumar R., Swaminathan K., Ponpandian N. (2016) Facile synthesis of yeast cross-linked Fe$_3$O$_4$ nanoadsorbents for efficient removal of aquatic environment contaminated with As(V). *Journal of Colloid and Interface Science* **484**, 183–195. DOI: 10.1016/j.jcis.2016.08.081.

[141] Liao Z., Wang H., Lv R., Zhao P., Sun X., Wang S., Su W., Niu R., Chang J. (2011) Polymeric Liposomes-Coated Superparamagnetic Iron Oxide Nanoparticles as Contrast Agent for Targeted Magnetic Resonance Imaging of Cancer Cells. *Langmuir* **27**, 3100–3105. DOI: 10.1021/la1050157.

[142] Chen B., Hatamie S., Garu P., Heravi P., Chen J., Liu B., Wei Z., Yao D. (2020) Synthesis of iron-oxide magnetic nanoparticles coated with dextran of varied molecular mass using a facile ball-milling method. *Micro & Nano Letters* **15**, 645–650. DOI: 10.1049/mnl.2019.0811.

[143] Javid A., Ahmadian S., Saboury A.A., Kalantar S.M., Rezaei-Zarchi S. (2013) Chitosan-Coated Superparamagnetic Iron Oxide Nanoparticles for Doxorubicin Delivery: Synthesis and Anticancer Effect Against Human Ovarian Cancer Cells. *Chemical Biology & Drug Design* **82**, 296–306. DOI: 10.1111/cbdd.12145.

[144] Karaagac O., Köçkar H. (2022) Improvement of the saturation magnetization of PEG coated superparamagnetic iron oxide nanoparticles. *Journal of Magnetism and Magnetic Materials* **551**, 169140. DOI: 10.1016/j.jmmm.2022.169140.

[145] Karimzadeh I., Aghazadeh M., Ganjali M.R., Norouzi P., Shirvani-Arani S., Doroudi T., Kolivand P.H., Marashi S.A., Gharailou D. (2016) A novel method for preparation of bare and poly(vinylpyrrolidone) coated superparamagnetic iron oxide nanoparticles for biomedical applications. *Materials Letters* **179**, 5–8. DOI: 10.1016/j.matlet.2016.05.048.

[146] Wang Y., Xu C., Chang Y., Zhao L., Zhang K., Zhao Y., Gao F., Gao X. (2017) Ultrasmall Superparamagnetic Iron Oxide Nanoparticle for T_2-Weighted Magnetic Resonance Imaging. *ACS Applied Materials & Interfaces* **9**, 28959–28966. DOI: 10.1021/acsami.7b10030.

[147] Chee H.L., Gan C.R.R., Ng M., Low L., Fernig D.G., Bhakoo K.K., Paramelle D. (2018) Biocompatible Peptide-Coated Ultrasmall Superparamagnetic Iron Oxide Nanoparticles for *In Vivo* Contrast-Enhanced Magnetic Resonance Imaging. *ACS Nano* **12**, 6480–6491. DOI: 10.1021/acsnano.7b07572.

[148] Frantellizzi V., Conte M., Pontico M., Pani A., Pani R., De Vincentis G. (2020) New Frontiers in Molecular Imaging with Superparamagnetic Iron Oxide Nanoparticles (SPIONs): Efficacy, Toxicity, and Future Applications. *Nuclear Medicine and Molecular Imaging* **54**, 65–80. DOI: 10.1007/s13139-020-00635-w.

[149] Chen C., Ge J., Gao Y., Chen L., Cui J., Zeng J., Gao M. (2022) Ultrasmall superparamagnetic iron oxide nanoparticles: A next generation contrast agent for magnetic resonance imaging. *Wiley Interdiscip Rev Nanomed Nanobiotechnol.* **14**. DOI: 10.1002/wnan.1740.

[150] Hervault A., Thanh N.T.K. (2014) Magnetic nanoparticle-based therapeutic agents for thermo-chemotherapy treatment of cancer. *Nanoscale* **6**, 11553–11573. DOI: 10.1039/C4NR03482A.

[151] Zhuang M., Chen X., Du D., Shi J., Deng M., Long Q., Yin X., Wang Y., Rao L. (2020) SPION decorated exosome delivery of TNF-α to cancer cell membranes through magnetism. *Nanoscale* **12**, 173–188. DOI: 10.1039/C9NR05865F.

[152] Luque-Michel E., Lemaire L., Blanco-Prieto M.J. (2021) SPION and doxorubicin-loaded polymeric nanocarriers for glioblastoma theranostics. *Drug Delivery and Translational Research* **11**, 515–523. DOI: 10.1007/s13346-020-00880-8.

[153] Tan L.K.S., How C.W., Low L.E., Ong B.H., Loh J.S., Lim S.-Y., Ong Y.S., Foo J.B. (2023) Magnetic-guided targeted delivery of zerumbone/SPION co-loaded in nanostructured lipid carrier into breast cancer cells. *Journal of Drug Delivery Science and Technology* **87**, 104830. DOI: 10.1016/j.jddst.2023.104830.

[154] Al-Musawi S., Albukhaty S., Al-Karagoly H., Sulaiman G.M., Jabir M.S., Naderi-Manesh H. (2020) Dextran-coated superparamagnetic nanoparticles modified with folate for targeted drug delivery of camptothecin. *Advances in Natural Sciences: Nanoscience and Nanotechnology* **11**, 045009. DOI: 10.1088/2043-6254/abc75b.

[155] Al-Obaidy R., Haider A.J., Al-Musawi S., Arsad N. (2023) Targeted delivery of paclitaxel drug using polymer-coated magnetic nanoparticles for fibrosarcoma therapy: *in vitro* and *in vivo* studies. *Scientific Reports* **13**, 3180. DOI: 10.1038/s41598-023-30221-x.

[156] Samani R.K., Maghsoudinia F., Asgari M., Atarod M., Mehrgardi M.A., Tavakoli M.B. (2023) Superparamagnetic iron oxide nanoparticle-loaded nanodroplets for dual-modal

ultrasound/magnetic resonance imaging-guided drug delivery. *New Journal of Chemistry* **47**, 20193–20203. DOI: 10.1039/D3NJ02856A.

[157] Nguyen M.P., Thuy V.T.T., Kim D. (2020) Integration of iron oxide nanoparticles and polyaspartamide biopolymer for MRI image contrast enhancement and an efficient drug-delivery system in cancer therapy. *Nanotechnology* **31**, 335712. DOI: 10.1088/1361-6528/ab8f49.

[158] Wu L., Chen L., Liu F., Qi X., Ge Y., Shen S. (2017) Remotely controlled drug release based on iron oxide nanoparticles for specific therapy of cancer. *Colloids and Surfaces B: Biointerfaces* **152**, 440–448. DOI: 10.1016/j.colsurfb.2017.01.015.

[159] Tu Z., Zhang B., Yang G., Wang M., Zhao F., Sheng D., Wang J. (2013) Synthesis of poly(ethylene glycol) and poly(vinyl pyrrolidone) co-coated superparamagnetic iron oxide nanoparticle as a pH-sensitive release drug carrier. *Colloids and Surfaces A: Physicochemical and Engineering Aspects* **436**, 854–861. DOI: 10.1016/j.colsurfa.2013.08.019.

[160] Khan A., Kumar Sahu N. (2020) Folate encapsulation in PEG-diamine grafted mesoporous Fe_3O_4 nanoparticles for hyperthermia and *in vitro* assessment. *IET Nanobiotechnology* **14**, 881–888. DOI: 10.1049/iet-nbt.2020.0101.

[161] Ong Y.S., Bañobre-López M., Costa Lima S.A., Reis S. (2020) A multifunctional nanomedicine platform for co-delivery of methotrexate and mild hyperthermia towards breast cancer therapy. *Materials Science and Engineering: C* **116**, 111255. DOI: 10.1016/j.msec.2020.111255.

[162] Mirzaghavami P.S., Khoei S., Khoee S., Shirvalilou S., Mahdavi S.R., Pirhajati Mahabadi V. (2021) Radio-sensitivity enhancement in HT29 cells through magnetic hyperthermia in combination with targeted nano-carrier of 5-Flourouracil. *Materials Science and Engineering: C* **124**, 112043. DOI: 10.1016/j.msec.2021.112043.

[163] Inbaraj S., Chen B.H. (2012) *In vitro* removal of toxic heavy metals by poly(γ-glutamic acid)-coated superparamagnetic nanoparticles. *International Journal of Nanomedicine* **7**, 4419. DOI: 10.2147/IJN.S34396.

[164] Wanna Y., Chindaduang A., Tumcharern G., Phromyothin D., Porntheerapat S., Nukeaw J., Hofmann H., Pratontep S. (2016) Efficiency of SPIONs functionalized with polyethylene glycol bis(amine) for heavy metal removal. *Journal of Magnetism and Magnetic Materials* **414**, 32–37. DOI: 10.1016/j.jmmm.2016.04.064.

[165] Samrot A. V, Sahithya C.S., Selvarani A J., Pachiyappan S., Kumar S S. (2019) Surface-Engineered Super-Paramagnetic Iron Oxide Nanoparticles For Chromium Removal. *International Journal of Nanomedicine* **Volume 14**, 8105–8119. DOI: 10.2147/IJN.S214236.

[166] Bilgic A., Cimen A. (2023) Synthesis, characterisation, adsorption studies and comparison of superparamagnetic iron oxide nanoparticles (SPION) with three different amine groups functionalised with BODIPY for the removal of Cr(VI) metal ions from aqueous solutions. *International Journal of Environmental Analytical Chemistry* **103**, 1866–1891. DOI: 10.1080/03067319.2021.1884240.

[167] Sharma G., Kumar A., Sharma S., Naushad Mu., Prakash Dwivedi R., ALOthman Z.A., Mola G.T. (2019) Novel development of nanoparticles to bimetallic nanoparticles and their composites: A review. *Journal of King Saud University - Science* **31**, 257–269. DOI: 10.1016/j.jksus.2017.06.012.

[168] Stephanie R., Kim M.W., Kim S.H., Kim J.-K., Park C.Y., Park T.J. (2021) Recent advances of bimetallic nanomaterials and its nanocomposites for biosensing applications. *TrAC Trends in Analytical Chemistry* **135**, 116159. DOI: 10.1016/j.trac.2020.116159.

[169] Luo S., Liu Y., Rao H., Wang Y., Wang X. (2017) Fluorescence and magnetic nanocomposite $Fe_3O_4@SiO_2@Au$ MNPs as peroxidase mimetics for glucose detection. *Analytical Biochemistry* **538**, 26–33. DOI: 10.1016/j.ab.2017.09.006.

[170] Huang C.-L., Hsieh W.-J., Lin C.-W., Yang H.-W., Wang C.-K. (2018) Multifunctional liposomal drug delivery with dual probes of magnetic resonance and fluorescence imaging. *Ceramics International* **44**, 12442–12450. DOI: 10.1016/j.ceramint.2018.04.034.

[171] Zhao H.Y., Liu S., He J., Pan C.C., Li H., Zhou Z.Y., Ding Y., Huo D., Hu Y. (2015) Synthesis and application of strawberry-like Fe_3O_4-Au nanoparticles as CT-MR dual-modality contrast agents in accurate detection of the progressive liver disease. *Biomaterials* **51**, 194–207. DOI: 10.1016/j.biomaterials.2015.02.019.

[172] Le Guével X., Prinz E.-M., Müller R., Hempelmann R., Schneider M. (2012) Synthesis and characterization of superparamagnetic nanoparticles coated with fluorescent gold nanoclusters. *Journal of Nanoparticle Research* **14**, 727. DOI: 10.1007/s11051-012-0727-6.

[173] Wang C., Yao Y., Song Q. (2015) Gold nanoclusters decorated with magnetic iron oxide nanoparticles for potential multimodal optical/magnetic resonance imaging. *Journal of Materials Chemistry C* **3**, 5910–5917. DOI: 10.1039/C5TC00290G.

[174] Shibu E.S., Sugino S., Ono K., Saito H., Nishioka A., Yamamura S., Sawada M., Nosaka Y., Biju V. (2013) Singlet-Oxygen-Sensitizing Near-Infrared-Fluorescent Multimodal Nanoparticles. *Angewandte Chemie International Edition* **52**, 10559–10563. DOI: 10.1002/anie.201304264.

[175] Ostruszka R., Halili A., Pluháček T., Rárová L., Jirák D., Šišková K. (2024) Advanced protein-embedded bimetallic nanocomposite optimized for *in vivo* fluorescence and magnetic resonance bimodal imaging. *Journal of Colloid and Interface Science* **663**, 467–477. DOI: 10.1016/j.jcis.2024.02.116.

[176] Cho S., Shin H.Y., Kim M. Il. (2017) Nanohybrids consisting of magnetic nanoparticles and gold nanoclusters as effective peroxidase mimics and their application for colorimetric detection of glucose. *Biointerphases* **12**, 01A401. DOI: 10.1116/1.4974198.

[177] Chen H., Wang Y., Wang T., Shi D., Sun Z., Xia C., Wang B. (2016) Application prospective of nanoprobes with MRI and FI dual-modality imaging on breast cancer stem cells in tumor. *Journal of Nanobiotechnology* **14**, 52. DOI: 10.1186/s12951-016-0195-8.

[178] Bal W., Sokołowska M., Kurowska E., Faller P. (2013) Binding of transition metal ions to albumin: Sites, affinities and rates. *Biochimica et Biophysica Acta (BBA) - General Subjects* **1830**, 5444–5455. DOI: 10.1016/j.bbagen.2013.06.018.

[179] Tankovskaia S.A., Abrosimova K. V., Paston S. V. (2018) Spectral demonstration of structural transitions in albumins. *Journal of Molecular Structure* **1171**, 243–252. DOI: 10.1016/j.molstruc.2018.05.100.

[180] Hirayama K., Akashi S., Furuya M., Fukuhara K. (1990) Rapid confirmation and revision of the primary structure of bovine serum albumin by ESIMS and frit-FAB LC/MS. *Biochemical and Biophysical Research Communications* **173**, 639–646. DOI: 10.1016/S0006-291X(05)80083-X.

[181] Majorek K.A., Porebski P.J., Dayal A., Zimmerman M.D., Jablonska K., Stewart A.J., Chruszcz M., Minor W. (2012) Structural and immunologic characterization of bovine, horse, and rabbit serum albumins. *Molecular Immunology* **52**, 174–182. DOI: 10.1016/j.molimm.2012.05.011.

[182] Peters T. (1985) Serum Albumin. In: *Advances in Protein Chemistry*., pp. 161–245. Academic Press. DOI: 10.1016/S0065-3233(08)60065-0.

[183] Baler K., Martin O.A., Carignano M.A., Ameer G.A., Vila J.A., Szleifer I. (2014) Electrostatic Unfolding and Interactions of Albumin Driven by pH Changes: A Molecular Dynamics Study. *The Journal of Physical Chemistry B* **118**, 921–930. DOI: 10.1021/jp409936v.

[184] Li R., Wu Z., Wangb Y., Ding L., Wang Y. (2016) Role of pH-induced structural change in protein aggregation in foam fractionation of bovine serum albumin. *Biotechnology Reports* **9**, 46–52. DOI: 10.1016/j.btre.2016.01.002.

[185] Ostruszka R., Šišková K. (2022) Optimization of Synthesis of Bovine Serum Albumin-Encapsulated Fluorescent Gold Nanoclusters. In: *The 3rd International Online-Conference on Nanomaterials*., p. 15. Basel Switzerland: MDPI. DOI: 10.3390/materproc2022009015.

[186] Li H.-W., Yue Y., Liu T.-Y., Li D., Wu Y. (2013) Fluorescence-Enhanced Sensing Mechanism of BSA-Protected Small Gold-Nanoclusters to Silver(I) Ions in Aqueous Solutions. *The Journal of Physical Chemistry C* **117**, 16159–16165. DOI: 10.1021/jp403466b.

[187] Lin H., Imakita K., Fujii M., Sun C., Chen B., Kanno T., Sugimoto H. (2017) New insights into the red luminescent bovine serum albumin conjugated gold nanospecies. *Journal of Alloys and Compounds* **691**, 860–865. DOI: 10.1016/j.jallcom.2016.08.300.

[188] Zoppellaro G., Ostruszka R., Siskova K. (2024) Engineered protein-iron and/or gold-protein-iron nanocomposites in aqueous solutions upon UVA light: Photo-induced electron transfer possibilities and limitations. *Journal of Photochemistry and Photobiology A: Chemistry* **450**, 115415. DOI: 10.1016/j.jphotochem.2023.115415.

[189] Ostruszka R., Půlpánová D., Pluháček T., Tomanec O., Novák P., Jirák D., Šišková K. (2023) Facile One-Pot Green Synthesis of Magneto-Luminescent Bimetallic Nanocomposites with Potential as Dual Imaging Agent. *Nanomaterials* **13**, 1027. DOI: 10.3390/nano13061027.

[190] Simms G.A., Padmos J.D., Zhang P. (2009) Structural and electronic properties of protein/thiolate-protected gold nanocluster with "staple" motif: A XAS, L-DOS, and XPS study. *The Journal of Chemical Physics* **131**. DOI: 10.1063/1.3268782.

[191] Weerawardene K.L.D.M., Aikens C.M. (2016) Theoretical Insights into the Origin of Photoluminescence of $Au_{25}(SR)_{18}^-$ Nanoparticles. *Journal of the American Chemical Society* **138**, 11202–11210. DOI: 10.1021/jacs.6b05293.

[192] Siskova K., Tucek J., Machala L., Otyepkova E., Filip J., Safarova K., Pechousek J., Zboril R. (2012) Air-stable nZVI formation mediated by glutamic acid: solid-state storable material exhibiting 2D chain morphology and high reactivity in aqueous environment. *Journal of Nanoparticle Research* **14**, 805. DOI: 10.1007/s11051-012-0805-9.

[193] Šišková K., Machala L., Tuček J., Kašlík J., Mojzeš P., Zbořil R. (2013) Mixtures of l-Amino Acids as Reaction Medium for Formation of Iron Nanoparticles: The Order of Addition into a Ferrous Salt Solution Matters. *International Journal of Molecular Sciences* **14**, 19452–19473. DOI: 10.3390/ijms141019452.

[194] Babes L., Denizot B., Tanguy G., Le Jeune J.J., Jallet P. (1999) Synthesis of Iron Oxide Nanoparticles Used as MRI Contrast Agents: A Parametric Study. *Journal of Colloid and Interface Science* **212**, 474–482. DOI: 10.1006/jcis.1998.6053.

[195] Andrade Â.L., Souza D.M., Pereira M.C., Fabris J.D., Domingues R.Z. (2010) pH effect on the synthesis of magnetite nanoparticles by the chemical reduction-precipitation method. *Química Nova* **33**, 524–527. DOI: 10.1590/S0100-40422010000300006.

[196] Ueno H.M., Urazono H., Kobayashi T. (2014) Serum albumin forms a lactoferrin-like soluble iron-binding complex in presence of hydrogen carbonate ions. *Food Chemistry* **145**, 90–94. DOI: 10.1016/j.foodchem.2013.07.143.

[197] Jolivet J.-P., Chanéac C., Tronc E. (2004) Iron oxide chemistry. From molecular clusters to extended solid networks. *Chem. Commun.* **4**, 477–483. DOI: 10.1039/B304532N.

[198] Cao X.-L., Li H.-W., Yue Y., Wu Y. (2013) pH-Induced conformational changes of BSA in fluorescent AuNCs@BSA and its effects on NCs emission. *Vibrational Spectroscopy* **65**, 186–192. DOI: 10.1016/j.vibspec.2013.01.004.

[199] Russell B.A., Kubiak-Ossowska K., Mulheran P.A., Birch D.J.S., Chen Y. (2015) Locating the nucleation sites for protein encapsulated gold nanoclusters: a molecular dynamics and fluorescence study. *Physical Chemistry Chemical Physics* **17**, 21935–21941. DOI: 10.1039/C5CP02380G.

27

5. Seznam publikací

I   **Ostruszka R.**, Zoppellaro G., Tomanec O., Pinkas D., Filimonenko V., Šišková K. (2022) Evidence of Au(II) and Au(0) States in Bovine Serum Albumin-Au Nanoclusters Revealed by CW-EPR/LEPR and Peculiarities in HR-TEM/STEM Imaging. *Nanomaterials*, **12**:1425. DOI: https://doi.org/10.3390/nano12091425.

II   **Ostruszka R.**, Půlpánová D., Pluháček T., Tomanec O., Novák P., Jirák D., Šišková K. (2023) Facile One-Pot Green Synthesis of Magneto-Luminescent Bimetallic Nanocomposites with Potential as Dual Imaging Agent. *Nanomaterials*, **13**:1027. DOI: https://doi.org/10.3390/nano13061027.

III   Zoppellaro G., **Ostruszka R.**, Šišková K. (2024) Engineered protein-iron and/or gold-protein-iron nanocomposites in aqueous solutions upon UVA light: Photo-induced electron transfer possibilities and limitations. *Journal of Photochemistry & Photobiology A: Chemistry* **450**:115415. DOI: https://doi.org/10.1016/j.jphotochem.2023.115415.

IV   **Ostruszka R.**, Halili A., Pluháček T., Rárová L., Jirák D., Šišková K. (2024) Advanced protein-embedded bimetallic nanocomposite optimized for *in vivo* fluorescence and magnetic resonance bimodal imaging. *Journal of Colloid And Interface Science* **663**, 467-477. DOI: https://doi.org/10.1016/j.jcis.2024.02.116.